

AD-A128 612

LATITUDINAL VARIATIONS OF AURORAL-ZONE IONIZATION  
DISTRIBUTION(U) SRI INTERNATIONAL MENLO PARK CA  
J F VICKREY ET AL. FEB 83 AFOSR-TR-83-0389

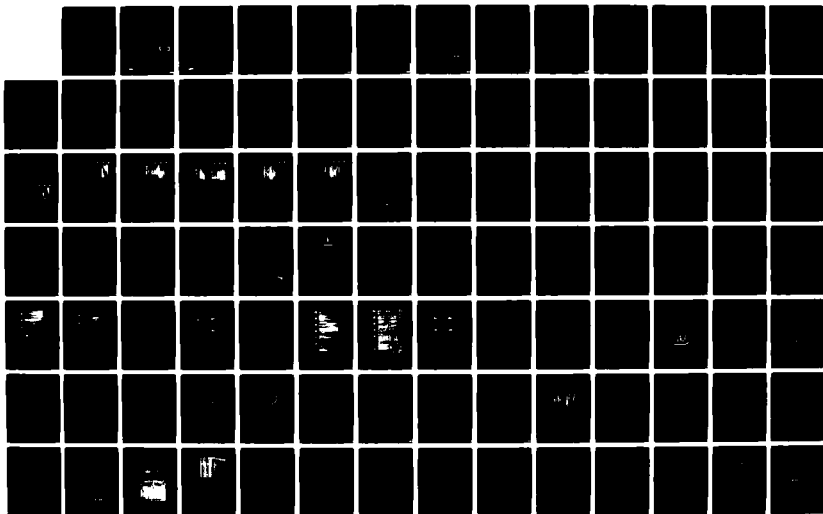
1/3

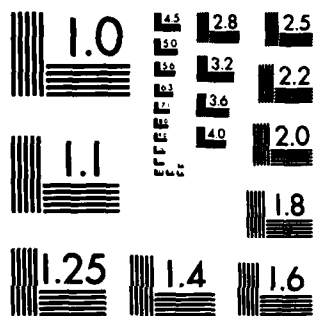
UNCLASSIFIED

F49620-80-C-0014

F/G 4/1

NL





MICROCOPY RESOLUTION TEST CHART  
NATIONAL BUREAU OF STANDARDS-1963-A

10

AD A128612

Final Scientific Report

February 1983

**LATITUDINAL VARIATIONS OF AURORAL-ZONE  
IONIZATION DISTRIBUTION**

By: JAMES F. VICKREY ROBERT M. ROBINSON ROLAND T. TSUNODA

Prepared for:

DEPARTMENT OF THE AIR FORCE  
AIR FORCE OFFICE OF SCIENTIFIC RESEARCH (AFSC)  
BOLLING AIR FORCE BASE  
WASHINGTON, DC 20332  
Attention: LT. COL. TED S. CRESS

CONTRACT F49620-80-C-0014

DTIC  
ELECTE  
MAY 26 1983  
B

DTIC FILE COPY

Approved for public release;  
distribution unlimited.



333 Ravenswood Avenue  
Menlo Park, California 94025 U.S.A.  
(415) 326-6200  
Cable: SRI INTL MPK  
TWX: 910-373-2046

83 05 23 02 8

# SRI International



*Final Scientific Report*

*February 1983*

## **LATITUDINAL VARIATIONS OF AURORAL-ZONE IONIZATION DISTRIBUTION**

**By: JAMES F. VICKREY      ROBERT M. ROBINSON      ROLAND T. TSUNODA**

*Prepared for:*

DEPARTMENT OF THE AIR FORCE  
AIR FORCE OFFICE OF SCIENTIFIC RESEARCH (AFSC)  
BOLLING AIR FORCE BASE  
WASHINGTON, DC 20332  
Attention: LT. COL. TED S. CRESS

CONTRACT F49620-80-C-0014

SRI Project 1181

AIR FORCE OFFICE OF SCIENTIFIC RESEARCH (AFSC)  
NOTICE OF TRANSFER OF RIGHTS  
This technology is the property of the Air Force and is  
approved for release under E.O. 11652-12.  
Distribution is unlimited.  
MATTHEW J. KEMER  
Chief, Technical Information Division

*Approved by:*

ROBERT S. LEONARD, *Director*  
*Radio Physics Laboratory*  
DAVID D. ELLIOTT, *Vice President*  
*Research and Analysis Division*

333 Ravenswood Avenue • Menlo Park, California 94025 • U.S.A.  
(415) 326-6200 • Cable: SRI INTL MPK • TWX: 910-373-2048



UNCLASSIFIED

SECURITY CLASSIFICATION OF THIS PAGE (When Data Entered)

REPORT DOCUMENTATION PAGE		READ INSTRUCTIONS BEFORE COMPLETING FORM
1. REPORT NUMBER <b>AFOSR-TR- 83 - 0389</b>	2. GOVT ACCESSION NO. <b>AD-A128612</b>	3. RECIPIENT'S CATALOG NUMBER
4. TITLE (and Subtitle)  <b>LATITUDINAL VARIATIONS OF AURORAL-ZONE IONIZATION DISTRIBUTION</b>		5. TYPE OF REPORT & PERIOD COVERED  <b>Final Scientific Report Covering the period 01 Dec 1979 through 30 Nov 1982</b>
7. AUTHOR(s)  <b>James F. Vickrey Robert M. Robinson Roland T. Tsunoda</b>		6. PERFORMING ORG. REPORT NUMBER  <b>SRI Project 1181</b>
9. PERFORMING ORGANIZATION NAME AND ADDRESS  <b>SRI International 333 Ravenswood Avenue Menlo Park, California 94025</b>		8. CONTRACT OR GRANT NUMBER(s)  <b>F49620-80-C-0014</b>
11. CONTROLLING OFFICE NAME AND ADDRESS  <b>Air Force Office of Scientific Research Building 410 Bolling AFB, D.C. 20332</b>		10. PROGRAM ELEMENT, PROJECT, TASK AREA & WORK UNIT NUMBERS  <b>61102F 2310/A2</b>
14. MONITORING AGENCY NAME & ADDRESS (if diff. from Controlling Office)		12. REPORT DATE <b>Feb. 1983</b>
		13. NO. OF PAGES <b>214</b>
		15. SECURITY CLASS. (of this report)  <b>Unclassified</b>
16. DISTRIBUTION STATEMENT (of this report)  <b>Approved for public release; distribution unlimited.</b>		15a. DECLASSIFICATION/DOWNGRADING SCHEDULE  <b>N/A</b>
17. DISTRIBUTION STATEMENT (of the abstract entered in Block 20, if different from report)		
18. SUPPLEMENTARY NOTES		
19. KEY WORDS (Continue on reverse side if necessary and identify by block number)  <b>Ionospheric Conductivities Plasma Structure Convection Diffusion Convective Instabilities</b> <i>ionization in the auroral zone</i>		
20. ABSTRACT (Continue on reverse side if necessary and identify by block number)  <b>During the past three years SRI International has conducted a research program supported by the Air Force Office of Scientific Research to study ionization in the auroral zone. This study involved data reduction and analysis to determine (1) the electrodynamics of the auroral E layer and (2) the origin and evolution of high-latitude F-region plasma-density structure. Data obtained by the Chatanika incoherent-scatter radar as well as by rockets and satellites were used in the study. The results are especially useful in characterizing the morphology of E-region</b>  <b>continued</b>		

**DD FORM 1473**  
1 JAN 73  
EDITION OF 1 NOV 65 IS OBSOLETE

1  
UNCLASSIFIED  
SECURITY CLASSIFICATION OF THIS PAGE (When Data Entered)

UNCLASSIFIED

SECURITY CLASSIFICATION OF THIS PAGE (When Data Entered)

19. KEY WORDS (Continued)

20. ABSTRACT (Continued)

conductivity enhancements, and the production, transport, and decay of F-region plasma throughout the auroral zone. The relationship between currents (both perpendicular and field-aligned) and electric fields has also been studied. In addition to these experimental investigations, SRI has contributed new theoretical concepts in the areas of cross-field plasma diffusion and global plasma-density irregularity morphology.

## CONTENTS

I	INTRODUCTION . . . . .	1
II	AURORAL E-REGION STUDIES . . . . .	3
	A. Auroral Zone Ionospheric Conductivity . . . . .	3
	B. Relationship Between Ionospheric Conductivity and Birkeland Currents . . . . .	5
	C. Relative Contributions of Conductivity and Electric Field to the Auroral Electrojets . . . . .	6
	D. Variability of the Harang Discontinuity . . . . .	7
	E. Energy Deposition by Precipitating Particles and Joule Dissipation in the Auroral Ionosphere . . . . .	7
III	AURORAL F-REGION IONIZATION STRUCTURE . . . . .	11
	A. A Model of High-Latitude Irregularity Morphology . . . . .	11
	B. E-Region Effects on F-Region Cross-Field Diffusion . . . . .	12
	C. Coordinated Radar Measurements with ISIS 1 . . . . .	13
	D. East-West Structure in the Auroral F-Region . . . . .	15
	E. Sources of Auroral F-Region Plasma Density Enhancements . . . . .	15
IV	LIST OF JOURNAL PUBLICATIONS AND INVITED REVIEW PRESENTATIONS PRODUCED UNDER SUPPORT FROM THIS CONTRACT . . . . .	17
	A. Journal Publications . . . . .	17
	B. Manuscripts in Preparation . . . . .	18
	C. Invited Review Talks . . . . .	19
V	REFERENCES . . . . .	21
APPENDIX:	Reprints/Preprints of Selected Publications Produced Under Support From This Contract . . . . .	23

## I INTRODUCTION

Supported by the Air Force Office of Scientific Research, we have conducted an intensive research program during the past three years. The research has been concentrated in two broad areas: (i) the electro-dynamics and structure of the auroral E-layer, and (ii) the origin, evolution, and morphology of high-latitude F-region plasma density structure. The principle experimental resource used in this research has been data collected with the Chatanika incoherent-scatter radar; however, ancillary measurements from rockets and satellites have been used when possible where appropriate. In addition to experimental investigations, we have contributed new theoretical concepts in the areas of cross-field plasma diffusion and global plasma-density irregularity morphology.

Because of the breadth of this research effort, summarizing the results is somewhat cumbersome. Therefore, in the following two sections we have briefly listed the principal conclusions of most of our separate studies. The list is grouped according to the two main research areas mentioned above. This is followed by a list of the twenty journal publications produced all or in part under this contract. Finally, we conclude with an appendix containing reprints and preprints of those journal articles in which a principal contributing author was supported by this contract.



Accession For	
NTIS GRA&I	<input checked="checked" type="checkbox"/>
DTIC TAB	<input type="checkbox"/>
Unannounced	<input type="checkbox"/>
Justification	
PER CALL JC	
By	
Distribution/	
Availability Codes	
Dist	Avail and/or Special
A	

## II AURORAL E-REGION STUDIES

Our auroral E-region studies have been principally based on eight days of synoptic Chatanika radar data in which the radar beam scanned the magnetic meridian. The days represent a variety of seasons and magnetic conditions. With this technique, the radar is able to measure the altitude-latitude distribution of electron density and line-of-sight plasma drift, from which the electric field, conductivity, and current are determined. Also, by examining many such successive scans, the latitude-local time variations of the auroral ionosphere may be determined. Although the limits of the scans vary slightly from one experiment to another, gathering useful data to a minimum elevation angle of  $15^\circ$  is generally possible. Thus, at the 100-km altitude, geomagnetic latitudes from  $62^\circ$  to  $68^\circ$  are scanned.

### A. Auroral Zone Ionospheric Conductivity

A key element in modelling the magnetosphere-ionosphere circuit is the auroral zone ionospheric conductivity because it represents the "load" on the magnetospheric generator and in large part, determines the ionospheric closure path for field-aligned currents. A consistent description of the gross, large-scale features of auroral zone conductivity morphology is beginning to emerge. Our observations, as well as those of others indicate, however, that the temporal and spatial microstructure of high-latitude ionospheric phenomena seldom show consistently repeatable patterns, particularly during substorms. Among the conductivity patterns that seem typical are:

- (1) During the daytime ( $\chi \leq 87^\circ$ ), the solar contribution to conductivity is well represented by  $\Sigma_p = 5 \cos^{1/2}(\chi)$  and  $\Sigma_H = 10 \cos^{1/2}(\chi)$ , where  $\chi$  is the solar zenith angle. These conductivities can be considered as the minimum present, with substantial increases occurring during substorms.

- (2) The nighttime height-integrated Hall and Pedersen conductivities within the diffuse aurora are generally 4 mho to 12 mho and 2 mho to 6 mho, respectively. South of the diffuse aurora, within the trough, they are at times  $< 0.5$  mho. During substorms, the Hall and Pedersen conductivities increase to values exceeding 50 mho and 25 mho, respectively.
- (3) The typical latitude/local-time precipitation pattern expands southward during substorm conditions and intensifies, thus enhancing the ionospheric conductivity. Later, as the recovery phase begins, the precipitation pattern contracts northward and diminishes. The precipitation onset and cessation can, at times, be as abrupt as a few minutes.
- (4) The southern boundary of the diffuse aurora  $B_{DA}$  in the midnight sector moves equatorward with increasing magnetic activity. We found that for the very quiet December day ( $K_p = 1+$ ; College K = 0)  $B_{DA} \geq 69^\circ$  geomagnetic latitude; on the April day ( $K_p = 2-$ ; College K = 1)  $B_{DA} \approx 65^\circ$ ; and for the very active November day ( $K_p = 4+$ ; College K = 7)  $B_{DA}$  was  $< 62^\circ$ . This equatorward motion is similar to that reported by other investigators [e.g., Lui et al., 1975; Sheehan and Carovillano, 1978], although the data base presented here is too small to derive an empirical relationship.

Among the features of our observations which do not fit a generally expected pattern are:

- (1) During the negative bay magnetic disturbance on a December day,  $\Sigma_H$  was considerably enhanced at southern latitudes and  $\Sigma_p$  was not. This is an indication of a hard energy spectrum of the precipitating electrons at these latitudes. Because this

event was observed at 1500 UT (0500 LT), it apparently was not the southern edge of a westward traveling surge.

- (2) On an April day the Harang discontinuity was quite sharp in local time; at the northernmost latitudes the Harang discontinuity was  $\leq 30$  min of local time in width and became narrower with decreasing latitude. This is in contrast to the Chatanika observations of Wedde et al. [1977] and Horwitz et al. [1978], which show the width of the Harang discontinuity to be 2 to 3 hours at the northernmost latitudes and  $\sim 1$  hour in the south. Another unusual feature observed on this day was a decrease in  $\Sigma_H/\Sigma_P$ , which indicates a decreasing precipitating particle hardness associated with the Harang discontinuity.

#### B. Relationship Between Ionospheric Conductivity and Birkeland Currents

Triad satellite field-aligned current measurements were combined with Chatanika radar electron-density measurements to study the latitudinal distribution of conductivity in the various field-aligned current regions. In the Region 2 field-aligned current sheet of the evening sector, the Pedersen conductivity increases linearly with latitude across the current sheet. The value of the Pedersen conductivity at the equatorward edge of the sheet varied inversely with the width of the current sheet. Also, the total change in Pedersen conductivity was large if the conductivity at the equatorward edge was small. In Region 1, enhanced conductivities were found more often in the poleward portion of the current sheet. In the Region 2 current sheet of the morning sector, the Pedersen conductivity was between 8 and 16 mho and relatively uniform across the current sheet. The Hall conductivity was higher and showed much larger latitudinal variations. The ionization in the Region 2 current sheet of the morning sector was produced by precipitating electrons from a Maxwellian source of density between 0.3 and 0.5  $\text{cm}^{-3}$ . This source was hotter and denser than the source of precipitation in the Region 2 current sheet of the evening sector. When incorporated into auroral electrodynamic models,

these results may be important in realistically accounting for observed variations in electric field and current.

C. Relative Contributions of Conductivity and Electric Field  
To the Auroral Electrojets

A fundamental question of auroral physics is whether the magnetosphere is a constant-voltage source of a constant-current source. Observationally, we examine the relationships between the magnitude of the electrojet currents and the electric field and conductivity. We have done this in a study combining Chatanika radar profiles of electric field and conductivity versus latitude with data from the Alaska magnetometer chain. We have found that the character of the electrojets is a function of local time. In the region of moderate-to-large eastward electrojet ( $j_x \geq 0.2$  A/m) in the evening sector, the northward electric field is the main contributor to the magnitude of electrojet current, in the sense that the field magnitude is larger compared with the southward field magnitude in the westward electrojet. However, when the eastward electrojet is very weak, say  $j_x < 0.2$  A/m, the electric field can maintain a reasonably large value of 10 to 20 mV/m. Thus, the intensification of an already moderate eastward electrojet seems principally to be caused by an enhancement of the northward electric field. If the eastward electrojet current density is very small, however, any increase or decrease may depend on small changes (maximum 10 mho) in the Hall conductivity.

Our study indicates that the westward electrojet may have two modes: one in which the contributions to the electrojet magnitude are "conductivity dominant," and the other in which the contributions to the electrojet magnitude are "electric-field dominant." Statistically, the westward electrojet near midnight and in early morning hours is principally characterized by the relatively high Hall conductivity, whereas the westward electrojet in the late morning sector is dominated by the large southward electric field. The latter behavior is similar to that of the eastward electrojet in the evening sector, although the sense of the electric field is reversed. However, an important difference is that the Hall conductivity can become high in the late morning westward electrojet (as high



as 50 mho) while the maximum conductivity for the evening eastward electrojet was less than 20 mho in our data set. In other words, both the southward field and the Hall conductivity appear to be important contributors to the intense westward electrojet in the late morning sector.

#### D. Variability of the Harang Discontinuity

Traditionally, the Harang discontinuity has been defined in terms of ground magnetic-field variations. Often, the electrojet currents are assumed Hall currents; hence, the current reversal coincides with the reversal of the convection electric field. For purposes of modelling, the reversal of the electric field is of greater significance because the physical processes occurring within the Harang discontinuity can be most effectively understood in terms of electric-field signatures. Because of the extensive use of ground magnetic-fluctuation signatures to define and describe the Harang discontinuity, we decided to compare the two signatures directly using Chatanika observations and Alaska magnetometer chain data.

The Harang discontinuity, as defined by the reversal of the north-south electric field, is 1 to 2° poleward of the discontinuity identified by the conventional method of using ground magnetic perturbations. The relative location of auroral conductivity enhancements with respect to the electric field reversal, is quite variable, depending perhaps upon substorm time. During relatively quiet times and the early stage of a substorm, a conductivity enhancement occurs only on the poleward side of the Harang discontinuity defined by the electric-field reversal, whereas the enhancement surges equatorward extending beyond the discontinuity during the maximum to recovery phase of a substorm.

#### E. Energy Deposition by Precipitating Particles and Joule Dissipation in the Auroral Ionosphere

The contribution to high-latitude thermospheric heating by particle precipitation and Joule dissipation of electric fields often dominates the direct solar EUV input. This energy deposition by particles and

electric fields, which can be highly structured, spatially and temporally, can perturb the atmospheric electron density, ion composition, electron and ion temperatures, and neutral air motion. In our studies we have concentrated on two aspects of auroral energy deposition:

- (i) The partitioning of energy deposition between precipitating particles and Joule heating. (The motivation here is that Joule heating preferentially heats ions while precipitating electrons preferentially heat thermal electrons through the production of low-energy secondaries; hence the thermospheric response to, and the altitude of, energy deposition may be different for the two sources.)
- (ii) Variations of the rate of energy deposition with local time.

As in all of our studies we must emphasize that the day-to-day variability of auroral phenomena is very large. Thus, any particular day's data may appear quite different from any composite characterization. Nevertheless, on the basis of eight days of synoptic data we have characterized the morphology of auroral energy deposition as follows:

- (1) The Joule heating rate and the precipitating particle energy deposition rate increase with increasing electrojet current, i.e., with increasing substorm intensity.
- (2) The pattern of precipitating particle energy deposition in the auroral zone moves rapidly southward and intensifies during a substorm, recedes northward, and diminishes during the substorm recovery phase.
- (3) The particle energy deposition rate associated with the morning-sector westward electrojet is higher than that for the evening-sector eastward electrojet.
- (4) The rate of increase in particle energy deposition with increasing westward electrojet current is equal to or exceeds that for an eastward electrojet current.
- (5) The Joule heating rate for a given magnitude of electrojet current is higher in the evening-sector eastward electrojet than in the morning-sector westward electrojet.

- (6) The rate of increase of Joule heating with electrojet current intensity is larger for an eastward electrojet than for a westward electrojet.
- (7) Joule heating generally dominates particle energy deposition in the premidnight sector. However, the daily averages of both energy inputs are roughly equal.
- (8) Energy is deposited by both Joule heating and precipitating particles at lower altitudes in the morning sector than in the premidnight sector.

We found that Banks' [1977] description of the Joule heating pattern as "horseshoe shaped" and corresponding to the auroral oval with a minimum in the midnight sector is generally valid for both particle and Joule heating. However, the Harang discontinuity, where the minimum of Joule heating occurs, can be very narrow in local time. Moreover, if a sub-storm occurs near local midnight, there may be no minimum at all. Perhaps more importantly, the horseshoe must be viewed as asymmetrical with respect to local midnight. The opposing asymmetries of particle and Joule heating are self-consistent when viewed in terms of the change in ionospheric conductivity between the evening and morning sectors. Morning-sector precipitation tends to be harder than evening-sector precipitation, and thus enhances the Hall-to-Pedersen conductivity ratio [see Section II-A]. As a result, the westward electrojet current vector is more nearly perpendicular to the electric field, and therefore less dissipative than is the eastward electrojet current.

### III AURORAL F-REGION IONIZATIO STRUCTURE

The plasma in the auroral F layer is structured horizontally (perpendicularly to the earth's magnetic field) on scales ranging from tens of kilometers to meters. This structure can result from a variety of sources, including structured particle precipitation, structured electric-field patterns, and plasma instabilities [see review by Vickrey and Kelley, 1982]. In addition to the purely scientific interest in this plasma structure there are practical reasons for studying it: it can hinder satellite communications and surveillance systems.

The great range of irregularity scale sizes present in the auroral F region makes it necessary to combine different experimental techniques. For example, the Chatanika incoherent-scatter radar can resolve irregularities of about 10-km scale size. Scintillation measurements are sensitive to irregularities in the medium scale regime ( $\leq 1$  km), and in situ probes can resolve structure down to meters. Our F-layer studies have benefitted greatly from drawing upon all of these techniques and we foresee that future studies, by necessity, will also require multi-instrument observations.

#### A. A Model of High-Latitude Irregularity Morphology

We have developed a simple model of irregularity morphology at high latitudes based on specifying (i) the "source function" in latitude and local time of irregularity production, (ii) the (scale-size dependent) lifetime of irregularities once produced, and (iii) the redistribution of irregularities by convection during their lifetime. Although this model framework is simple, it has proven very useful in the interpretation of a wide range of observations. For example the model reproduces the following key aspects of irregularity morphology:

- (1) Observations of irregularities throughout the polar regions.

- (2) A reduction of irregularity amplitude in the central polar cap.
- (3) A steep gradient in irregularity intensity at the equatorward edge of the nighttime magnetospheric convection zone.
- (4) An asymmetry between the dusk and dawn sectors of the equatorward boundary of the high-latitude irregularity zone during magnetically quiet times.

Because F-region irregularities are observed over a much larger area of the polar ionosphere than is structured precipitation, convection must play an important role in distributing these irregularities. However, because the diffusive lifetime of irregularities is proportional to the square of the scale size, 100-km scale structures cannot survive the transit of the polar cap without an additional production source. We suggest that the  $\vec{E} \times \vec{B}$ /current convective instability, which can be driven by field-aligned currents, electric fields, or both, is the key process that provides a source of wave energy at the intermediate scale and that drift waves play an important role at smaller scales. The lifetime of large-scale (10-km) irregularities may be reduced slightly below that expected from classical diffusion, but not enough to prevent their crossing the polar cap. On the other hand, these combined processes increase the time during which smaller-scale structure is observed in the plasma.

#### B. E-Region Effects on F-Region Cross-Field Diffusion

The dominant process involved in determining the lifetime of F-region irregularities is the diffusion of plasma across magnetic field lines. Because these field lines electrically couple the E and F regions, the plasma populations in the two zones interact. Thus, the presence of a dense E-region, as is often the case in the auroral zone, can strongly affect the F-region diffusion rate, and, hence, the lifetime of F layer irregularities. We have developed a simple model of classical cross-field diffusion which includes E region coupling. The model shows that:

- (1) The classical cross-field plasma diffusion rate in the F-region ionosphere can be increased by an order of magnitude or more when the magnetic field lines connect to a highly conducting E-layer below.
- (2) The cross-field diffusion rate is strongly affected by the height of the F-layer and the ratio of E- to F-region Pedersen conductivities.
- (3) The presence of a conducting E region slows instability growth and limits the lifetime of small-scale F-region irregularities, once their production source is removed, but does not prevent the routine operation of instabilities in the high-latitude ionosphere.
- (4) E-region image striations tend to slow F-region diffusion but are themselves damped by recombination if the background E-region electron density exceeds a value,  $n_c$ , given by  $n_c \approx 2 \times 10^4 / \lambda^2 \text{ cm}^{-3}$ , where  $\lambda$  is measured in kilometers.

To further examine Point (4) on image striations, we have developed a simple linear model of image formation. An image results principally from a converging velocity field operating on a compressible ion gas. Our model shows that this process is highly scale size selective. By comparing our model to equatorial rocket measurements we have shown that the spectrum of density structure observed off the magnetic equator is consistent with that expected from the image formation process (which depends on scale size and density) driven by the gravitational Rayleigh-Taylor instability operating on the bottomside F layer at the equator itself.

#### C. Coordinated Radar Measurements with ISIS 1

In addition to the studies involving only the radar data (and to some extent plasma theory), we conducted coordinated measurements with the Chatanika radar and the ISIS 1 satellite. These simultaneous measurements included the topside sounder and cylindrical electrostatic probe (CEP) when the satellite was at a height of about 700 m.

The variation of electron density with invariant latitude at the satellite, at least on the scale of a hundred to a few hundred kilometers, agreed reasonably well with the radar results even though the satellite displacement changed from almost coincident to about 500 km magnetic west of the radar scan path. Two scatter signatures observed on the ISIS ionograms were associated with two particular large-scale irregularities that were identified in the radar data. These irregularities had dimensions of a few tens of kilometers in the magnetic north-south direction. A density enhancement was observed in the CEP data corresponding to one of these irregularities. The scattering detected by the sounder was caused by 30-to-60-m wavelength irregularities (small scale) that presumably were created by instabilities operating on the edges of the large-scale irregularities. The small scale irregularities, however, were observed outside the region in which the gradient-drift instability operates. These irregularities thus either convected to the point of observation or were field-aligned extensions of irregularities generated at lower heights.

ISIS 1 telemetry dropouts resulting from small- or medium-scale irregularities, and enhanced irregularities down to about 200-m scale size observed with the CEP, were observed where the large-scale density gradients were greatest. Natural, intense, Cerenkov radio noise was observed on the ionograms recorded in the auroral zone, indicating the presence of precipitating keV electrons. A few minutes after these ionograms were recorded the radar scanned the same invariant latitude region and a large-scale ionization enhancement or "blob," not present 13 min earlier, had developed in the bottomside F layer. A statistical study using ISIS 1 data indicated that spread F caused by irregularities near the satellite height have, in general, a sharp equatorial boundary that tends to occur a few degrees equatorward of the region where keV electrons precipitate. This agrees with the modeling results described in Section III-A.

#### D. East-West Structure in the Auroral F-Region

As has been alluded to in the earlier discussion, large-scale plasma density enhancements appear to be an integral feature of the auroral F region. These enhancements, which we have termed "blobs," were initially discovered and studied using Chatanika radar data that were taken with the radar scanning the magnetic meridian. Although these early studies provided a great deal of information on the latitudinal structure of blobs, they were not optimized for detecting east-west structure.

In November 1981, we conducted a specific campaign to measure and study any east-west structure in blobs. The zonal density gradients are generally less steep than meridional ones, but, nevertheless, can be significant. In one particular blob, we found that the observed longitudinal structure was consistent with production by precipitation at the largest scales ( $\geq 500$  km) and by the gradient drift instability at scale sizes of  $\sim 150$  km. Although the smaller scale structure was consistent with the gradient drift process, it may have also been produced by structured precipitation. The resolution of which process is dominant will require experiments that combine in situ particle detector data with the radar measurements.

#### E. Sources of Auroral F-Region Plasma Density Enhancements

Preliminary evidence suggests that blobs in the auroral F layer are produced by two distinct sources of localized soft-particle precipitation. One source is believed associated with the inner edge of the central plasma sheet where the electron energy has been found to soften with decreasing magnetic L-shell values. Enhanced low-energy electron precipitation from this magnetospheric region produces the "boundary blob," a persistent feature found near the equatorward boundary of the auroral oval. The boundary blob is extended in longitude, often exceeding 12 hours of local time. The other source that produces more longitudinally confined blobs is believed to be inverted-V events. Although other sources may exist beside the soft-particle precipitation associated with the inner edge of the plasma sheet and inverted-V events, the identified sources provide a useful foundation from which the physics of F-region plasma-density structure may be studied.



IV LIST OF JOURNAL PUBLICATIONS AND INVITED REVIEW  
PRESENTATIONS PRODUCED UNDER SUPPORT FROM THIS CONTRACT

A. Journal Publications

- Vickrey, J. F., R. R. Vondrak, and S. J. Matthews, "The Diurnal and Latitudinal Variation of Auroral-Zone Ionospheric Conductivity," J. Geophys. Res., Vol. 86, No. A1, pp. 65-75 (January 1981).
- Kelley, M. C., J. F. Vickrey, C. W. Carlson, and R. Torbert, "On the Origin and Spatial Extent of High Latitude Irregularities," J. Geophys. Res., Vol. 87, No. A6, pp. 4469-4475 (June 1982).
- Vickrey, J. F., and M. C. Kelley, "The Effects of a Conducting E-Layer on F-Region Cross-Field Plasma Diffusion," J. Geophys. Res., Vol. 87, No. A6, pp. 4461-4468 (June 1982).
- Vickrey, J. F., R. R. Vondrak and S. J. Matthews, "Energy Deposition by Precipitating Particles and Joule Dissipation in the Auroral Ionosphere," J. Geophys. Res., Vol. 87, No. A7, pp. 5184-5196 (July 1982).
- Vickrey, J. F. and M. C. Kelley, "Irregularities and Instabilities in the Auroral F-Region," in High Latitude Space Plasma Physics (Plenum Publishing Corp., New York, N.Y.) in press, 1982.
- Muldrew, D. B. and J. F. Vickrey, "High Latitude F Region Irregularities Observed Simultaneously with ISIS 1 and the Chatanika Radar," J. Geophys. Res., Vol. 87, No. A10, pp. 8263-8272 (October 1982).
- Rino, C. L., and J. F. Vickrey, "Recent Results in Auroral Zone Scintillation Studies," J. Atmos. Terr. Phys., Vol. 44, No. 10, pp. 875-887 (1982).
- Tsunoda, R. T., and J. F. Vickrey, "Evidence of East-West Structure in Large-Scale Auroral F-Region Ionization Enhancements," submitted to J. Geophys. Res., 1982.
- Kamide, Y., and J. F. Vickrey, "Relative Contribution of Ionospheric Conductivity and Electric Field to the Auroral Electrojets," Accepted for publication in J. Geophys. Res., 1982.
- Kamide, Y., and J. F. Vickrey, "Variability of the Harang Discontinuity as Observed by the Chatanika Radar and the IMS Alaska Magnetometer Chain," in press, Geophys. Res. Letts., 1982.

Gonzales, C. A., M. C. Kelley, R. A. Behnke, J. F. Vickrey, R. Wand and J. Holt, "On the Latitudinal Variations of the Ionospheric Electric Field During Magnetospheric Disturbances," submitted to J. Geophys. Res., 1982.

Villain, J. P., R. A. Greenwald, and J. F. Vickrey, "HF Ray Tracing in the Auroral Zone Using Measured Meridional Electron Density Distributions," submitted to Radio Sci., 1982.

Vickrey, J. F., M. C. Kelley, and R. Pfaff, "Low Altitude Image Striations Associated with Bottomside Equatorial Spread F--Observations and Theory," submitted to J. Geophys. Res., 1982.

Ahn, B.-H., R. M. Robinson, Y. Kamide, and S.-I. Akasofu, "Electric Conductivities, Electric Fields, and Auroral Particle Energy Injection Rate in the Auroral Ionosphere and Their Empirical Relations to the Horizontal Magnetic Disturbances," submitted to J. Geophys. Res., 1982.

B. Manuscripts in Preparation

Tsunoda, R. T., and R. M. Robinson, "Solar Cycle Dependence of Plasma Density Enhancements in the Auroral F-Region," to be submitted to J. Geophys. Res., 1983.

Tsunoda, R. T., and R. M. Robinson, "Properties of F-Region Plasma Density Enhancements near the Equatorward Boundary of the Auroral Oval," to be submitted to J. Geophys. Res., 1983.

Robinson, R. M., S. Mende, R. Vondrak, and S. Harris, "Simultaneous Incoherent Scatter and Photometric Observations of a TYPE A Red Aurora," to be submitted to J. Geophys. Res., 1983.

Tsunoda, R. T., R. M. Robinson, and C. Senior, "Two Possible Sources of Plasma-Density Enhancements in the Auroral F-Layer," to be submitted to Geophys. Res. Letts., 1983.

Robinson, R. M., and T. A. Potemra, "Latitudinal Variations of Auroral Zone Conductivity Within the Field-Aligned Current Sheets," to be submitted to J. Geophys. Res., 1983.

Robinson, R. M., R. T. Tsunoda, and C. I. Meng, "A Source of F-Region Ionization Enhancements at the Equatorward Edge of the Auroral Oval," to be submitted to J. Geophys. Res., 1983.

C. Invited Review Talks

Vickrey, J. F., "A Review of Recent Chatanika Results," lecture presented at the United Kingdom EISCAT School, University of Leicester, Leicester, England (September 1980).

Vickrey, J. F., M. C. Kelley, and C. L. Rino, "A Review of High-Latitude Ionospheric Irregularities-Experimental Results," International Association of Geomagnetism and Aeronomy, Fourth Scientific Assembly, Edinburgh, Scotland (August 1981).

Rino, C. L., and J. F. Vickrey, "Recent Results in Auroral-Zone Scintillation Studies," URSI, XXth General Assembly, Washington, D.C. (August 1981).

Vickrey, J. F., and M. C. Kelley, "Irregularities and Instabilities in the Auroral F-Region," Nobel Symposium on Problems in High-Latitude Magnetospheric/Ionospheric Plasma Physics and Strategies for the Solution, Kiruna, Sweden (March 1982).

Vickrey, J. F., and M. C. Kelley, "Structured Plasma in the Auroral Ionosphere," 1982 International Conference on Plasma Physics, Goteborg, Sweden (June 1982).

Vickrey, J. F., and C. L. Rino, "Joint Incoherent-Scatter and Scintillation Observations of High Latitude Ionospheric Irregularities--Implications for Global Morphology," URSI International Symposium on Radio Probing of the High-Latitude Ionosphere and Atmosphere: New Techniques and New Results, Fairbanks, Alaska (August 1982).

#### REFERENCES

- Banks, P. M., "Observations of Joule and Particle Heating in the Auroral Zone," J. Atmos. Terr. Phys., Vol. 39, No. 2, pp. 179-193 (February 1977).
- Horwitz, J. L., J. R. Doupnik, and P. M. Banks, "Chatanika Radar Observations of the Latitudinal Distributions of Auroral Zone Electric Fields, Conductivities, and Currents," J. Geophys. Res., Vol. 83, No. A10, pp. 1463-1481 (October 1978).
- Lui, A. T. Y., C. D. Anger, and S.-I. Akasofu, "The Equatorward Boundary of the Diffuse Aurora and Auroral Substorms as Seen by the ISIS 2 Auroral Scanning Photometer," J. Geophys. Res., Vol. 80, No. 25, pp. 3603-3614 (September 1975).
- Sheehan, R. E., and R. L. Carovillano, "Characteristics of the Equatorward Auroral Boundary near Midnight Determined from DMSP Images," J. Geophys. Res., Vol. 83, pp. 4749-4754 (October 1978).
- Vickrey, J. F., and M. C. Kelley, "Irregularities and Instabilities in the Auroral F-Region," in High Latitude Space Plasma Physics (Plenum Publishing Corp., New York, N.Y.) in press, 1982.
- Wedde, T., J. R. Doupnik, and P. M. Banks, "Chatanika Observations of the Latitudinal Structure of Electric Fields and Particle Precipitation on November 21, 1975," J. Geophys. Res., Vol. 82, No. 19, pp. 2743-2757 (July 1977).

Appendix:

PREPRINTS/REPRINTS OF SELECTED PUBLICATIONS

PRODUCED UNDER SUPPORT FROM THIS CONTRACT

APPENDIX  
TABLE OF CONTENTS

The Diurnal and Latitudinal Variation of Auroral Zone Ionospheric Conductivity ( <u>JGR</u> , <u>86</u> (A1), 65-75, January 1, 1981) . . . . .	27
The Effects of a Conducting E Layer on Classical F Region Cross-Field Plasma Diffusion ( <u>JGR</u> , <u>87</u> (A6), 4461-4468, June 1, 1982) . . . . .	39
On the Origin and Spatial Extent of High- Latitude F Region Irregularities ( <u>JGR</u> , <u>87</u> (A6), 4469-4475, June 1, 1982). . . . .	47
Energy Deposition by Precipitating Particles and Joule Dissipation in the Auroral Ionosphere ( <u>JGR</u> , <u>87</u> (A7), 5184-5196, July 1, 1982) . . . . .	55
Irregularities and Instabilities in the Auroral F Region (High Latitude Space Plasma Physics) . . . . .	69
High-Latitude F Region Irregularities Observed Simultaneously with ISIS 1 and the Chatanika Radar ( <u>JGR</u> , <u>87</u> (A10), 8263-8272, October 1, 1982). . . . .	89
Recent Results in Auroral-Zone Scintillation Studies ( <u>JATP</u> , <u>44</u> (10), 875-887, 1982) . . . . .	99
Variability of the Harang Discontinuity as Observed by the Chatanika Radar and the IMS Alaska Magnetometer Chain ( <u>GRL</u> , <u>10</u> (2), 159-162, February 1983) . . . . .	111
Evidence of East-West Structure in Large-Scale F-Region Plasma Enhancements in the Auroral Zone (Submitted to <u>JGR</u> , 1982). . . . .	117
Relative Contribution of Ionospheric Conductivity and Electric Field to the Auroral Electrojets (Submitted to <u>JGR</u> , 1982). . . . .	149
Low-Altitude Image Striations Associated with Bottomside Equatorial Spread F--Observations and Theory (Submitted to <u>JGR</u> , 1983) . . . . .	181

## The Diurnal and Latitudinal Variation of Auroral Zone Ionospheric Conductivity

JAMES F. VICKREY, RICHARD R. VONDRAK, AND STEPHEN J. MATTHEWS

Radio Physics Laboratory, SRI International, Menlo Park, California 94025

The great spatial and temporal variability of auroral ionospheric conductivity significantly influences the ionospheric closure path for high-latitude, field-aligned currents. Because these closure paths can extend to low latitudes, changes in auroral zone conductivity can influence the global electric field distribution. In this paper, synoptic Chatanika radar observations of auroral zone conductivity that cover  $\sim 62^\circ$  to  $68^\circ$  geomagnetic latitude are presented. They are representative of quiet winter, active winter, and equinoctial conditions. During the daytime the solar contribution to the height-integrated conductivity is well represented by  $\Sigma_{p,H} \approx (5, 10) \cos^{1/2}(\chi)$ , where  $\chi$  is the solar zenith angle. The nighttime, height-integrated Pedersen and Hall conductivities ( $\Sigma_p$  and  $\Sigma_H$ ) in the electron density trough are, at times, below our detection threshold of  $\sim 0.5$  mho. Following magnetic substorm onset, enhanced conductivity regions move southward and intensify. As the recovery phase begins, the conductivity pattern recedes northward and diminishes. The onset and cessation of precipitation associated with these events can be as abrupt as a few minutes. In one example the behavior of  $\Sigma_p$  and  $\Sigma_H$  are examined in the vicinity of the Harang discontinuity, which was quite sharp ( $\approx 30$  min) in local time. At the Harang discontinuity on that day, the ratio of  $\Sigma_H$  to  $\Sigma_p$  decreased, indicating a softening of the precipitating energy distribution.

## INTRODUCTION

Our understanding of the large-scale current systems of the magnetosphere and ionosphere has evolved greatly in recent years, largely as a result of the growing number of in situ and ground-based measurements of high-latitude phenomena. (Recent reviews of this subject include: Kamide [1979]; Potemra [1979]; Stern [1979]; and Swift [1979]). The general morphology (at least during magnetically quiet times) of auroral zone electrodynamics is emerging. For example, large-scale electric field measurements from satellites [Cauffman and Gurnett, 1971; Heppner, 1977], balloons [Mozer and Lucht, 1974], and radars [Rino et al., 1974; Banks and Doupnik, 1975; Tsunoda, 1975; Greenwald, 1977; Evans et al., 1980] are generally consistent with a two-celled magnetospheric convection pattern such as Axford and Hines [1961] originally proposed. Also, it is well established that field-aligned, or Birkeland, currents are a permanent feature of the high-latitude ionosphere-magnetosphere system [Zmuda and Armstrong, 1974; Iijima and Potemra, 1976a, b].

Recent evidence indicates that the magnetospheric circuit is coupled to the ionosphere not only at high latitudes but globally as well. Observational evidence has directly linked ionospheric electric field perturbations at the equator with high-latitude disturbances [Gonzales et al., 1979; Gonzales, 1979; Kelley et al., 1979].

Attempts in modeling the global ionospheric circuit combine the statistical distribution of field-aligned currents, observed by the Triad satellite [Iijima and Potemra, 1976a, b; 1978], with a global conductivity model to determine the electric field distribution [Nisbet et al., 1978; Nopper and Carovillano, 1978; Kamide and Matsushita, 1979a, b; Gizler et al., 1979]. These modeling efforts have met with some success in reproducing the quiet-time global electric field pattern. Indeed, they have shown that for reasonable conductivity distributions, some portion of the high-latitude field-aligned current is closed by ionospheric currents as far away as the equator. A major difficulty in these models, however, lies in taking proper account of the auroral zone conductivity whose rapid temporal changes alter the transionospheric current clo-

sure path and, presumably, represent a time-varying load to the magnetospheric generator. Furthermore, present models generally do not take into account the interdependence between the field-aligned current distribution and the ionospheric conductivity variations. One purpose of this paper is to present synoptic Chatanika incoherent scatter observations of auroral zone conductivity during varying magnetic conditions that can aid in modeling the global patterns of electric field and current.

Brekke et al. [1974], Mehta [1978], Horwitz et al. [1978], and others have given examples of conductivity measurements by the Chatanika radar. In this paper we present three sets of data from continuous observations of approximately 24-hours duration. These data have a spatial and temporal resolution which is improved over previous measurements. We selected the 3 days of data to illustrate auroral ionospheric behavior for a variety of magnetic conditions and different seasons. Thus, in addition to contrasting magnetically quiet and active winter days, we present data from equinoctial conditions, which illustrate the solar contribution to ionospheric conductivity. We have analyzed the data to determine the ionospheric electric field, current, conductivity, and auroral energy deposition over the latitude range of approximately  $62^\circ$  to  $68^\circ$ . In this paper we concentrate on the conductivity variations; the detailed discussion of other electrodynamic parameters will be given in a later paper.

## TECHNIQUE

The observational mode employed for the measurements discussed below consists of continuous scans of the radar beam in the magnetic meridional plane [Vondrak and Baron, 1976]. With this technique the radar beam is able to probe the altitude/latitude distribution of electron density and line-of-sight plasma drift from which the electric field, conductivity, and current are determined. Also, by examining many such successive scans, the latitude/local time variations of the auroral ionosphere may be examined. Although the limits of the scan vary slightly from one experiment to another, it is generally possible to gather useful data to a minimum elevation angle of  $15^\circ$ . Thus, at the 100-km altitude, geomagnetic latitudes from  $62^\circ$  to  $68^\circ$  are scanned. The scan rate is typically

Copyright © 1981 by the American Geophysical Union.

Paper number 80A0910.  
0148-0227/81/080A-0910\$01.00

65

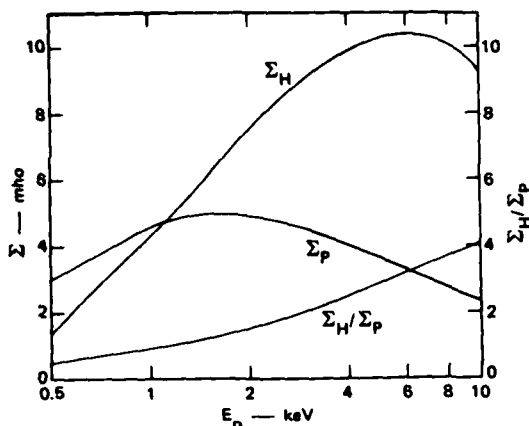


Fig. 1. Dependence of height-integrated Hall and Pedersen conductivities on the characteristic energy of precipitating electrons. The incoming electrons are assumed to have isotropic Maxwellian distribution, and the total particle flux at each energy is normalized to an incident energy flux of  $1 \text{ erg/cm}^2 \cdot \text{s}$ .

$0.2^\circ/\text{s}$ , and the data are averaged for 15 s. Depending on the scan limits, full scans are completed in 10 to 12 min. Electron density samples were obtained at range intervals of 4.5 km. The Hall and Pedersen conductivities are calculated from the measured electron densities and a model of the altitude variation of the neutral atmosphere and ion-neutral collision frequency.

The Hall conductivity  $\sigma_H$  and Pedersen conductivity  $\sigma_P$  are determined from the electron and ion momentum equations

that lead to the standard relation between the perpendicular electric field  $E$  and current  $j$ :

$$j = \sigma_P E - \sigma_H E \times B/B$$

The expressions used for the conductivity calculations are

$$\sigma_P = (ne/B)[\Omega_i \nu_i / (\Omega_i^2 + \nu_i^2)]$$

and

$$\sigma_H = (ne/B)[\nu_i^2 / (\Omega_i^2 + \nu_i^2)]$$

where  $n$  is electron density,  $e$  is the absolute value of the electron charge,  $B$  is the magnetic field strength,  $\Omega_i$  is the ion gyro-frequency, and  $\nu_i$  is the ion-neutral collision frequency. The effect of electron-neutral collisions is not included because it normally makes a negligible contribution to the total conductivity. The ion-neutral collision frequency is computed from the formula

$$\nu_i (\text{s}^{-1}) = 3.75 \times 10^{-10} n_n (\text{cm}^{-3})$$

where  $n_n$  is the total neutral number density obtained from the 1000°K thermosphere model of Banks and Kockarts [1973]. The collision frequency coefficient that we use is one half of the value given by Banks and Kockarts [1973], in order to take into account the reduced mass in transforming from the center-of-mass system to the laboratory system [cf. Rees and Walker, 1968; Stubbe, 1968]. Previous studies that have not included this reduction factor [e.g., Brekke et al., 1974; Mchta, 1978; Horwitz et al., 1978] have resulted in overestimates of the height-integrated conductivity by 5% to 30%, typically.

In the following section we present latitude/local time distributions of the height-integrated conductivities. The altitude profile of the conductivities is generally integrated between

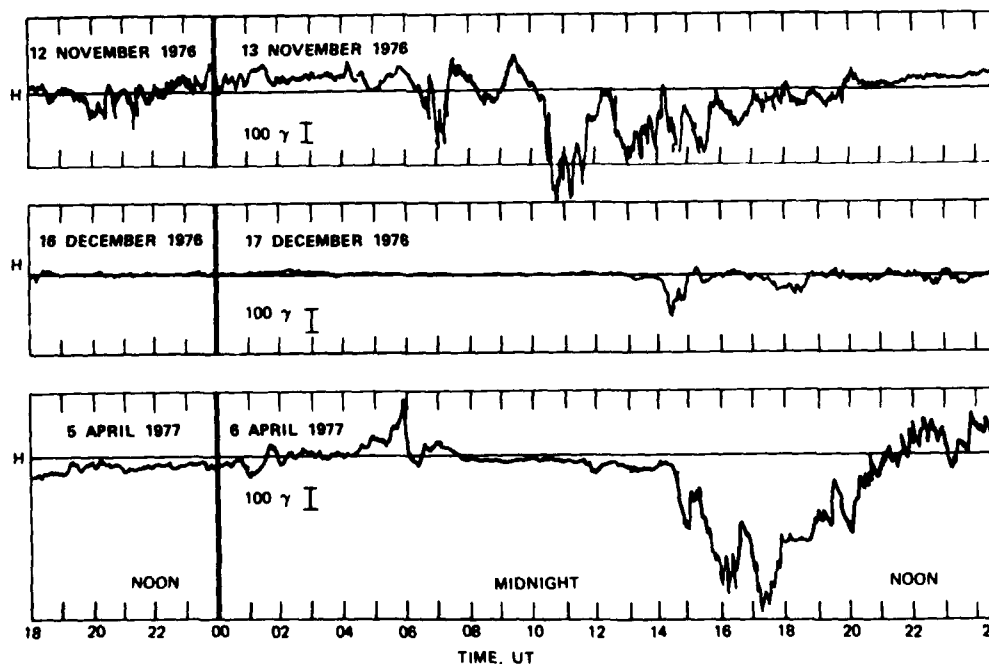


Fig. 2. Horizontal component of the college magnetograms for the 3 days of this study.



TABLE 1. Variation of Geomagnetic Activity and Solar Zenith Angle

Time, UT	November 13, 1976			December 17, 1976			April 6, 1977		
	Solar Zenith Angle, deg	College K	Kp	Solar Zenith Angle, deg	College K	Kp	Solar Zenith Angle, deg	College K	Kp
0000-0300	88-103	3	4+	92-106	1	2	63-79	3	4
0300-0600	103-121	3	4	106-125	1	2	79-97	4	4
0600-0900	121-133	6	5	125-138	0	1-	97-108	5	3
0900-1200	133-127	7	4+	138-133	0	1+	108-105	1	2-
1200-1500	127-110	7	4+	133-116	4	2+	105-89	4	4-
1500-1800	110-92	4	4+	116-98	4	3-	89-71	6	6-
1800-2100	92-83	4	4+	98-89	3	3+	71-59	5	6+
2100-2300	83-88	2	3-	89-92	3	4-	59-63	4	7

the altitudes of 70 km and 170 km; generally, the contribution to total conductivity at lower and higher altitudes is negligible.

The angular resolution of each measurement is given by the convolution of the  $0.6^\circ$  antenna beam width and the  $3^\circ$  of antenna motion during the 15-s integration period. Since at low elevation angles the height integration includes measurements from different latitudes, the latitude resolution of the measurements depends on elevation angle. Because the major contribution to the height-integrated conductivity is typically within an altitude extent of not more than 40 km however, the true latitudinal resolution at  $45^\circ$  elevation is about 40 km.

The measured height-integrated conductivities are useful

indicators of the flux and energy distribution of the precipitating auroral electrons that produce nighttime E region ionization. The dependence of the Hall and Pedersen conductivities on the characteristic electron energy  $E_0$  is shown in Figure 1. The incoming electrons are assumed to have isotropic Maxwellian distribution of the form  $f(E) = f_0 E \exp(-E/E_0)$ ; the total flux at each energy is normalized to an incident energy flux  $\Phi_E$  of  $1 \text{ erg/cm}^2 \cdot \text{s}$ . The conductivities are computed from steady state ionization profiles derived from the altitude profiles of energy deposition [Rees, 1963; Berger et al., 1970] as described by Vondrak and Baron [1976]. As expected, for soft electron fluxes that produce ionization primarily at high altitudes, the Pedersen conductivity is larger than

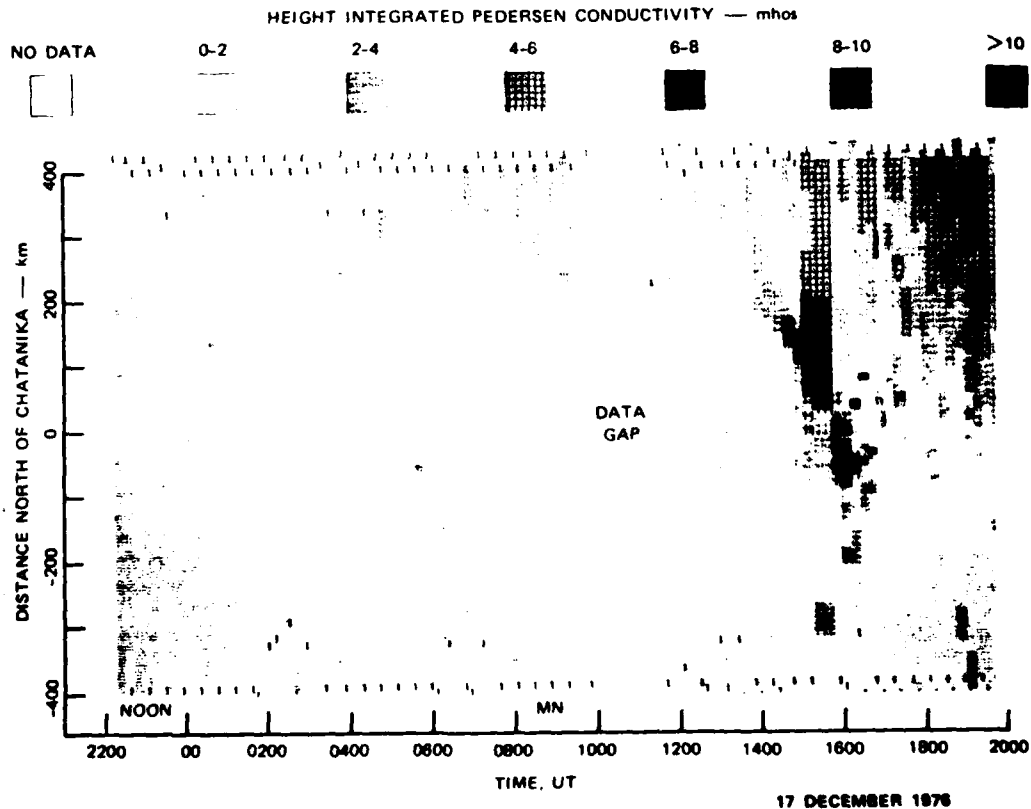


Fig. 3. Latitude-local time map of height-integrated Pedersen conductivity for December 17, 1976.

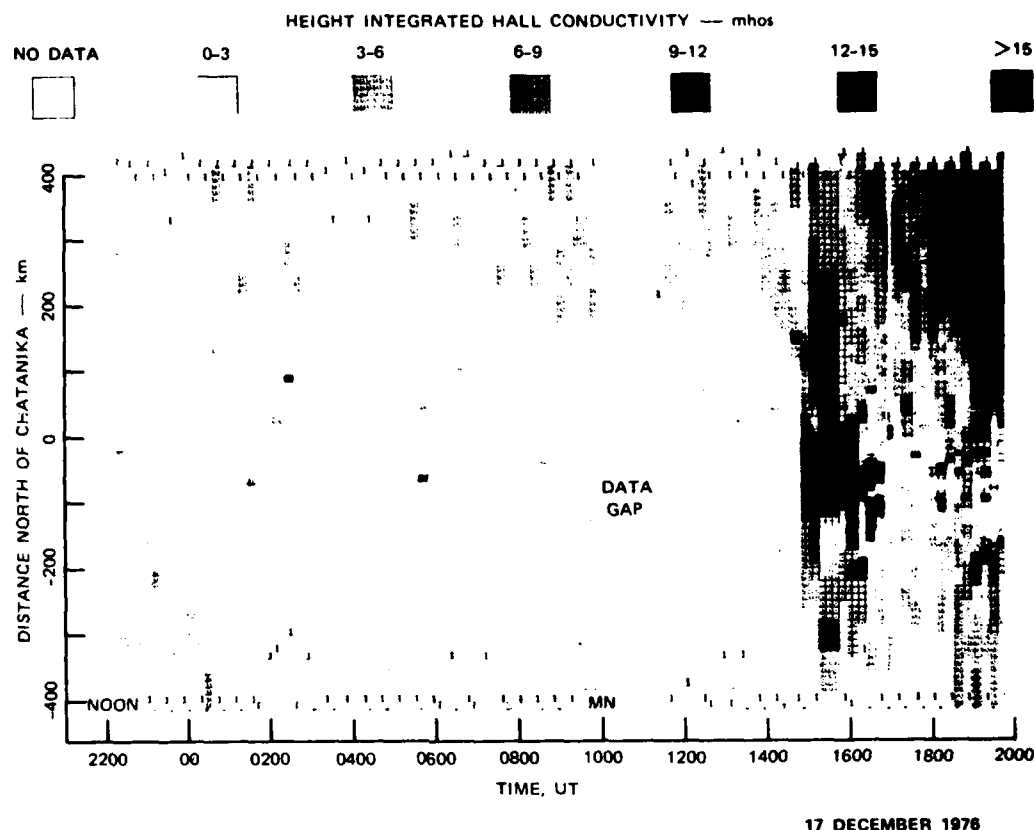


Fig. 4. Latitude-local time map of height-integrated Hall conductivity for December 17, 1976.

the Hall conductivity. As the characteristic energy of the electrons increases, they penetrate deeper into the atmosphere and result in larger Hall conductivity. The conductivity depends upon both the energy distribution and the total energy flux; in the steady state the conductivity is proportional to  $(\Phi_e)^{1/2}$ . For a given energy distribution, however, the ratio of conductivities is independent of total energy flux.

#### OBSERVATIONS AND INTERPRETATIONS

The three data sets that we will discuss were obtained on November 12-13, 1976; December 16-17, 1976; and April 5-6, 1977. Figure 2 displays the  $H$  component of the College magnetogram for these 3 days. The December day was very quiet until  $\sim 1500$  UT, when there was a negative bay of  $\sim 160$   $\gamma$ . During the April day a premidnight positive bay disturbance occurred at 0600 UT, and a series of larger ( $>700$   $\gamma$ ) substorms began around 1430 UT. These substorms continued well into the morning sector. November 13 to 14 was magnetically active throughout the period of observation. The data from these 3 days display a variety of magnetic activity, with examples of substorms occurring essentially at all local time sectors. Table 1 shows the variations of College  $K$ ,  $K_p$ , and solar zenith angle for the 3 days. Owing to the large solar zenith angles in November and December at Chatanika, the contribution of solar-produced ionization to ionospheric conductivity was significant only on the April day.

Figure 3 is a latitude/local time map of height-integrated Pedersen conductivity  $\Sigma_p$  for December 16-17, 1976. The ordinate represents the distance north of Chatanika, calculated for a reference height of 120 km. Generally, the peak of the altitude profiles of both the Pedersen and Hall volume conductivities are within 10 km of that reference height. The abscissa is universal time (local time = UT - 10 hours). The data gap from  $\sim 1000$  UT to 1100 UT results from the antenna being in a nonscanning mode. Figure 3 shows that from local noon until 10 PM,  $\Sigma_p$  was essentially uniform and less than 2 mho. The data are somewhat noisy during this time, however, because of the small amount of ionization present, particularly in the south. From  $\sim 0800$  UT to 1300 UT the conductivity is slightly enhanced at distances greater than 250 km north of Chatanika. This enhancement is associated with the equatorward boundary of the diffuse aurora. The precipitation associated with the negative bay magnetic disturbance at 1500 UT is evidenced by the enhanced  $\Sigma_p$  during this time. The southward progression and intensification of the precipitation (and hence conductivity) is a common occurrence following the onset of magnetic substorms.

Figure 4 shows, for the same day, a latitude/local time map of the height-integrated Hall conductivity in the same format as Figure 3. As one would expect, the variations in  $\Sigma_H$  are similar to those of  $\Sigma_p$ , with the quiet nighttime Hall conductivity south of the diffuse aurora being less than 3 mho. It

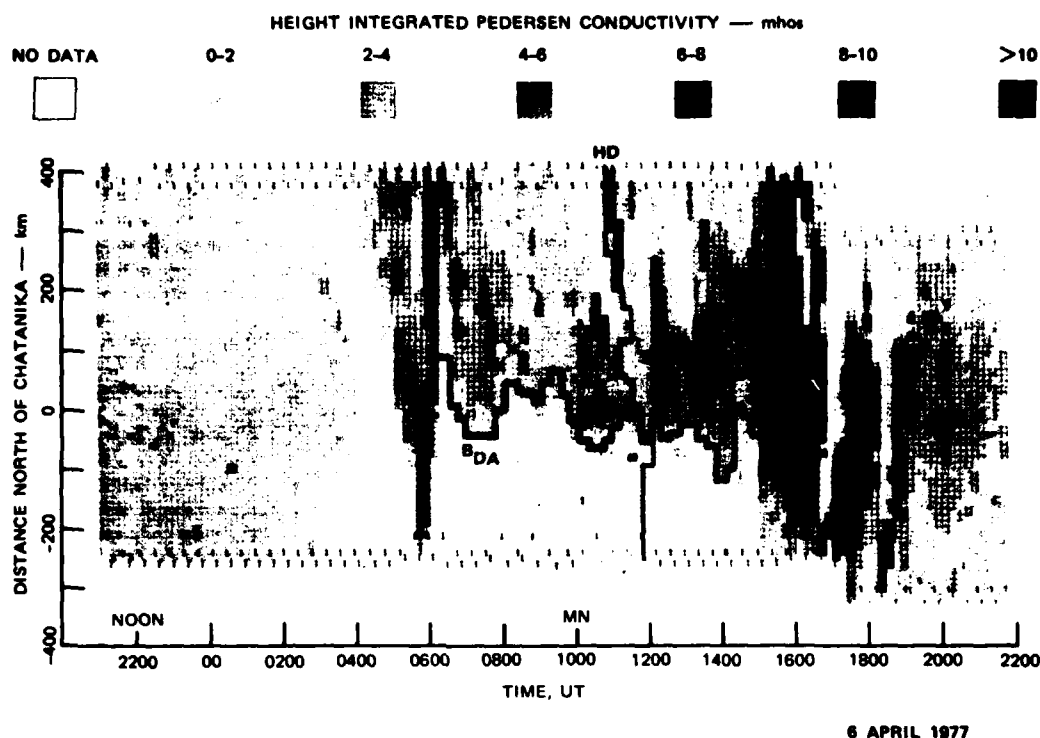


Fig. 5. Latitude-local time map of height-integrated Pedersen conductivity for April 6, 1977.

is interesting to compare the enhancements in  $\Sigma_H$  with those of  $\Sigma_P$  during the substorm at 1500 UT. Of particular interest is the fact that  $\Sigma_H$  is enhanced at the southernmost latitudes, and  $\Sigma_P$  is not. Thus, at the southern border of the precipitation pattern, the precipitating electron energy distribution is harder than further north. At these latitudes current flow is less dissipative than in the north, where the Pedersen conductivity is also enhanced. This pattern of precipitation, in which  $\Sigma_H$  is enhanced and  $\Sigma_P$  is essentially unaffected, does not appear to be typical of most substorms, as we shall see. However, this condition cannot always be diagnosed because after the onset of a substorm, the southernmost region of precipitation often moves south of the radar field-of-view.

Figure 5 shows a latitude/local time map of  $\Sigma_P$  for April 5-6, 1977. Shortly after 1700 UT the scan limits of the radar were changed, which produced the discontinuity in the latitudinal coverage of the map. Simultaneous with the positive bay event at ~0600 UT, there was a southward progression of an enhanced conductivity region. As mentioned above, this is a typical pattern following substorm onset. The conductivity enhancement ended quite abruptly in the south as the recovery phase began. The series of substorms in the late morning sector (1500 UT to 1900 UT) produced an interesting conductivity distribution, namely, there were three regions of enhanced conductivity, at ~1430 UT-1630 UT, 1700 UT-1800 UT, and 1830 UT-1900 UT, which were separated by conductivity 'holes.' As in the positive bay event just described, the holes are produced by an abrupt decrease in precipitation at the onset of the substorm recovery phase (as determined from the College magnetogram).

The thick line in Figure 5 represents the location of the equatorward boundary of the diffuse aurora between 0600 UT and 1500 UT. We define this boundary as the southernmost latitude at which the peak *E* region electron density is greater than  $10^5 \text{ cm}^{-3}$ , the electron density normally observed in the diffuse aurora. This electron density is also consistent with rocket and satellite measurements [e.g., *Lui et al.*, 1977; *Evans and Moore*, 1979] that find the diffuse aurora to be generally produced by precipitating electrons with an energy flux of about  $1 \text{ erg/cm}^2\text{-s}$  and a characteristic Maxwellian energy of 0.5 to 2 keV. The ionization profiles generated by such elec-

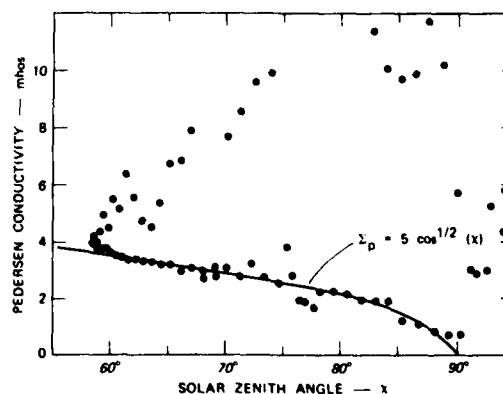


Fig. 6. Scatter plot of height-integrated Pedersen conductivity versus solar zenith angle for April 6, 1977.

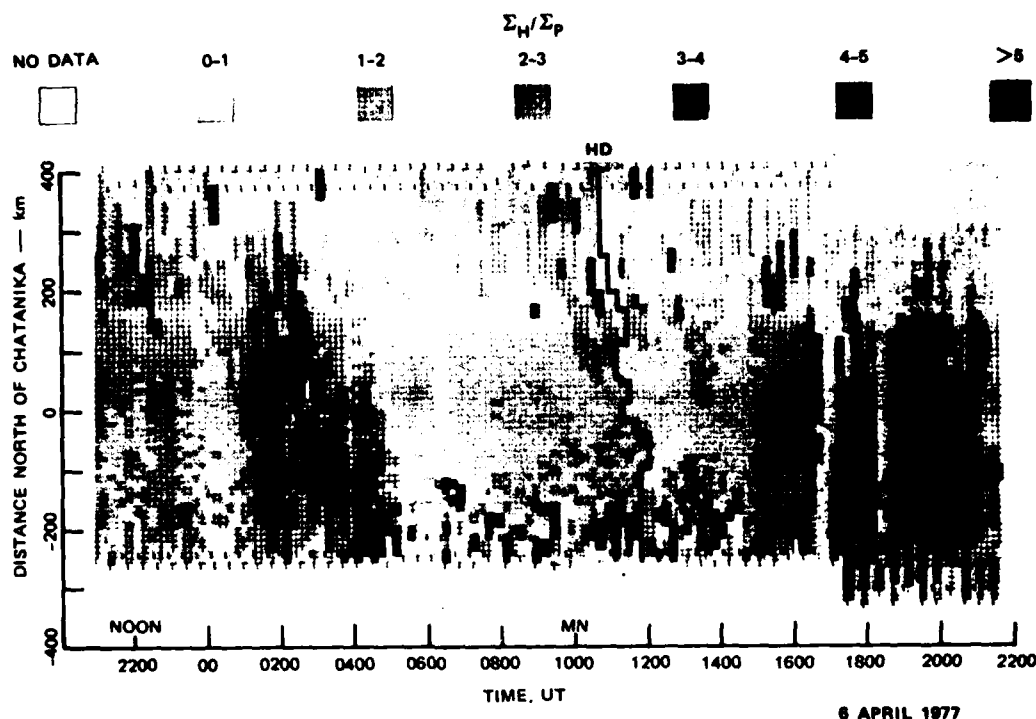


Fig. 7. Latitude-local time map of the ratio of Hall conductivity to Pederson conductivity for April 6, 1977.

tron beams have a peak density of about  $10^5 \text{ cm}^{-3}$  in the altitude interval of 115 to 140 km. During this entire period, when the College  $K$  index and  $K_p$  ranged between 1 and 5 and 2 to 4, respectively, the southern boundary of the diffuse aurora remained within 100 km of the Chatanika latitude of  $65^\circ$ . For the more quiet December day described above, this boundary was generally  $\geq 250$  km north of Chatanika during this time. As was the case for the December data, the height-integrated Pedersen conductivity at night, south of the diffuse aurora, is typically  $< 2$  mho.

During the daytime (1500 UT to 0500 UT) there is a solar contribution to conductivity on the April day. The variations in conductivity that are due to solar photoionization are illustrated in Figure 6, which is a scatter plot of  $\Sigma_p$  values, measured nearly overhead at Chatanika, as a function of solar zenith angle  $\chi$ . There are clearly large enhancements that are due to particle precipitation associated with substorms, but the minimum values, which presumably are due primarily to solar effects, follow the curve  $\Sigma_p = 5 \cos^{1/2}(\chi)$  quite well for  $\chi \leq 87^\circ$ . A similar relationship was found for  $\Sigma_H$  but with  $\Sigma_H$  being typically twice  $\Sigma_p$ . The parametric relation used is reasonable because in the steady state case photoionization produces a Chapman layer whose peak electron concentration is proportional to  $\cos^{1/2}\chi$ . However, for the limited data in Figure 6, other parametric relations are adequate representations, including the linear fit used by Mehta [1978]. The relationships for conductivity that are found here give lower values than those obtained by Mehta [1978], presumably because of the difference in collision models that were used in the analyses.

Figure 7 shows the variations in the ratio  $\Sigma_H/\Sigma_p$  for the April day. This ratio gives an indication of the hardness of precipitation when ionization is not primarily due to solar illumination. For example, as shown in Figure 1, the conductivity ratio increases from 0.9 to 4 as the characteristic energy of a Maxwellian beam increases from 1 keV to 10 keV. The enhancements in this ratio from 0100 UT to 0500 UT result from particle precipitation and are not an effect of the solar zenith angle. During the morning series of substorms, the Hall conductivity exceeded 50 mhos, with the ratio  $\Sigma_H/\Sigma_p$  greater than 5. Interestingly, the ratio  $\Sigma_H/\Sigma_p$  appeared to maximize at some latitudes before the abrupt cutoff that is associated with the morning sector precipitation holes of Figure 5. However, precipitation hardening is not always followed by a rapid cessation of precipitation. Moreover, the rapidity of the precipitation cessation apparent in Figures 4 and 6 at all latitudes within view is unusual. Typically, the behavior of the precipitation pattern is to move southward and intensify, then move back northward and gradually diminish.

It is interesting to examine the spatial and temporal variations in conductivity and precipitation hardness near the vicinity of the Harang discontinuity. The discontinuity was located by examining the time of reversal of the measured east-west current at each latitude and is represented by the thin line in Figures 5 and 7. On this particular day, the Harang discontinuity was found to be quite sharp in local time ( $\leq 30$  min), even at the northernmost latitudes. This is to be contrasted with the Chatanika observations of Wedde *et al.* [1977] and Horwitz *et al.* [1978], which showed the width of the Harang discontinuity to be 2 to 3 hours at the northernmost lati-

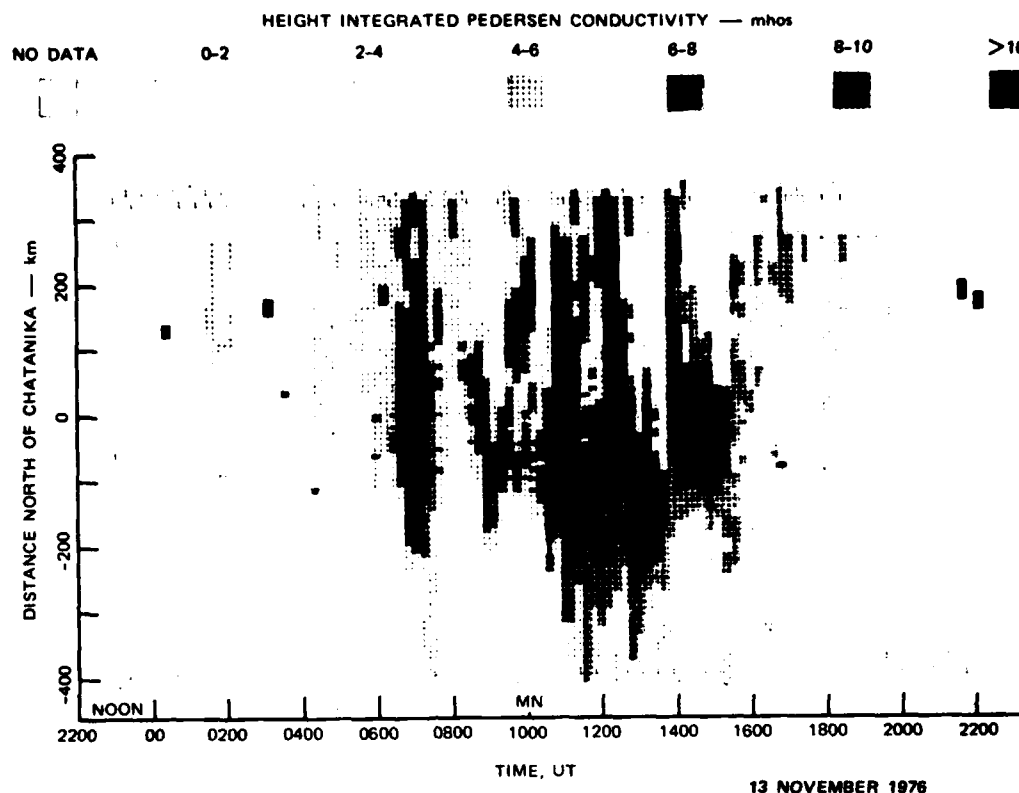


Fig. 8. Latitude-local time map of the height-integrated Pedersen conductivity for November 13, 1976.

tudes and  $\sim 1$  hour in the south. As can be seen from Figure 5, the precipitation was enhanced and, hence, so was the conductivity on the morning side of the Harang discontinuity. This agrees with the observations of Wedde *et al.* [1977]. However, although the precipitating particle flux was enhanced, the characteristic energy of that flux decreased.

In the conventional theoretical picture of magnetosphere-ionosphere coupling, one would expect an upward field-aligned current to flow at the Harang discontinuity fault line. The thought is that this current is carried by hard, precipitating electrons, and hence an auroral arc might be expected along the Harang discontinuity fault line. However, Figure 7 shows that coincident with the Harang discontinuity is a decrease in the ratio of the Hall conductivity to the Pedersen conductivity. Thus, on this particular day, the precipitation energy spectrum associated with the Harang discontinuity softened. This softening explains the discrepancy between our estimate of the width (in local time) of the Harang discontinuity, based on the reversal of the east-west current, and the values given by Wedde *et al.* [1978], which were based on the reversal of the north-south electric field. In the vicinity of the Harang discontinuity, the predominant electric field component is westward. Thus, if the Pedersen conductivity in this region is dominant over the Hall conductivity, the east-west current reversal may be only slightly affected by the reversal of the north-south electric field component.

It should be pointed out that our measurements of the local

time variations of the Harang discontinuity give no information on the instantaneous longitudinal structure of the discontinuity. As a result there is an ambiguity between spatial and temporal variations in the data. The Scandinavian Twin Auroral Radar Experiment (Stare) radar measurements reported by Nielsen and Greenwald [1979] do contain information on the longitudinal structure of the electric field pattern. Their data, which cover latitudes from  $68^\circ$  to  $72^\circ$ , show the discontinuity to be east-west aligned but temporally dynamic. During periods of high  $K_p$  the discontinuity can surge equatorward with speeds up to 600 m/s. However, as Chatanika passed beneath the discontinuity on April 5-6,  $K_p$  was 2- and the College  $K$  index was 1. Under such quiet conditions, Nielsen and Greenwald's observations indicate that the speed at which the discontinuity might move is  $\sim 50$  m/s. Such speeds are too slow to explain the sharpness, in local time, of the discontinuity over our entire field of view in terms of a temporally dynamic discontinuity. Rather, it seems more likely that during a magnetically quiet period Chatanika rotated beneath a more-or-less fixed (spatially) discontinuity which was north-south aligned. This does not contradict the results of Nielsen and Greenwald, since at the higher latitudes of the Stare observations the discontinuity becomes east-west aligned in the premidnight sector.

On November 13, 1976, magnetic activity was present throughout the data-taking period, with 100- $\gamma$  positive bay activity from 2300 UT to 0600 UT and a 1300- $\gamma$  negative bay,

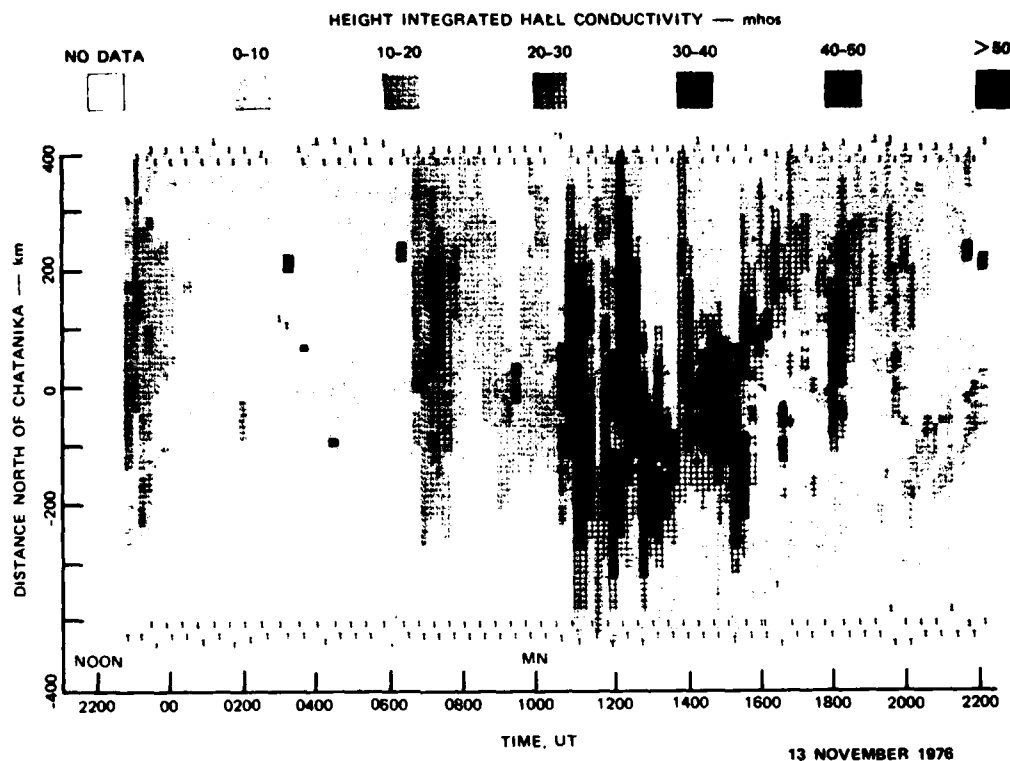


Fig. 9. Latitude-local time map of the height-integrated Hall conductivity for November 13, 1976.

beginning at 1030 UT. Figures 8 and 9 illustrate the latitude/local time variations in  $\Sigma_p$  and  $\Sigma_H$ . On this day the southern boundary of the diffuse aurora was located well south of Chatanika, from 0600 UT to ~1700 UT. During this same time interval,  $K_p$  was 4+ and the College  $K$  index reached 7.

To illustrate the altitude/latitude variations in electron density and conductivity that are associated with the latitude/local time maps discussed above, we present in Figures 10 and 11 the distributions in the magnetic meridional plane of the Hall and Pedersen volume conductivities  $\sigma_H$  and  $\sigma_P$ , respectively, and the electron density  $N_e$ , along with the latitudinal variations of  $\Sigma_H$  and  $\Sigma_P$  for two scans from November 13, 1976. The distributions shown in Figure 10 were measured at 1000 UT (2230 magnetic local time, MLT), when the College  $H$  component had just returned to the quiescent level from a period of positive bay magnetic activity. Thus, although these distributions are not representative of quiet conditions in the midnight sector, they do illustrate nonsubstorm conditions [Vondrak et al., 1977]. Under these conditions, the diffuse aurora was relatively uniform and unstructured, with its southern boundary located approximately 180 km south of Chatanika at this time. The Hall and Pedersen volume conductivities are, of course, also quite uniform with latitude, and they maximize at altitudes slightly below and above, respectively, the height of the electron density peak at ~115 km.

In contrast to Figure 10 are the distributions of conductivity and electron density measured under substorm conditions in the midnight sector at 1100 UT (~2330 MLT), as shown in Figure 11. In this case the peak electron density is consid-

erably higher (a factor of ~4) than it was in Figure 10. Also, the height of the  $E$  region peak  $N_e$  is ~100 km. The hardening of precipitation, and resultant lowering of the  $E$  region peak during the substorm, greatly enhanced the Hall volume conductivity (by a factor of ~16) over its nonsubstorm value. Also, the maximum of  $\sigma_H$  occurred near 100-km altitude. Of course, the height-integrated conductivities were also enhanced dramatically (note the scale change between Figures 10 and 11). During the substorm the southern boundary of the diffuse aurora moved far south of Chatanika and out of the field of view of the radar. Near Chatanika, the density and conductivity distributions (particularly  $\sigma_H$ ) became highly structured with latitude compared to the nonsubstorm case.

#### SUMMARY

As was discussed in the introduction, a consistent description of the gross features of high-latitude ionosphere/magnetosphere morphology appears to be emerging. The observations presented here and elsewhere illustrate, however, that the temporal and spatial microstructure of high-latitude ionospheric phenomena seldom show consistently repeatable patterns, particularly during substorms. Among the features that seem typical are:

1. During the daytime ( $\chi \leq 87^\circ$ ), the solar contribution to conductivity is well represented by  $\Sigma_p = 5 \cos^{1/2}(\chi)$  and  $\Sigma_H = 10 \cos^{1/2}(\chi)$ , where  $\chi$  is the solar zenith angle. This can be considered as the minimum conductivity present, with substantial increases occurring during substorms.
2. The nighttime height-integrated Hall and Pedersen

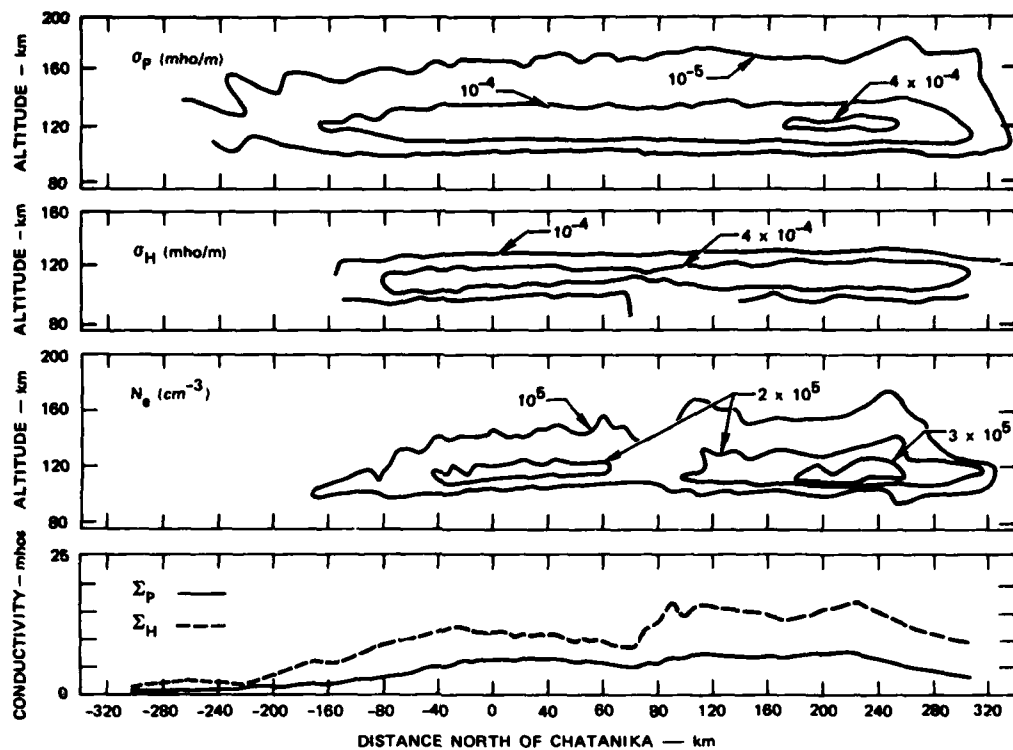


Fig. 10. Altitude-latitude variation of volume Pedersen and Hall conductivities and electron density with the associated latitudinal variations of height-integrated conductivity for active but nonsubstorm conditions.

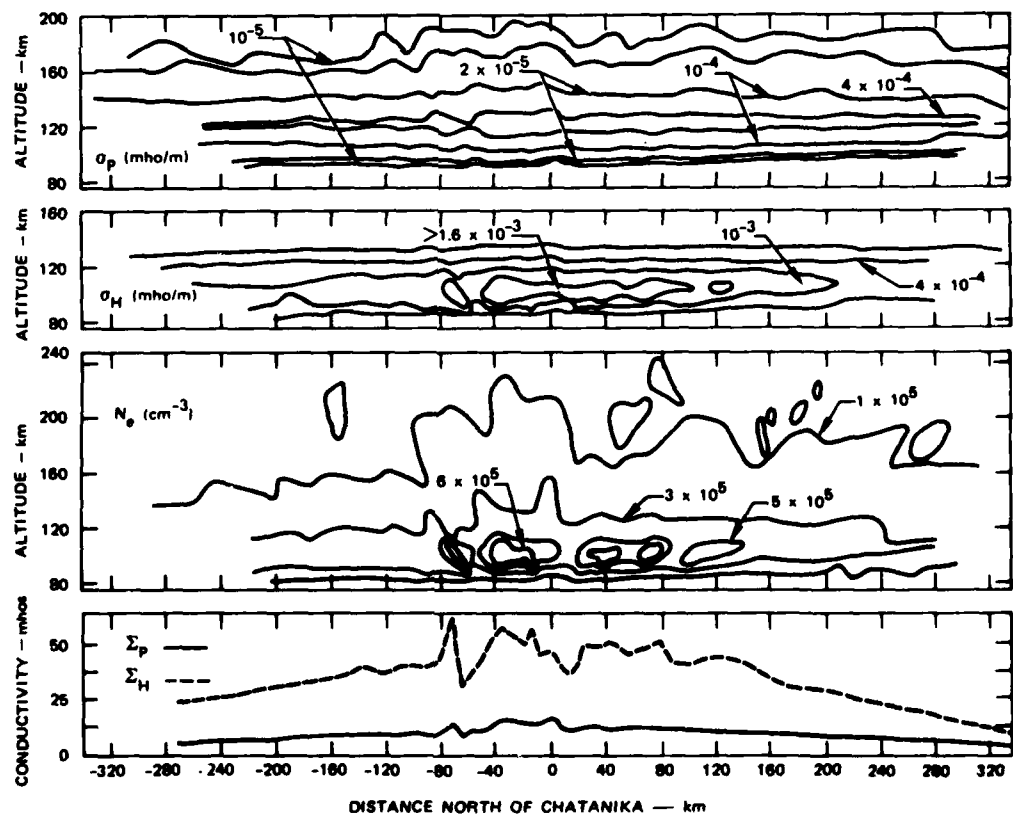


Fig. 11. Altitude-latitude variation of volume Pedersen and Hall conductivities and electron density with the associated latitudinal variation of height-integrated conductivity for active substorm conditions.

conductivities within the diffuse aurora are generally 4 mho to 12 mho and 2 mho to 6 mho, respectively. South of the diffuse aurora, within the trough, they are at times <0.5 mho. During substorms, the Hall and Pedersen conductivities increase to values exceeding 50 mho and 25 mho, respectively.

3. The typical latitude/local time behavior of precipitation during substorm conditions is to move south and intensify, thus enhancing the ionospheric conductivity. Later, as the recovery phase begins, the precipitation pattern moves northward and diminishes. The precipitation onset and cessation can, at times, be as abrupt as a few minutes.

4. The southern boundary of the diffuse aurora  $B_{DA}$  in the midnight sector moves equatorward with increasing magnetic activity. We found that for the very quiet December day ( $K_p = 1+$ ; College  $K = 0$ )  $B_{DA} \approx 69^\circ$  geomagnetic latitude; on the April day ( $K_p = 2-$ ; College  $K = 1$ )  $B_{DA} \approx 65^\circ$ ; and for the very active November day ( $K_p = 4+$ ; College  $K = 7$ )  $B_{DA}$  was  $<62^\circ$ . This equatorward motion is similar to that reported by other investigators [e.g., Lui et al., 1975; Sheehan and Carovillano, 1978], although the data base presented here is too small to derive an empirical relationship.

Among the observed features of this data set, which do not fit a generally expected pattern, are:

i. During the negative bay magnetic disturbance on the December day,  $\Sigma_H$  was considerably enhanced at southern latitudes where  $\Sigma_p$  was not. This is an indication of a hard energy spectrum of the precipitating electrons at these latitudes. Since this event was observed at 1500 UT (0500 LT), it apparently was not the southern edge of a westward traveling surge.

2. On the April day the Harang discontinuity was observed to be quite sharp in local time, at the northernmost latitudes the Harang discontinuity was  $\leq 30$  min of local time in width and became narrower with decreasing latitude. This is to be contrasted with the Chatanika observations of Wedde et al. [1977] and Horwitz et al. [1978], which showed the width of the Harang discontinuity to be 2 to 3 hours at the northernmost latitudes and  $\sim 1$  hour in the south. Another unusual feature observed on this day was a decrease in  $\Sigma_H/\Sigma_p$  indicative of a decreasing precipitating particle hardness associated with the Harang discontinuity.

**Acknowledgments.** We wish to acknowledge the helpful comments of R. T. Tsunoda. This work was supported by the Air Force Office of Scientific Research under Contract F49620-80-C-0014 and by the National Science Foundation under Grant ATM-7823658. Radar operations were supported by the Defense Nuclear Agency under Contract DNA 001-77-C-0042. Radar operations were performed by H. Burch, C. Code, and M. McCready.

The Editor thanks R. A. Greenwald and J. L. Horwitz for their assistance in evaluating this paper.

#### REFERENCES

- Axford, W. I., and C. O. Hines, A unifying theory of high-latitude geophysical phenomena and geomagnetic storms, *Can. J. Phys.*, **39**, 1433-1464, 1961.
- Banks, P. M., and J. R. Doupnik, A review of auroral zone electrodynamics deduced from incoherent scatter radar observations, *J. Atmos. Terr. Phys.*, **37**, 951-999, 1975.
- Banks, P. M., and G. Kockarts, *Aeronomy*, Part A, Academic, New York, 1973.
- Berger, M. J., S. M. Seltzer, and K. Maeda, Energy deposition by auroral electrons in the atmosphere, *J. Atmos. Terr. Phys.*, **32**, 1015-1045, 1970.
- Brekke, A., J. Doupnik, and P. Banks, Incoherent scatter measurements of E region conductivities and currents in the auroral zone, *J. Geophys. Res.*, **79**, 3773-3790, 1974.
- Caulfield, D. P., and D. A. Gurnett, Double-probe measurements of convection electric fields with the Injun 5 satellite, *J. Geophys. Res.*, **76**, 6014-6027, 1971.
- Evans, D. S., and T. E. Moore, Precipitating electrons associated with the diffuse aurora: Evidence for electrons of atmospheric origin in the plasma sheet, *J. Geophys. Res.*, **84**, 6451-6457, 1979.
- Evans, J. V., J. M. Holt, W. L. Oliver, and R. H. Wand, Millstone Hill incoherent scatter observations of auroral convection over  $60^\circ \leq \Lambda \leq 75^\circ$ , 2, Initial results, *J. Geophys. Res.*, **85**, 41-54, 1980.
- Gizler, V. A., V. S. Semenov, and D. A. Troshichev, Electric fields and currents in the ionosphere generated by field-aligned currents observed by Triad, *Planet. Space Sci.*, **27**, 223-231, 1979.
- Gonzales, C. A., Electric fields in the low-latitude ionosphere and their relationship to magnetospheric and interplanetary phenomena, Ph.D. thesis, Cornell Univ., Ithaca, N. Y., 1979.
- Gonzales, C. A., M. C. Kelley, B. G. Fejer, J. F. Vickrey, and R. F. Woodman, Equatorial electric fields during magnetically disturbed conditions, 2, Implications of simultaneous auroral and equatorial measurements, *J. Geophys. Res.*, **84**, 5803-5812, 1979.
- Greenwald, R. A., Recent advances in the use of radar auroral backscatter to measure ionospheric electric fields, in *Dynamical and Chemical Coupling Between the Neutral and Ionized Atmosphere*, edited by B. Grandal and J. A. Holter, pp. 291-312, D. Reidel, Hingham, Mass., 1977.
- Heppner, J. P., Empirical models of high-latitude electric field, *J. Geophys. Res.*, **82**, 1115-1125, 1977.
- Horwitz, J. L., J. R. Doupnik, and P. M. Banks, Chatanika radar observations of the latitudinal distributions of auroral zone electric fields, conductivities, and currents, *J. Geophys. Res.*, **83**, 1463-1481, 1978.
- Iijima, T., and T. A. Potemra, The amplitude distribution of field-aligned currents at northern high latitudes observed by Triad, *J. Geophys. Res.*, **81**, 2165-2174, 1976a.
- Iijima, T., and T. A. Potemra, Field-aligned currents in the dayside cusp observed by Triad, *J. Geophys. Res.*, **81**, 5971-5979, 1976b.
- Iijima, T., and T. A. Potemra, Large-scale characteristics of field-aligned currents associated with substorms, *J. Geophys. Res.*, **83**, 599-612, 1978.
- Kamide, Y., Recent progress in observational studies of electric fields and currents in the polar ionosphere: A review, *Antarc. Rec.*, **63**, 61-231, 1979.
- Kamide, Y., and S. Matsushita, Simulation studies of ionospheric electric fields and currents in relation to field-aligned currents, 1, Quiet periods, *J. Geophys. Res.*, **84**, 4083, 1979a.
- Kamide, Y., and S. Matsushita, Simulation studies of ionospheric electric fields and currents in relation to field-aligned currents, 2, Substorms, *J. Geophys. Res.*, **84**, 4099, 1979b.
- Kelley, M. C., B. G. Fejer, and C. A. Gonzales, An explanation for anomalous equatorial ionospheric electric fields associated with a northward turning of the interplanetary magnetic field, *Geophys. Res. Lett.*, **6**, 301, 1979.
- Lui, A. T. Y., C. D. Anger, and S.-I. Akasofu, The equatorward boundary of the diffuse aurora and auroral substorms as seen by the Isis 2 auroral scanning photometer, *J. Geophys. Res.*, **80**, 3603, 1975.
- Lui, A. T. Y., D. Venkatesan, C. D. Anger, S.-I. Akasofu, W. J. Heikila, J. D. Winningham, and J. R. Burrows, Simultaneous observations of particle precipitation and auroral emissions by the Isis 2 satellite in the 19-24 MLT sector, *J. Geophys. Res.*, **82**, 2210-2226, 1977.
- Mehra, N. C., Ionospheric electrodynamics and its coupling to the magnetosphere, Ph.D. thesis, Univ. of Calif., San Diego, 1978.
- Mozer, F. S., and P. Lucht, The average auroral zone electric field, *J. Geophys. Res.*, **79**, 1001-1006, 1974.
- Neilsen, E., and R. A. Greenwald, Electron flow and visual aurora at the Harang discontinuity, *J. Geophys. Res.*, **84**, 4189-4200, 1979.
- Nisbet, J. S., M. J. Miller, and L. A. Carpenter, Currents and electric fields in the ionosphere due to field-aligned auroral currents, *J. Geophys. Res.*, **83**, 2647, 1978.
- Nopper, R. W., and R. L. Carovillano, Polar-equatorial coupling during magnetically active periods, *Geophys. Res. Lett.*, **5**(8), 699-702, 1978.
- Potemra, T. A., A review of U.S. progress for the 1975-1978 IUGG Quadrennial Report, *Rev. Geophys. Space Phys.*, **17**, 640-656, 1979.
- Rees, M. H., Auroral ionization and excitation by incident energetic electrons, *Planet. Space Sci.*, **11**, 1209-1218, 1963.
- Rees, M. H., and J. C. G. Walker, Ion and electron heating by auroral



- electric fields, *Ann. Geophys.*, **24**, 1, 1968.
- Rino, C. L., V. B. Wickwar, P. M. Banks, S.-I. Akasofu, and E. Rigger, Incoherent scatter radar observations of westward electric fields, 2, *J. Geophys. Res.*, **79**, 4669-4678, 1974.
- Sheehan, R. E., and R. L. Carovillano, Characteristics of the equatorward auroral boundary near midnight determined from DMSP images, *J. Geophys. Res.*, **83**, 4749, 1978.
- Stern, D., Electric fields in the earth's magnetosphere, *Rev. Geophys. Space Phys.*, **17**(4), 626-640, 1979.
- Stubbe, P., Frictional forces and collision frequencies between moving ion and neutral gases, *J. Atmos. Terr. Phys.*, **30**, 1965-1986, 1968.
- Swift, D. W., Auroral mechanisms and morphology, *Rev. Geophys. Space Phys.*, **17**(4), 681-696, 1979.
- Tsunoda, R. T., Electric field measurements above a radar scattering volume producing 'diffuse' auroral echoes, *J. Geophys. Res.*, **80**, 4297-4306, 1975.
- Vondrak, R., and M. J. Baron, A method of obtaining the energy distribution of auroral electrons from incoherent scatter radar measurements, in *Radar Probing of the Auroral Plasma*, edited by A. Brekke, pp. 315-330, Scandinavian University Books, Oslo, Norway, 1977.
- Vondrak, R. R., and M. J. Baron, Radar measurements of the latitudinal variation of auroral ionization, *Radio Sci.*, **11**, 939-946, 1976.
- Vondrak, R. R., G. Smith, V. Hatfield, R. Tsunoda, V. Frank, and P. Perreault, Chatanika model of the high-latitude ionosphere for application to HF propagation prediction, final report, *SRI Proj. 6056*, Menlo Park, Calif., 1977.
- Wedde, T., J. R. Doupnik, and P. M. Banks, Chatanika observations of the latitudinal structure of electric fields and particle precipitation on November 21, 1975, *J. Geophys. Res.*, **82**(19), 2743-2751, 1977.
- Zmuda, A. J., and J. C. Armstrong, The diurnal flow pattern of field-aligned currents, *J. Geophys. Res.*, **79**, 4611-4619, 1974.

(Received May 6, 1980;  
revised June 13, 1980;  
accepted June 18, 1980.)

# The Effects of a Conducting *E* Layer on Classical *F* Region Cross-Field Plasma Diffusion

JAMES F. VICKREY

*Radio Physics Laboratory, SRI International, Menlo Park, California 94025*

MICHAEL C. KELLEY

*School of Electrical Engineering, Cornell University, Ithaca, New York 14853*

The rate of cross-field plasma diffusion in the *F* region ionosphere is significantly increased when the magnetic field lines thread a highly conducting *E* region below. This reduces the lifetime of small-scale *F* region electron density irregularities in the polar ionosphere where the presence of a highly conducting *E* region is commonplace. A simple model is developed to describe the effects of a conducting *E* layer on classical *F* region plasma diffusion. In the absence of an *E* region, the difference in ion and electron diffusion rates leads to a charge separation and, hence, to an electrostatic field that retards ion diffusion. When the highly conducting magnetic field lines are tied to a conducting *E* region, however, electrons can flow along *B* to reduce the ambipolar diffusion electric field, and ions can proceed perpendicular to *B* at a rate approaching their own (higher) diffusion velocity. It is shown that the enhanced total diffusion rate that results depends strongly on the height of the *F* layer and on the ratio of the *E* to *F* region Pedersen conductivities. Although the enhanced classical diffusion rate hastens the removal of irregularities once their production source is removed, it is not a strong enough damping mechanism to prevent instabilities from operating routinely in the polar ionosphere. However, the *E* region probably plays an important role in determining the scale size of the irregularities that are favored. *E* region 'images' may be important for low *E* region electron densities and small scale sizes, in which case the diffusion rate is lowered. However, if the *E* region conductivity is high, the presence of images only reduces the *F* region cross-field plasma diffusion rate by about 25% from the ion rate. We hypothesize that the spectrum of high-latitude plasma density irregularities is controlled at large scales ( $\lambda \geq 10$  km) by structured soft electron precipitation and classical diffusion. Smaller scale waves are produced by plasma instabilities operating on the edges of the large scale structures. The generalized  $\vec{E} \times \vec{B}$  instability (including the current convective process) acts to strengthen waves in the intermediate scale size ( $100 \text{ m} \leq \lambda \leq 10 \text{ km}$ ) in regions where the geometry is appropriate or where field-aligned currents are significant. Universal drift waves transfer energy from the intermediate scale to smaller structures but are ineffectual at large scales. The classical diffusion process described herein is applied (in conjunction with a model of irregularity production and convection) to the problem of explaining the morphology of the large scale high-latitude irregularities in a companion paper (Kelley et al., this issue). The anomalous diffusion due to the instabilities mentioned above is also described in more detail.

## 1. INTRODUCTION

Highly structured *F* region plasma is a ubiquitous feature of the polar cap, auroral, and subauroral zone ionosphere as well as the nighttime magnetic equator. In a companion paper [Kelley et al., this issue] hereinafter referred to as paper 1, we discuss the origin and spatial extent of high-latitude irregularities. This paper examines the role of classical diffusion in removing irregularities once they are produced, and the effect of diffusion on the growth rate of plasma instabilities.

A simple model is developed to describe the effects of a conducting *E* layer on diffusion processes in the *F* region. We show that the presence of the *E* layer conductor enhances the cross-field ambipolar diffusion constant over that appropriate for an insulating *E* region. The essential physics of our model are briefly described below.

The plasma-density gradient at the edge of an irregularity has an associated pressure gradient that tends to make the plasma diffuse away from dense regions and into areas where the plasma is less dense. Because of their large mass

difference, ions and electrons do not have the same diffusion constant. In the *F* region ionosphere, ions have a higher diffusion rate perpendicular to the magnetic field than electrons, which are highly magnetized. Consequently, when the ions try to diffuse away from the electrons, an electrostatic field is produced, which retards ion diffusion. The net result is that the plasma, as a whole, diffuses at the slow electron rate. If, however, we introduce a highly conducting *E* region, to which the *F* layer irregularities are electrically connected, the electrons can move along the magnetic field to and from the *E* region to neutralize the space charge associated with the electrostatic field. The circuit is completed in the *E* region by horizontal ion motion.

With a reduced electric field, the ions can now diffuse across the magnetic field in the *F* layer more rapidly, approaching the ion diffusion rate as the electric field goes to zero. The electrical system which evolves is closed by ions moving across the magnetic field in the *E* region in response to the electric field mapped down from above. Note that in this system, electrons never leave a given flux tube except by the slow process of electron diffusion or by recombination in the *E* region. In time, the ions and electrons gather in the *E* region below an enhancement of *F* layer plasma forming an 'image' [Francis and Perkins, 1975] which, as

Copyright 1982 by the American Geophysical Union.

Paper number 2A0430.  
0148-0227/82/002A-0430\$05.00

4461

pointed out by J. Fedder (personal communication, 1982), can convect with the velocity of the *F* layer irregularity. However, for reasonable values of *E* region electron density and irregularity scales  $\geq 1$  km, we show below that images do not seriously affect the diffusion process. Thus, for an infinitely conducting *E* region, classical diffusion proceeds at the ion (rather than the electron) rate. As will be shown, this rate is strongly dependent on the altitude of the *F* layer irregularities.

## 2. MODEL DESCRIPTION

Our goal is to model the decay of horizontally structured *F* region plasma including the effects of a conducting *E* region. As a simplification we consider the combined effects of parallel diffusion, gravity, and recombination to act independently of the processes considered here and to result in an additional temporal decay as modeled by Schunk *et al.* [1976]. Our neglect of these effects is justified because we are only concerned with processes that reduce horizontal (perpendicular to the magnetic field) density gradients. We assume that parallel diffusion, for example, will operate at such a rate that the vertical *F* layer profile maintains a Chapman shape on all flux tubes. However, the integral of electron density along the individual flux tubes can be different, and parallel diffusion (by definition) cannot reduce the difference. In the *F* region, recombination is linearly proportional to the electron density [Rishbeth and Garriott, 1969]. Thus, recombination will reduce the absolute density on adjacent flux tubes equally (for small amplitude irregularities) and will not reduce the horizontal density gradient. We make the following additional simplifying assumptions in our model:

1. The *E* region is a uniform conducting medium with height-integrated Pedersen conductivity  $\Sigma_P^E$ . We show below that *E* region irregularity 'image' density fluctuations [Francis and Perkins, 1975; Goldman *et al.*, 1976], which modify  $\Sigma_P^E$ , are not important in the diffusion process provided that the *E* region density is high enough ( $n \geq 2 \times 10^4/\lambda^2 \text{ cm}^{-3}$  where  $\lambda$  is the irregularity scale size measured in km).

2. The density structure,  $n(z, \vec{r}, t)$ , can be separated mathematically into a form,  $Z(z)N(\vec{r}, t)$ , where  $\vec{r}$  is a vector in the plane perpendicular to  $\vec{B}$  (assumed to be vertical).

3. The conductivity parallel to  $\vec{B}$  is sufficiently high that the electric field is independent of altitude  $z$ .

4. Quasi-neutrality holds: ( $n_e \approx n_i \approx n$ ).

The ion and electron continuity equations are [Rishbeth and Garriott, 1969]

$$\frac{\partial n_i}{\partial t} + \nabla \cdot \vec{\Gamma}_i = P_i - L_i = 0 \quad (1a)$$

$$\frac{\partial n_e}{\partial t} + \nabla \cdot \vec{\Gamma}_e = P_e - L_e = 0 \quad (1b)$$

where  $\vec{\Gamma}_j = n_j \vec{V}_j$  is the flux, and  $P_j$  and  $L_j$  are the production and loss of each species.  $\vec{\Gamma}_j$  in turn is given by

$$\vec{\Gamma}_j = \frac{\hat{\sigma}_j \cdot \vec{E}}{q_j} - \hat{d}_j \cdot \nabla n \quad (2)$$

where  $q_j$  is the species charge, and  $\hat{\sigma}_j$  and  $\hat{d}_j$  are the Pedersen conductivity and diffusion tensors, respectively, of species  $j$ .

For the reasons just described, we ignore production and loss in the *F* region and consider the vertically dependent parameters of (1) and (2) to be decoupled from the perpendicular ones. Note that the conductivity and diffusion tensors are diagonal in the *F* region and that the assumption (3) is equivalent to  $\sigma_{\parallel} = \infty$ . Thus, we only need expressions for  $\sigma_{j\perp}$  and  $d_{j\perp}$ , where  $\perp$  denotes the component perpendicular to the magnetic field. These expressions are

$$\sigma_{j\perp} = \frac{nq_j^2 \nu_j}{\Omega_j^2 m_j} \quad (3)$$

$$d_{j\perp} = \frac{K_B T_j \nu_j}{\Omega_j^2 m_j} = \zeta_{\text{Larmor},j}^2 \nu_j \quad (4)$$

where  $K_B$  is Boltzmann's constant, and  $\Omega_j$ ,  $T_j$ ,  $\zeta_{\text{Larmor},j}$ , and  $m_j$  are the gyrofrequency, temperature, Larmor radius, and mass of species  $j$ , respectively. Since we are interested in *F* region processes,  $\nu_i$  is the ion-neutral collision frequency and  $\nu_e$  the electron-ion collision frequency.

Note that while we ignore recombination losses in the *F* region, they cannot be ignored in the *E* region. Indeed, production and loss of electrons in the *E* region are necessary assumptions in the model since the electron gas is incompressible and images have been ignored (see appendix).

Our model is illustrated schematically in Figure 1. For the calculations below, the irregularities are considered to be cylindrically symmetric about the geomagnetic field  $\vec{B}$ . It is easily shown, however, that all the results presented below are equally valid for sheetlike irregularity geometry as well. We assume that the flux tubes extend to infinity; hence, only the boundary condition at the lower border is of concern. This is certainly valid in the polar cap and probably does not introduce significant error for the long, closed field lines of the auroral zone. Farley [1959] has shown that field line mapping of equipotentials between the *E* and *F* regions is only valid for wavelengths of approximately 1 km and larger. Thus, strictly speaking, our computations are valid only in this regime.

It is convenient to consider  $z_0$  as an altitude in the low-density valley between the *E* and *F* layers so that *F* region and *E* region phenomena are easily distinguished. Such a valley region is often present even during the occurrence of particle precipitation [e.g., Vickrey *et al.*, 1980].

If we substitute (2) into (1) and integrate over height, we obtain for the ion continuity equation:

$$\frac{\partial N}{\partial t}(\vec{r}, t) = -\frac{1}{q_i} \nabla_{\perp} \cdot \{ \Sigma_i^F \vec{E}(\vec{r}, t) - q_i D_{i\perp} \nabla N(\vec{r}, t) \} \quad (5)$$

where

$$N(\vec{r}, t) = \int_{z_0}^{\infty} n(\vec{r}, z, t) dz \quad (6)$$

$$\Sigma_i^F = \int_{z_0}^{\infty} \sigma_{i\perp} dz \quad (7)$$

and

$$D_{i\perp} = \frac{1}{N(\vec{r}, t)} \int_{z_0}^{\infty} d_{i\perp} n(\vec{r}, z, t) dz \quad (8)$$

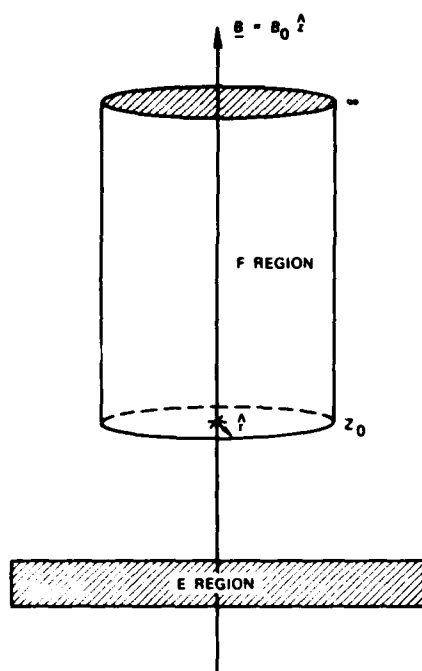


Fig. 1. Schematic illustration of the present model showing the surface over which the integration in equation (10) is performed.

To solve (5), a relationship between the electric field and the density gradient is needed. This comes from the charge continuity equation

$$\nabla \cdot \mathbf{J} = 0 \quad (9)$$

(where  $\mathbf{J}$  is current), which is implied by our assumption of quasi-neutrality. Equation (9) must hold throughout the cylindrical volume of Figure 1, and hence the integral of (9) over that volume (or any other) must vanish. If we convert the volume integral to a surface integral by using Gauss's theorem (note the azimuthal symmetry), we have

$$2\pi \int_{z_0}^{\infty} \{ (\sigma_{i\perp} \hat{\mathbf{E}}(r, t) - q_i d_{i\perp} \nabla n(z, r, t)) + \{ \sigma_{e\perp} \hat{\mathbf{E}}(r, t) - q_e d_{e\perp} \nabla n(z, r, t) \} dz - 2\pi \int_0^r J_z(z_0, \zeta, t) \zeta d\zeta = 0 \quad (10)$$

The last term is negative because the outward normal to the volume of Figure 1 is antiparallel to the  $z$  axis. We have ignored current flow through the top of the  $F$  layer. Carrying out the height integration for the first two terms we have

$$r(\Sigma_i^F + \Sigma_e^F) \hat{\mathbf{E}}(r, t) - q_i d_{i\perp} - D_{e\perp} \nabla n(r, t) = \int_0^r J_z(\zeta, t) \zeta d\zeta \quad (11)$$

Since  $\hat{\mathbf{E}}(r, t)$  is independent of altitude, the current parallel to  $\mathbf{B}$  is equal to the divergence of the horizontal  $E$  layer

current that results from the electric field caused by the irregularity. Furthermore, since the  $E$  region Pedersen conductivity is assumed constant

$$J_z(z_0) = -\Sigma_P^E \nabla_{\perp} \cdot \hat{\mathbf{E}}(\zeta, t) \quad (12)$$

Substituting (12) into the right-hand side of (11) we have, in cylindrical coordinates,

$$J_z(z_0) = -\Sigma_P^E \int_0^r \zeta \left[ \frac{1}{\zeta} \frac{\partial}{\partial \zeta} (\zeta E(\zeta, t)) \right] d\zeta = -\Sigma_P^E r E(r, t) \quad (13)$$

Hence, (13) and (11) yield a solution for  $E$  in terms of  $\nabla n$ :

$$\hat{\mathbf{E}}(r, t) = \left[ \frac{q_i (D_{i\perp} - D_{e\perp})}{\Sigma_i^F + \Sigma_e^F + \Sigma_P^E} \right] \nabla_{\perp} n(r, t) \quad (14)$$

Equation (14) is the desired relationship between the electric field and density gradient including the effects of a conducting  $E$  region. Since  $D_{i\perp} \gg D_{e\perp}$  and  $\Sigma_i^F \gg \Sigma_e^F$  in the  $F$  region, (14) can be simplified for the case of an insulating  $E$  region, ( $\Sigma_P^E \rightarrow 0$ ), to the following:

$$\hat{\mathbf{E}}_{\text{insulator}}(r, t) = \frac{K_B T_i}{q_i} \frac{\nabla_{\perp} n}{N} \quad (15)$$

Thus,  $E_{\text{insulator}}$  is the ambipolar electric field required to cancel the ion current that would otherwise be caused by the pressure gradient. This supports the physical description of cross-field diffusion given in the introduction. Equation (14) shows that this ambipolar electric field is reduced (shorted out) by the presence of the conducting  $E$  layer. Evidence that this phenomenon occurs in the polar ionosphere is presented in Figure 2, which shows low-frequency electrostatic fluctuations [Kelley and Mozer, 1972] measured on the OV1-17 satellite. These fluctuations have been shown to be due to irregularities drifting with the medium [Temerin, 1979]. The plot shows the variation of the average signal in the northern and southern polar latitudes for a wavelength of  $\sim 100$  m. The lower values in the summer hemisphere are consistent with our conclusion that the  $E$  region conductivity controls the electric field strength. Individual orbits also display smaller electric fields in the summer polar regions than in the nearly simultaneously sampled winter polar cap.

Now we substitute the electric field expression of (14) into the ion continuity equation (5) to obtain

$$\frac{\partial N}{\partial t}(r, t) = \nabla_{\perp} \cdot \left\{ \left[ \frac{\Sigma_i^F}{\Sigma_i^F + \Sigma_e^F + \Sigma_P^E} \cdot (D_{e\perp} - D_{i\perp}) + D_{i\perp} \right] \nabla_{\perp} n(r, t) \right\} \quad (16)$$

Equation (16) is not in the form of a diffusion equation; e.g.,

$$\frac{\partial N}{\partial t}(r, t) = D_{\perp} \nabla_{\perp}^2 N(r, t) \quad (17)$$

because  $D_{e\perp}$  and  $\Sigma_e^F$  are density dependent (through the electron-ion collision terms) and therefore are dependent on  $r$ . (Note, however, that  $\Sigma_e^F \ll \Sigma_i^F$ .) If it were not for these dependences, then (16) would reduce exactly to (17) with the following limiting values:

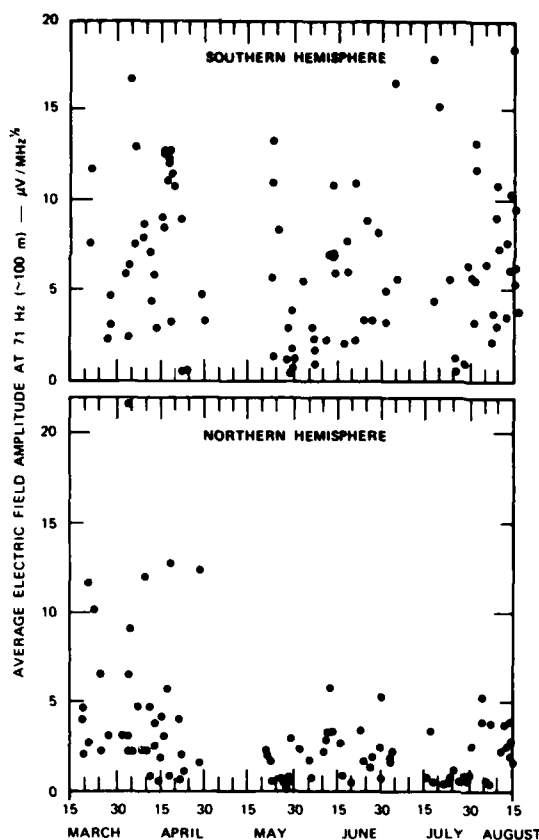


Fig. 2. Average amplitude of electrostatic fluctuations in the northern and southern polar ionosphere as measured by the OVI-17 satellite. Fluctuations are reduced in amplitude in the sunlit hemisphere.

$$\begin{aligned} D_{\perp} &= 2D_{e\perp} \text{ for } \Sigma_P^E \rightarrow 0 \\ D_{\perp} &= D_{e\perp} \text{ for } \Sigma_P^E \gg \Sigma_P^F \end{aligned} \quad (18)$$

This illustrates that in the nonconducting  $E$  region case the ion fluxes due to  $\vec{E}$  and  $\nabla N$  cancel, and slow electron diffusion dominates irregularity decay. For an infinitely conducting  $E$  layer, parallel electron mobility shorts out the ambipolar electric field completely, and ion diffusion proceeds unimpeded.

In the next section, we will present the numerical results obtained by approximating (16) by (17) under more general conditions than the limiting cases given by (18). Before doing so, let us give an estimate of the accuracy of that approximation. In Figure 3a is the radial profile of peak  $F$  region electron density for a Gaussian irregularity of peak density  $1 \times 10^6 \text{ cm}^{-3}$  at  $r = 0$  and characteristic scale of 10 km. The background ionosphere is assumed to have a peak  $F$  region density of  $10^5 \text{ cm}^{-3}$ . Panels (b) through (e) of Figure 3 show comparisons (under varying conditions) of evaluating  $(\partial N / \partial t)(r, t)|_{t=0}$  by (17) and by performing the divergence operation of (16) numerically. Figure 3b corresponds to the assumption that  $\Sigma_P^E \gg \Sigma_P^F$ . As one would expect, the approximation is very good (within  $\sim 3\%$ ) in this case. Panel

3c shows the same comparison of (16) and (17) for the case where  $\Sigma_P^E(r) = \Sigma_P^F(r)$ . In other words, it is assumed that  $E$  region irregularity images exist that exactly map the changing  $F$  region Pedersen conductivity. In this case the two expressions agree within about 5%. Figure 3d illustrates the situation where the  $E$  region Pedersen conductivity is constant and equal to the  $F$  region conductivity at  $r = 0$ . The two curves in this case agree within about 15%. The final panel, Figure 3e, was calculated assuming  $\Sigma_P^E = 0$ . For this case the approximation was only accurate to within about 50%. The situation of most interest to the present study is when  $\Sigma_P^E$  is significant and (for reasons to be explained more fully below) constant. Thus, we would expect our numerical results of the next section to be accurate to within  $\sim 15\%$  despite our use of the simplified expression (17).

If we write the density distribution in terms of its spatial Fourier components, then each obeys an algebraic equation of the form

$$\frac{\partial N(k_{\perp}, t)}{\partial t} = -k_{\perp}^2 D_{\perp} N(k_{\perp}, t) \quad (19)$$

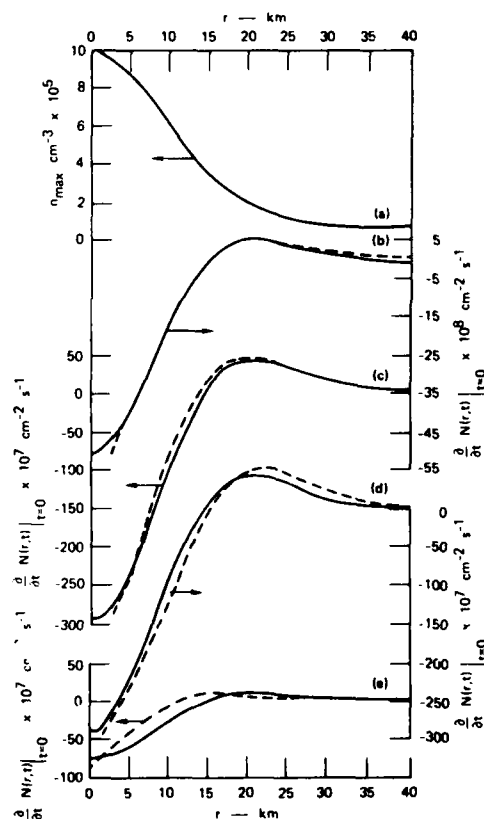


Fig. 3. The radial dependence of plasma density and the temporal derivative of plasma density at  $t = 0$  under various conditions. The top panel shows the radial variation of  $F$  region peak density for a cylindrically symmetric gaussian, 10 km irregularity. Panels (b) through (e) show comparisons between (16) and (17) for the following conditions, respectively  $\Sigma_P^E = \infty$ ,  $\Sigma_P^E(r) = \Sigma_P^F(r)$ ,  $\Sigma_P^E(r) = \Sigma_P^F(r = 0)$ , and  $\Sigma_P^E = 0$ . The arrows point to the appropriate scale for each set of curves.

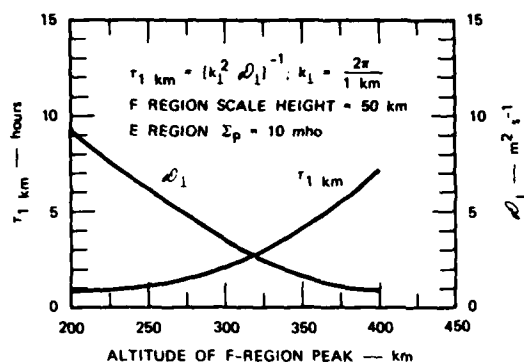


Fig. 4. Dependence of cross-field diffusion rate  $D_{\perp}$  and lifetime of 1-km scale irregularities  $\tau_{1km}$  on the altitude of the  $F$  layer. The  $F$  region peak electron density is fixed at  $5 \times 10^5 \text{ cm}^{-3}$ .

The solution for this is

$$N(k_{\perp}, t) = N(k_{\perp}) e^{-k_{\perp}^2 D_{\perp} t} \quad (20)$$

At the level of the present discussion of the temporal decay of irregularities, an equation of this form is sufficiently accurate and yields a time constant of  $\tau = (k_{\perp}^2 D_{\perp})^{-1}$ . Moreover, an exact solution does not give results that are markedly different from those obtained by using this approximation [see *Huba and Ossakow*, 1981].

We now turn to the question of  $E$  region images that we ignored earlier by requiring  $\Sigma_p^E$  to be constant. This effect is thought important for barium cloud striation studies [Francis and Perkins, 1975; Goldman et al., 1976] and possibly in regions of localized large electric fields impressed by magnetospheric effects [Banks and Yasuhara, 1978]. We show in the appendix, however, that  $E$  region recombination will restrain the growth of images provided the background  $E$  region density  $n_0$  exceeds  $10^4/\lambda^2$ , where  $\lambda$  is the scale size of the irregularity in kilometers. Since our interest here is in scale sizes  $\geq 1$  km, the present approach is appropriate in the auroral zone and summer polar cap, but may not be appropriate everywhere in the winter polar cap.

### 3. NUMERICAL RESULTS

To gain some insight into the magnitude of the  $E$  region conductivity effects on  $F$  region diffusion, we have approximated (16) by (17) with

$$D_{\perp} = \frac{\Sigma_p^F}{\Sigma_p^F + \Sigma_p^E + \Sigma_p^E} [D_{\perp}^e - D_{\perp}^i] + D_{\perp}^i \quad (21)$$

To calculate values of  $D_{\perp}$  and  $\Sigma_p$ , we have used the Jacchia 1972 neutral atmosphere model with an exospheric temperature of 1000°K. The ion and electron temperatures were assumed equal to the model neutral temperature. The ion-neutral collision frequency was calculated by using the coefficients of Schunk and Walker [1973]. The electron-ion collision frequency was estimated by  $\nu_{ei} = 54 n(z) T_e^{-3/2}$  [Banks and Kockarts, 1973]. The needed electron density profile was assumed to have a Chapman shape with  $n(z)$  given by

$$n(z) = n_{\max}(z_{\max}) \exp \left\{ \frac{1}{2} \left[ 1 - \frac{(z - z_{\max})}{H} - e^{-(z - z_{\max})/H} \right] \right\} \quad (22)$$

where  $n_{\max}$  is the maximum  $F$  region electron density,  $z_{\max}$  is the altitude of the  $F$  layer peak, and  $H$  is the scale height. For all the calculations presented here,  $H$  was fixed at 50 km and  $z_0$  was taken to be 180 km.

Figure 4 shows the variations in  $D_{\perp}$  and the irregularity decay time constant,  $\tau_{1km} = (k_{\perp}^2 D_{\perp})^{-1}$ , for 1-km scale length irregularities as a function of the altitude of the  $F$  layer peak. As is shown in the figure, the lifetime of  $F$  region irregularities increases as the height of the  $F$  layer increases. This is to be expected since the ion-neutral collision frequency decreases exponentially with altitude.

Figure 5 shows the variations of  $\tau_{1km}$  and  $D_{\perp}$  as a function of the ratio of  $E$  to  $F$  region Pedersen conductivity. The altitude of the  $F$  region peak is fixed at 350 km. As was discussed previously,  $D_{\perp}$  ranges from  $2D_{\perp}^e$  (for  $\Sigma_p^E = 0$ ) to  $D_{\perp}^i$  (for  $\Sigma_p^E/\Sigma_p^F \gg 1$ ). At the point  $\Sigma_p^E = \Sigma_p^F$ ,  $D_{\perp}$  is one-half the ion rate.

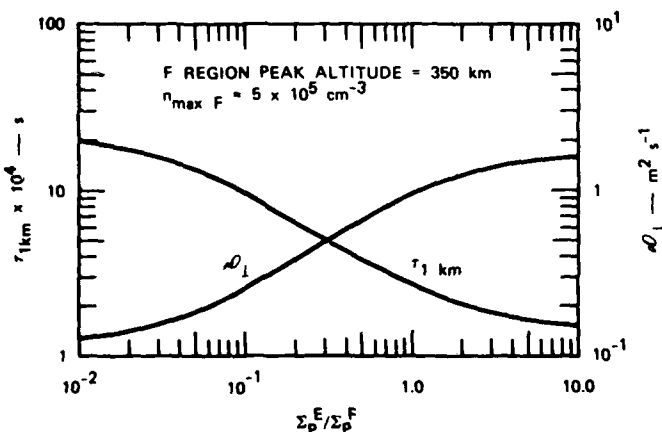


Fig. 5. The dependence of cross-field diffusion rate  $D_{\perp}$  and lifetime of 1-km scale irregularities  $\tau_{1km}$  on the ratio of  $E$  to  $F$  region Pedersen conductivities. The  $F$  layer altitude and peak density are fixed.

A 10-km scale irregularity can thus survive diffusion for days, provided the flux tube does not move into a sunlit portion of the ionosphere. After an irregular ionosphere has been sunlit for several hours, one expects the low-density 'holes' between ionization enhancements to be filled in, and the entire *F* region should reach a common maximum density. The exact time scale for this process is being examined and will be presented elsewhere. Recombination effects do not initially affect relative fluctuations in plasma density since both enhanced and depleted regions decay at the same rate. However, if overall decay proceeds for a time period on the order of five or more hours, the dominant  $O^+$  ion can be removed above  $\sim 600$  km and leave only  $H^+$  and  $He^+$  [Heelis *et al.*, 1981]. Since these ion species are not formed in the process that creates *F* layer structures, the predominant recombination of  $O^+$  will result in a smooth ionosphere. In paper 1 these transport and decay effects are discussed more fully.

At the 1-km scale size the diffusive decay rate is 100 times faster than at 10 km, and significant loss occurs in several hours. As is discussed in more detail in paper 1, wherever convection is rapid (in the inertial reference frame), irregularities at this scale can populate the high-latitude region from sources in the auroral oval. At 100 m, however, decay is quite rapid. Even with only classical diffusion, a nonconducting *E* region, and no instabilities operating, very few irregularities should exist at this scale. However, such small scale irregularities are observed [Fejer and Kelley (1980) and references therein]; hence, other processes must contribute to their growth.

Field-aligned currents are known to play a role in producing short-wavelength waves in plasmas. For example, the current convective instability [Ossakow and Chaturvedi, 1979] has been suggested as an important irregularity production process when magnetospheric currents are present in the same region of space as horizontal density gradients. We can examine the magnitude of the field-aligned current that is imposed by horizontal *F* region density gradients due to the classical diffusion process described above. Substituting (14) into (12), we obtain an expression for the field-aligned current at the base of the *F* region,  $z_0$ :

$$J_z(z_0) = - \frac{\sum_p^F q \lambda (D_{\perp p} - D_{\parallel p})}{\sum_p^F + \sum_p^E + \sum_p^F} \nabla_{\perp}^2 N(r, t) \quad (23)$$

The maximum field-aligned current that can be drawn from the density gradient 'battery' is given by ( $\sum_p^E \gg \sum_p^F$ ):

$$J_{z, \max}(z_0) = - q (D_{\perp i} - D_{\parallel i}) \nabla_{\perp}^2 N \quad (24a)$$

$$J_{z, \max}(k_{\perp}) \sim - q (D_{\perp i}) k_{\perp}^2 N(k) \quad (24b)$$

which, for our standard *F* region model with a peak density of  $5 \times 10^5 \text{ cm}^{-3}$  at 350 km, amounts to  $\sim 0.01 \mu\text{A/m}^2$  exiting the base of the ionosphere for a 10-km scale size irregularity. Note that if the irregularity spectrum  $|\Delta N(k_{\perp})|^2$  has a power law dependence of  $k_{\perp}^{-2}$ , then  $J_{z, \max}(z_0)$  is proportional to  $k_{\perp}$ . Thus, smaller irregularities produce larger parallel currents. However, the levels of current expected are still small enough that the plasma is stable to the current convective process, except perhaps in the *F* layer valley region where the electron density can be very low.

We note here, and in paper 1, that while the enhanced classical perpendicular diffusion rate  $D_{\perp}$  considered here is

considerably larger than that included in the current convective instability growth rate calculations of Vickrey *et al.* [1980] (who considered only the  $D_{\perp}$  contribution), it is still small in comparison with the driving term (which in their case was the electric field). Hence, the role of the *E* region is to slow instability growth [see Völk and Haerendel, 1971] and to hasten the removal of irregularities once the driving source is removed. The highly conducting *E* region does not, however, prevent the instability from operating.

#### 4. SUMMARY

The major results of this study are briefly summarized as follows:

1. The classical cross-field plasma diffusion rate in the *F* region ionosphere can be increased by an order of magnitude or more when the magnetic field lines connect to a highly conducting *E* layer below.
2. The cross-field diffusion rate is strongly affected by the height of the *F* layer and the ratio of *E* to *F* region Pedersen conductivities.
3. The presence of a conducting *E* region slows instability growth and limits the lifetime of small-scale *F* region irregularities once their production source is removed, but does not prevent the routine operation of instabilities in the high-latitude ionosphere.
4. The present diffusion model is applied, in conjunction with an irregularity production and convection model, to the problem of explaining the global morphology of high-latitude irregularities in a companion paper by Kelley *et al.* [this issue]. The role of anomalous diffusion is also discussed therein.
5. *E* region images tend to slow diffusion but are themselves damped by recombination if the background *E* region electron density exceeds a value  $n_c$  given by  $n_c \approx 2 \times 10^4 / \lambda^2 \text{ cm}^{-3}$ , where  $\lambda$  is measured in kilometers.

#### APPENDIX

The physical mechanism whereby an *E* region image is formed and affects the diffusion of an *F* region structure can be understood as follows. Ions move across the magnetic field in both the *E* and *F* regions, but the electrons that maintain quasi-neutrality cannot do so. They move down the field line from the *F* to the *E* layer in the region of high electron density in the *F* layer and up the field line in the flux tube with lower *F* region electron density. Note that the height integrated plasma content in each flux tube remains the same if recombination is ignored; plasma is merely redistributed between the *F* and the *E* layers. The 'image' results from the subsequent enhancement of plasma density in the initially uniform *E* region below the *F* region enhancement. The image will reduce the decay rate of the *F* region structure by limiting the field-aligned current that would otherwise reduce the ambipolar electric field. Since it is this field which impedes ion diffusion, the formation of *E* region images reduces the *F* region cross-field diffusion rate.

To include the effects of images in our model, we must retain  $\sum_p^E$  inside the divergence operator in (12) and include the possibility of ion diffusion-driven current in the *E* layer, that is,

$$J_z(z_0) = - \nabla_{\perp} \cdot \left\{ \sum_p^E \left( \vec{E} - \frac{K_B T_p^E}{q} \frac{\nabla N^E}{N^E} \right) \right\} \quad (A1)$$

where we have assumed for simplicity that  $T_i^E$ , the  $E$  region ion temperature, does not vary in the image. Substituting into (11) as before, we have

$$\dot{E} = \frac{1}{\Sigma_p^E + \Sigma_i^F + \Sigma_e^F} \{q(D_{i1}^F - D_{e1}^F) \nabla N^F + qD_{i1}^E \nabla N^E\} \quad (A2a)$$

which can be written as

$$\dot{E} = \frac{1}{\Sigma_p^E} \left[ \frac{\Sigma_i^F K_B T_i^F}{q} \frac{\nabla N^F}{N^F} - \frac{\Sigma_e^F K_B T_e^F}{q} \frac{\nabla N^F}{N^F} + \frac{\Sigma_p^E K_B T_i^E}{q} \frac{\nabla N^E}{N^E} \right] \left/ \left( \frac{\Sigma_p^F}{\Sigma_p^E} + 1 \right) \right. \quad (A2b)$$

Note that  $\Sigma_e^F \ll \Sigma_i^F$  and for the present case of interest (i.e.,  $\Sigma_p^E \gg \Sigma_p^F$ ) this reduces to

$$\dot{E} \approx \frac{\Sigma_p^F}{\Sigma_p^E} \frac{K_B T_i^F}{q} \frac{\nabla N^F}{N^F} + \frac{K_B T_i^E}{q} \frac{\nabla N^E}{N^E} \quad (A3)$$

Here it is useful to point out that the sense of the  $E$  region image 'battery' is the same as the ambipolar electric field that tends to suppress ion diffusion. However, for a highly conducting  $E$  region, diffusion would proceed at the slow electron rate only if the following condition were fulfilled:

$$\frac{\nabla N^E}{N^E} \approx \frac{T_i^F}{T_i^E} \frac{\nabla N^F}{N^F} \quad (A4)$$

Note that since the  $F$  region temperature is typically  $\sim 1000^\circ\text{K}$ , while the  $E$  region temperature is  $\sim 250^\circ\text{K}$ , the  $E$  region images would have to have a scale size of one-fourth that of the  $F$  layer irregularities in order to slow diffusion to the rate of the electrons. This cannot happen in the steady state analysis considered here, and hence,  $F$  region diffusion is enhanced by a conducting  $E$  layer even if it contains images. For the situation ( $\lambda$  irregularity =  $4 \lambda$  image) to occur, the  $E$  region images must survive long enough for  $F$  region diffusion to reduce the irregularity gradient scale by a factor of 4. However, in view of the discussion below on  $E$  region recombination, this implies a low  $E$  region electron density and hence, low conductivity. We can calculate the  $F$  region cross-field diffusion rate for a highly conducting  $E$  layer containing images by setting  $\Sigma_p^F/\Sigma_p^E = 0$  and  $\nabla N^E/N^E = \nabla N^F/N^F$  in (A3), and substituting the result into the ion continuity equation (5). This yields  $D_1 = D_{i1}^F (1 - T_i^E/T_i^F)$ . Thus, the presence of images in a highly conducting  $E$  layer only reduces the  $F$  region cross-field plasma diffusion rate by about 25% from the ion rate.

Let us now briefly examine the question of image formation. Images must build up in the presence of recombination effects that are quite rapid in the  $E$  region. From the ion continuity equation we have

$$\frac{\partial n}{\partial t} + \nabla \cdot (n\mathbf{V}) = P - L \quad (A5)$$

where  $P$  is the production rate and  $L$  is the loss rate. Production is unaffected by the image since it is due only to the incoming solar or particle flux and the uniform neutral density. Let us consider the initial state when no image exists, and calculate the rate at which the image grows by

gathering plasma together and decays away by recombination,

$$\frac{\partial n}{\partial t} = -n\alpha(\nabla \cdot \mathbf{V}) - \alpha n_0^2 \quad (A6)$$

$$\frac{\partial}{\partial t} \left( \frac{n}{n_0} \right) = -\nabla \cdot \mathbf{V} - \alpha n_0$$

where  $\alpha$  is the recombination rate and  $\mathbf{V}$  is the ion velocity perpendicular to  $\bar{B}$  in the  $E$  layer. An upper limit on  $\mathbf{V}$  is the maximum value of the ion Pedersen drift parallel to the radial electric field due to our cylindrical irregularity. That maximum Pedersen drift occurs near 130-km altitude and is given by

$$V_i^{\max} = \frac{1}{2} \frac{E}{B} = \frac{1}{2B} \frac{\Sigma_p^F}{\Sigma_p^E} \frac{K_B T_i^F}{q} \frac{\nabla N^F}{N^F} \quad (A7)$$

where we have made use of (A3).

With the radial ambipolar electric field inward,  $-(\nabla \cdot \mathbf{V})$  is positive and therefore tends to build up the image density. However, this convergence must overcome the  $\alpha n_0$  term in (A6) for the image to grow. The divergence term is scale size-dependent, and thus, as is pointed out by Francis and Perkins [1975], the images will grow against recombination for small scale sizes but will be suppressed at large scales. By combining (A6) and (A7), we can calculate the critical  $E$  region density  $n_c$  below which an image irregularity of wave number  $k$  will grow. This critical density is given by:

$$n_c \leq \frac{k^2 \frac{\Sigma_p^F}{\Sigma_p^E} \frac{K_B T_i^F}{q}}{2\alpha B} \quad (A8)$$

Since we have already noted (for field line mapping considerations) that our development is valid for  $\lambda \geq 1000$  m, let us evaluate  $n_c$  for such a scale size by taking  $T_i^F = 1000^\circ\text{F}$ ,  $\alpha = 2 \times 10^{-7} \text{ cm}^3/\text{s}$  [see Vickrey et al., 1982], a conservative value of  $\Sigma_p^F/\Sigma_p^E = 0.1$ , and  $B = 0.5$  G. These values yield  $n_c \leq 1.7 \times 10^4 \text{ cm}^{-3}$ . Thus for kilometer scale sizes and larger and for  $E$  region densities above a few times  $10^4 \text{ cm}^{-3}$ , recombination will curtail growth of images and our neglect of images is justified.

**Acknowledgments.** The authors acknowledge very helpful discussions with C. L. Rino, B. G. Fejer, R. A. Heelis, and J. Fedder. This work was supported by the Defense Nuclear Agency under contract DNA001-81-C-0076 and by the Air Force Office of Scientific Research under contract F49620-80-C-0014. The work at Cornell was partially supported under a contract from the Office of Naval Research.

The Editor thanks E. Ott and another referee for their assistance in evaluating this paper.

#### REFERENCES

- Banks, P. M., and G. Kockarts, *Aeronomy*, Part A, Academic, New York, 1973.
- Banks, P. M., and F. Yasuhara, Electric fields and conductivity in the nighttime  $E$  region: A new magnetosphere-ionosphere-atmosphere coupling effect, *Geophys. Res. Lett.*, 5, 1047-1050, 1978.
- Farley, D. T., Jr., A theory of electrostatic fields in a horizontally stratified ionosphere subject to a vertical magnetic field, *J. Geophys. Res.*, 64, 1225, 1959.
- Fejer, B. G., and M. C. Kelley, Ionospheric irregularities, *Rev. Geophys. Space Phys.*, 18, 401, 1980.
- Francis, S. H., and F. W. Perkins, Determination of striation scale



- sizes for plasma clouds in the ionosphere, *J. Geophys. Res.*, **80**, 3111, 1975.
- Goldman, S. R., L. Baker, S. L. Ossakow, and A. J. Scannapieco, Striation formation associated with barium clouds in an inhomogeneous ionosphere, *J. Geophys. Res.*, **81**, 5097-5113, 1976.
- Heelis, R. A., J. A. Murphy, and W. B. Hanson, A feature of the behavior of  $\text{He}^+$  in the nightside high-latitude ionosphere during equinox, *J. Geophys. Res.*, **86**, 59, 1981.
- Huba, J. D., and S. L. Ossakow, Diffusion of small-scale density irregularities during equatorial spread  $F$ , *Memo. Rep. 4521*, Naval Res. Lab., Washington, D. C., 1981.
- Kelley, M. C., and F. S. Mozer, A satellite survey of vector electric fields in the ionosphere at frequencies of 10 to 500 Hz. 1, Isotropic, high-latitude electrostatic emissions, *J. Geophys. Res.*, **77**, 4158, 1972.
- Kelley, M. C., J. F. Vickrey, C. W. Carlson, and R. Torbert, On the origin and spatial extent of high-latitude  $F$  region irregularities, *J. Geophys. Res.*, this issue.
- Ossakow, S. L., and P. K. Chaturvedi, Current convective instability in the diffuse aurora, *Geophys. Res. Lett.*, **6**, 322, 1979.
- Rishbeth, H., and O. K. Garriott, *Introduction to Ionospheric Physics*, Academic, New York, 1969.
- Schunk, R. W., and J. C. G. Walker, Theoretical ion densities in the lower atmosphere, *Planet. Space Sci.*, **21**, 1875, 1973.
- Schunk, R. W., P. M. Banks, and W. J. Raitt, Effects of electric fields and other processes upon the nighttime high-latitude  $F$  layer, *J. Geophys. Res.*, **81**, 3271, 1976.
- Temerin, M., Polarization of high latitude ionospheric turbulence as determined by analysis of data from the OV1-17 satellite, *J. Geophys. Res.*, **84**, 5935, 1979.
- Vickrey, J. F., C. L. Rino, and T. A. Potemra, Chatanika/TRIAD observations of unstable ionization enhancements in the auroral  $F$  region, *Geophys. Res. Lett.*, **1**, 789, 1980.
- Vickrey, J. F., R. R. Vondrak, and S. J. Matthews, Energy deposition by precipitating particles and Joule dissipation in the auroral ionosphere, *J. Geophys. Res.*, **87**, in press, 1982.
- Völk, H. J., and G. Haerendel, Striations in ionospheric ion clouds, 1, *J. Geophys. Res.*, **76**, 4541, 1971.

(Received July 14, 1981;  
revised March 9, 1982;  
accepted March 18, 1982.)

# On the Origin and Spatial Extent of High-Latitude *F* Region Irregularities

MICHAEL C. KELLEY

*School of Electrical Engineering, Cornell University, Ithaca, New York 1485.*

JAMES F. VICKREY

*Radio Physics Laboratory, SRI International, Menlo Park, California 94025*

C. W. CARLSON AND R. TORBERT<sup>1</sup>

*Space Science Laboratory, University of California, Berkeley, California 94720*

Further evidence is presented that structured soft-electron precipitation is an important source of large-scale ( $\lambda \geq 10$  km) *F* region ionization irregularities in the high-latitude ionosphere. We show that large amplitude, 20-km to 80-km structured plasma exists in both the daytime and nighttime auroral oval. In the latter case, the structured *F* layer plasma has been observed to convect into and through the field of view of the Chatanika radar. Here, and in a companion paper, we hypothesize that this soft electron precipitation is the primary source of high-latitude structure and that convection acts to distribute the irregular plasma throughout the polar ionosphere. Indeed, at the observed production scale (20–80 km), irregularities can easily convect throughout the high-latitude region with negligible decay from classical or anomalous diffusion, including the effects of a conducting *E* region. Our convection/decay model also explains the following observed features of published high-latitude irregularity data: (1) The steep gradient in irregularity intensity at the equatorward edge of the nighttime magnetospheric convection zone. (2) The existence of irregularities throughout the polar cap. (3) The reduction of irregularity intensity in the central polar cap. (4) The dawn-dusk asymmetry in the equatorward boundary of the high-latitude irregularity zone. On the other hand, if classical theory is applied to a 100-m scale structure, diffusion should rapidly limit the irregularities to an area within a few degrees of the production zone, a prediction not upheld by experimental data. Thus, plasma instabilities must operate on the large-scale structures to produce the observed intermediate scale (100 m  $< \lambda < 10$  km) power law irregularity spectra. Calculations of the  $\vec{E} \times \vec{B}$  instability growth rate in its generalized form, which includes field-aligned currents (the current convective instability), shows that growth should occur. The universal drift instability should then operate on these intermediate scale features. We suggest that this latter instability maintains the shorter scale plasma structure at the expense of a more rapid decay of the intermediate scale irregularities in a cascade-like process. Enhanced, turbulent diffusion can reduce significantly the lifetime of the intermediate scale irregularities but not of the larger structures, which can therefore still transit the polar cap.

## 1. INTRODUCTION

Plasma in the high-latitude *F* region ionosphere is highly structured on a scale from tens of kilometers to tens of meters [Dyson *et al.*, 1974; Clark and Raitt, 1976; Phelps and Sagalyn, 1976]. This irregular nature is shared by the electrical structure of the region, as determined from polar orbiting satellite electric field measurements [Maynard and Heppner, 1970; Kelley and Mozer, 1972; Laaspere *et al.*, 1971]. Scintillation of radio stars and satellite transmissions by kilometer scale structures in electron density also show that irregularities are a common feature of the high-latitude *F* region [Aarons *et al.*, 1969; Aarons and Allen, 1971; Aarons and Allen, 1973; Rino and Matthews, 1980].

Mechanisms suggested as a source for this structure include direct production by particle precipitation, plasma instabilities, and turbulent mixing by electrostatic fields (see Fejer and Kelley [1979] for references). Irregularities observed throughout the polar cap and equatorward of the

auroral oval in most local time sectors suggest that transport and/or multiple processes are involved.

In this paper we present further evidence for the importance of direct production of macroscale irregularities by structured soft electron fluxes. We then apply a simple model for transport and decay of such structures and discuss the role of plasma instabilities in the production of smaller scale irregularities on the gradients of the larger scale structures. Our goal is not to create a complete model for high-latitude irregularities but to develop some of the principles and concepts for developing such a model. Some of the relationships used here involve classical and anomalous perpendicular plasma diffusion and are derived in a companion paper [Vickrey and Kelley, this issue], hereinafter referred to as paper 2. We define large scale structures to have wavelengths  $\lambda \geq 10$  km, intermediate scale to have  $0.1 \text{ km} \leq \lambda \leq 10$  km, transition wavelengths to have  $10 \text{ m} \leq \lambda \leq 100 \text{ m}$  and short wavelengths to have  $\lambda < 10 \text{ m}$ .

## 2. EVIDENCE FOR AND CHARACTERISTICS OF THE DIRECT PRODUCTION OF MEDIUM-SCALE PLASMA IRREGULARITIES BY SOFT ELECTRON PRECIPITATION

There is previously published evidence that structured soft-particle precipitation can directly produce irregularities

<sup>1</sup>Now at Physics Department, University of California at San Diego, La Jolla, California 92037.

Copyright 1982 by the American Geophysical Union.

Paper number 2A0428.  
0148-0227/82/002A-0428\$05.00

4469

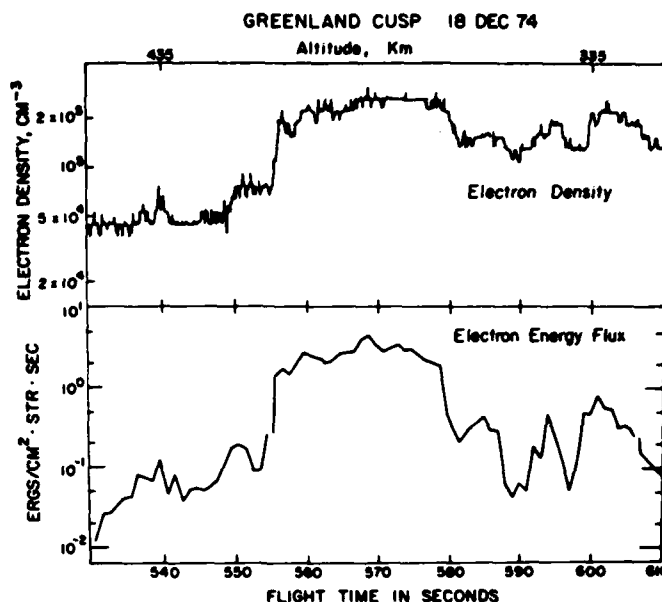


Fig. 1. Simultaneous in-situ measurements of electron density and precipitating auroral electron energy flux in the polar cusp.

in the auroral oval. For example, *Dyson and Winningham* [1974] showed with simultaneous measurements that the equatorward boundary of the severe topside irregularity zone in the polar cusp is collocated with the boundary for soft (300 eV) auroral electron fluxes. Figure 1 shows a high spatial resolution comparison of the electron density and electron fluxes in the polar cusp (dayside auroral oval) during part of a rocket flight from Sondre Stromfjord, Greenland. The rocket was fired at an azimuth aligned at roughly  $45^\circ$  to the auroral oval. The total energy flux in electrons between 50 eV and 5 keV is plotted in Figure 1 along with the plasma density measured with a planar ion probe mounted at the tip of the vehicle. (These measurements were normalized by using measurements of the lower hybrid frequency [Temerin and Kelley, 1980].) The differential energy flux spectrum was peaked near 800 eV in the flux enhancement centered at 570 s, near 300 eV at 595 s, and near 500 eV at 602 s [Torbert and Carlson, 1980]. The correlation between energy flux and electron density is quite good. Owing to the high altitude of the observations, the effect cannot be temporal in nature since the production of plasma by precipitating soft electrons occurs at lower alti-

tudes and the newly formed plasma diffuses upward relatively slowly. In their type 1 case, for example, *Roble and Rees* [1977] have shown that an enhancement of plasma density to a value in excess of  $10^5 \text{ cm}^{-3}$  could occur in response to the observed electron fluxes at the rocket altitude in about 100 s. Thus, we conclude that the variation is spatial and the plasma density structure mirrors that of the precipitating soft electrons.

The ion current (normalized to density near apogee) detected by the instrument during the latter two-thirds of the flight when structured plasma was detected, is plotted in Figure 2. The absolute instrument response is degraded somewhat as the rocket descends, but the relative fluctuation level should be reasonably reliable. The spectrum obtained by Fourier transformation of the data shown in Figure 2 is presented in Figure 3. Approximate scale sizes are plotted across the upper axis. No single velocity can be used to transform frequency to wavelength in the data set

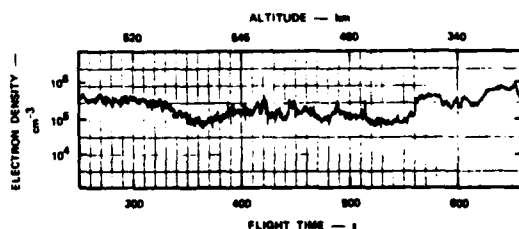


Fig. 2. In-situ electron density measurement from the latter two-thirds of the rocket flight of Figure 1 during which structured plasma was detected.

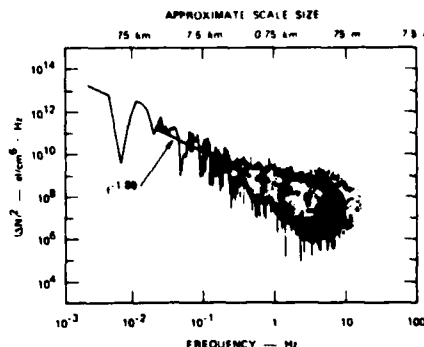


Fig. 3. The spectrum of irregularities obtained from a spectral analysis of the electron density measurements shown in Figure 2.

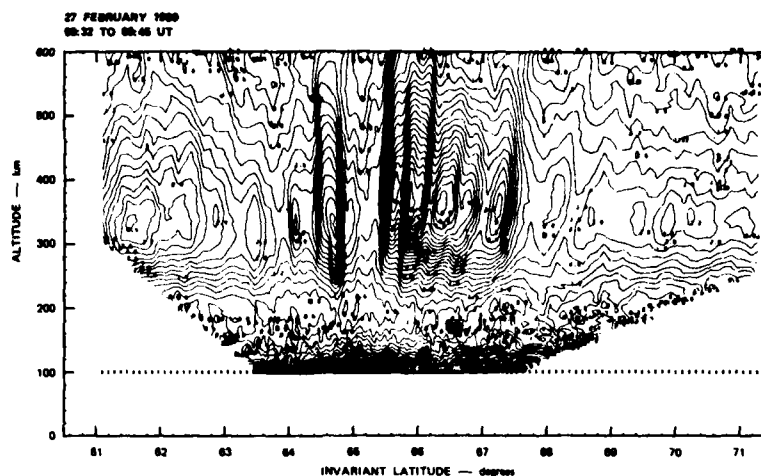


Fig. 4. Altitude/latitude variation of electron density in the midnight sector auroral zone measured by the Chatanika radar. The contour interval is  $2 \times 10^4 \text{ cm}^{-3}$ .

because of the variable background electric field during the event [Jorgensen *et al.*, 1980]. The straight line is a least-squares fit to a power law in the frequency range of 0.02–0.4 Hz and displays a slope of  $-1.89 \pm 0.2$ . The data points plotted are averages of the Fourier components over factors of 2 in frequency. At the lowest frequencies the high-power spectral density includes effects of the varying altitude of the rocket. However, the jump in power by 3 orders of magnitude with a peak near 0.015 Hz is a good measure of the outer scale for horizontal structure in the data sample, which is thus in the range of 50–80 km. Note that a straight line fit to the larger frequency range of  $f > 0.02$  Hz yields a slope of only  $-1.6$ .

The waveform and power spectrum in Figures 2 and 3 bear a striking resemblance to Figures 5 and 6 in the paper by Kelley *et al.* [1980], which presented rocket observations of density structure measured with a Langmuir probe operated in the electron regime in the midnight auroral oval. Their spectrum peaked at 50–60 km and had a spectral index of  $-1.9$  in approximately the same (limited) wavelength range noted above. In both cases, the spectral slope seemed to get more shallow at higher  $k$  values (higher frequency). Values of the negative index were from 1.2 to 1.3 at the largest  $k$  values. The nighttime oval spectrum, when expressed in the units used in Figure 3, was about a factor of 2–4 less in its absolute electron density fluctuation level than the dayside oval case. This is consistent with other observations of the relative intensity of dayside versus nightside auroral oval fluctuations [Kelley and Mozer, 1972] and the characterization of the cusp as a severe topside irregularity zone by Dyson and Winningham [1974].

Vickrey *et al.* [1980], using the Chatanika incoherent-scatter radar, have presented examples of field-aligned ionization enhancements in the midnight sector auroral zone that have latitudinal dimensions comparable to the outer scale evident in the cusp data shown in Figure 3. The data are collected while the radar beam continuously scans the magnetic meridian. Thus, in approximately 12 min the radar can map out the altitude/latitude distribution of electron density over more than  $10^\circ$  of latitude in the F region. For

our present purposes we have reanalyzed the data of Vickrey *et al.* [1980] with a 5-s integration period. This yields a horizontal resolution of  $\sim 10$  km at 350-km altitude. The result is presented in Figure 4, which shows contours of constant electron density as a function of altitude and latitude. Note that the data have been transformed into a coordinate system with straight, vertical magnetic field lines. The X's at the bottom of the figure show the latitude resolution of the data is a result of changing the antenna scan rate during the scan.

The ionization enhancement, or plasma 'blob,' at  $\sim 61.5^\circ$  invariant latitude was probably not fully resolved. However, the series of blobs located nearly overhead at Chatanika appear to be resolved and show a quasi-periodic structure in the scale size regime near 50 km. To quantify this discussion, we performed a spectral analysis of the density variations as a function of latitude at a fixed height. The procedure used was the same as that for the rocket data of Figure 3. Figure 5 shows the one-dimensional spectral density function,  $|\Delta N(k)|^2$ , corresponding to the radar measurements at 350 km altitude. As one would expect from Figure 4, there is a dramatic peak in  $|\Delta N(k)|^2$  at the input scale size  $2\pi/k \approx 50$  km. Thus, the outer scale of irregularities observed in the

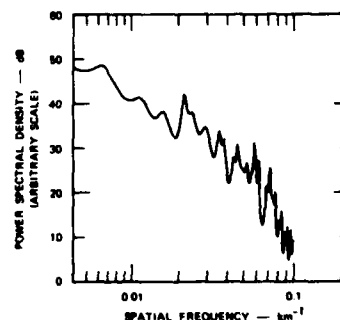


Fig. 5. The spectrum of electron density irregularities obtained by spectrally analyzing the radar measurements of the latitudinal variations of electron density at 350-km altitude.

polar cusp is the same as that observed in the midnight sector of the auroral oval.

Vickrey [1981] analyzed the latitudinal distribution of electron and ion temperatures ( $T_e$  and  $T_i$ ) associated with the ionization enhancements of Figure 4. He found that while  $T_i$  showed no indication of the density enhancement,  $T_e$  was reduced within the blob. This is to be expected since the energy loss rate of the electron gas increases with increasing electron density. However, this characteristic suggests that the blob was produced sometime earlier because one would expect  $T_e$  to be increased inside the blob if it were concurrently produced by precipitation. Many other examples of multiple  $F$  region ionization enhancements have been detected at Chatanika.

Because the blobs in Figure 4 were observed to drift southward into the radar field of view with the westward electric field, the production region is north of Chatanika, perhaps at the northern edge of the nightside auroral oval. This interpretation is supported by the observations of Carlson and Kelley [1977], Foster and Burrows [1976], and D. Hardy (personal communication, 1981), who have all reported soft electron precipitation at the northern edge of the nightside auroral oval. This region probably maps into the plasma sheet near the last closed field line. Strongly enhanced ( $>10^6 \text{ cm}^{-3}$ ) structured  $F$  region plasma has also been reported in the polar cap in association with red auroral emissions [Weber and Buchau, 1981], soft electron precipitation (D. Hardy, personal communication, 1980), and scintillations (S. Bu, personal communication, 1980). These polar cap arcs often occur during  $B_z$  north conditions and may indicate contact with interplanetary magnetic field lines 'connected' to polar cusp field lines and magnetosheath electrons.

Although other sources of localized  $F$  region density enhancements are possible [Vickrey, 1981], the observations mentioned above suggest that much of the large-scale structure (outer scale  $\sim 50 \text{ km}$ ) in the high-latitude  $F$  region plasma is caused by precipitation of soft electrons in the atmosphere. The source region is likely to be an annular ring at the poleward edge of the auroral oval whose field lines map into the plasma sheet or plasma mantle near the polewardmost closed field line.

Since structured plasma is observed over a much larger region within the polar ionosphere than is precipitation of soft electrons, transport must play an important role in determining irregularity morphology. As discussed in detail in paper 2, large-scale ( $\geq 10 \text{ km}$ ) irregularities have a very long lifetime. Also, the observations of Vickrey *et al.* [1980] show that these large irregularities convect with the background electric field and can thus be transported a great distance from where they were produced. In the next section we combine the model production region just described with a simple convection pattern and the diffusion model of paper 2. We then investigate the roles of transport and diffusive decay in determining the global morphology of  $F$  region irregularities.

### 3. DECAY AND TRANSPORT OF STRUCTURED HIGH-LATITUDE IONIZATION

Prior studies of the production and decay of the high-latitude ionosphere, such as those by Schunk *et al.* [1976] and Roble and Rees [1977], have considered a horizontally stratified system and emphasized the vertical and temporal

dependence of ionization density. We take as experimentally verified the existence of precipitation-produced ionization enhancements with limited horizontal extent. We then study the effect of the limited horizontal dimension on the lifetime of the enhancement. To progress, we assume that the effects studied by Schunk *et al.* [1976] in the vertical coordinate can be decoupled from the decay caused by horizontal gradient-driven diffusion. That is, the gradual process of subsidence and recombination-driven decay are assumed to operate in parallel with the effects described here. In the following discussion, we simply multiply the scale-size-dependent decay by the time constant associated with parallel diffusion and recombination.

Horizontal diffusion is, of course, inhibited in the ionosphere by the magnetic field. Ions dominate since their large gyro-radius allows a larger spatial displacement after each collision than do electrons. As discussed by Chen [1974], the rate at which plasma diffuses across  $\hat{B}$  depends on the boundary conditions at the end of the magnetic field lines. If the field lines are very long or are terminated by an insulator, a space charge electric field builds up due to the difference between ion and electron diffusion rates. It then retards the ion flux and lowers the overall plasma diffusion rate. For an insulating  $E$  region, the resulting diffusion proceeds at the slower electron diffusion rate. If the field lines are terminated by a perfect conductor, the electrons can flow freely along magnetic field lines to cancel the retarding electric field; hence, diffusion proceeds at the more rapid ion rate.

In paper 2 we derive an approximate diffusion coefficient for  $F$  region irregularities:

$$D_{\perp} = \frac{\sum_j F}{\sum_j F + \sum_j F^E + \sum_j F^E} (D_{e\perp} - D_{i\perp}) + D_{i\perp} \quad (1)$$

where  $\sum_j F$  is the height-integrated Pedersen conductivity for species  $j$ ;  $D_{j\perp}$  is the height-integrated product of the electron density and perpendicular diffusion coefficient for species  $j$  (normalized to the total electron content); and  $\sum_j F^E$  is the height-integrated Pedersen conductivity in the  $E$  region. In the derivation we assume quasi-neutrality, infinitely conducting magnetic field lines, and a uniform (unchanging) conductivity in the  $E$  region. In addition, we assume that the functional form of the plasma density could be written as the product of an altitude term times a function of the horizontal and time variables. This mathematical construction results in an expression that, if interpreted as a diffusion equation, yields the diffusion coefficient in (1). The  $F$  region height integral is taken from an altitude (180 km) just above the  $E$  layer and extends to infinity. For a perpendicular spatial wave number  $k_{\perp}$ , the decay time constant is given by  $\tau = (k_{\perp}^2 D_{\perp})^{-1}$ . A number of curves relating  $D_{\perp}$  and  $\tau$  to  $F$  and  $E$  region parameters are presented in paper 2.

The effect of transport and classical diffusive decay is illustrated in Figure 6a for intermediate (1 km) scale size irregularities. The peak  $F$  region density is assumed to be  $5 \times 10^5 \text{ cm}^{-3}$  in the production zone, with the density maximum at a height of 350 km. A Chapman layer is also assumed (see paper 2). Winter conditions are taken so as to emphasize the effects of auroral production and decay. A dashed line marks the terminator at 350-km altitude during winter and equinox. The flow lines are taken from Spiro *et al.* [1978] for quiet conditions and are drawn in a reference frame fixed to the sun. That is, the reference frame is noncorotating. The  $E$

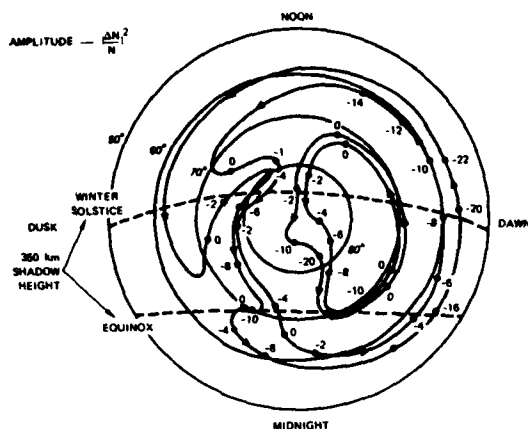


Fig. 6a

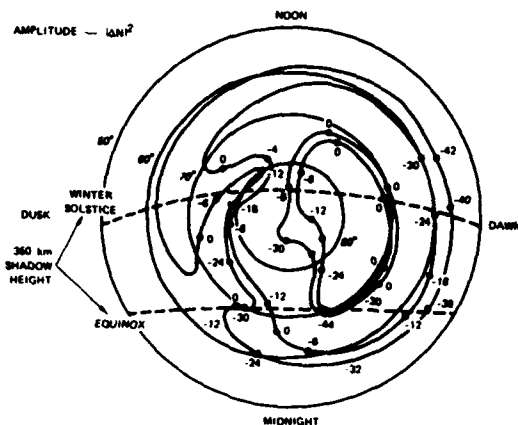


Fig. 6b

Fig. 6. Illustration of the latitude and local time variations (in the inertial frame) of the amplitude (in dB) of 1-km scale electron density irregularities predicted by combining (1) a source of large-scale input irregularities at the poleward edge of the discrete auroral oval (where the amplitude is reset to zero dB), (2) the classical cross field diffusion model of Vickrey and Kelley [this issue], including the effects of a conducting E region, and (3) the convection model of Spiro *et al.* [1978]. Figure 6a shows  $|\Delta N/N|^2$ , while Figure 6b includes the effects of recombination decay on the amplitude of density fluctuations.

region height-integrated conductivity is taken from Wallis and Budzinski [1981]. Whenever a flow line intersects the poleward edge of the discrete auroral oval, the amplitude of  $(\Delta N/N)^2$  for 1-km irregularities is reset to 0 dB. Subsequent numbers denote the decrease in  $(\Delta N/N)^2$  in dB along the path. A similar plot for 10-km structures would show almost negligible decay since it acts 100 times more slowly at that scale size. Figure 6b shows the overall decay of the ionosphere because of recombination, which adds approximately 4 dB per hour of travel time for the irregularity and the background. This plot, then, is more representative of the spectral strength  $|\Delta N|^2$ ; hence, it is perhaps more descriptive of scintillation effects. When the absolute density decayed to  $5 \times 10^3 \text{ cm}^{-3}$ , the recombination decay was halted. In such a case, the assumption of an  $O^+$  plasma is no longer valid, and longer lived ions may dominate the  $F_2$  layer composition [Heelis *et al.*, 1981].

A number of conclusions can be drawn from these figures. Once formed, 10-km size relative fluctuations can survive transport throughout the polar cap and auroral zone if sunlight does not illuminate the region for a prolonged period. At 1-km scale the classical diffusion discussed here and in paper 2 has a significant effect in some regions of the polar cap and auroral zone. For example, a very deep irregularity 'hole' can be formed in the central polar cap, as experimentally reported by Kelley and Mozer [1972]. This is primarily due to the long length of time a flux tube can spend in the central polar region. Even in the 10-km case, a very sharp gradient in irregularity intensity is formed at the equatorward edge of the nighttime magnetospheric convection zone—not the auroral oval. This is in excellent agreement with many studies of the high-latitude irregularity boundary (see review by Fejer and Kelley [1980]). Note that other sources of plasma density irregularities, such as mid-latitude spread  $F$  and processes associated with plasma density gradients near the  $F$  region trough can also contribute to irregularity formation at times.

In relatively quiet times the post-sunset local time region

1800 to 2100 between  $60^\circ$  and  $68^\circ$  should not contain many irregularities since, in the nonrotating frame, flux tubes only enter this region from the sunlit sector. For the same reason, the equatorward boundary of the irregularity zone should be at higher latitudes in the dusk sector than in the dawn sector, to which midnight-sector auroral oval irregularities can rapidly convect. This is in agreement with the ISIS results reported by Sagalyn *et al.* [1974], who showed the boundary to be about  $3^\circ$  higher in latitude in the dusk sector for  $Kp \leq 3$ . The difference was less pronounced for  $Kp \geq 3$ . This is reasonable since, with increasing magnetic activity, large convection speeds can dominate over the corotation velocity at lower latitudes in the local time sector near and just after dusk.

Before leaving this section we must ask whether anomalous diffusion can dominate the evolution of large scale features. Gary [1980] has calculated a diffusion coefficient  $D_a$  resulting from universal drift waves given by

$$D_a = \frac{4\pi}{9} \left( \frac{T_e}{T_i} \right)^{4/3} \left( \frac{kT_i}{m_i} \right)^{3/2} \frac{1}{\Omega_i^2} \frac{1}{n} \left( \frac{\partial n}{\partial X} \right) \quad (2a)$$

where the last term is the inverse of the gradient scale length  $L_D$  driving the waves. This can also be written

$$D_a = \left( \frac{4\pi}{a} \right) \left( \frac{T_e}{T_i} \right)^{4/3} \rho_i^2 \left( \frac{V_i}{L_D} \right) \quad (2b)$$

Where  $V_i$  is the ion thermal speed and  $\rho_i$  is the ion gyro radius. Since the classical diffusion coefficient is independent of the gradient scale length, we can set  $D_a = D_{i\perp}$  to determine at what length,  $L_c$ , anomalous diffusion becomes important. For  $T_i = T_e = 1000^\circ\text{K}$ ,  $B = 0.5 \text{ G}$ , an  $O^+$  plasma and using  $D_{i\perp} = 1.6 \text{ m}^2/\text{s}$ , we find  $L_c = 3700 \text{ m}$ . We thus conclude that large scale features are unaffected by anomalous drift wave diffusion and will easily survive cross polar cap convection. Bohm diffusion is another candidate for anomalous transport. A quasi-empirical measure of the

Bohm diffusion coefficient has been developed in laboratory work, and is given by

$$D_B = \frac{1}{16} \rho^2 \Omega_i \quad (3)$$

which can be readily compared to (2b). This expression yields  $D_B = 110 \text{ m}^2/\text{s}$  for the ionospheric conditions outlined above. Thus, the decay time,  $\tau_B = (k^2 D_B)^{-1}$ , for a 10 km structure is still very long—approximately 5 hours. Therefore, large scale features are essentially unaffected by anomalous diffusion.

#### 4. THE ROLE OF INSTABILITIES IN PRODUCING STRUCTURED *F* REGION PLASMA

The foregoing discussion shows that a 1-km scale structure displays a significant classical decay in polar transport, and of course, an even more rapid decay if anomalous diffusion operates. The 100-m scale, of course, decays two orders of magnitude more quickly. Thus, if additional production processes are ignored, one would expect an absence of 100-m scale irregularities in the polar cap. However, this contradicts the results of a number of experiments which have shown that structures of this scale do populate vast regions of the polar cap. Thus, there must be additional sources of irregularity formation at the intermediate and transition scales.

At the 1-km scale, the  $\vec{E} \times \vec{B}$  instability [Linson and Workman, 1970; Simon, 1963] is a prime candidate for production. Vickrey *et al.* [1980] have already shown simultaneous measurements of irregularities (via their scintillation effects), and horizontal gradients of plasma density associated with large-scale plasma enhancements, electric fields, and field-aligned currents. They calculated the growth rate due to current convective instability (a generalized form of the  $\vec{E} \times \vec{B}$  instability that includes the effects of field-aligned currents) and showed collocation of 1-km scale structures and positive growth rate. As discussed in paper 2, the growth rates given by Vickrey *et al.* should be modified somewhat to incorporate the perpendicular diffusion coefficient that includes the effects of the conducting *E*-region. However, this has little effect on their results and certainly does not prevent the instability from operating at the 1-km scale. *F* region structures such as those shown in Figure 4 are a common feature of the auroral ionosphere. They are of limited latitudinal extent and thus, gradients exist in both the poleward and equatorward direction. Since the zonal electric field is seldom zero, the  $\vec{E} \times \vec{B}$  process must operate on one edge or the other.

The growth rate for the  $\vec{E} \times \vec{B}$  instability is given by

$$\gamma = \frac{E_0}{BL} - k^2 D_\perp \quad (4)$$

For  $L = 10 \text{ km}$ ,  $E_0/B = 200 \text{ m/s}$ , and using a classical diffusion coefficient  $D_\perp = 1.6 \text{ m}^2/\text{s}$  ( $\Sigma_P^E \gg \Sigma_P^F$ ), the critical wavelength where diffusion balances growth is about 60 m. That is, positive growth occurs for all wavelengths greater than 60 m. According to the theory of Keskinen and Ossakow [1981], a power law should extend from this wavelength to some smaller, 'minimum scale' in the medium. Kelley and Baker [1982] have suggested that the classical diffusion rate  $D_\perp$  in (4) be replaced by the anomalous rate given by (2). If this is done, the critical wavelength is scale length  $L$ . Using the same conditions as above,  $\lambda_m = 210 \text{ m}$ . At smaller

scales, i.e., the transition and short wavelength regime, the irregularity spectrum would be determined by the drift waves themselves. In either case, the  $\vec{E} \times \vec{B}$  instability can create structure over the full spatial range observed experimentally by operating on the edges of large scale density structures that are properly oriented with respect to the electric field and neutral wind.

The current convective instability [Ossakow and Chaturvedi, 1979], which is a generalized form of the  $\vec{E} \times \vec{B}$  instability that includes the destabilizing effects of parallel drifts due to field aligned currents, can operate even when the geometric relationship between  $\vec{E}$  and  $\vec{\nabla}N$  is stable. Thus, this process may also contribute to the irregularity spectrum for  $\lambda \leq$  several km.

There are some important distinctions between the current-driven current convective instability and the pure  $\vec{E} \times \vec{B}$  instability. The growth rate of the current driven instability maximizes at altitudes where the density is low (in the *F*<sub>1</sub> region valley). Also, since  $k_\parallel \neq 0$ , parallel diffusion can be the dominant damping mechanism. This is not true for the  $\vec{E} \times \vec{B}$  instability. Thus, although it is possible for the current-driven instability to operate at the *F* region peak, it does not necessarily do so. Hence, the  $\vec{E} \times \vec{B}$  instability may be more effective in producing scintillation effects (which depend on the absolute electron density fluctuations) than the current-driven current convective instability. We note in passing that the field-aligned currents that destabilize the current convective process must be carried by thermal plasma. In regions such as auroral arcs, where some part of the net current is carried by energetic electrons, care must be taken in applying this theory.

#### 5. SUMMARY

We have shown that soft particle precipitation is an important source of structured *F* region plasma in the auroral ionosphere. These large-scale irregularities (tens of kilometers) have long lifetimes and thus can convect far away from where they are produced. These structures may also be unstable and thus produce smaller scale irregularities. The ultimate spectrum of irregularities produced in the *F* region is a complicated balance of instability growth and damping that depends on *E* region conditions as well as the state of the magnetosphere (through  $\vec{E}$  and  $\vec{J}_\parallel$ ). The limited in-situ observations that exist indicate that the spectrum of irregularities has a power law form ( $k^{-n}$ ) with  $n$  being approximately 2, but there is a hint of spectral softening at large  $k$  values.

We have combined a simple morphological model of large-scale irregularity production with the cross-field diffusion model of Vickrey and Kelley [this issue] and the convection pattern of Spiro *et al.* [1978] to give a schematic representation of the global morphology of *F* region irregularities. This pattern reproduces several aspects of high-latitude irregularity morphology that have been observed, including (1) observations of irregularities throughout the polar regions, (2) a reduction of irregularity amplitude in the central polar cap, (3) a steep gradient in irregularity intensity at the equatorward edge of the nighttime magnetospheric convection zone, and (4) an asymmetry between the dusk and dawn sectors of the equatorward boundary of the high-latitude irregularity zone during magnetically quiet times.

Because *F* region irregularities are observed over a much larger area of the polar ionosphere than is structured precipi-

tation, convection must play an important role in distributing these irregularities. However, since the diffusive lifetime of irregularities is proportional to  $k^{-2}$ , 100-m scale structures cannot survive the transit of the polar cap without an additional production source. We suggest that the  $\vec{E} \times \vec{B}$ /current convective instability, which can be driven by field-aligned currents, electric fields, or both, is the key process that provides a source of wave energy at the intermediate scale and that drift waves play an important role at smaller scales. The lifetime of large-scale (10-km) irregularities may be reduced slightly below that expected from classical diffusion, but not enough to prevent their crossing the polar cap. On the other hand, these combined processes increase the time during which smaller scale structure is observed in the plasma.

**Acknowledgments.** The authors acknowledge helpful discussions with C. L. Rino and R. C. Livingston. The spectral analysis for Figure 5 was performed by R. C. Livingston and N. B. Walker. The convection pattern used to produce Figures 5 and 6 was computed by Shawn Quegan. Work at SRI International was supported by the Defense Nuclear Agency under contract DNA001-81-C-0076 and by the Air Force Office of Scientific Research under contract F49620-80-C-0014. Chatanika radar operations were supported by the National Science Foundation under grant ATM-7823658. Work at Cornell was supported by NASA. The Greenland cusp rocket campaign was made in collaboration with the Max-Planck Institut für Extraterrestrische Physik (Garching, West Germany) and the Danish Meteorological Institute and was supported in part by NASA grant NGR-05-003-239 to U. C. Berkley. The work at Cornell was partially supported under a contract from the Office of Naval Research.

## REFERENCES

- Aarons, J., J. P. Mullen, and H. E. Whitney, The scintillation boundary, *J. Geophys. Res.*, **74**, 884, 1969.
- Aarons, J., and R. S. Allen, Scintillation boundary during quiet and disturbed magnetic conditions, *J. Geophys. Res.*, **76**, 170, 1971.
- Aarons, J., and R. S. Allen, Scintillation boundary during quiet and disturbed magnetic conditions, *J. Geophys. Res.*, **78**, 7441, 1973.
- Carlson, C. W., and M. C. Kelley, Observations and interpretation of particle and electric field measurements inside and adjacent to an active auroral arc, *J. Geophys. Res.*, **82**, 2349, 1977.
- Clark, D. H., and W. J. Raitt, The global morphology of irregularities in the topside ionosphere as measured by the total ion current probe on ESRO-4, *Planet. Space Sci.*, **24**, 873, 1976.
- Chen, F. F., *Introduction to Plasma Physics*, Plenum Press, New York, 1974.
- Dyson, P. L., and J. D. Winningham, Topside ionospheric spread F and particle precipitation in the dayside magnetospheric clefts, *J. Geophys. Res.*, **79**, 5219, 1974.
- Dyson, P. L., J. P. McClure, and W. B. Hanson, In-situ measurements of the spectral characteristics of F Region ionospheric irregularities, *J. Geophys. Res.*, **79**, 1497, 1974.
- Fejer, B. G., and M. C. Kelley, Ionospheric irregularities, *Rev. Geophys. Space Phys.*, **18**, 401, 1980.
- Foster, J. C., and J. R. Burrows, Electron fluxes over the polar gap, 1. Intense keV fluxes during poststorm quieting, *J. Geophys. Res.*, **81**, 6016, 1976.
- Gary, S. P., Wave particle transport from electrostatic instabilities, *Phys. Fluids*, **23**, 1193, 1980.
- Heelis, R. A., J. A. Murphy, and W. B. Hanson, A feature of the behavior of  $He^+$  in the nightside high-latitude ionosphere during equinox, *J. Geophys. Res.*, **86**, 59, 1981.
- Jorgensen, T. S., I. S. Mikkelsen, K. Lassen, G. Haerendel, E. Rieger, A. Valenzuela, F. S. Mozer, M. Temerin, B. Holback, and L. Bjorn, Electric fields in the dayside auroral oval, *J. Geophys. Res.*, **85**, 2891-2901, 1980.
- Kelley, M. C., and K. D. Baker, On the freezing of barium cloud striations at the kilometer scale, submitted to *Geophys. Res. Lett.*, 1982.
- Kelley, M. C., and F. S. Mozer, A satellite survey of vector electric fields in the ionosphere at frequencies of 10-500 Hz. 1. Isotropic, high-latitude electrostatic emissions, *J. Geophys. Res.*, **77**, 4158, 1972.
- Kelley, M. C., K. D. Baker, J. C. Ulwick, C. L. Rino, and M. J. Baron, Simultaneous rocket probe, scintillation, and incoherent scatter observations of irregularities in the auroral zone ionosphere, *Radio Sci.*, **15**, 491, 1980.
- Keskinen, M. J., and S. L. Ossakow, On the spatial power spectrum of the  $\vec{E} \times \vec{B}$  gradient drift instability in ionospheric plasma clouds, *Memo. Rep. 4494*, Naval Res. Lab., Washington, D. C., 1981.
- Laaspere, T., W. D. Johnson, and L. C. Semperebon, Observations of auroral hiss LHR noise and other phenomena in the frequency range 20 Hz to 540 kHz on OGO 6, *J. Geophys. Res.*, **76**, 4477, 1971.
- Linson, L. M., and J. B. Workman, Formation of striations in ionospheric plasma clouds, *J. Geophys. Res.*, **75**, 3211, 1970.
- Maynard, N. C., and J. P. Heppner, Variations in electric fields from polar orbiting satellites, *Particles and Fields in the Magnetosphere*, edited by B. McCormac, p. 247, D. Reidel, Hingham, Mass., 1970.
- Ossakow, S. L., and P. K. Chaturvedi, Current convective instability in the diffuse aurora, *Geophys. Res. Lett.*, **6**, 332, 1979.
- Phelps, A. D., and R. C. Sagalyn, Plasma density irregularities in the high-latitude topside ionosphere, *J. Geophys. Res.*, **81**, 515, 1976.
- Rino, C. L., and S. J. Matthews, On the morphology of auroral-zone radiowave scintillation, *J. Geophys. Res.*, **85**, 4139, 1979.
- Roble, R. G., and M. H. Rees, Time-dependent studies of the aurora: Effects of particle precipitation on the dynamic morphology of ionospheric and atmospheric properties, *Planet. Space Sci.*, **25**, 991, 1977.
- Sagalyn, R. S., M. Smiddy, and M. Ahmed, High-latitude irregularities in the topside ionosphere based on ISIS thermal probe, *J. Geophys. Res.*, **79**, 4552, 1974.
- Schunk, R. W., P. M. Banks, and W. J. Raitt, Effects of electric fields and other processes upon the nighttime high-latitude F layer, *J. Geophys. Res.*, **81**, 3271, 1976.
- Simon, A., Instability of a partially ionized plasma in crossed electric and magnetic fields, *Phys. Fluids*, **6**, 382, 1963.
- Spiro, R. W., R. A. Heelis, and W. B. Hanson, Ion convection and the formation of the mid-latitude F region ionization trough, *J. Geophys. Res.*, **83**, 4255, 1978.
- Temerin, M., and M. C. Kelley, Rocket-borne wave measurements in the dayside auroral oval, *J. Geophys. Res.*, **85**, 2915-2924, 1980.
- Torbert, R. B., and C. W. Carlson, Evidence for parallel electric field particle acceleration in the dayside auroral oval, *J. Geophys. Res.*, **85**, 2909, 1980.
- Vickrey, J. F., Radar observations of structured plasma in the high-latitude F region, *SRI Final Rep.*, SRI International, Menlo Park, Calif., 1981.
- Vickrey, J. F., and M. C. Kelley, The effects of a conducting E layer on classical F region cross-field plasma diffusion, *J. Geophys. Res.*, this issue.
- Vickrey, J. F., C. L. Rino, and T. A. Potemra, Chatanika/TRIAD observations of unstable ionization enhancements in the auroral F region, *Geophys. Res. Lett.*, **7**, 789-792, 1980.
- Wallis, D. D., and E. E. Budzinski, Empirical models of height-integrated conductivities, *J. Geophys. Res.*, **86**, 125, 1981.
- Weber, E. J., and J. Buchau, Polar cap F layer auroras, *Geophys. Res. Lett.*, **8**, 125, 1981.

(Received July 14, 1981;  
accepted July 16, 1981.)



## Energy Deposition by Precipitating Particles and Joule Dissipation in the Auroral Ionosphere

JAMES F. VICKREY, RICHARD R. VONDRAK,<sup>1</sup> AND STEPHEN J. MATTHEWS

Radio Physics Laboratory, SRI International, Menlo Park, California 94025

Eight days of synoptic data from the Chatanika incoherent scatter radar have been analyzed in an attempt to determine the characteristic morphology of auroral zone energy deposition by Joule heating and precipitating particles. The observations cover invariant latitudes between  $\sim 62^\circ$  and  $68^\circ$ . The composite spatial morphology derived from these eight days of data shows that morning sector particle precipitation deposits energy into the thermosphere at a faster rate and at lower altitudes than evening sector precipitation. The Joule heating rate has the opposite asymmetry about midnight, i.e., more Joule heating results for a given premidnight eastward electrojet current than for the same morning sector westward electrojet current intensity. This complementary asymmetry about midnight between the Joule and particle precipitation heating rates is consistent with the changes in ionospheric conductivity implied by the local time variation of precipitating particle hardness. The Joule heating rate generally dominates particle energy deposition in the premidnight sector. However, the daily averages of the two energy sources are roughly equal.

### INTRODUCTION

It is well-established that the contribution to high-latitude thermospheric heating by particle precipitation and Joule dissipation of electric fields often dominates the direct solar EUV input. This energy deposition by particles and electric fields, which can be highly structured both spatially and temporally, can perturb the atmospheric electron density, ion composition, electron and ion temperatures, and neutral air motion [Hays *et al.*, 1973; Brekke, 1976; Banks, 1977; Roble, 1977; Rees, 1963; Brekke and Rino, 1978; Banks *et al.*, 1981].

Because Joule heating preferentially heats ions, whereas precipitating electrons heat thermalized electrons, the thermospheric response to the two heat sources may be expected to be different. Also, the altitudes at which energy deposition takes place are different for the two sources. As discussed by Brekke and Rino [1978], differences in the altitude where energy deposition is maximum can have important implications for the effectiveness with which global atmospheric disturbances are generated by auroral processes. It is a commonly held view that the global effects of Joule heating on the neutral atmosphere are more important than those of particle heating. The logic of this viewpoint is that although the particle energy deposition rate can at times greatly exceed the Joule heating rate (particularly within an auroral arc), electric fields extend over large areas of the earth and have a long duration. Furthermore, the transfer of energy and momentum to the neutrals from the ion gas is more efficient than from a precipitating electron flux.

In addition to the expected differences in thermospheric response to heating by energetic particles and electric fields mentioned above, the heating rates themselves have a distinct evening-morning asymmetry. For example, Brekke and Rino [1978] pointed out that the altitude at which Joule

heating maximizes is significantly higher in the evening eastward electrojet than in a morning-sector westward electrojet. For a given current density, currents that flow at higher altitudes are more efficient at heating the atmosphere. Brekke and Rino [1978] found the heating efficiency to be ten times larger in a positive bay than in a negative bay substorm.

The magnitude of energy input by precipitating particles often has the opposite asymmetry about midnight to that of Joule heating, although the asymmetry in the altitude of maximum energy deposition is in the same sense. The opposing asymmetry can be understood by considering the relationships between the precipitating particle energy and the resulting ionospheric conductivity that affects both the height at which current flows and the direction of the current flow relative to the electric field direction. As a general rule (although there are exceptions), morning sector precipitation is more energetic than evening sector precipitation and produces ionization at lower altitudes [e.g., Wallis and Budzinski, 1981]. However, since the Hall mobility peaks at a lower altitude than the Pedersen mobility, morning sector currents (which are associated with harder electron fluxes) have a greater tendency to flow in the Hall direction and hence are less dissipative than evening sector currents.

To examine in detail these trends for the partitioning of magnetospheric energy deposition, as well as its spatial and temporal variability, we have analyzed eight days of synoptic data collected by the Chatanika incoherent scatter radar. These data represent a variety of magnetic conditions, with examples of substorms occurring at essentially all local time sectors. By viewing this relatively large body of synoptic data collectively, the 'average' auroral zone pattern of electrodynamics begins to emerge. We have analyzed the data to determine the ionospheric electric field, current, conductivity, and energy deposition rate over the invariant latitude range of approximately  $62^\circ$  to  $68^\circ$  for *E* region heights. The latitude-local time variations of conductivity are discussed in Vickrey *et al.* [1981]. In this paper we concentrate on the auroral zone energy deposition patterns; the detailed discussion of electric fields and currents will be presented elsewhere.

<sup>1</sup> Now at Lockheed Palo Alto Research Laboratory, Palo Alto, California 94304.

Copyright 1982 by the American Geophysical Union.

Paper number 2A0545.  
0148-0227/82/002A-0545\$05.00

5184

## TECHNIQUE

The observational mode employed for the measurements discussed below consists of continuous scans of the radar beam in the magnetic meridional plane [Vondrak and Baron, 1976]. With this technique, the radar beam is able to probe the altitude-latitude distribution of electron density and line of sight plasma drift, from which the electric field, conductivity, and current are determined. Also, by examining many such successive scans, the latitude-local time variations of the auroral ionosphere may be examined. Although the limits of the scans vary slightly from one experiment to another, it is generally possible to gather useful data to a minimum elevation angle of  $15^\circ$ . Thus, at the 100-km altitude, geomagnetic latitudes from  $62^\circ$  to  $68^\circ$  are scanned. The scan rate is typically  $0.2 \text{ deg/s}$ , and the data are averaged for 15 s. Depending on the scan limits, full scans are completed in 10 to 12 min. Electron density samples were obtained at range intervals of 4.5 km. The angular resolution of each measurement is given by the convolution of the  $0.6^\circ$  antenna beam width and the  $3^\circ$  of antenna motion during the 15-s integration period. Since at low-elevation angles the height integration includes measurements from different latitudes, the latitude resolution of the measurements depends on elevation angle [see Vickrey et al., 1981].

The use of electron density profiles from Chatanika to estimate the height-integrated energy deposition from precipitating electrons  $Q_p$  has been described by several authors [Wickwar et al., 1975; Wedde et al., 1977; Banks, 1977;

Vondrak and Baron, 1977]. Wickwar et al. [1975] found the radar determinations of  $Q_p$  to agree very well with estimates made by photometric procedures.

The assumptions made to determine  $Q_p$  are that (1) steady state conditions hold in the ionosphere during the data integration period, (2) ion transport can be ignored (this limits the height range to  $< 160 \text{ km}$ ), (3) particle precipitation is the sole source of ion production, and (4)  $35 \text{ eV}$  ( $5.6 \times 10^{-11} \text{ ergs}$ ) are expended per ion-electron pair produced. If these assumptions are valid, then we can simply write:

$$Q_p (\text{erg cm}^{-2} \text{s}^{-1}) = 5.6 \times 10^{-6} \int_{E \text{ region}} \alpha_{\text{eff}}(h) N^2(h) dh \quad (1)$$

where  $\alpha_{\text{eff}}(h)$  is the effective recombination coefficient ( $\text{cm}^3 \text{s}^{-1}$ ),  $N$  is electron density ( $\text{cm}^{-3}$ ), and  $h$  is height (km). For the data presented below, the height integration extends from 85 km to 160 km.

The effective recombination coefficient in the  $E$  region has been measured or computed by several authors. Figure 1 shows a composite of these measurements. For the present study we have taken  $\alpha_{\text{eff}}(h) = 2.5 \times 10^{-6} \exp(-h/51.2)$  for  $h > 85 \text{ km}$  as a reasonable fit to the various profiles.

The theory of atmospheric heating by Joule dissipation of ionospheric Pedersen currents has been developed by Cole [1962, 1971, 1975]. The rate of Joule heating  $q_j$  at height  $h$  is given by

$$q_j(h) = \sigma_p(h) [E_\perp + u(h) \times B]^2 \quad (2)$$

where  $E_\perp$  is the height independent perpendicular (to  $B$ ) electric field,  $u$  is the neutral wind velocity, and  $B$  is the geomagnetic field. The Pedersen conductivity  $\sigma_p(h)$  is determined from the measured electron density and a model ion-neutral collision frequency profile [e.g., Brekke et al., 1974; Vickrey et al., 1981]. In what follows, we present estimates of the height-integrated Joule heating rate  $Q_j$  given by

$$Q_j = \Sigma_p [E_\perp + U \times B]^2 \quad (3)$$

where  $\Sigma_p$  is the height-integrated Pedersen conductivity and  $U$  is the height-integrated  $E$  region neutral wind.

Since the antenna line of sight was constrained to lie within the magnetic meridional plane, no direct measurement of the north-south electric field component (east-west ion drift in the  $F$  region) was made. This component can be inferred, however, by using the method described by Doupnik et al. [1977] and de la Beaujardiere et al. [1977, 1981]. Briefly, if one assumes that the ion velocity component parallel to  $B$  can be ignored in comparison with the perpendicular component (which is usually a very good assumption in the auroral zone), then at  $F$  region heights the line of sight ion drift is a measure of the east-west electric field component, provided the angle between the radar beam and  $B$  is sufficiently large. The range gate centered in the  $E$  region, however, measures an ion velocity that is not caused solely by  $E \times B$  drift. Rather, at these low altitudes ion-neutral collisions rotate the ion velocity vector toward the direction of  $E$ . By using a model collision frequency profile, the degree of rotation can be assessed, and the ion equations of motion can be solved simultaneously at two heights (one where collisions are important and one where they are not) for the two components of  $E_\perp$ . A comparison of this technique with simultaneous barium cloud drifts has shown good agreement [see Mikkelsen et al., 1980]. For a discussion of the uncer-

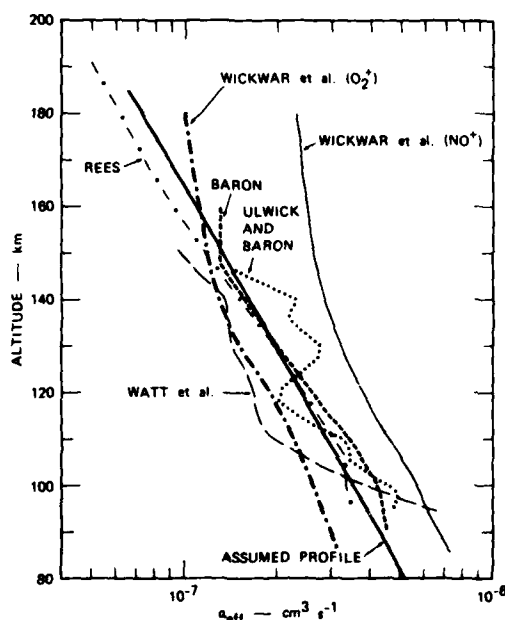


Fig. 1. Altitude profiles of the effective recombination coefficient in the  $E$  region. The curves labeled Rees, Wickwar et al. ( $\text{O}_2^+$ ), and Wickwar et al. ( $\text{NO}^+$ ) are based on laboratory measurements of the electron-ion recombination coefficient combined with a model atmosphere [Wickwar et al., 1975; Evans et al., 1977]. The profiles taken from Baron [1974], Ulwick and Baron [1973], and Watt et al. [1974] are based on auroral measurements with the Chatanika radar, rocket, and satellite experiments. The heavy solid line is the altitude profile of the effective recombination coefficient used in this paper.

tainties in determining the two components of electric field using this technique, see de la Beaujardiere et al. [1981] and Mikkelsen et al. [1981].

Thus,  $U \times B$  is the only term of (3) that cannot be inferred from the present data. Within the  $E$  region the neutral wind is usually highly variable, but the wind speed is nearly always less than 100 m/s [Heppner and Miller, 1982]. For this reason, the neutral wind contribution to  $Q_J$  is not significant if the Joule heating rate exceeds  $3\text{--}5 \text{ ergs cm}^{-2} \text{ s}^{-1}$  [Banks, 1977]. However, rather than ignore the effect of  $U$  completely, we have attempted to model its effect. A simple neutral wind model was constructed by fitting sinusoids through the radar measurements of  $E$  region winds presented by Brekke et al. [1973], as shown in Figure 2. The results for the northward  $U_N$  and eastward  $U_E$  components of neutral wind are given by

$$U_N = 100 \cos [(UT - 10) \cdot 360/12] \text{ m/s} \quad (4)$$

$$U_E = 100 \cos [(UT - 14) \cdot 360/12] \text{ m/s} \quad (5)$$

where  $UT$  is the universal time. The maximum value of  $U$  from the model ( $100 \text{ m s}^{-1}$ ) will have a similar effect to a 5 mV/m bias in  $E$ . This contribution is negligible except during very quiet periods (e.g., daytime) when the electric field is very small.

#### OBSERVATIONS AND DISCUSSION

The eight days of data used in the present study are listed in Table 1. Of the four radar runs of 24-hour duration, three were collected during winter, and one (April 5–6, 1977) was from near equinoctial conditions. The 24-hour runs were made from local noon to local noon; the 12-hour runs were collected during summer nighttime.

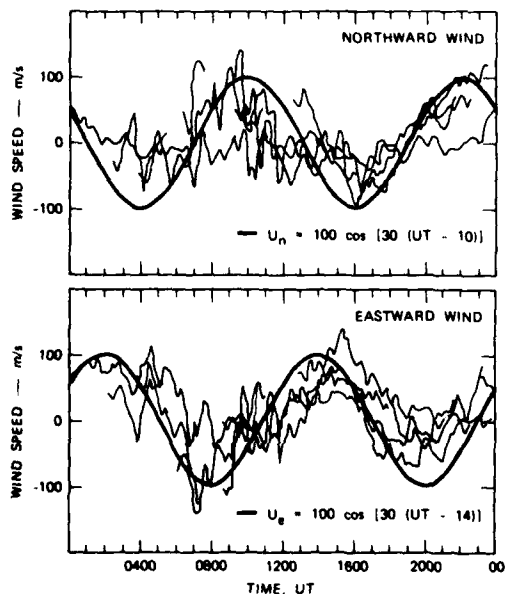


Fig. 2. Composite of neutral wind measurements made by Brekke et al. [1973]. The sinusoidal functions shown were used in the present study to model the effects of the neutral winds, which were not measured.

TABLE 1. Summary of Data Analyzed

Date	Duration, hours	Magnetic Activity
Nov. 13, 1976	24	$\Sigma Kp = 33+$
Dec. 17, 1976	24	$\Sigma Kp = 18-$
April 6, 1977	24	$\Sigma Kp = 35+$
Dec. 20, 1977	24	$\Sigma Kp = 7-$
July 7, 1978	12	$\Sigma Kp = 23$
July 28, 1978	12	$\Sigma Kp = 12$
Aug. 10, 1978	12	$\Sigma Kp = 13$
Aug. 24, 1978	12	$\Sigma Kp = 9-$

To illustrate the amount of local magnetic activity present during the eight data sets, the  $H$  component of the College magnetograms are presented in Figures 3a and 3b. Also indicated is the time interval of the radar measurements. It is seen that a wide variety of magnetic conditions are contained in the data set, with examples of substorms occurring in both the evening and morning sectors. The frequency of occurrence of positive and negative bay events is fairly well-balanced in the data set, although the negative bay substorms are markedly more intense than the positive bays. This agrees with previous studies [e.g., Allen and Kroehl, 1975] that show that negative bays are generally twice as large as simultaneous positive bays. Despite this imbalance in current intensity, the Joule heating rate associated with positive bay substorms can be comparable to or even larger than that caused by a westward electrojet, as we shall see.

Although each individual day has many interesting features, our purpose here is to summarize the qualitative or 'average' pattern of auroral energy deposition. Therefore, rather than presenting a detailed description of all of the data listed in Table 1, we will examine two days, April 5–6, 1977, and November 12–13, 1976, pointing out the characteristic patterns that typify the data set as a whole.

#### Data From April 5–6, 1977

April 5–6, 1977, was a very interesting day geophysically (see Figure 3). A moderate ( $\sim 300 \gamma$ ) positive bay occurred in the early evening sector; there was a very quiet passage through the midnight sector and then a series of large ( $\sim 800 \gamma$ ) substorms occurred in the late morning sector. Thus this data set provides an excellent opportunity to contrast the energy deposited in the thermosphere during an isolated positive bay with that caused by a series of negative bay substorms.

To make use of these measurements in global models of the thermosphere, it would be convenient to assume that Chatanika is measuring a 'representative slice' of the auroral oval and that temporal changes in the Chatanika data represent (at least to some extent) longitudinal variations along the auroral oval. Although it is impossible to separate these space/time ambiguities with a single radar, we can use magnetograms from other geographical locations to establish whether the local magnetic conditions at College reflect auroral conditions globally. Magnetograms were obtained from five observatories (Tixie Bay, College, Churchill, Narsarsuaq, and Abisko) that were approximately evenly spaced in longitude. From these magnetograms, an AE index was derived as the total range of  $H$  component deviations from the quiet time level [Davis and Sugiura, 1966; Allen and Kroehl, 1975]. Figure 4 shows the AE index for April 6, 1977. The fact that the variations in AE, which is a global

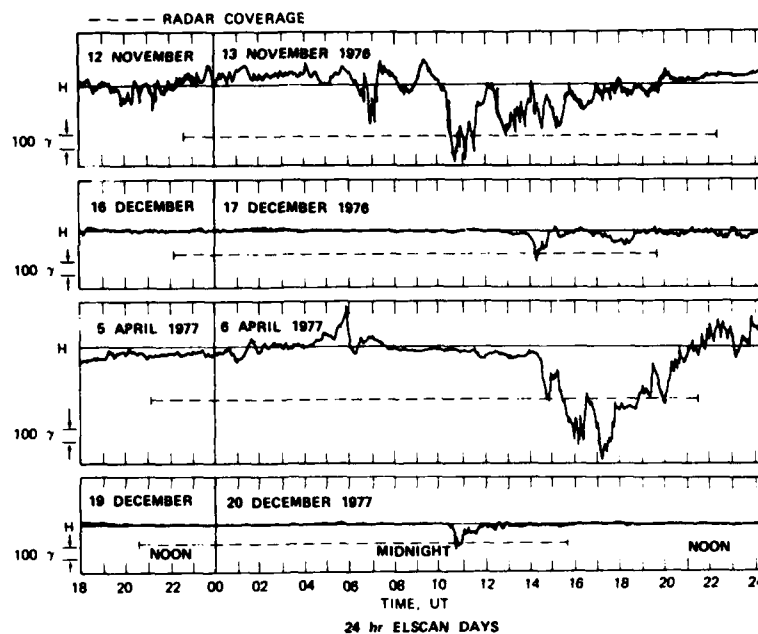


Fig. 3a

Fig. 3. Horizontal component of the College magnetograms for the eight days of this study. (a) 24-hour Elscan days. (b) 12-hour Elscan days.

magnetic index, generally occurred simultaneously with the magnetic bay activity at College lends credence to the interpretation that Chatanika is sampling ionospheric conditions that are representative of the entire auroral oval and are not isolated local events.

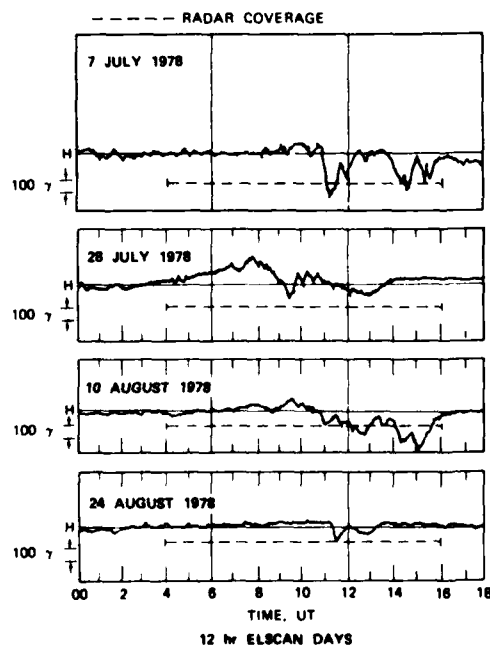


Fig. 3b

Figure 5 shows the latitude-local time variations of the precipitating particle energy deposition rate  $Q_p$  for April 5–6, 1977. The ordinate is the distance north of Chatanika calculated for a reference height of 120 km; the abscissa is universal time (local midnight is 1000 UT). Associated with each of the substorms that were apparent in the magnetogram of Figure 3 is an enhancement of precipitation energy flux. During the positive bay event at 0600 UT,  $Q_p$  exceeds  $10 \text{ ergs cm}^{-2} \text{ s}^{-1}$ , but during the morning substorms at about 1600 UT,  $Q_p > 30 \text{ ergs cm}^{-2} \text{ s}^{-1}$ . The morning sector substorm precipitation was considerably harder than that associated with the 0600 UT positive bay, as evidenced by the ratio of Hall-to-Pedersen conductivity,  $\Sigma_H/\Sigma_P$  [e.g., Brekke *et al.*, 1974; Vickrey *et al.*, 1981]. For example, at 0600 UT  $\Sigma_H/\Sigma_P \approx 1$ –2, which indicates a characteristic energy  $E_0$  of the precipitating particle flux (assuming an isotropic Maxwellian distribution) of  $\sim 1$  to 3 keV, whereas near 1800 UT, where  $\Sigma_H/\Sigma_P > 5$ ,  $E_0$  exceeded 10 keV.

During the substorms there is a southward progression

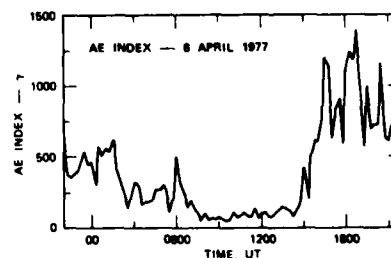


Fig. 4. The AE index for April 6, 1977.

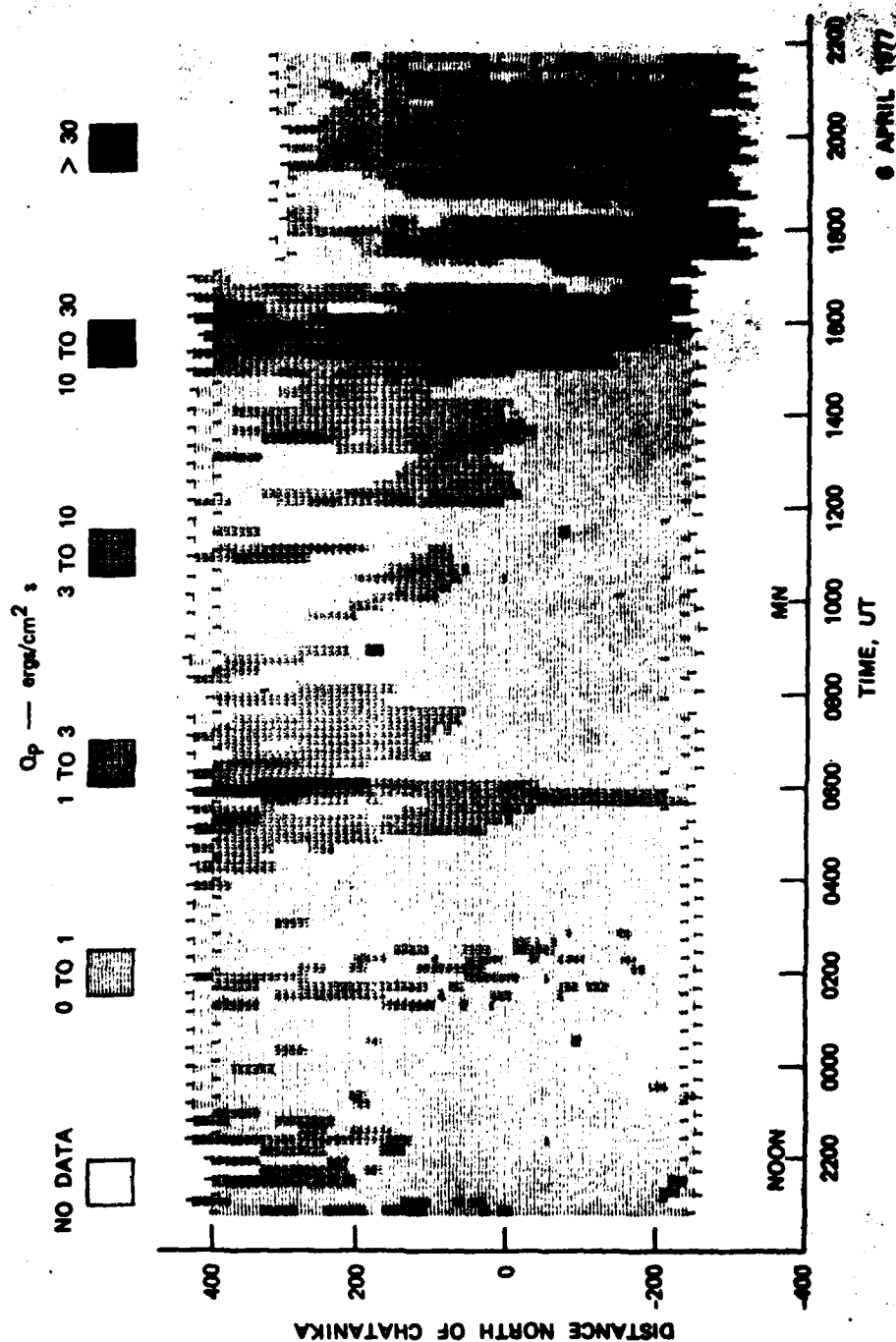


Fig. 5. Latitude-local time map of the precipitating particle energy deposition rate for April 6, 1977.

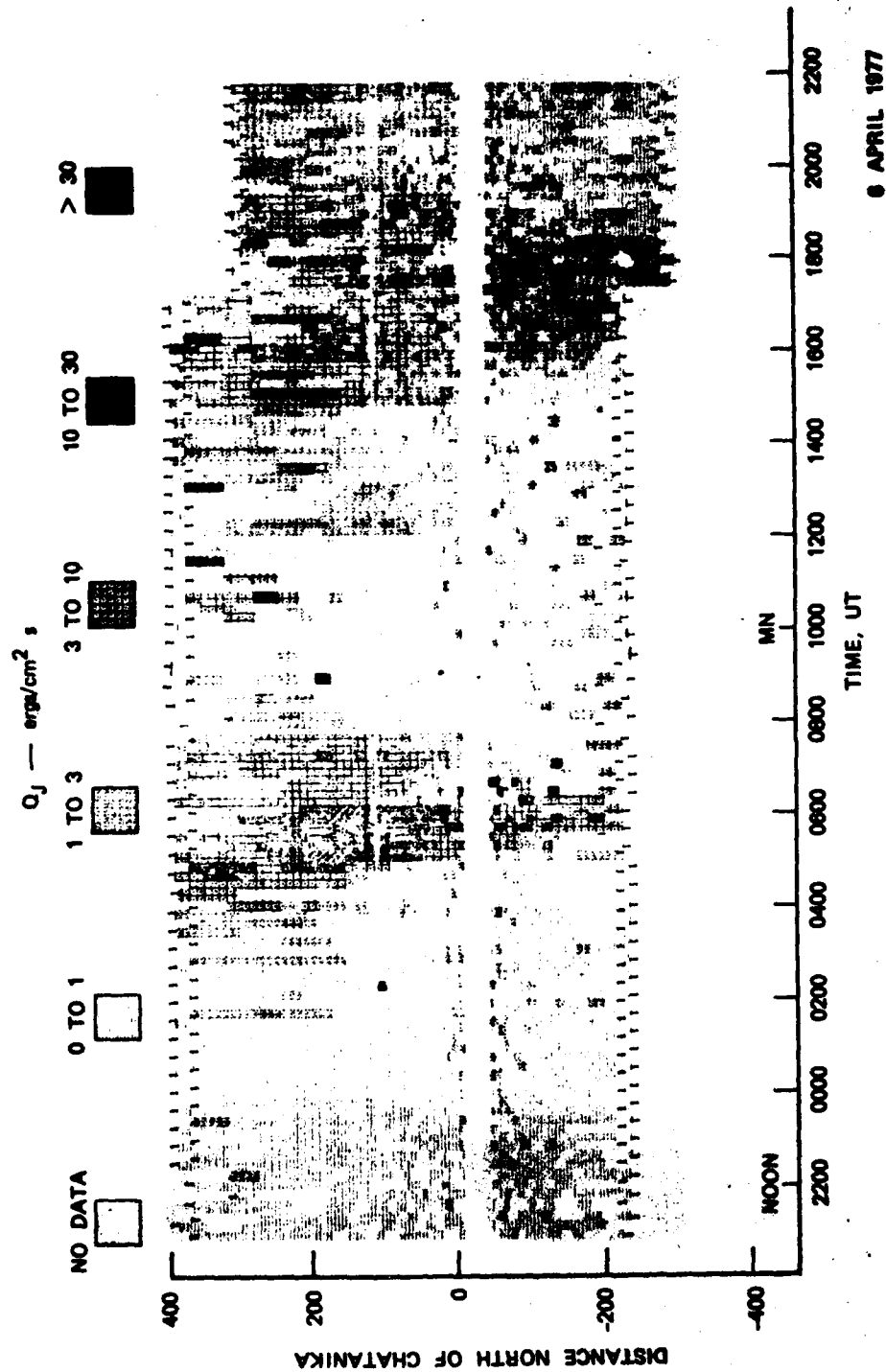


Fig. 6. Latitude-local time map of the height-averaged Joule heating rate for April 6, 1977.

and enhancement of precipitation and therefore of precipitation energy flux  $Q_p$ . During the substorm recovery phases, the regions of enhanced  $Q_p$  recede to the north and diminish in intensity. The 'turn-on' and cessation of enhanced  $Q_p$  can be as abrupt as a few minutes, as evidenced by the abrupt reduction in  $Q_p$  during the recovery phases between the morning series of substorms.

Figure 6 shows the latitude-local time variations of height-averaged Joule heating rate  $Q_J$  calculated by using (3). As was the case for particle heating, there are substantial increases in the Joule heating rate associated with substorm activity. Moreover, there is a southward progression and intensification of  $Q_J$  associated with substorm onset. As the magnetic activity subsides, the region of enhanced Joule heating recedes back to the North and diminishes. Thus the large-scale patterns in latitude and local time of Joule heating are similar to those of particle heating. Furthermore, the magnitudes of the two energy sources are comparable.

The gross pattern of Joule heating illustrated in Figure 6 is in good agreement with that suggested by Banks [1977]; namely, that Joule heating occurs in a 'horseshoe-shaped' pattern around the auroral oval with a minimum in the midnight sector. However, recall that on this particular day there was very little global magnetic activity around local midnight at Chatanika.

Nevertheless, in examining the eight days of data presented here as well as six other days of data discussed by Banks *et al.* [1981], this qualitative picture seems valid. It should be stressed, however, that Joule heating is always enhanced during substorms. Therefore, on a day in which there was an isolated substorm in the midnight sector, for example, this pattern would not be valid. At any rate, for the purpose of modeling thermospheric response to Joule heating, a horseshoe-shaped pattern is preferable to a uniform ring as a source function. However, it should be noted that the heating efficiency of the evening-sector eastward electrojet is much higher than that of the morning-sector westward current. For example, in Figure 6 the enhanced Joule heating rate associated with the 0600 UT positive bay was comparable to or perhaps slightly exceeded that associated with the morning series of substorms, even though the magnitude of the current was 3 to 4 times less. This behavior should be expected from the following simplified view of the physics:  $Q_J \sim \Sigma_p E^2$ . But since the electrojet currents are principally Hall currents,  $|J| \sim \Sigma_H |E|$ , which implies  $Q_J = (\Sigma_p / \Sigma_H^2) \cdot J^2$ . Thus, for a given level of current in the eastward and westward electrojets the Joule heating rate will be less in the morning sector where  $\Sigma_p / \Sigma_H^2$  is reduced.

Although the large-scale patterns in latitude-local time of energy deposition by particles and Joule heating are similar, there are significant differences. For example, the rapid cessation of particle energy flux associated with substorm recovery that is so apparent in Figure 5 is conspicuously absent from  $Q_J$  in Figure 6. Also, there are isolated patches of particle heating in the midnight sector that are not accompanied by enhanced Joule heating. To show the relative contributions of Joule and particle precipitation to total energy input, each of the meridian scans was integrated in latitude. The temporal variation of the latitudinally integrated energy input is shown in Figure 7. This plot shows that Joule heating dominates the premidnight sector energy input, but both inputs are important in the postmidnight sector. During the entire day, the average energy input by

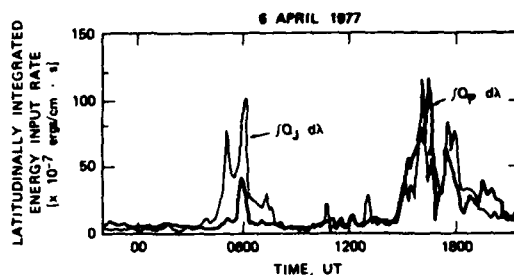


Fig. 7. Temporal variations of the latitudinally integrated energy deposition rates due to precipitating particles and Joule heating for April 6, 1977.

precipitating particles was equal to approximately 80% of the average Joule heating.

To examine further the behavior of energy deposition as a function of substorm intensity, and in particular the partitioning of that energy between particles and Joule heating, we show in Figure 8 scatter plots of  $Q_p$  and  $Q_J$  as a function of electrojet current intensity for April 5–6, 1977. The electrojet current was determined at each latitude from the electric field and E region height-integrated conductivity measured by the radar. The distinction between eastward and westward current in these plots allows the asymmetry between evening sector and morning sector energy deposition to be examined. As was obvious from the magnetograms in Figure 3, the morning-sector substorm currents were more intense than those measured during the premidnight positive bay at 0600 UT. It is interesting to note that this is true despite the fact that the driving northward electric field was reduced by approximately a factor of 2. This indicates that under some conditions (particularly in the morning sector), increases in the ionospheric conductivity are the principal source of increases in electrojet current and Joule heating. Similar findings have been reported by Foster *et al.* [1981].

Other general morphological features of interest that are illustrated in Figure 8 include the following: (1) there is a general increase in both Joule and particle energy deposition with increasing electrojet current; (2) particle energy deposition in the morning-sector westward electrojet is more intense and increases more rapidly with electrojet current than in the premidnight sector; and (3) Joule heating has the opposite asymmetry, i.e., more energy is deposited for a given electrojet current intensity in the premidnight sector than is deposited in the morning sector. As was pointed out in the introduction, the latter two opposing asymmetries can be understood in terms of the changing conductivity. Morning-sector precipitation is, in general, harder (and thus deposits more energy at lower altitudes) than evening sector precipitation. These harder electron fluxes in the morning sector enhance the Hall conductivity. Thus, morning sector currents have a greater tendency to flow in the Hall direction than premidnight sector currents and are therefore less dissipative.

A comparison of Figures 8c and 8d creates the impression that a linear dependence of  $Q_J$  on electrojet current may be sufficient to describe the postmidnight sector, but that perhaps a higher order dependence is required for the premidnight sector. However, it should be pointed out that such a steep dependence is hinted at in only one other of the eight days examined. In general, a roughly linear depen-

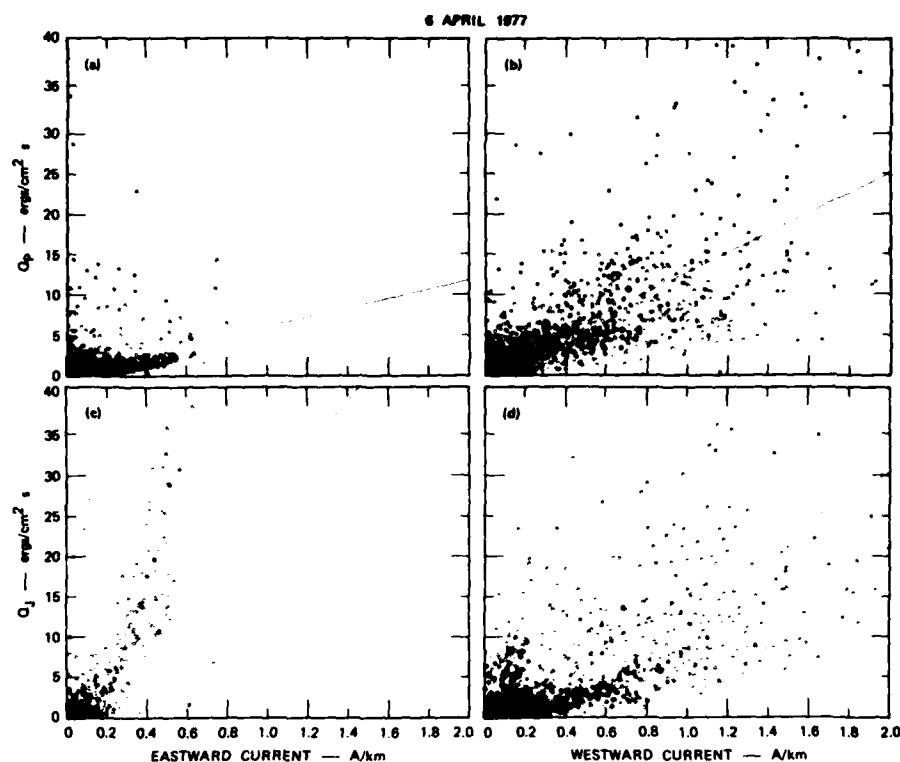


Fig. 8. Scatter plots of particle and Joule energy deposition rates as a function of electrojet current for April 6, 1977.

dence (with, obviously, a great deal of scatter) of  $Q_p$  and  $Q_J$  on electrojet current is observed. The degree of asymmetry between pre-midnight and post-midnight particle and Joule energy deposition varies from day to day but was discernible (although, in some cases was not striking) on all days that contained substorms in both periods.

To improve models of the thermosphere, we would like to have a relationship between energy deposition at high latitudes and auroral activity. The problem is that convenient indices of auroral activity are not necessarily related directly to energy input. For example, the AE index reflects the global magnitude of electrojet current flow. However, as we have seen, this current flow is influenced by changes in both the conductivity and the driving electric field. Nevertheless, in comparing Figures 4 and 7 there appears (qualitatively, at least) to be a relationship between AE and total energy input. To examine this relationship in more detail, we have constructed in Figure 9 a scatter plot of latitudinally integrated Joule heating rate versus the AE index for April 6, 1977. We have only included time periods after 0400 UT because the radar was well south of the diffuse auroral boundary before that time (see Figure 5 of Vickrey *et al.* [1981]). As might be expected from the discussion above, there is no striking relationship between these quantities.

#### Data From November 12–13, 1976

As is apparent from the magnetogram of Figure 3 as well as from the radar data presented below, November 12–13,

1976, was a period of virtually continuous and intense magnetic activity at Chatanika. Of particular interest to the present study are the patterns of energy deposition during the substorms that occurred in the midnight sector because these observations complement those from the quiet midnight sector of April 5–6, 1976.

The latitude-local time variations of particle energy deposition and Joule heating ( $Q_p$  and  $Q_J$ , respectively) for November 12–13, 1976, are shown in Figures 10 and 11. The substorm behavior for  $Q_p$  is similar to that described for April 5–6, 1977; namely, as the substorm intensity increases, the pattern of particle energy deposition moves rapidly south and intensifies, then recedes north and diminishes with the recovery phase of the substorm. Also, it is again apparent that there was considerably more particle heating associated with the westward electrojet than with the eastward electrojet. (Note from Figure 3 that the enhancement in  $Q_p$  at ~0700 UT corresponds to a negative bay on the magnetogram.)

A comparison of Figures 10 and 11 shows that there was considerably more particle heating (both pre-midnight and post-midnight) than Joule heating during this active period. Also, it is interesting that there is much less correlation between the morphologies of precipitation enhancements and Joule heating enhancements compared with the correlation of the same morphologies on April 5–6, 1977. Indeed, the enhancements of particle energy deposition can be identified with specific magnetogram features. This is further



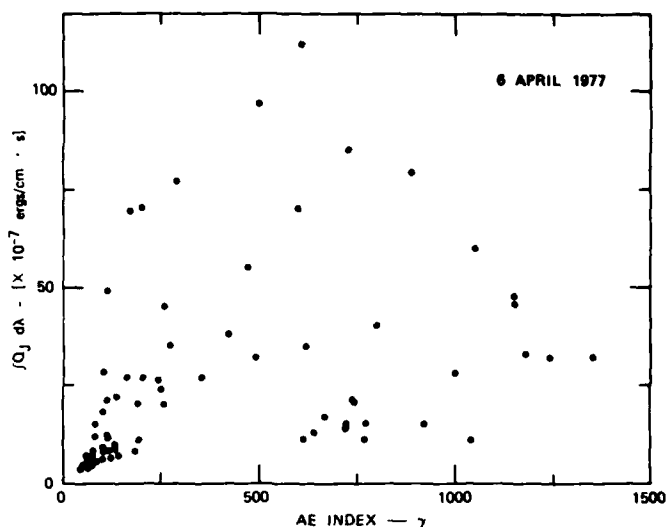


Fig. 9. Scatter plot of latitudinally integrated Joule heating rate ( $\int Q_J d\lambda$ ) versus the AE index for April 6, 1977.

evidence of the strong control of ionospheric conductivity on electrojet current. The Joule heating pattern, on the other hand, was relatively uniform throughout the midnight sector. Since the height-integrated Pedersen conductivity  $\Sigma_P$  was highly structured during this period [see Vickrey *et al.*, 1981], it follows that the electric field strength was roughly anticorrelated with  $\Sigma_P$ . Such tendencies for anticorrelation have been observed before (see, for example, *de la Beaujardiere et al.* [1977, 1981] and *Foster et al.* [1981]). However, it is important to note that the anticorrelation is not perfect. Recall, for example, that the large-scale patterns of  $Q_P$  and  $Q_J$  were similar on the April day. This lack of direct anticorrelation between electric field and conductivity indicates that the magnetosphere is neither a simple constant voltage nor a constant current energy source.

Figure 12 presents scatter plots of particle and Joule energy deposition as a function of electrojet current intensity for November 12–13, 1976. These results tend to confirm the previous discussion of Figure 10. There was, on the average, more energy deposited by precipitating particles in regions of the westward electrojet than in regions of the eastward electrojet. However, for this day the rate of increase of  $Q_P$  with increasing electrojet current,  $J_\perp$  (found from a linear least-squares-fit analysis), was roughly the same for the two electrojet directions. This is not particularly unusual when viewed in terms of the entire data set examined. On four of the eight days,  $\partial Q_P / \partial J_\perp$  was larger for the eastward electrojet than for the westward electrojet; on only one day was it smaller. On the other three days, there was not a significant difference in  $\partial Q_P / \partial J_\perp$  with current direction.

Figures 12c and 12d show, as expected, that the Joule heating rate  $Q_J$  was comparable for both eastward and westward electrojets on this day. The rate of increase of  $Q_J$  with electrojet current ( $\partial Q_J / \partial J_\perp$ ) was only slightly larger for the eastward electrojet than for a westward current. This asymmetry was more pronounced in the data set as a whole and was noticeable on seven of the eight days examined.

For each of the eight days, the meridional scans were

integrated in latitude to give a profile in time of the energy input of the two sources between 62° and 68°. The average values for particle deposition energy and Joule heating are summarized in Table 2. Plotting any of the first three columns of data in Table 2 against an index of daily magnetic activity, such as  $\Sigma K_P$  in Table 1, shows only a very general correlation with increasing activity. A significant null result, however, is that the ratio of  $Q_P$  to  $Q_J$  plotted against  $\Sigma K_P$  shows no correlation at all. For the days of our experiments, either Joule heating or particle deposition energy could be the predominant heating source, regardless of average magnetic activity.

#### SUMMARY

Eight days of synoptic Chatanika radar data have been analyzed to determine the latitudinal and temporal morphology of auroral energy deposition. The days were selected to represent a variety of seasons and magnetic activity. Two illustrative days of data have been examined in detail, and the trends representative of the data set as a whole were pointed out. Particular attention was paid to the partitioning of energy deposition between precipitating particles and Joule heating because these heat sources may produce different thermospheric responses. The asymmetries in the two heating rates between the evening and morning sectors were examined in some detail.

It is hoped that the patterns that emerge when this relatively large amount of synoptic data is viewed as a whole will be characteristic and thus suitable for model input conditions. However, it is important to emphasize that the day-to-day variability of auroral zone electrodynamics is very large, and thus any particular day's data may appear quite different from our composite characterization. With these limitations in mind, we can characterize the morphology of auroral energy deposition as follows:

1. There is an increase in both the Joule heating rate and the precipitating particle energy deposition rate with increas-

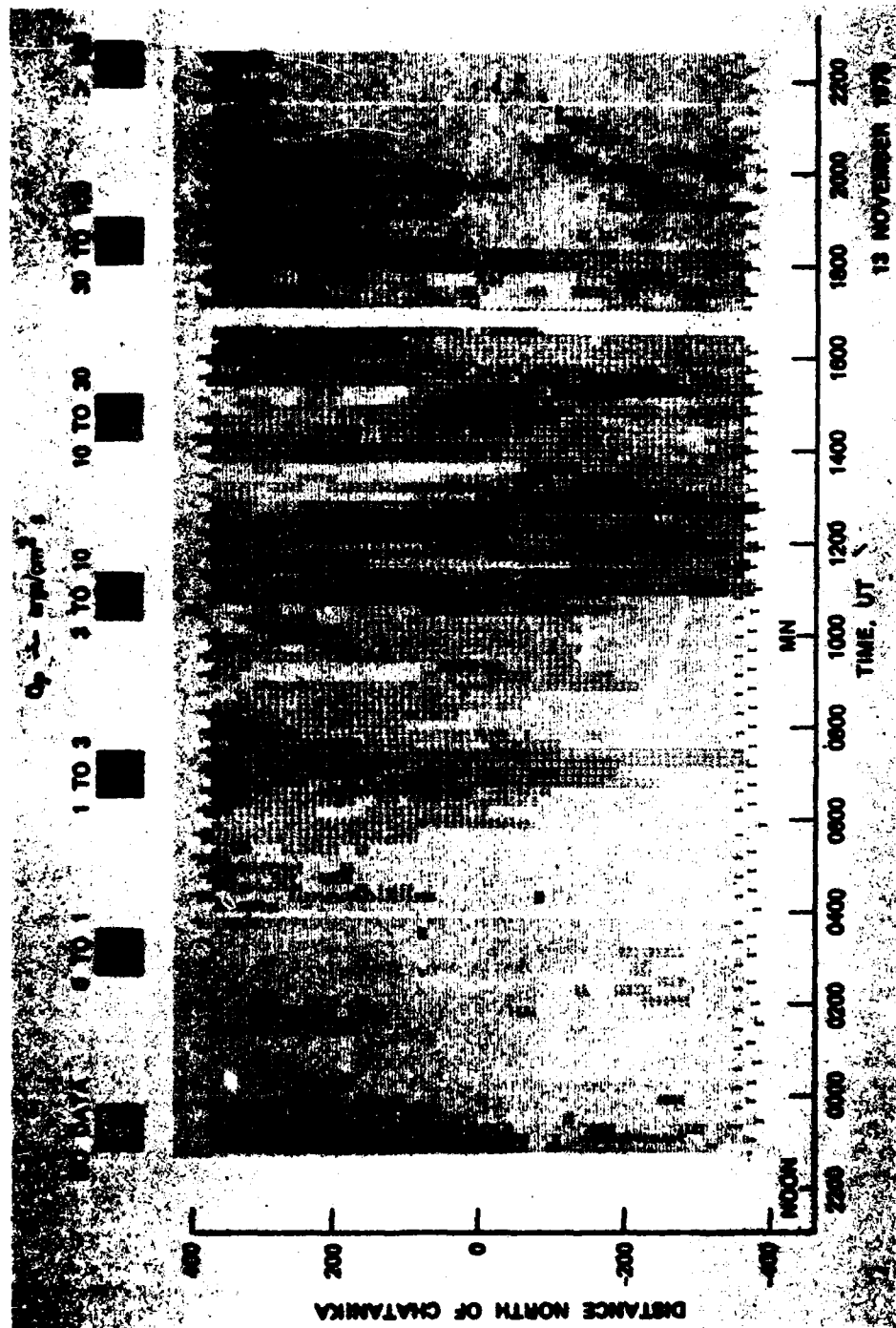


Fig. 10. Latitude-local time map of precipitating particle energy deposition rate for November 13, 1976.

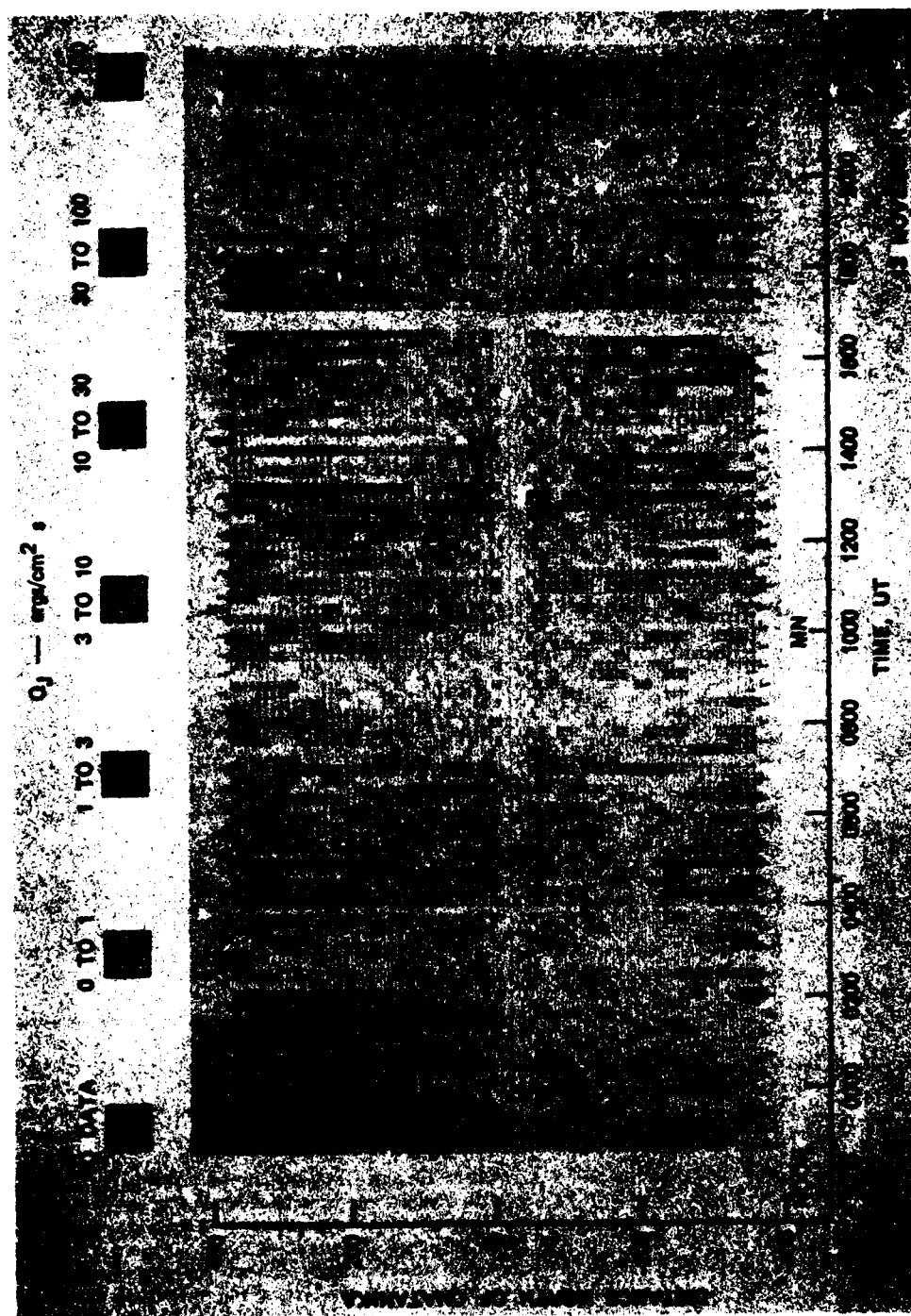


Fig. 11. Latitude-local time map of height-integrated Joule heating rate for November 13, 1976.

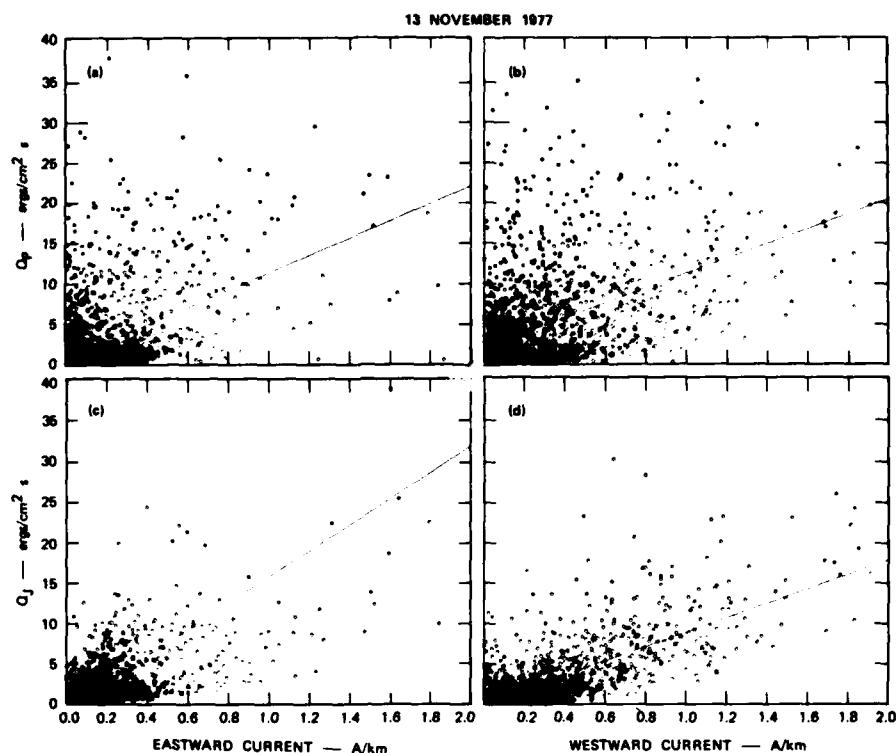


Fig. 12. Scatter plots of precipitating particle and Joule energy deposition rates as a function of electrojet current for November 13, 1976.

ing electrojet current, i.e., with increasing substorm intensity.

2. The pattern of precipitating particle energy deposition in the auroral zone moves rapidly southward and intensifies during a substorm, then recedes to the north and diminishes during the substorm recovery phase.

3. The particle energy deposition rate associated with the morning-sector westward electrojet is higher than that for the evening-sector eastward electrojet.

4. The rate of increase in particle energy deposition with increasing westward electrojet current is equal to or exceeds that for an eastward electrojet current.

5. The Joule heating rate for a given magnitude of electrojet current is higher in the evening-sector eastward electrojet than in the morning-sector westward electrojet.

6. The rate of increase of Joule heating with electrojet current intensity ( $\partial Q_J / \partial J_{\perp}$ ) is larger for an eastward electrojet than for a westward electrojet.

7. Joule heating generally dominates particle energy deposition in the premidnight sector. However, the daily averages of both energy inputs are roughly equal.

8. Energy is deposited by both Joule heating and precipitating particles at lower altitudes in the morning sector than in the premidnight sector.

We find that Banks' [1977] description of the Joule heating pattern as 'horseshoe shaped' and corresponding to the auroral oval with a minimum in the midnight sector is generally valid for both particle and Joule heating. However, it is important to keep in mind that the Harang discontinuity, where the minimum of Joule heating occurs, can be very narrow in local time. Moreover, if a substorm occurs near local midnight, there may be no minimum at all. Perhaps more important, the horseshoe must be viewed as an asymmetrical one with respect to local midnight. The opposing asymmetries of particle and Joule heating are self-consistent when viewed in terms of the change in ionospheric conductivity between the evening and morning sectors. Morning sector precipitation tends to be harder than evening-sector precipitation and thus enhances the Hall-to-Pedersen conductivity ratio [see Vickrey et al., 1981]. As a result, the westward electrojet current vector is more nearly perpendic-

TABLE 2. Summary of the Partitioning of Energy Deposition Between Precipitating Particles and Joule Heating for the Eight Days

Date	$an^2$ , ergs/ $\text{cm}^2 \text{ s}$	$J \cdot E$ , ergs/ $\text{cm}^2 \text{ s}$	Total Energy Deposition Rate, ergs/ $\text{cm}^2 \text{ s}$	$an^2/J \cdot E$
Nov. 13, 1976	3.53	2.43	5.96	1.45
Dec. 17, 1976	0.68	0.91	1.59	0.75
April 6, 1977	2.47	3.04	5.51	0.81
Dec. 20, 1977	0.97	1.41	2.38	0.68
July 7, 1978	2.30	1.29	3.59	0.56
July 28, 1978	1.20	1.43	2.63	0.83
Aug. 10, 1978	0.57	0.48	1.05	1.20
Aug. 24, 1978	1.10	0.55	1.65	2.06

ular to the electric field, and therefore less dissipative, than is the eastward electrojet current.

**Acknowledgments.** This work was supported by the Air Force Office of Scientific Research under contract F49620-80-C-0014 and by the National Science Foundation under grant ATM-7823658. Radar operations were supported by the Defense Nuclear Agency under contract DNA 001-77-C-0042. Radar operations were performed by H. Burch, C. Code, and M. McCready.

The Editor thanks A. Brekke and J. C. Foster for their assistance in evaluating this paper.

#### REFERENCES

- Allen, J. H., and H. W. Kroehl, Spatial and temporal distributions of magnetic effects of auroral electrojets as derived from AE indices, *J. Geophys. Res.*, **80**, 3667-3677, 1975.
- Banks, P. M., Observations of Joule and particle heating in the auroral zone, *J. Atmos. Terr. Phys.*, **39**, 179-193, 1977.
- Banks, P. M., J. C. Foster, and J. R. Doupnik, Chatanika radar observations relating to the latitudinal and local time variation of Joule heating, *J. Geophys. Res.*, **86**, 6869-6878, 1981.
- Baron, M. J., Electron densities within aurorae and other auroral E region characteristics, *Radio Sci.*, **9**, 2, 341-348, 1974.
- Brekke, A., Electric fields, Joule and particle heating in the high latitude thermosphere, *J. Atmos. Terr. Phys.*, **38**, 887-895, 1976.
- Brekke, A., and C. L. Rino, High-resolution altitude profiles of the auroral zone energy dissipation due to ionospheric currents, *J. Geophys. Res.*, **83**, 2517-2524, 1978.
- Brekke, A., J. R. Doupnik, and P. M. Banks, A preliminary study of the neutral wind in the auroral E region, *J. Geophys. Res.*, **78**, 8235-8250, 1973.
- Brekke, A., J. R. Doupnik, and P. M. Banks, Incoherent scatter measurements of E region conductivities and currents in the auroral zone, *J. Geophys. Res.*, **79**, 3773-3790, 1974.
- Cole, K. D., Joule heating of the upper atmosphere, *Aust. J. Phys.*, **15**, 223-235, 1962.
- Cole, K. D., Electrodynamical heating and movement of the thermosphere, *Planet. Space Sci.*, **19**, 59-75, 1971.
- Cole, K. D., Energy deposition in the thermosphere caused by the solar wind, *J. Atmos. Terr. Phys.*, **37**, 939-949, 1975.
- Davis, T. N., and M. Sugiura, Auroral electrojet activity index AE and its universal time variations, *J. Geophys. Res.*, **71**, 3, 785-801, 1966.
- de la Beaujardiere, O., R. Vondrak, and M. Baron, Radar observations of electric fields and currents associated with auroral arcs, *J. Geophys. Res.*, **82**, 5051-5062, 1977.
- de la Beaujardiere, O., R. Vondrak, R. Heelis, W. Hanson, and R. Hoffman, Auroral arc electrodynamic parameters measured by AE-C and the chatanika radar, *J. Geophys. Res.*, **86**, 4671-4685, 1981.
- Doupnik, J. R., A. Brekke, and P. M. Banks, Incoherent scatter radar observations during three sudden commencements and a Pc 5 event on August 4, 1972, *J. Geophys. Res.*, **82**, 499-514, 1977.
- Evans, D. S., N. C. Maynard, J. Trøim, T. Jacobsen, and A. Egeland, Auroral vector electric field, and particle comparisons, 2, Electrodynamics of an arc, *J. Geophys. Res.*, **82**, 2235-2249, 1977.
- Foster, J. C., J. R. Doupnik, and G. S. Stiles, Ionospheric convection and currents in the midnight sector on November 8, 1979, *J. Geophys. Res.*, **86**, 2143-2148, 1981.
- Hays, P. B., R. A. Jones, and M. H. Rees, Auroral heating and the composition of the neutral atmosphere, *Planet. Space Sci.*, **21**, 559-573, 1973.
- Heppner, J. P., and M. L. Miller, Thermospheric winds at high latitudes from chemical release observations, *J. Geophys. Res.*, **87**, 1633-1647, 1982.
- Mikkelsen, I. S., T. S. Jorgensen, M. C. Kelley, M. F. Larsen, E. Pereira, and J. F. Vickrey, Neutral winds and electric fields in the dusk auroral oval, 1, measurements, *J. Geophys. Res.*, **86**, 1513-1524, 1981.
- Rees, M. H., Auroral ionization and excitation by incident energetic electrons, *Planet. Space Sci.*, **11**, 1209-1218, 1963.
- Roble, R. G., The thermosphere, in *Studies in Geophysics: The Upper Atmosphere and Magnetosphere*, chap. 3, pp. 57-71, The National Research Council, Washington, D. C., 1977.
- Ullwick, J. C., and M. J. Baron, Simultaneous rocket probe and incoherent-scatter measurements during an aurora, paper presented at URSI Conference on Incoherent Scatter, Tromsø, Norway, June 12-16, 1973.
- Vickrey, J. F., R. R. Vondrak, and S. J. Matthews, The diurnal and latitudinal variation of auroral zone ionospheric conductivity, *J. Geophys. Res.*, **86**, 65-75, 1981.
- Vondrak, R. R., and M. J. Baron, Radar measurements of the latitudinal variation of auroral ionization, *Radio Sci.*, **11**, 939-946, 1976.
- Vondrak, R. R., and M. J. Baron, A method of obtaining the energy distribution of auroral electrons from incoherent scatter radar measurements, in *Radar Probing of the Auroral Plasma*, edited by A. Brekke, Scandinavian University Books, Tromsø, 1977.
- Wallis, D. D., and E. E. Budzinski, Empirical models of height integrated conductivities, *J. Geophys. Res.*, **86**, 125-137, 1981.
- Watt, T. M., L. L. Newkirk, and E. G. Shelley, Joint radar-satellite determination of the effective recombination coefficient in the auroral E region, *J. Geophys. Res.*, **79**, 4725-4731, 1974.
- Wickwar, V. B., M. J. Baron, and R. D. Sears, Auroral energy input from energetic electrons and Joule heating at Chatanika, *J. Geophys. Res.*, **80**, 4364-4367, 1975.
- Wedde, T., J. R. Doupnik, and P. M. Banks, Chatanika observations of the latitudinal structure of electric fields and particle precipitation on November 21, 1975, *J. Geophys. Res.*, **82**, 2743-2751, 1977.

(Received December 28, 1981;  
revised March 1, 1982;  
accepted April 7, 1982.)

# IRREGULARITIES AND INSTABILITIES IN THE AURORAL F REGION

James F. Vickrey

Michael C. Kelley

Radio Physics Laboratory  
SRI International  
Menlo Park, CA 94025

School of Electrical Engineering  
Cornell University  
Ithaca, NY 14853

## INTRODUCTION

The Earth's F-region ionospheric plasma displays structure perpendicular to the magnetic field on scales from hundreds of kilometers down to centimeters. The physical processes that operate over such a wide range of scale sizes are, of course, very diverse. At the largest scales ( $\lambda \geq 10$  km), production, loss, and transport of structured plasma are dominated by aeronomical processes including energy sources of magnetospheric origin. At intermediate ( $0.1 \text{ km} < \lambda < 10 \text{ km}$ ) and small ( $\lambda < 100 \text{ m}$ ) scales, plasma instabilities and cross-field plasma diffusion are often the dominant physical processes controlling the plasma structure. However, because nonlinear plasma processes can couple structures in one scale length regime to other spatial frequencies, the entire spectrum of irregularities must be studied as a whole.

Polar orbiting satellites find two main zones of maximum irregularity occurrence in the F-layer ionosphere, as detected by both plasma density and electric field fluctuation sensors. One is located near the nighttime magnetic equator. The other zone is located throughout the vast high-latitude region bounded roughly by the polar cusp in the local time zone 0800-1400 and by the equatorial boundary of the high-latitude convection pattern at other local times. This equatorward boundary for the polar zone of structure is thus well equatorward of the classical auroral oval at most local times.

In both of these irregularity zones, the structured plasma can disrupt transionospheric radio wave communication channels. Hence, the interest is practical as well as purely scientific in understanding the processes that control the production, evolution, and

decay of plasma structure. The equatorial zone has received the most attention in the recent past in both the theoretical and experimental arenas. This is in part due to the relatively large data base available from radar and rocket measurements at the equator. Perhaps more importantly, however, the aeronomic processes are simpler and the sources of free energy capable of driving the F-region plasma dynamics are fewer at the equator than at high latitudes. For example, at mid- and low-latitudes, F-region dynamics are governed principally by neutral atmospheric winds and waves and the dynamo electric field; at high latitudes, these processes are accompanied by particle precipitation, magnetospheric convection electric fields, and auroral current systems flowing parallel and perpendicular to the magnetic field. Nevertheless, the considerable progress made recently in defining and understanding the key physical processes that structure plasma at the equator can also be beneficial to high-latitude studies because many of the processes occurring there (particularly the plasma instabilities) are analogous.

In the next section, we briefly summarize the present understanding of high-latitude plasma structuring phenomena and present a set of working hypotheses that form a framework for investigating the origin and spatial extent of high-latitude irregularities. In the concluding section, we point out the areas for future study that may have the greatest impact on improving this framework. Emphasis is placed on the important contributions that the DE and VIKING spacecraft as well as the EISCAT incoherent-scatter facility may yield.

#### MECHANISMS RESPONSIBLE FOR THE OBSERVED MORPHOLOGY OF F-REGION PLASMA STRUCTURE AT HIGH LATITUDES

To predict the observed F-region plasma structure on a global basis, there are three fundamental questions that must be answered: (1) When and where are plasma density irregularities produced? (2) How long do they last? (3) How far do they convect during their lifetime?

##### Irregularity Production

Perhaps the most obvious source of structured plasma at high latitudes is the structured particle precipitation responsible for the aurora. Using satellite data, Dyson and Winningham (1974) showed a one-to-one correlation between the 300 eV electron flux boundary and the penetration of an irregular plasma region. The spatial and temporal structure of incoming precipitation has not yet been examined in sufficient detail (particularly at the low particle energies that produce F-layer ionization) to definitively assess the direct contribution of the spatial spectrum of precipitation to that of the

resulting ionization. However, during one rocket flight from Greenland the outer scale of precipitation and plasma density were observed in-situ simultaneously to be  $\sim 50$  km, a value that is similar to that observed in the F-layer ionization enhancements, as measured by incoherent-scatter radar (Kelley et al., 1982). This agreement suggests that structured soft-particle precipitation is a major source of large-scale F-region plasma density irregularities.

An example of large-scale F-layer density structure, as measured by the Chatanika incoherent-scatter radar, is illustrated in Figure 1, which shows contours of constant electron density as a function of altitude and invariant latitude. The data are displayed in a coordinate system with straight, vertical magnetic field lines. These observations from the midnight vector (LT = UT - 10 hours) show F-region ionization enhancements or plasma "blobs" that reach  $\sim 5-6 \times 10^5 \text{ cm}^{-3}$ , which is approximately an enhancement by a factor of five over the background. Plasma-density enhancements ranging from a factor of two to ten over the background are very commonplace at Chatanika. These blobs are often observed to convect into the radar field of view from the north (i.e., following the usual midnight-sector convection pattern) and their appearance is not necessarily associated with magnetic activity (Vickrey et al., 1980).

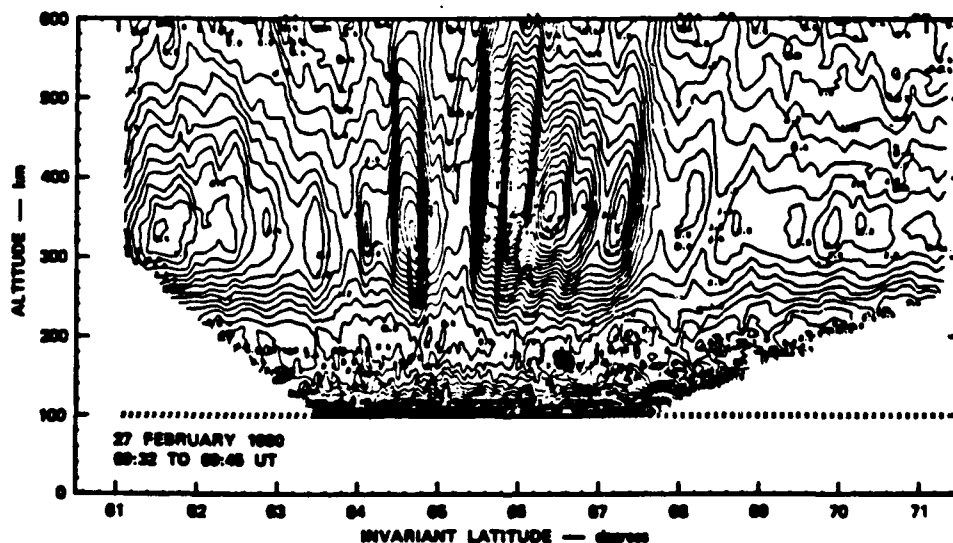


FIGURE 1 ALTITUDE/LATITUDE VARIATION OF ELECTRON DENSITY IN THE MIDNIGHT-SECTOR AURORAL ZONE MEASURED BY THE CHATANIKA RADAR. The contour interval is  $2 \times 10^4 \text{ cm}^{-3}$ .



4

These plasma blobs can be considered analogous to equatorial "bubbles" because they provide large-scale density gradients upon which convective plasma instabilities can operate to produce intermediate- and small-scale plasma structures. Indeed, the steep blob edges are unstable to the gradient drift instability (Linson and Workman, 1970) on one side or the other, depending on the local configuration of electric field and neutral wind. Ossakow and Chaturvedi (1979) have pointed out that field-aligned currents, which are known to be a permanent feature of the high latitude ionosphere, are also a destabilizing factor. Vickrey et al. (1980) combined measurements from the Chatanika radar and TRIAD satellite to show that the large-scale plasma blobs are linearly unstable to a generalized form of the  $E \times B$  instability that includes the effects of field-aligned currents. They also verified the existence of intermediate-scale plasma structure ( $\lambda \approx 1$  km) associated with the blobs by detecting scintillation enhancements on the TRIAD 150-MHz telemetry signal. Other evidence for "edge"-related plasma instabilities comes from a rocket flight across an auroral arc (Kelley and Carlson, 1977; Kelley et al., 1975). At the edge of the arc intense (10 mV/m) oxygen ion cyclotron waves were observed as were broadband short wavelength electrostatic emissions with  $k_{\perp} \rho_i \approx 1$ , where  $\rho_i$  is the ion gyro radius. Field-aligned currents, perpendicular plasma shear flow, and parallel sheared-electron flow (Keskinen, private communication, 1982) have all been invoked to explain these waves. Above the arc itself, the F layer was smooth at these smaller scales.

An important difference between the operation of convective instabilities at the nighttime equatorial ionosphere and at high latitudes is the presence of a highly conducting, precipitating-particle-produced E layer in the auroral zone to which the F-region irregularities are connected via the geomagnetic field. E-region "shorting" reduces the growth rate of the convective instabilities and, as will be discussed more fully below, reduces the lifetime of F-layer irregularities for scale sizes large enough to map to the E layer [i.e.,  $\lambda \gtrsim 1$  km; Vickrey and Kelley (1982)]. However, the presence of the E layer may make it possible to tap the magnetospheric energy source that might otherwise not be available.

An additional source of structured plasma density at high latitudes is the structure in the magnetospheric convection electric field. This structuring of plasma density can come about in two principal ways. First, where the electric field is large, there can be a large velocity difference between ions and neutrals as well as an increase in ion temperature over the neutral gas temperature because of enhanced Joule heating. Both of these effects increase the recombination rate of  $O^+$  with  $N_2$  and result in a change of ion composition from  $O^+$  to  $NO^+$ . Because the  $NO^+$  recombination rate is relatively large, a density depletion can occur wherever the electric field is enhanced (i.e.,  $E \gtrsim 40$  mV/m). Such effects have been observed at Chatanika (Kelly and Wickwar, 1981). Although we expect

this process to be important only at large scales, detailed studies of the magnitude of electric field gradients have not been performed to date.

Second, structured electric fields can produce structured density by simply mixing flux tubes that have varying plasma density (Fejer and Kelley, 1980). A turbulent magnetospheric electric field acting on a horizontal density gradient can thus produce much the same result as a local convective instability. Extreme examples of such turbulent fields are often observed in the winter polar cap during periods of extended  $B_z$  north conditions. (An example from OGO-6 (Heppner, 1977) is shown in Figure 2.) No study has been conducted to date, however, regarding the size of velocity shears normally observed in the lower ionosphere and at what scale sizes they might stir plasma of varying density. Kintner (1976) found shear frequencies ( $dV/dx$ ) the order of  $10^{-1}$  to  $10^{-2}$  Hz in the upper ionosphere ( $\sim 2000$ -km altitude). Mozer et al. (1979) have pointed out that electrostatic shocks are imbedded in regions of intense turbulent electric fields. However, how these map to the F layer is not clear because of the strong evidence for collocated parallel electric fields. Kelley and Carlson (1977) found a shear frequency of 20 Hz in an arc-boundary crossing, but that may be an extreme case.

#### Irregularity Lifetime

The second element in our framework for understanding the morphology of structured plasma at high latitudes is irregularity

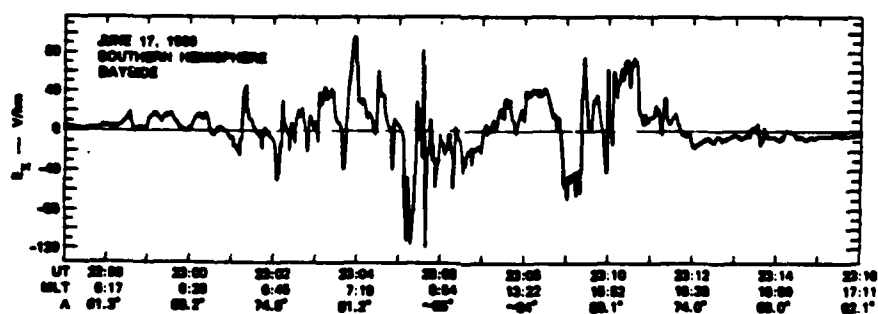


FIGURE 2 AN EXAMPLE OF HIGHLY IRREGULAR ELECTRIC FIELDS IN THE DAYSIDE WINTER HEMISPHERE. [Heppner, 1977]

lifetime. Because we are considering plasma structure in the F layer where recombination is linearly proportional to the electron density, recombination will reduce the absolute density on adjacent flux tubes equally (for small amplitude irregularities) and hence, will not reduce horizontal density structure. Thus, the major process governing the removal of F-region plasma density irregularities, once they are produced, is cross-magnetic-field plasma diffusion. A possibly important process that is ignored in the present discussion is the damping of irregularities by convection into a region in which (or a temporal variation resulting in which) the electric field and neutral wind configuration is stabilizing.

The plasma density gradient at the edge of an irregularity has an associated pressure gradient that tends to cause the plasma to diffuse away from regions of more dense plasma and into areas of less dense plasma. The diffusion rate,  $d_j$  ( $= \rho_j v_j$  where  $\rho_j$  is the Larmor radius and  $v_j$  is the collision frequency for species  $j$ ), is larger for ions than for electrons in the F layer because their gyro radius and, hence, their horizontal displacement per collision is much larger than for electrons (even though their collision frequency with neutrals is less than the electron ion collision frequency). However, when the ions try to diffuse away from the electrons, an electrostatic field is produced, which retards ion diffusion. The net result is that the plasma, as a whole, diffuses at twice the slow electron rate.

Let us now consider the effects of a highly conducting auroral E-region, to which the F-layer irregularities may be electrically connected. The electrons in the F layer can easily move along the magnetic field to the E region. In the E region, they participate in horizontal current systems to short out the ambipolar electrostatic field that would otherwise retard ion diffusion. Thus, for a highly conducting E region, classical diffusion proceeds at the ion (rather than the electron) rate. Because ions carry the cross field current and electrons the parallel current, an "image" forms in the E region and acts to slow the net diffusion. However, recombination prevents this for a scale-size  $\lambda$  if  $n \geq 10^4/\lambda^2$ , where  $\lambda$  is in km and  $n$  is  $\text{cm}^{-3}$  (Vickrey and Kelley, 1982).

Vickrey and Kelley (1982) have constructed a simple model of classical cross-field plasma diffusion in the F region including E-region conductivity effects. They have found that the cross-field diffusion rate depends strongly on the height of the E and F layers as well as their peak electron densities. The fundamental quantity governing the diffusion rate, however, is the ratio of Pedersen conductivities in the E and F regions,  $\Sigma_E/\Sigma_F$ . Figure 3 shows the cross-field diffusion rate,  $D_1$ , and lifetime,  $\tau_1$  km, of one-kilometer-scale irregularities [ $\tau_1 = (\lambda^2/4\pi^2 D_1)$ ] as a function of  $\Sigma_E/\Sigma_F$  for typical F-region parameters. The presence of a highly conducting E region can enhance the F-region cross-field plasma diffusion rate by an order of magnitude.

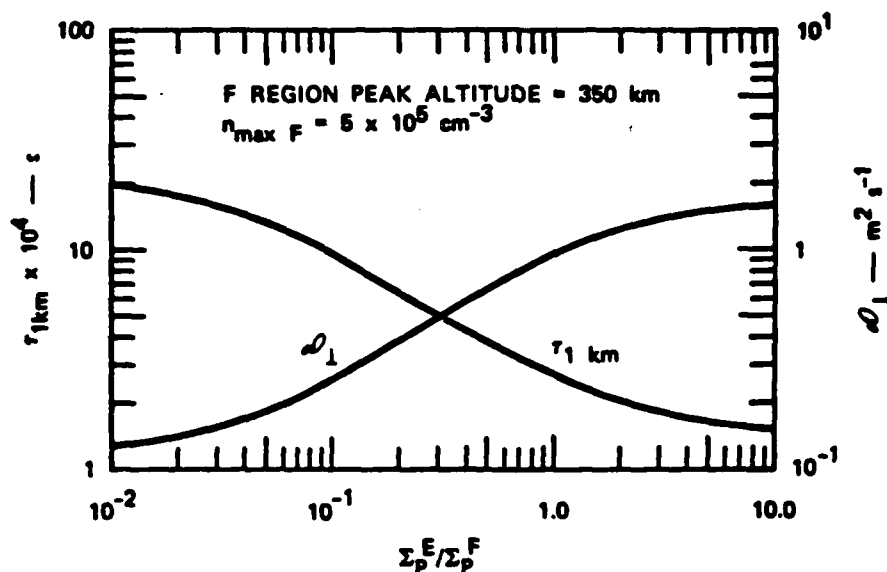


FIGURE 3 THE DEPENDENCE OF CROSS-FIELD DIFFUSION RATE,  $D_1$ , AND LIFETIME OF ONE-KM-SCALE IRREGULARITIES,  $\tau_1$  km, ON THE RATIO OF E- TO F-REGION PEDERSEN CONDUCTIVITIES. The F-layer altitude and peak density are fixed.

#### High-Latitude Convection

The final element necessary to explain high-latitude irregularity morphology is convection. Large-scale unstable blobs of plasma such as that shown in Figure 1 are observed to convect with the background electric field (Vickrey et al., 1980). These large-scale features have very long lifetimes and, thus, can convect far from their origins. Plasma instabilities operating on their edges may produce small-scale plasma structure all along the way. This "cascade" to small scale reduces the lifetime of the large-scale features, but not enough to prevent their transit across the polar cap (Kelley et al., 1982). This scenario can explain the presence of plasma structure throughout the polar regions of the earth even though "source" regions may be quite localized.

As a framework it is useful to see to what extent a classical aeronomic viewpoint can explain the data. To this end Kelley et al. (1982) have quantified a classical picture of irregularity formation

and distribution by combining simple models of irregularity production and loss with a two-celled magnetospheric convection pattern. They considered a simple "source" region of irregularities to be an annular ring near the poleward edge of the auroral oval. This source is a region in which satellites have recorded soft precipitating particle fluxes (Poster and Burrows, 1976; Hardy, private communication). The irregularity lifetime was calculated using the classical diffusion model of Vickrey and Kelley (1982), which includes E-region conductivity effects. The global E-region conductivity distribution assumed was that given by Wallis and Budzinski (1981). The convection model assumed was that given by Spiro et al., (1978). Figure 4 shows the results obtained by Kelley et al., (1982). The trajectories (in the inertial frame) of four flux tubes across the polar cap and around the auroral zone are shown. The numbers indicate the amplitude in dB of one-kilometer-scale irregularities,  $|\Delta N/N|_2^2$ , where N is electron density. The amplitude is reset to 0 dB whenever the trajectories cross the source region near the poleward edge of the auroral oval. A similar plot for 10-km structures would show almost negligible decay, because diffusion acts 100 times more slowly at that scale size.

Figure 5 is a similar plot that includes the overall decay of the ionosphere because of recombination, which adds approximately 4 dB per hour of travel time for the irregularity and the background. This plot, then, is more representative of the spectral strength  $|\Delta N|^2$ ; hence, it is perhaps more descriptive of scintillation effects. The peak F-region density is assumed  $5 \times 10^8 \text{ cm}^{-3}$  in the production zone, with the density maximum at a height of 350 km. A Chapman layer is also assumed (Vickrey and Kelley, 1982). Winter conditions are taken so as to emphasize the effects of auroral production and decay. A dashed line marks the terminator at 350-km altitude during winter and equinox. When the absolute density decayed to  $5 \times 10^7 \text{ cm}^{-3}$ , the recombination decay was stopped. In such a case, the assumption of an  $O^+$  plasma is no longer valid, and longer-lived ions may dominate the F<sub>2</sub> layer composition (Heelis et al., 1981).

Despite the simplicity of this first attempt to assess the relative roles of production, convection, and decay in determining high-latitude irregularity morphology, this model leads to a number of useful conclusions. For example, 10-km size density fluctuations can survive transport throughout the polar cap and auroral zone if sunlight does not illuminate the region for a prolonged period. At one-km scale, the classical diffusion discussed here and in Vickrey and Kelley (1982) has a significant effect in some regions of the polar cap and auroral zone. For example, a very deep irregularity "hole" can be formed in the central polar cap, as experimentally reported by Kelley and Mozer (1972). This is primarily due to the long time that a flux tube can spend in the central polar region. Even in the 10-km case, a very sharp gradient in irregularity

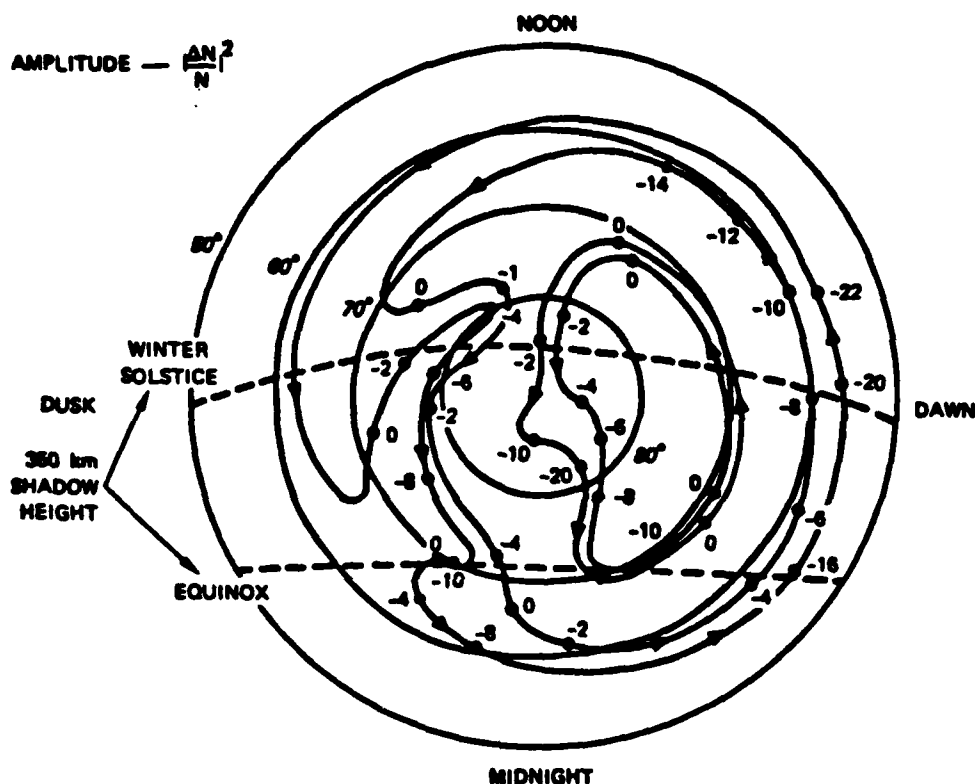


FIGURE 4 ILLUSTRATION OF THE LATITUDE AND LOCAL-TIME VARIATIONS (IN THE INERTIAL FRAME) OF THE AMPLITUDE (IN dB) OF ONE-KM-SCALE ELECTRON DENSITY IRREGULARITIES  
[Kelley et al., 1982]

intensity is formed at the equatorward edge of the nighttime magnetospheric-convection zone--not the auroral oval. This agrees excellently with many studies of the high-latitude irregularity boundary (see review by Fejer and Kelley, 1980). However, other sources of plasma density irregularities, such as mid-latitude spread F and processes associated with plasma density gradients near the F-region trough can also contribute to irregularity formation at times.

In relatively quiet times, the postsunset local-time region, 1800 to 2100, between 60° and 68° should not contain many irregularities because, in the nonrotating frame, flux tubes only enter this

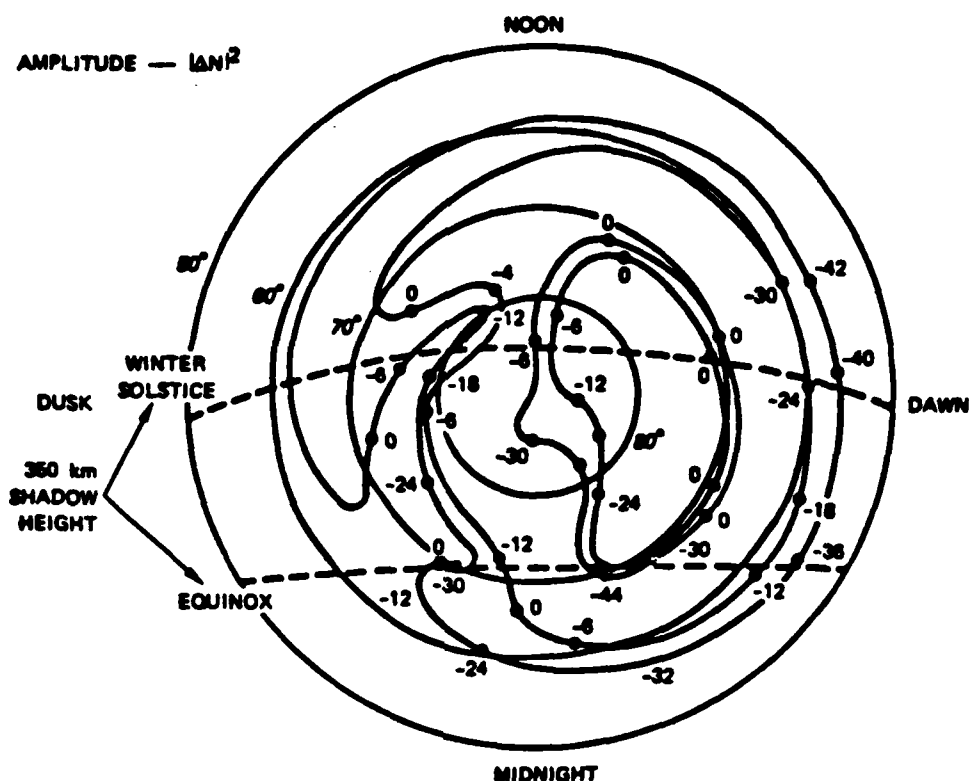


FIGURE 5 ILLUSTRATION OF THE LATITUDE AND LOCAL-TIME VARIATIONS (IN THE INERTIAL FRAME) OF THE AMPLITUDE (IN dB) OF ONE-KM-SCALE ELECTRON DENSITY IRREGULARITIES INCLUDING THE EFFECTS OF RECOMBINATIONAL DECAY

region from the sunlit sector. For the same reason, the equatorward boundary of the irregularity zone should be at higher latitudes in the dusk sector than in the dawn sector, to which midnight-sector auroral-oval irregularities can rapidly convect. This agrees with the ISIS results reported by Sagalyan et al., (1974), who showed that the boundary was about  $3^\circ$  higher in latitude in the dusk sector for  $K_p \leq 3$ . The difference was less pronounced for  $K_p \geq 3$ . This is reasonable because, with increasing magnetic activity, large convection speeds can dominate over the corotation velocity at lower latitudes in the local time sector near and just after dusk.

We turn now to ways in which the classical model does not fit the observations. Figure 6 shows the average electric field strength at 31 Hz ( $\sim 200$ -m scale fluctuations) measured by the OVI-17 satellite (Kelley and Mozer, 1972) as a function of invariant latitude. Note that the irregularity amplitude has a latitudinal trend that is qualitatively similar to that expected from Figures 4 and 5 in a noon-to-midnight cross section. Namely, there is a strong source of irregularities in the polar cusp, a decay of irregularity amplitude in the central polar cap, and another source region in the midnight-sector auroral oval. These observations make it apparent, however, that the simple model illustrated in Figures 4 and 5 grossly misrepresents the amplitude of small-scale irregularities; for example, the decrease in amplitude for 200-m scales in Figures 4 and 5 should be multiplied by a factor of 25. However, the amplitude decrease actually observed across the polar cap for 200-m scales is even less than that expected for kilometer-scale structures. These data thus suggest that intermediate- and small-scale irregularities are continuously generated throughout the polar cap, probably on the unstable edges of the larger-scale blobs. As mentioned above, such a cascade process would

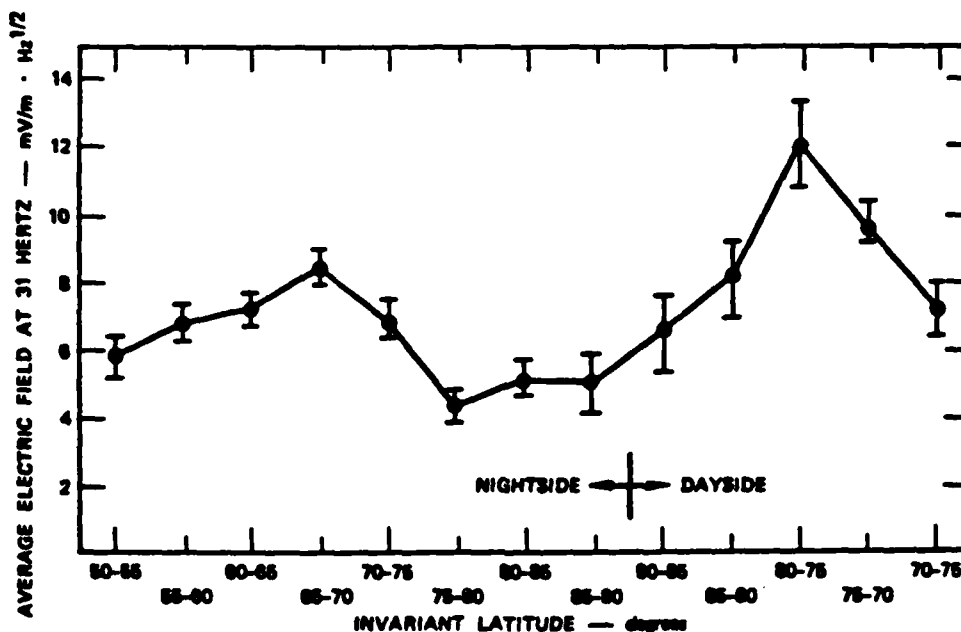


FIGURE 6 AVERAGE ELECTRIC-FIELD STRENGTH AT 200-m SCALE AS A FUNCTION OF LATITUDE



hasten the removal of large-scale features, but not enough to prevent their transit through the polar cap.

It is interesting to turn the problem around by interpreting Figure 6 in terms of anomalous diffusion at large scales. This can be done as follows: Suppose the irregularity spectrum,  $S(k) = |\Delta N(k)|^2$ , has a rigid shape (e.g.,  $S(k) \propto k^{-2}$ ) as a set of adjacent flux tubes convect across the polar cap. Then, the decrease in amplitude of 200-m irregularities reflects a decrease in energy stored at the input scale, which is of order  $\lambda \approx 10$  km. The quasi-exponential spatial decrease in irregularity amplitude in Figure 6 between  $75^\circ$  invariant latitude on the dayside cusp and  $75^\circ$  on the nightside can be converted to an effective diffusion rate,  $D_{\text{eff}}$ , if we assume the average antisunward drifts from the Spiro et al. (1978) convection model. This exercise leads to an effective diffusion rate that is within ~60 percent of the Bohm diffusion rate measured empirically in laboratory plasmas. This  $D_{\text{eff}}$  is approximately 100 times faster than the classical diffusion rate.

The above calculation is obviously too approximate and based on too many unverified assumptions to prove conclusively that Bohm diffusion or any other specific diffusion process is operating in the polar cap. Nonetheless, it strongly suggests that some anomalous process is operating that is much faster than classical diffusion. To proceed in the future, it will be necessary to measure the complete spectrum of irregularities and their associated electric fields across the polar regions to distinguish between anomalous diffusion processes due to various microinstabilities (e.g., Gary, 1980). This will be discussed more fully in the section below on future directions.

### Irregularity Geometry

Any viable theory for the formation and evolution of plasma structure must ultimately account for the observed geometry of plasma density irregularities. Auroral-zone scintillation measurements from the Wideband satellite show enhancements in scintillation whenever the propagation vector lies in the plane of the local L-shell, not just when it coincides with the local magnetic field line. This phenomenon suggests that the intermediate-scale (~1 km) irregularities responsible for the scintillation are L-shell-aligned sheet-like structures rather than simple rods. This unexpected geometry has been confirmed by spaced-receiver scintillation measurements in the midnight sector auroral zone. These measurements show a high ratio (up to 10 to 1) of spatial coherence in the magnetic east-west direction as compared to the north-south direction (Rino et al., 1978). The linear gradient drift and current convective instabilities operating on the meridional density gradients shown in Figure 1 tend to produce irregularities with a

A  $k$  vector in the east-west plane; i.e., orthogonal to the geometry of the kilometer-scale structures that is actually observed. This apparent paradox has been addressed by Chaturvedi and Ossakow (1979a, b), whose analysis shows that the linearly unstable mode of the gradient drift and current convective instabilities can transfer energy through nonlinear coupling to a (linearly stable) mode whose wave vector lies in the plane of the density gradient.

Recently, Keskinen and Ossakow (1982) have performed numerical simulations of the gradient drift and current convective instabilities operating on a blob such as shown in Figure 1 for typical auroral F-region conditions. They have found that the primary and associated (secondary) small-scale structures can be oriented in either the north-south or east-west direction depending on the ambient electric field magnitude and direction. Because the meridional electric-field component in the auroral zone is typically five times the zonal component, any primary (north-south) structure can be quickly destabilized by the meridional electric-field component to produce secondary structure, which is east-west aligned.

Another mechanism for producing kilometer-scale east-west structures in the auroral zone can result if the large-scale blobs themselves are not infinitely extended in the east-west direction. Any large-scale zonal gradients can be acted upon by the meridional electric field to produce (primary) east-west aligned structure. Recently, a campaign of experiments with the Chatanika radar was conducted to measure east-west structure of the large-scale blobs. The preliminary results from those experiments indicate that although the east-west scale lengths can be very much longer than those north-south (particularly during magnetically quiet times), there are also occasions when the east-west extent of the blobs is comparable to the meridional extent (Tsunoda, private communication).

Another process that might explain the observed anisotropy of medium-scale irregularities at high latitudes is the behavior of an incompressible fluid in a sheared convective-flow pattern. A very simple example is illustrated schematically in Figure 7. The situation was constructed to be similar to the premidnight sector convective flow pattern out of the polar cap, where flow is principally sun-aligned, and into the auroral oval, where flow is principally zonal. An irregularity represented by the ellipsoid contour of constant electron density was chosen to be initially sun aligned (i.e., perpendicular to what is observed in the auroral zone). Because the F region plasma is incompressible, the area of the ellipsoid remains constant. The equatorward tip of the irregularity enters the region of westward flow before the poleward tip. Therefore, the irregularity becomes either kinked or smoothly rotated (depending on the ratio of irregularity size,  $L_{\text{irregularity}}$ , to shear (or rotation) size,  $L_{\text{shear}}$ ) as it drifts further south. In

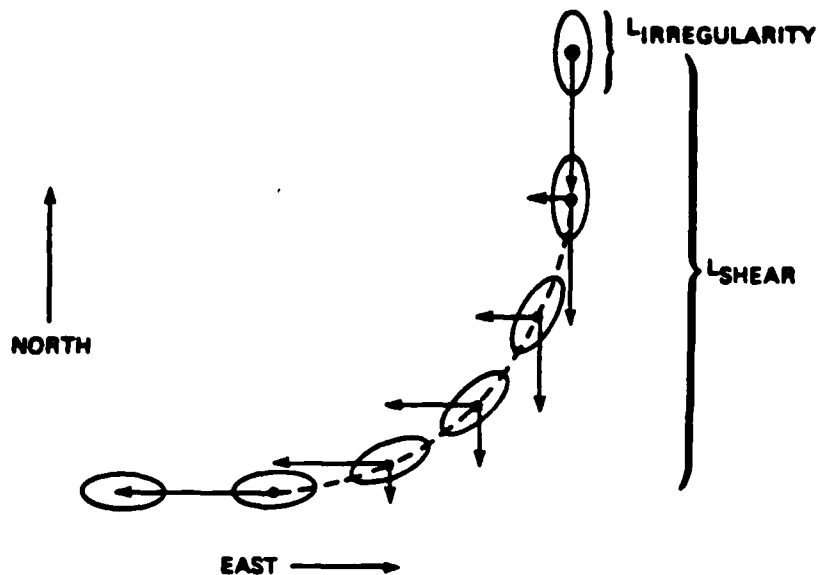
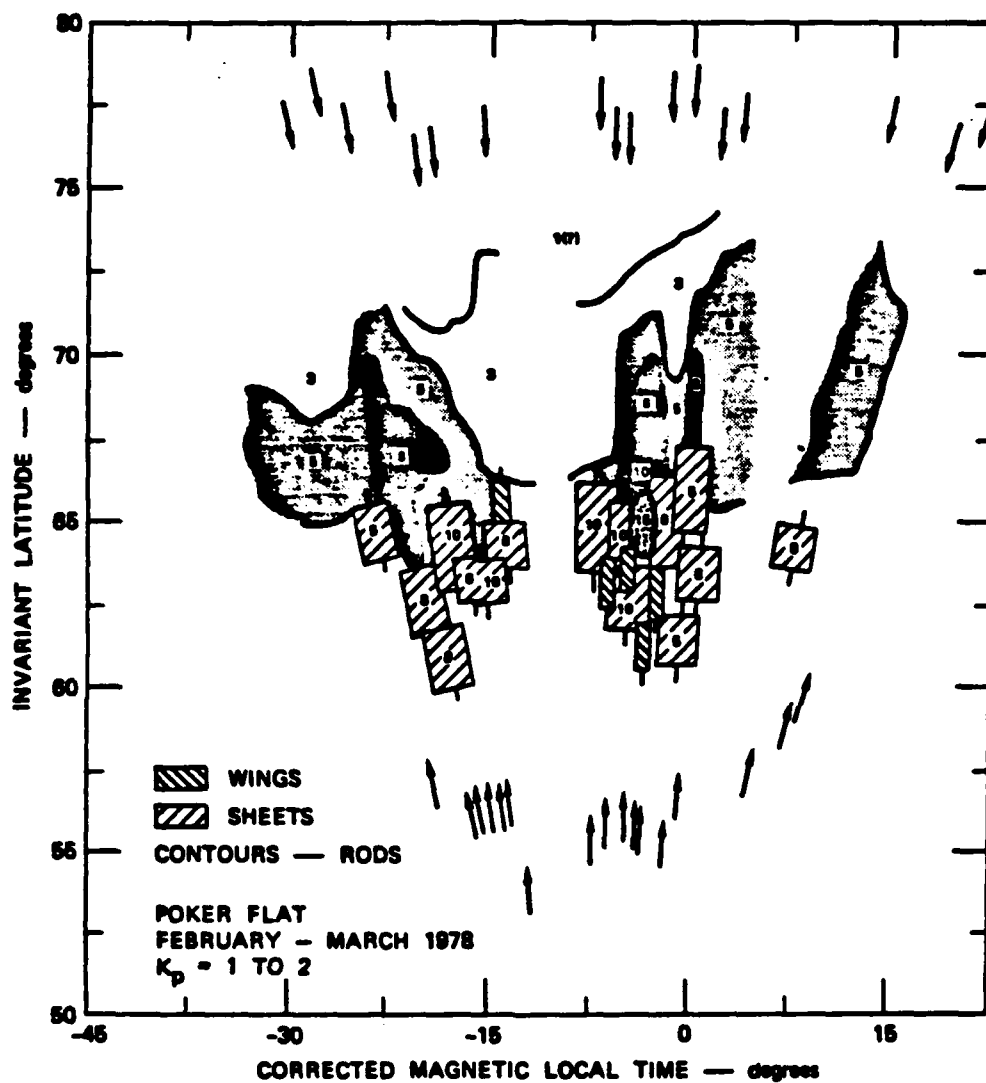


FIGURE 7 SCHEMATIC ILLUSTRATION OF AN ANISOTROPIC IRREGULARITY  
SUBJECTED TO A SHEARED FLOW PATTERN

general, however, we expect the irregularity to be aligned with the streamlines of flow. Thus this model predicts east-west aligned sheets in the auroral oval except perhaps very near the Harang discontinuity. It is interesting to note that a conservative velocity shear (given by assuming that a 500 m/s meridional flow in the polar cap changes to a 500 m/s westward flow in the auroral oval over a meridional distance of 500 km) is on the order of  $10^{-3}$  Hz. This value is comparable to the  $\vec{E} \times \vec{B}$  instability growth rates observed by Vickrey et al. (1980) for an unstable blob. Thus, by the time an irregularity has formed, it should already be rotated to align with flow lines.

Evidence that convection may indeed influence irregularity geometry can be found in the latitude-local time variations of anisotropy determined from spaced receiver scintillation measurements. Figure 8 shows the preliminary results of such a compilation (R. C. Livingston, private communication) for Wideband Satellite passes recorded at Poker Flat, Alaska ( $65^\circ$  invariant latitude, Local Time = UT - 10 hours) during February and March of 1978. The data show a dramatic change in kilometer scale irregularity anisotropy



**FIGURE 8** LATITUDE-LOCAL-TIME VARIATION OF IRREGULARITY ANISOTROPY. The numbers indicate the degree of elongation along  $\vec{B}$  normalized to the minimum cross field dimension. Wings (sheets) have an east-west elongation that is one-half (equal to) their elongation along  $\vec{B}$ .

between the polar cap where irregularities appear to be isotropic or rod-like depending on local time and lower latitudes where irregularities can be sheet-like throughout the evening. Note that the elongation of the sheets and rods is reduced in the midnight sector (i.e., near the Harang discontinuity). One possible reason why the polar cap irregularities appear to be isotropic or rod-like may be that the winter polar cap flow is very irregular. A similar analysis of summer polar cap data (where flow is expected to be more regular) is underway.

#### FUTURE RESEARCH

Our framework for understanding high-latitude irregularity morphology consists of three simple component parts--irregularity production, transport, and decay. It is clear, however, that none of these component parts is well understood at present. Indeed, fundamental questions remain in each area that can be addressed by VIKING and EISCAT as well as other existing or proposed diagnostic instruments.

In the area of irregularity production, the source regions of large-scale blobs are known to be much more complicated than the simple ring used in the model of Kelley et al. (1982). For example, sun-aligned F layer polar cap arcs are known to be a strong source of radio wave scintillation (Weber and Buchau, 1980) and thus should be included in the "source function." This large-scale source function can be better defined by analyzing data from precipitating-particle detectors aboard polar-orbiting satellites and perhaps from satellite imaging. These measurements should be augmented by ground-based incoherent-scatter measurements that can probe the three-dimensional density structure that results from this precipitation. It is important that the particle detector have a high spatial resolution because at present the nature of the spatial spectrum of soft precipitation is unknown. For example, can structured precipitation directly produce structured ionization at kilometer scales and smaller or is precipitation only responsible for large-scale "seed" features upon which instabilities operate? Because the E-region conductivity produced by energetic precipitation is an important consideration for both the growth rate of convective instabilities and for the lifetime of irregularities once they are produced, the particle detector should also be sensitive to high energies so that the global conductivity pattern can be modeled.

It has been shown that convective plasma instabilities are operative in the high-latitude ionosphere. However, they have many important properties that merit further examination. For example, it is now becoming clear that the spectrum of irregularities present

on a given flux tube of plasma depends in a complicated way on the past history of that flux tube. Thermal diffusion operates slowly as compared to observed instability growth rates. Thus, instability growth is, to some extent, cumulative as a flux tube convects between unstable and benign regions. Therefore, to predict the amount of plasma structure at a given point, the minimum destabilizing influences a flux tube has encountered in crossing the polar regions must be assessed. These influences include the magnitude and direction of the electric field and neutral wind with respect to the density gradient as well as the amplitude of the field-aligned current, which is known to be a permanent feature of the auroral zone. Measurement of the latter can be performed by a satellite-borne vector magnetometer; however, detailed knowledge of the neutral wind pattern at high-latitudes requires more extensive ground-based optical measurements as well as improved modeling. Simultaneous in-situ measurement of  $\delta E$  and  $\delta n/n$  should help separate the various instability mechanisms. This has been used successfully at the magnetic equator to identify drift waves as an important contributor to the cascade of energy from long to short scale (Kelley et al., 1982).

High-latitude convection can be measured by polar orbiting satellites with electric-field detectors as well as incoherent-scatter radar. It is important to further characterize the global changes in this pattern caused by variations in the interplanetary magnetic field and solar wind conditions. Moreover, high spatial-resolution electric-field measurements are required to determine the magnitude of velocity shears. Furthermore, small-scale waves that are thought to play a role in anomalous diffusion (which may in turn be the controlling factor determining irregularity lifetime) can be detected and studied. For example, in the equatorial case, it has been shown that waves of the drift-mode type are more easily detected through their electric-field signatures and that the wave type can be identified through comparisons of  $\delta E$  and  $\delta n/n$  (Kelley et al., 1982). Other crucial elements in the study of anomalous diffusion are to measure the entire spectrum of density structure from hundreds of kilometers to meters, if possible, and to document spectral changes between the polar cap, auroral zone, and trough.

The complicated geometry of plasma density irregularities is an interesting area for further research. Whether this geometry is the result of precipitation structure, nonlinear saturation of a convective instability, a secondary instability, or simply a result of convective flow patterns is an open question. Certainly the answer will depend upon the scale size of interest. At large scales, combined ground-based optical and incoherent-scatter radar measurements may shed some light on the answer. At intermediate and small scales, further spaced-receiver scintillation measurements are required.

## REFERENCES

- Chaturvedi, P. K., and Ossakow, S. L., February 1979, Nonlinear stabilization of the  $E \times B$  gradient drift instability in ionospheric plasma clouds, J. Geophys. Res., 84:A2:419.
- Chaturvedi, P. K., and Ossakow, S. L., December 1979, Nonlinear stabilization of the current convective instability in the diffuse aurora, J. Geophys. Res. Letts., 6:12:957.
- Dyson, P. L., and Winningham, J. D., 1974, Topside ionospheric spread F and particle precipitation in the dayside magnetospheric clefts, J. Geophys. Res., 79:5219.
- Fejer, B. G., and Kelley, M. C., May 1980, Ionospheric irregularities, Rev. Geophys. and Space Sci., 18:2:401.
- Foster, J. C. and Burrows, J. R., December 1976, Electron fluxes over the polar cap: 1. Intense KeV fluxes during post-storm quieting, J. Geophys. Res., 81:34:6016.
- Gary, S. P., June 1980, Wave particle transport from electrostatic instabilities, Phys. Fluids, 23:6:1193.
- Heelis, R. A., Murphy, J. A., and Hanson, W. B., January 1981, A feature of the behavior of  $He^+$  in the nightside high-latitude ionosphere during equinox, J. Geophys. Res., 86:A1:59.
- Happner, J. P., March 1977, Empirical models of high-latitude electric fields, J. Geophys. Res., 82:7:1115.
- Kelley, M. C., and Carlson, C. W., 1977, Observation of intense velocity shear and associated electrostatic waves near an auroral arc, J. Geophys. Res., 82:2343.
- Kelley, M. C., and Mozer, F. S., August 1972, A satellite survey of vector electric fields in the ionosphere at frequencies of 10-500 Hz: 1. Isotropic, high-latitude electrostatic emissions, J. Geophys. Res., 77:22:4158.
- Kelley, M. C., Bering, C. E., and Mozer, F. S., 1975, Evidence that the ion cyclotron instability is saturated by ion heating, Phys. Fluids, 18:1590.
- Kelley, M. C., Vickrey, J. F., Carlson, C. W., and Torbert, R., 1982, On the origin and spatial extent of high-latitude F-region irregularities, J. Geophys. Res., in press.
- Kelley, M. C., Pfaff, C. R., Baker, K. D., Ulwick, J. C., Livingston, R. C., Rino, C. L., and Tsunoda, R. T., 1982, Simultaneous rocket probe and radar measurements of equatorial spread F--transitional and short wavelength results, submitted to J. Geophys. Res.
- Kelly, J. D., and Wickwar, V. B., September 1981, Radar measurements of high-latitude ion composition between 140 and 300-km altitude, J. Geophys. Res., 86:A9:7617.
- Keskinen, M. J., and Ossakow, S. L., January 1982, Nonlinear evolution of plasma enhancements in the auroral ionosphere: 1. Long wavelength irregularities, J. Geophys. Res., 87:144.
- Kintner, P. M., 1976, Observations of velocity shear driven plasma turbulence, J. Geophys. Res., 81:5114.

- Linson, L. M. and Workman, J. B., June 1970, Formation of striations in ionospheric plasma clouds, J. Geophys. Res., 75:16:3211.
- Moser, F. S., Cattell, C. A., Tererin, M., Torbert, R. B., Vonglinski, S., Woldorf, M., and Wygant, J., 1979, The dc and ac electric field, plasma density, plasma temperature, and field-aligned current experiments on the S3-3 satellite, J. Geophys. Res., 84:A10:5875.
- Ossakow, S. L., and Chaturvedi, P. K., April 1979, Current convective instability in the diffuse aurora, Geophys. Res. Letts., 6:4:322.
- Rino, C. L., Livingston, R. C., and Matthews, S. J., December 1978, Evidence for sheet-like auroral ionospheric irregularities, Geophys. Res. Letts., 5:12:1034.
- Sagalyn, R. S., Smiddy, M., and Ahmed, M., October 1974, High-latitude irregularities in the topside ionosphere based on ISIS 1 thermal probe, J. Geophys. Res., 79:28:4253.
- Spiro, R. W., Heelis, R. A., and Hanson, W. B., September 1978, Ion convection and the formation of the mid-latitude F-region ionization trough, J. Geophys. Res., 83:A9:4255.
- Vickrey, J. F., and Kelley, M. C., 1982, The effects of a conducting E layer on classical F-region cross-field plasma diffusion, submitted to J. Geophys. Res.
- Vickery, J. F., Rino, C. L., and Poterms, T. A., October 1980, Chatanika/Triad observations of unstable ionization enhancements in the auroral F region, Geophys. Res. Letts., 7:10:789.
- Wallis, D. D., and Budzinski, E. E., January 1981, Empirical models of height-integrated conductivities, J. Geophys. Res., 86:A1:125.
- Weber, E. J., and Buchau, J., January 1980, Polar cap F-layer auroras, Geophys. Res. Letts., 8:1:125.



# High-Latitude *F* Region Irregularities Observed Simultaneously With ISIS 1 and the Chatanika Radar

D. B. MULDREW

*Communications Research Centre, Department of Communications, Ottawa, Canada, K2H 8S2*

J. F. VICKREY

*Radio Physics Laboratory, SRI International, Menlo Park, California 94025*

Simultaneous measurements of the high-latitude ionosphere were made by the Chatanika radar and the ISIS 1 topside sounder and cylindrical electrostatic probe (CEP) when the satellite was at a height of about 700 km. The variation of enhancements and valleys of electron density with invariant latitude at the satellite, on the scale of a few hundred kilometers, agrees reasonably well with the radar results, even though the satellite displacement changed from almost coincident to about 500 km magnetic west of the radar scan path. These density enhancements comprise a collection of large-scale (tens of kilometers) irregularities or 'blobs.' Evidence for the formation of these blobs was obtained from the sounder. Natural, intense radio noise (hiss) was observed on the sounder ionograms recorded on the poleward side of the auroral zone, indicating the presence of precipitating kiloelectron volt electrons. A few minutes after these ionograms were recorded the radar scanned the same invariant latitude region and a large-scale ionization enhancement, or 'blob,' not present 13 minutes earlier, had developed in the bottomside *F* layer. ISIS 1 telemetry dropouts resulting from medium-scale irregularities, and enhanced irregularities down to about 200 m, observed with the CEP, are observed in association with blobs. Scatter signatures observed on the ISIS ionograms may be associated with large-scale irregularities that can be identified in the radar data. The scattering detected by the sounder is caused by 30- to 60-m wavelength irregularities (small-scale) that presumably are created by instabilities operating on the edges of the large-scale irregularities. The small-scale irregularities, however, are observed on both poleward and equatorward directed gradients. If the gradient-drift instability is responsible for these irregularities, then they either convect to the point of observation, are due to zonal gradients, or are field-aligned extensions of irregularities generated at lower heights.

## 1. INTRODUCTION

Large-scale (tens of kilometers) field-aligned irregularities, or blobs, which exist from the lower *F* region to a height of several hundred kilometers in the high-latitude ionosphere, have recently been observed by the Chatanika radar [Vickrey *et al.*, 1980]. Kelley *et al.* [1982] propose that these are generated by soft particle precipitation in the cleft and auroral zone. The irregularities produced in the cleft during daytime are carried over the pole and throughout the high-latitude region by magnetospheric convection. The irregularities generated in the auroral zone at night can be carried somewhat equatorward of the auroral zone. During this convection, classical diffusion [Vickrey and Kelley, 1982] will cause serious decay only of irregularities of about 1 km or less (small-scale). Irregularities in the size regime of  $\leq 100$  m, which are known to exist throughout the polar region, must then be generated by instabilities acting on the large-scale structures.

Scatter signals from these small-scale irregularities have previously been observed throughout the high-latitude region by the Alouette 1 topside sounder [Petrie, 1963; Calvert and Schmid, 1964]. The Alouette 1 sounder transmits radio waves between 0.5 and 11.5 MHz and then listens for ionospheric reflections or for signals backscattered from irregularities.

The combination of the ISIS 1 spacecraft and the Chatanika

radar is ideal for studying ionization irregularities. The radar can obtain electron density profiles with better large-scale resolution than the ISIS 1 sounder in a region of extreme horizontal gradients, and the sounder and ISIS 1 cylindrical electrostatic probes (CEP) [Findlay and Brace, 1969] can examine small-scale structure that is beyond the resolution of the radar. The CEP are Langmuir probes, which measure electron or ion current as the probe voltage is varied. The electron density is proportional to this current. In this paper, comparisons of ISIS and radar data give new insight into the east-west extent and spacial coexistence of different size irregularities and into the generation of both large- and small-scale irregularities.

## 2. LARGE-SCALE FEATURES IN THE AURORAL *F* REGION DEDUCED FROM THE CHATANIKA RADAR AND ISIS DATA

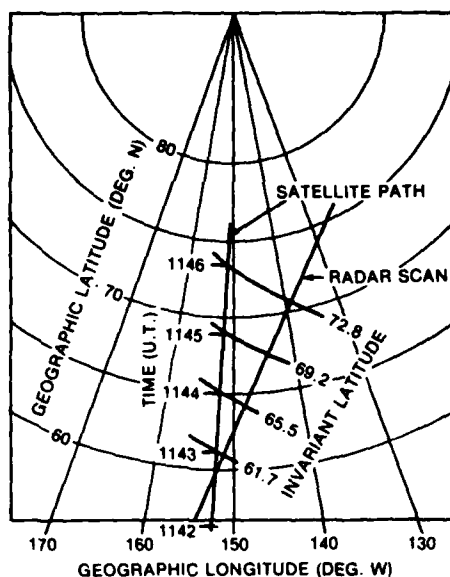
*Data.* Figure 1 shows the location of the Chatanika radar scan and of the ISIS 1 satellite trajectory on February 20, 1981, at about 1145 UT. The universal time is indicated along the satellite path. The invariant latitude at the satellite height ( $\sim 700$  km) is also given. In this case the radar scanned from south to north in the vertical, magnetic meridian plane. Near the south end of the scan ( $\sim 60^\circ$ ) the satellite path intersects the radar scan. At the north end the satellite is about 500 km west of the scan. Here and below, unless otherwise stated, latitude will be invariant latitude and east-west and north-south will mean magnetic east-west and magnetic north-south.

Figures 2 and 3 show the Chatanika radar results for February 20, 1981, between 1130:25 and 1144:23 and between 1144:50 and 1157:28 UT, respectively. The *Kp* value

Copyright 1982 by the American Geophysical Union.

Paper number 2A0783.  
0148-0227/82/002A-0783\$05.00

8263



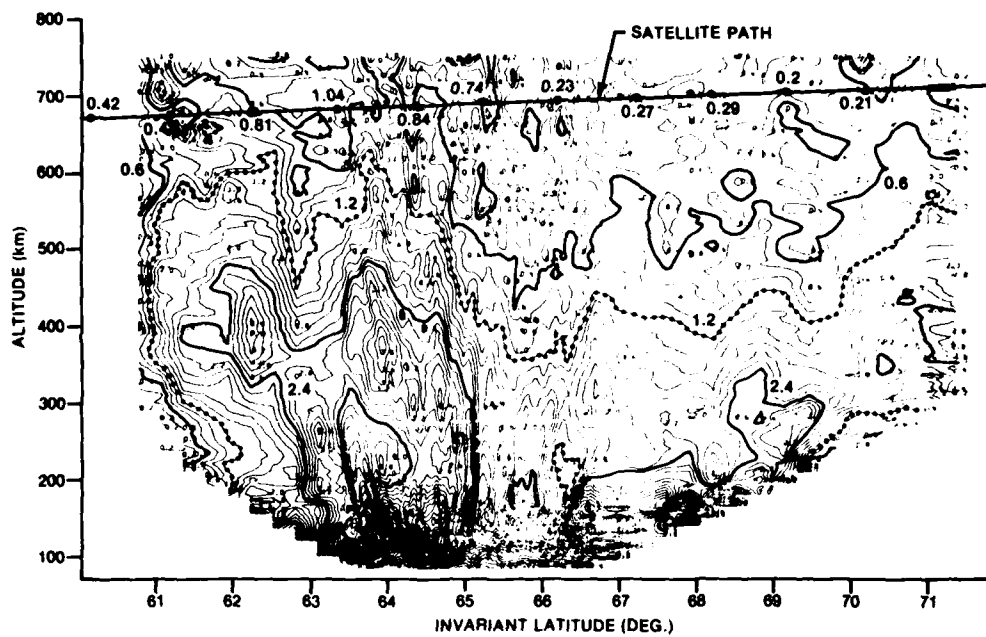


Fig. 3. Same as Figure 2 between 1144:50 and 1157:28 UT.

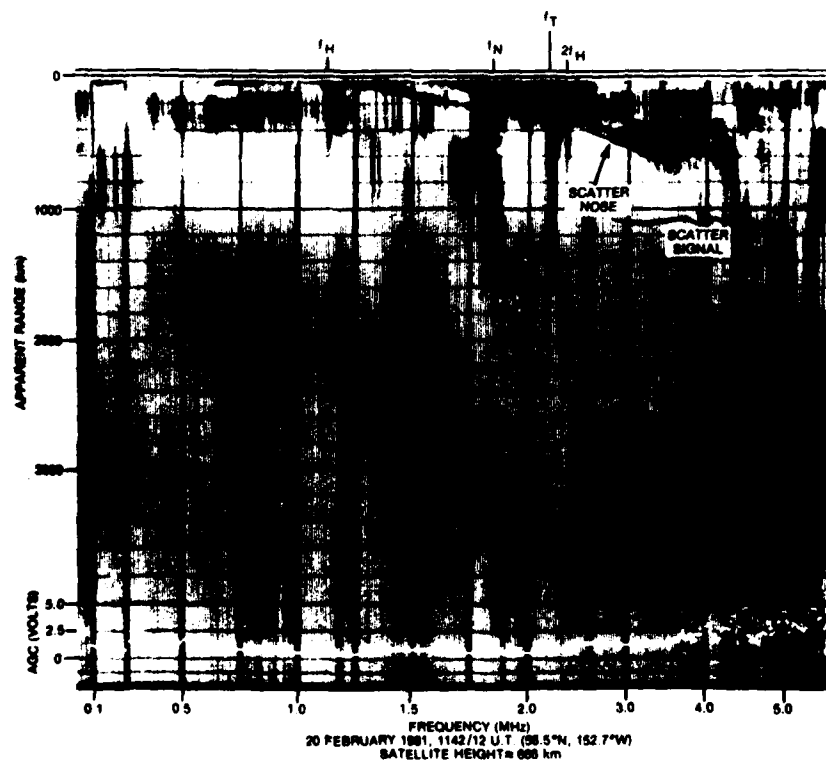


Fig. 4. ISIS I ionogram showing backscatter signature between 2.8 and 4.8 MHz. The satellite position is given in geographic coordinates. The invariant latitude is about 59.3°.

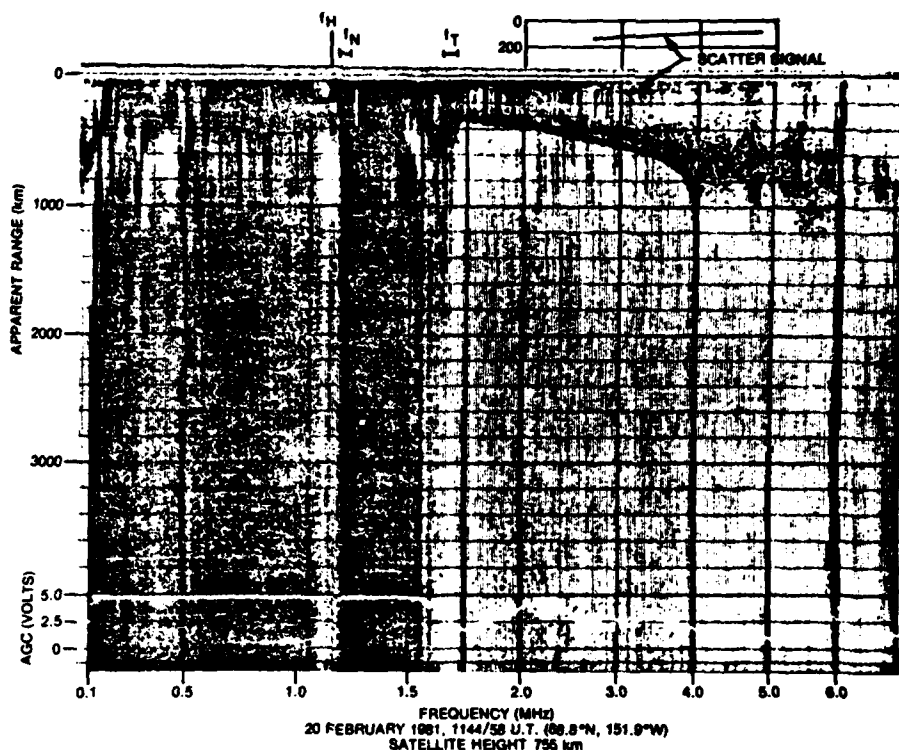


Fig. 5. ISIS 1 ionogram showing backscatter signature from about 2.5 to 4.8 MHz. Natural noise saturates the AGC between 0.1 and 1.6 MHz. The satellite position is given in geographic coordinates. The invariant latitude is about  $69.5^\circ$ .

400 km apparent range and from 0.35 to 6 MHz in Figure 4 is an example of this interference.

**Electron density comparison at the satellite height.** Density enhancements with a north-south dimension of a few tens to a few hundreds of kilometers, observed by the radar and by the satellite, will now be compared in order to learn about their east-west extension.

In Figure 4 the electron density at the satellite can be determined accurately from the plasma frequency ( $f_N$ ) resonance spike at 1.85 MHz. In Figure 5 the  $f_N$  resonance cannot be seen due to the high natural noise level, but the noise cutoff near  $f_T$  (between 1.6 and 1.7 MHz) and the extraordinary-wave-cutoff frequency at the satellite height (about 1.9 MHz) allows the plasma frequency of approximately 1.2 MHz to be calculated.

In Figure 6a the radar-determined electron density at the satellite height is obtained from Figures 2 and 3 and plotted as a function of invariant latitude by using a solid line (Figure 2) and a dashed line (Figure 3). The circles in Figure 6a are electron densities determined from the ISIS 1 ionograms. The error in the satellite points is about  $0.02 \times 10^5 \text{ cm}^{-3}$ . The density corresponding to the ionograms recorded at about  $71.2^\circ$  and  $72.2^\circ$  could not be determined with sufficient accuracy to plot. Because of the large range and resulting weakness of the received signal, the radar densities are only accurate to about 50% near 700 km height.

In Figure 6b the electron density from the CEP is plotted along with the sounder values (circles). Spin modulation

occurs from the start of the data to 1143:37 and from 1145:55 to the end of the data; this can only be clearly noticed during the first minute of data. The maximum value of the modulation cycle should be taken. At the times where no data is plotted the probe had an electrometer current range that was insensitive to both ion and electron current. However, ion current enhancements can occasionally be seen in this range, and enhancements of at least a factor of 2 are indicated in the figure. The densities between 1143:03 and 1143:37 and between 1145:20 and 1145:55 UT was obtained by normalizing to the densities obtained from the sounder at 1143:09 and 1143:25 UT. Other densities can be obtained directly from the probe current.

**Implications for east-west structure.** From Figure 1 it can be seen that the broad ionization valley between  $66^\circ$  and  $70^\circ$  (Figure 6a) observed by the radar thus extends at least 280 to 460 km westward to the satellite. Similarly, the region of enhanced ionization between  $61.5^\circ$  and  $65.5^\circ$  observed by the radar extends at least 40 to 250 km westward to the satellite. It can be seen (Figure 2) that in this region of enhanced ionization there is a considerable number of blobs existing in the topside F region.

Ionization enhancements of about a factor of 2 over ambient, which exist over a few tens of kilometers in the north-south direction, are observed in the radar data (e.g., at  $67.2^\circ$ ,  $68.4^\circ$ , and  $71.4^\circ$  in the 1130–1144 UT data of Figure 6a). These will be referred to as ionization 'spikes' to distinguish them from the much larger density increases

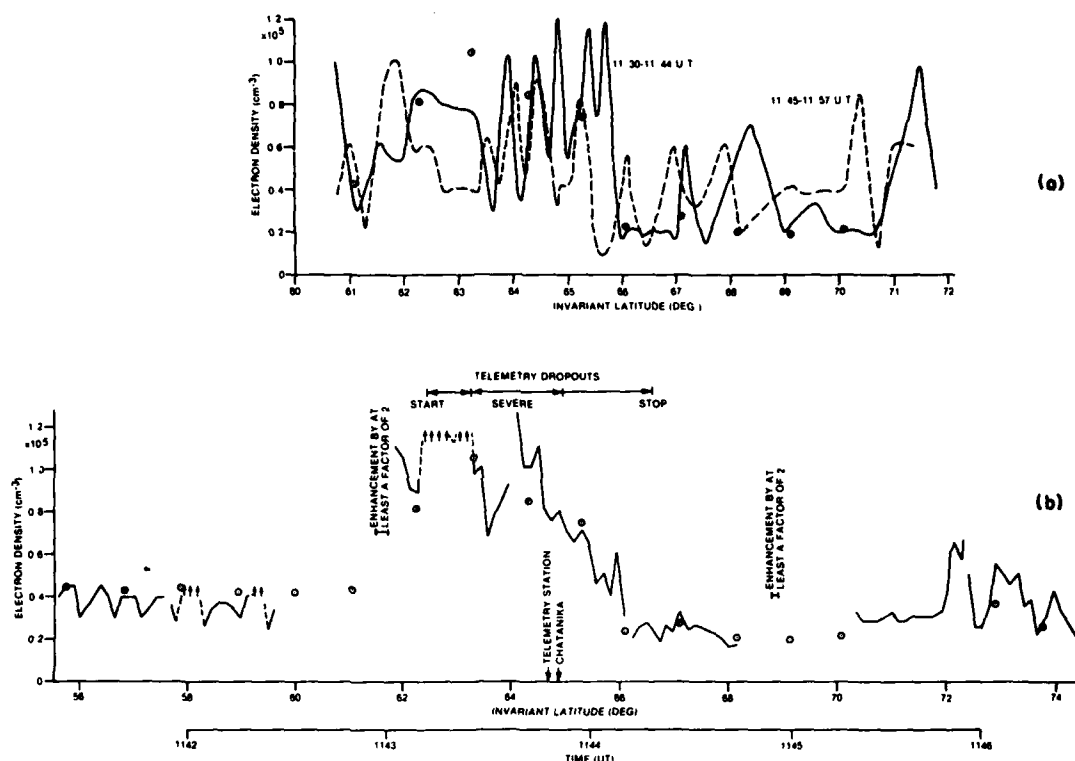


Fig. 6. Electron density at the ISIS 1 satellite height. The circles give the electron density obtained from the ISIS 1 ionograms. (a) Density obtained from Figure 2 (solid line) and Figure 3 (dashed line). (b) Density obtained from the cylindrical electrostatic probe on ISIS 1. Note the spin modulation in the first minute of data.

associated with blobs. It might appear that these are a consequence of the 50% error mentioned above; however, they are very likely real since similar spikes occur in the CEP data (e.g., the enhancement of at least a factor of 2 at 68.9° and 72.1° in Figure 6b). The CEP data were recorded a few minutes later and a few hundred kilometers west of the radar data. The accuracy of the probe densities varies with the electrometer current range of the probe in operation; but the maximum relative error of the plotted data in Figure 6b is about 10%. If these ionization spikes extend in the east-west direction for hundreds of kilometers, the same pattern as in the radar data would be expected in the CEP data, with a corrective displacement of roughly 0.5° southward as a result of convection. (Radar measurements of the drift indicate a southward drift of about 180 m/s.) East-west alignment does not seem to occur here. On the other hand, magnetic east-west radar scans (J. F. Vickrey, M. C. Kelley, R. T. Tsunoda, and M. A. McCready, private communication, 1982) indicate that for a particularly quiet magnetic case at the Chatanika latitude (64.8°), large-scale irregularities (e.g., ~50 km) can extend several hundred kilometers in the east-west direction near the peak of the *F* layer, although the effect is not so noticeable above about 600 km. However, more recent measurements by Tsunoda and Vickrey [1982] indicate that some large-scale blobs have an east-west extent comparable to their latitude extent.

### 3. ENERGETIC ELECTRON PRECIPITATION AND THE BIRTH OF A BLOB

Fortuitously, the sounder data for the time period under study contain clues on how blobs, such as those in the topside *F* layer between 63° and 66° latitude in Figure 2, are formed.

In Figure 5 there is a very intense level of natural noise or hiss between 0.1 MHz (low-frequency limit of the sounder) and the upper hybrid frequency near 1.7 MHz. Hiss is associated with kiloelectron volt electron precipitation in the auroral zone at night [Frank and Ackerson, 1972] and with a few hundred electron volts electron precipitation in the cusp region during the day.

The nighttime auroral hiss of Figure 5 has a similar character to the daytime cusp hiss studied by James [1973]. In Figures 1, 2, and 3 of James this hiss covers about an 8° latitude region, and energetic electrons exist in about a 3° zone at the center of the hiss region. It will be assumed here that precipitation on the nightside is also confined to a few degrees near the center of the hiss region. Figure 5 was recorded when ISIS 1 was at about 69° invariant latitude and hiss was observed between about 65° and 73°. Hence, at the time the ionogram of Figure 5 was recorded (1145 UT) it is likely that there was an intense energetic precipitation event in progress near 69°, the center of the hiss region.

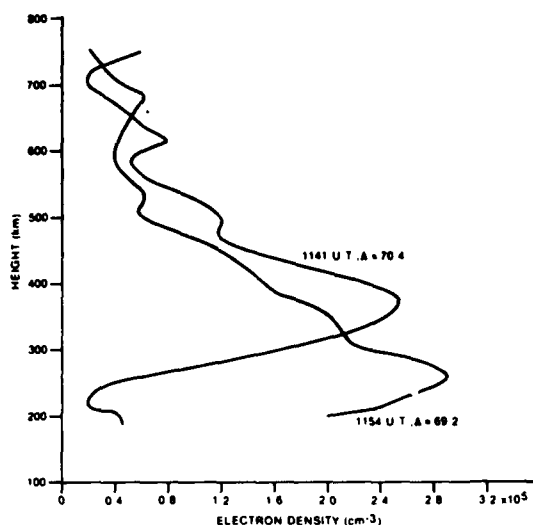


Fig. 7. Electron density profiles obtained from Figures 2 and 3 before and after (or during) an energetic electron precipitation event.

In Figure 2 the bottomside ionosphere from 67° to 72° is quite smooth, with little horizontal density gradient. The radar data in this latitude range were recorded just before 1145 UT. The radar plot for a period 13 min earlier than Figure 2 is similar to Figure 2 between 68° and 72°. However, Figure 3, recorded 13 min after Figure 2, shows a drastically modified bottomside ionosphere near 69°. It is reasonable to assume that this has been caused by the precipitation event recorded by ISIS 1. From Figure 1, ISIS 1 was about 300 km west of the radar scan at 69°.

A comparison of the density at 70.4° in Figure 2 and 69.2° (allowance for drift) in Figure 3 is shown in Figure 7. It is interesting to compare this with the results of Whitteker [1977], who made a model study of the response of the ionosphere to electron precipitation in the dayside cleft region where the spectrum of the precipitating electrons is about an order of magnitude softer.

In Figures 6 and 7 of Whitteker the following can be observed 10 min after 'turn on' of the electron precipitation and compared with Figure 10 of this paper:

1. The height of the *F* layer peak drops from about 325 km to 300 km.
2. The density of the *F* layer maximum increases by about 15%.
3. At 250 km there is a density increase of about 50% and at lower heights considerably more than this.
4. Between about 350 and 600 km there is a decrease in density of up to roughly 20%.

There is good agreement in this comparison. The major difference is the larger drop in the height of the *F* layer peak in Figure 7 from 370 to 260 km with a corresponding larger percentage increase in density at 260 km. However, this is to be expected because of the harder, more intense precipitation in the nighttime auroral zone (compare Figures 2 and 8 of Frank and Ackerson [1971] with Figure 2 of Whitteker).

Jones and Rees [1973] carried out calculations of the nighttime auroral ion density by using an electron energy

spectrum for nighttime conditions. Ten minutes after 'turn on' they obtained a density of about  $5 \times 10^5 \text{ cm}^{-3}$  at 200 km and  $4 \times 10^5 \text{ cm}^{-3}$  at 150 km. These values are considerably higher than those of Figure 7 at the corresponding heights. The 10-keV flux (see their equation 12) they used could be too intense to be applicable; it is about 40 times greater than that given in Figure 2 and 4 times greater than that given in Figure 8 of Frank and Ackerson [1971]. They also found density increases at all heights up to 840 km. This is not unreasonable, considering their model, since as a boundary condition they assumed zero thermal ionization flux at 1000-km height.

Thus it is likely that the ionospheric response shown in Figure 7 results from the precipitation event observed on the ISIS 1 ionograms recorded near 1145 UT. This implies that the precipitation occurs at approximately the same invariant latitude at the satellite and at the radar scan, which are separated by about 300 km in the east-west direction. It is then reasonable to conclude that we are observing the birth of a blob as a result of precipitation near 69.2° in Figure 3. As the new blob convects southward it will expand upward along the field. After about an hour it will probably be similar to the blobs observed between 63° and 66° in Figures 2 and 3. This is consistent with the model proposed by Kelley *et al.* [1982], except that the main contribution to the irregularity ionization may come from kiloelectron volt electrons rather than from electrons of a few hundred electron volts, as they propose.

#### 4. INTERMEDIATE- AND SMALL-SCALE IRREGULARITIES AS DEDUCED FROM THE CEP AND SOUNDER DATA

*Intermediate-scale irregularities observed with the CEP.* In Figure 6b the region over which there were dropouts of the 136-MHz telemetry is indicated. Under similar conditions, strong scintillations in the telemetry signal of the TRIAD satellite were observed by Vickrey *et al.* [1980]. In Figure 6b the first dropout occurred at 62.4°, the last at 66.6°, and severe dropouts occurred between 63.2° and 65.0°. In the region of the dropouts the density at the satellite was considerably enhanced and very variable. There were also blobs between the satellite and the telemetry station (0.2° south of Chatanika), as shown in Figure 2. Intense, medium-scale (~1-km) irregularities, which correspond in size to the Fresnel zone for the telemetry signal near the height of the *F* layer peak, are likely responsible for the telemetry dropouts. Presumably, these irregularities are generated by instabilities in the blobs, but because of the complex nature of the contours between the satellite and telemetry station, it cannot be determined if these medium-scale irregularities are confined to the region where the gradient-drift instability can operate [Kelley *et al.*, 1982].

Irregularities can also be observed directly in the probe current with a resolution of about 200 m. Variations in probe current cannot easily be distinguished from telemetry dropouts, and consequently the 200-m structure in the interesting region above the blobs was not studied. However, the large-scale irregularity (ionization 'spike') near 72.2° in Figure 6b has small-scale structure associated with it. This can be seen in Figure 8, where the CEP data recorded between 1145:44 and 1145:55 UT are presented. The expected voltage-current characteristic for a smooth ionosphere is drawn on some of the frames. The probe sensitivity changed at 1145:55, and data beyond this time are not shown. The ionization spike

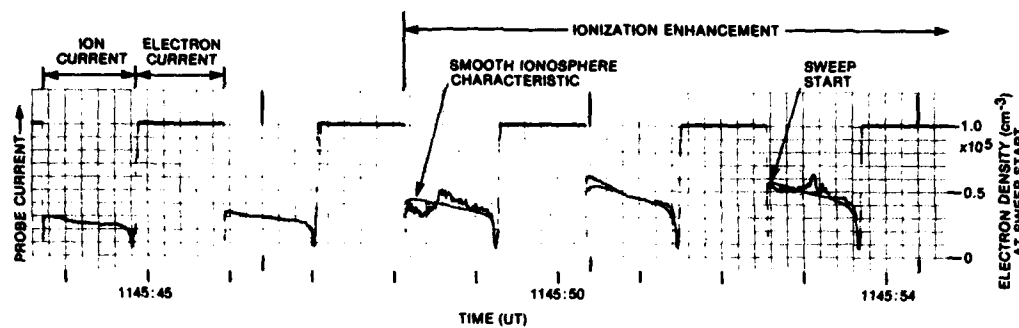


Fig. 8. Cylindrical electrostatic probe data recorded by ISIS 1, February 20, 1981, between 1145:43 and 1145:55 UT.

was actually observed until about 1145:58. It is about 70 km in north-south cross section, and the maximum enhancement is more than a factor of 2 over the background. Structure over a large range of sizes can be seen. Structure size near 5 km has about a 20% variation in density. Structure near the resolution limit of 200 m has a variation in density of a few percent. Significant medium-scale structure outside the spike was not observed.

The pulse repetition frequency of the sounder is about 30 Hz and is observed in the CEP data when the sounder frequency is near the plasma frequency. The sounder pulse repetition frequency contributes to the variation of probe current in the first half of the frame near 1145:49. However, the amplitude variations on consecutive maxima of the pulse modulations indicate that structure of size  $\geq 200$  m can be observed here as well as throughout the large-scale irregularity. That is, this structure is observed on both north- and south-directed density gradients in the ionization spike. Since 200-m structure takes about 1000 s or more to decay classically at this altitude [Vickrey and Kelley, 1982], the irregularities could have been generated elsewhere by the gradient-drift instability and then convected into this region.

*The equatorward boundary of the scatter region containing small-scale irregularities.* The scatter signal in Figure 4 has a well-defined, continuous leading edge (i.e., minimum apparent range boundary) that extends to at least 4.8 MHz at an apparent range of 300 km. At 3.7 MHz the apparent range is about 330 km. On the previous ionogram (not shown here) the leading edge of a similar scatter signal has an apparent range of about 480 km at 3.7 MHz (the maximum observed frequency), a difference of 150 km. Between ionograms the satellite traveled 140 km. Since the group velocity is slightly less than the free-space velocity of light, and the satellite is northbound, the above is consistent with a scattering region having a relatively sharp equatorward boundary that is located approximately northward of the satellite.

Note from Figure 1 that when the scatter signal of Figure 4 was recorded (1142:20 UT), the satellite was about 100 km east of the radar scan. Hence, assuming that the structures in Figure 2 extend at least 100 km in the east-west direction, then Figures 2 and 3 can be used to search for the structure responsible for the leading edge of the scatter signal on the ionogram. If it is also assumed that the small-scale irregularities are field aligned, then the scatter will be aspect sensitive. That is, the wave normal at the point of scatter must be very nearly perpendicular to the magnetic field in order that

the scatter energy return to the satellite, and the wavelength components of the irregularities must be about one half the radio wavelength (i.e., 30–60 m). Within a range of 300 km from the satellite the electron density is relatively low compared to the density of  $2.9 \times 10^5 \text{ cm}^{-3}$  required to reflect or considerably refract a wave of 4.8 MHz. Hence there will be little refraction at 4.8 MHz, and such a wave must have its wave normal approximately perpendicular to the magnetic field all the way from the satellite to the point of scatter. This implies that the scatter region is above the satellite height since the satellite is northbound in a region where the dip is about  $72^\circ$ . Allowing for refraction and decreased group velocity, the scatter can be calculated to come from near the circle in Figure 2 at 750-km height and  $61.6^\circ$ .

A similar calculation for the scatter signal on the ionogram recorded previous to the one in Figure 4 yields a scatter region marked by the circle at 770-km height and  $61.8^\circ$ . The electrometer range for the CEP was such that the density could not be measured accurately when the satellite was between  $61.6^\circ$  and  $61.8^\circ$ , but it could still be determined (see Figure 6b) that the density at  $61.7^\circ$  increased by at least a factor of 2 over that at  $61.6^\circ$  and  $61.8^\circ$ .

There is an irregularity centered at a height of 720 km and latitude  $62.2^\circ$  at about 1134 UT (Figure 2) that apparently drifts to a height of 710 km and  $61.1^\circ$  at about 1148 UT (Figure 3). These times are the estimated times that the radar was pointing in the direction of the irregularity. By linear interpolation, the central axis of this irregularity at 1142:20 is shown by the dashed line in Figure 2 at  $61.5^\circ$  when the scatter signal of Figure 4 was recorded. It thus appears that the sharp, well-defined leading edge of the scatter signal of Figure 4 is associated with the above-mentioned irregularity. However, it will be seen below that this irregularity cannot account for the whole scatter signal of Figure 4, and it appears that small-scale irregularities exist over a latitude range a few degrees northward of this particular irregularity.

*The size and shape of the scatter region estimated by ray tracing.* There is another interesting aspect to the scatter signal in Figure 4. In addition to having a continuous, minimum apparent range boundary existing from 4.8 MHz down to 2.8 MHz, the boundary is continuous around the minimum frequency, or 'nose,' at 2.8 MHz and remains continuous from 2.8 to at least 3.2 MHz at the maximum apparent range boundary. The continuity implies that this boundary is determined from a continuous region filled with small-scale irregularities. At 3.2 MHz the scatter signal has a

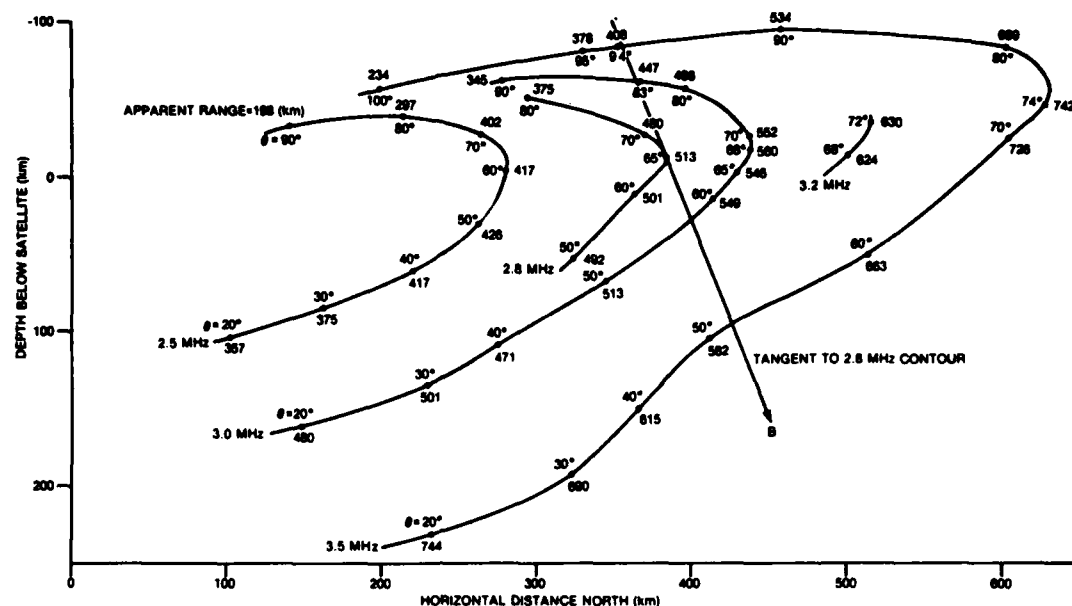


Fig. 9. The calculated location, in the vertical magnetic meridian plane, where the wave normals of ordinary wave rays from the satellite intersect the earth's magnetic field lines at  $90^\circ$ . The parameters are wave frequency and the initial angle of incidence  $\theta$  at the satellite. The apparent range to the scatter points is given along the curves. A horizontally stratified ionosphere model obtained from the ionogram traces is used.

thickness of about 250-km apparent range, and at 3.5 MHz the thickness is about 400 km. Ray tracing analysis indicates that the characteristics of the scatter signal can be explained on the basis of small-scale irregularities that extend from about the satellite height to 100 km above the satellite and to a horizontal distance of at least 300 km poleward of this boundary. Note in Figure 6b that 300 km is just about the size of the large and variable density increase between  $62^\circ$  and  $64.5^\circ$ .

It is worthwhile here to illustrate why, for north-south propagation, there is a sharp, maximum apparent range cutoff in the scatter. A simplified ionospheric model with no horizontal gradients is used for this purpose. The vertical density profile was obtained from the ISIS 1 extraordinary wave traces observed on ionograms recorded near  $59^\circ$  to  $60^\circ$  invariant latitude. Because of the complicated nature of the density contours in Figures 2 and 3, a detailed comparison should not be made between these ray tracing results and the observed scatter signal in Figure 4. More details of the ray tracing technique are given by Muldrew [1980]. The ray tracing results are shown in Figure 9. A large number of ordinary wave rays of various incident angles  $\theta$  at the satellite, where  $\theta = 0^\circ$  is vertically downward, various frequencies  $f$ , and propagating in the north-south meridian plane, were computed. Each curve in Figure 9 gives the locus, for a given frequency, of where these rays become perpendicular to the field. It is assumed that backscatter occurs at this point. Values of the parameter  $\theta$  and the apparent range are given along the curves. The apparent range for a given frequency goes through a maximum that corresponds to the maximum apparent range boundary in Figure 4. The minimum apparent range boundary is obtained

by assuming the small-scale irregularities have a sharp field-aligned boundary that is tangent to the 2.8-MHz curve in Figure 9. A plot of the expected scatter curve boundary for the model ionosphere is shown in Figure 10 by a solid line. Its agreement with that of Figure 3 is surprisingly good.

Ray tracing models that include east-west propagation indicate that the maximum apparent range boundary cannot be explained adequately by propagation that is not confined to the north-south magnetic meridian.

*Scatter from an isolated blob.* The ionograms recorded between  $61.1^\circ$  and  $67.3^\circ$  show intense spread, implying that there are small-scale irregularities throughout this whole region, consistent with the results of the preceding section; other individual scatter signatures of the type shown in Figure 4 and 5 cannot be identified because of this spread. Spread on the ionogram recorded at  $68.2^\circ$  (not shown) has decreased considerably, and an individual scatter signal can be seen in the reduced spread. The leading edge at 4.8 MHz has an apparent range of 250 km. In the following ionogram recorded at  $69.2^\circ$  (Figure 5) the leading edge of the scatter can be seen with an apparent range of 100 km at 4.8 MHz. Since the satellite moves about 140 km between the times these ionograms were recorded, the responsible irregularity is again approximately north of the satellite. Calculations indicate that the scatter in these two ionograms appears to be coming from the location of the O's in Figure 2 ( $70.4^\circ$ , 770 km and  $70.2^\circ$ , 740 km).

When the satellite was at  $70.3^\circ$ , the electrometer range of the CEP changed from the insensitive to the sensitive range. The last current scan in the insensitive range shows no density increase; a significant increase over the background should have been noticeable, had it occurred. The first



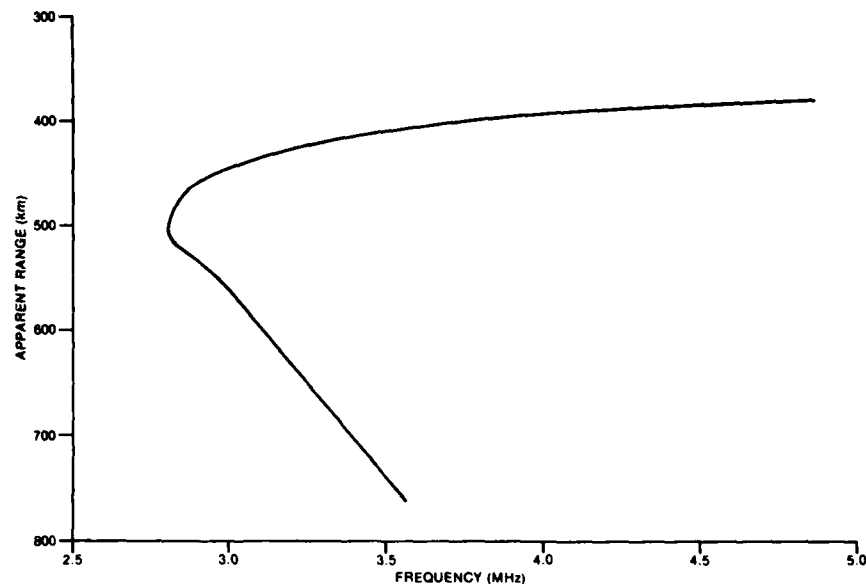


Fig. 10. Aspect-sensitive scatter boundary obtained by ray tracing. The boundary is determined by propagation confined to the north-south magnetic meridian plane.

current scan, the sensitive range shows a slight density increase of about 20% over the following few scans. The satellite travels about  $0.13^\circ$  per scan. The smallness of this density increase at the latitude at which backscatter is occurring might result from the satellite passing underneath the irregularity (see irregularity at  $70.1^\circ$ , 750 km in Figure 3). As discussed above, the scatter comes from above the satellite. The satellite data thus give supportive evidence, albeit speculative, that irregularities (of the type shown at  $70.1^\circ$ , 750 km in Figure 3) exist, having extremely large field-aligned density gradients. A consideration of radar errors relative to observed density values associated with the irregularity in Figure 3 indicate that the perturbation is probably real. Under normal conditions an irregularity with a field-aligned gradient of this magnitude would be expected to diffuse away in about a minute or less. Note that the irregularity at  $70.1^\circ$  and 750 km height in Figure 3 was apparently still present 13 min earlier at  $71.5^\circ$  and 720 km height in Figure 2.

The possibility that the scatter irregularity observed with the sounder is the east-west extension of the irregularity at  $70.1^\circ$ , 750 km in Figure 3 will now be considered. The central axis of the irregularity near 720 km height and  $71.5^\circ$  in Figure 2 has apparently drifted to  $70.1^\circ$  in Figure 3. When the satellite is near these latitudes, the irregularity axis (aligned with the magnetic field) should be located near the dashed line in Figure 2 ( $71.0^\circ$ ). The scatter region observed by the satellite thus appears to be about 80 km south of the central axis of the irregularity if the irregularity is aligned exactly in the east-west direction; the irregularity must also extend at least 350 km west of the radar scan. The 80-km north-south displacement is probably a bit too large to be explained by measurement errors and may indicate that two different irregularities are involved, the irregularity is not exactly east-west aligned, or the small-scale structure responsible

for the scatter starts south of the central axis of the irregularity. In any case, the tracelike appearance, or the thinness, of the scatter signal indicates that it comes from a relatively thin, isolated structure similar to the above-mentioned one of Figure 3.

*Possible source mechanisms for intermediate- and small-scale structure.* The possibility that the small-scale structure observed at satellite altitudes was generated by the gradient-drift instability will now be considered. The gradient-drift instability could operate on the dense blobs observed at lower altitudes, and the small-scale structure generated could be mapped upward to the satellite height. Farley [1959] considered mapping perpendicular electric fields from the E region to the F region and found that scale sizes greater than about 1 km were required. Above the height of the F layer peak, the parallel conductivity is much greater and the perpendicular Pedersen conductivity is much less than near the E layer. Using (3) and (9) of Farley [1959] and reasonable ionospheric parameters, it can be shown that an electric field, or an ionization irregularity with a scale size greater than a few tens of meters, can be mapped from the height of the F layer peak to the satellite height. In fact, field-aligned irregularities of about a 100-m scale size have been observed at high latitudes extending several hundreds of kilometers above the height of the F layer peak [Muldrew and Hagg, 1969].

The small-scale (30–60 m wavelength) irregularities responsible for the scattering observed by the satellite have lifetimes of about 1 min [Vickrey and Kelley, 1982]. Therefore, since they can only drift about 10 km in their lifetime but are observed throughout a wide latitude range, they must be generated by some instability over most of this latitude range. If mapping and the gradient-drift instability are the source of this structuring, then either (a) the blob structure at the F peak from  $63^\circ$  to  $66^\circ$  in Figure 2 has not been

completely resolved by the radar, i.e., there are many more places than appear in the figure where the density gradient has the correct sign for instability, or (b) there is a zonal gradient in density that is unstable. If the gradient-drift instability is not the source of this structuring, then some as yet unidentified instability is involved.

### 5. SUMMARY

A comparison of ISIS sounder and CEP data with Chatanika radar data has led to several conclusions about nighttime auroral ionization.

Enhancements, or valleys of ionization, that extend over a few hundred kilometers in the north-south direction also extend at least a few hundred kilometers in the east-west direction. These large enhancements consist of a collection of large-scale (several tens of kilometers) blobs existing from near the peak of the *F* layer to about 600-km height, with the density remaining high above the blobs. In a particular case, and probably in general, one or more blobs were observed forming in the bottomside *F* region on the poleward side of the auroral zone, owing to a kiloelectron volt precipitation event. The event had an east-west extent of at least 300 km. With time, this (these) blob(s) would convect equatorward and expand upward along the magnetic field.

Isolated blobs can exist near 700-km height and have extremely large field-aligned density gradients as well as large cross-field gradients. These can exist for at least 13 min, even though simple field-aligned diffusion yields a lifetime of less than 1 min. There are also less noticeable features in the radar data (called ionization 'spikes') that have about the same north-south dimensions as the isolated blobs but only have a density increase of about a factor of 2. These spikes are probably real because they are also observed in the CEP data. Individual spikes do not appear to be continuous over a few hundred kilometers in the east-west direction. One isolated spike observed in the CEP data had 5-km structure with about a 20% variation in density and 200-m structure with a few percent variation in density throughout its whole extent. This structure was not observed away from the spike. Presumably, this structure is due to large density gradients in the spike. If the gradient-drift instability is responsible, convection of this medium-scale structure could be occurring.

Intense medium-scale irregularities (~1 km), which cause telemetry dropouts, apparently exist between the satellite and telemetry station in the region where large-scale blobs in the topside *F* region are observed by the radar. These medium-scale irregularities are probably generated by instabilities on the blob edges. However, they could convect throughout the enhanced region from the unstable zones.

The minimum apparent range boundary of the sounder backscatter signal in Figure 4 implies the existence of a sharp irregularity boundary that is probably *L* shell aligned. Poleward of this boundary there exist 30–60 m irregularities. These small-scale irregularities exist throughout the 300-km or more north-south region above the blobs located in the

topside *F* region of Figure 2. This is a region of enhanced and variable electron density. Backscatter by 30–60 m irregularities can also occur for isolated ionization irregularities. If the gradient-drift instability is the source of small-scale irregularities at the satellite height, then either the irregularities are generated at lower heights and mapped along the field or zonal gradients are responsible; if not, then some other unidentified instability is involved.

**Acknowledgment.** We are grateful to L. H. Brace for his assistance in interpreting the ISIS 1 CEP data used in this paper. The work at SRI was supported by the Defense Nuclear Agency under contract DNA001-82-C-0021 and by the Air Force Office of Scientific Research under contract F49620-80-C-0014.

The editor thanks C. W. Carlson and M. C. Kelley for their assistance in evaluating this paper.

### REFERENCES

- Booker, H. G., A theory of scattering by nonisotropic irregularities with application to radar reflections from the aurora, *J. Atmos. Terr. Phys.*, **8**, 204, 1956.
- Calvert, W., and C. W. Schmid, Spread *F* observations by the Alouette topside sounder satellite, *J. Geophys. Res.*, **69**, 1839, 1964.
- Farley, D. T., Jr., A theory of electrostatic fields in a horizontally stratified ionosphere subject to a vertical magnetic field, *J. Geophys. Res.*, **64**, 1225, 1959.
- Findlay, J. A., and L. H. Brace, Cylindrical electrostatic probes employed on Alouette 2 and Explorer 31 satellites, *Proc. IEEE*, **57**, 1054, 1969.
- Frank, L. A., and K. L. Ackerson, Observations of charged particle precipitation into the auroral zone, *J. Geophys. Res.*, **76**, 3612, 1971.
- Frank L. A., and K. L. Ackerson, Local-time survey of plasma at low altitudes over the auroral zones, *J. Geophys. Res.*, **77**, 4116, 1972.
- James, H. G., Whistler-mode hiss at low and medium frequencies in the dayside-cusp ionosphere, *J. Geophys. Res.*, **78**, 4578, 1973.
- Jones, R. A., and M. H. Rees, Time-dependent studies of the aurora. I. Ion density and composition, *Planet. Space Sci.*, **21**, 537, 1973.
- Kelley, M. C., J. F. Vickrey, C. W. Carlson, and R. Tobert, On the origin and spatial extent of high-latitude *F* region irregularities, *J. Geophys. Res.*, **87**, 4469, 1982.
- Muldrew, D. B., Characteristics of ionospheric bubbles determined from aspect sensitive scatter spread *F* observed with Alouette I, *J. Geophys. Res.*, **85**, 2115, 1980.
- Muldrew, D. B., and E. L. Hagg, Properties of high-latitude ionospheric ducts deduced from Alouette II two-hop echoes, *Proc. IEEE*, **57**, 1128, 1969.
- Petrie, L. E., Topside spread echoes, *Can. J. Phys.*, **41**, 194, 1963.
- Tsunoda, R. T., and J. F. Vickrey, Evidence of east-west structure in large-scale auroral *F* region ionization enhancements, submitted to *Geophys. Res. Lett.*, 1982.
- Vickrey, J. F., and M. C. Kelley, The effects of a conducting *E* layer on classical *F* region cross-field plasma diffusion, *J. Geophys. Res.*, **87**, 4461, 1982.
- Vickrey J. F., C. L. Rino, and T. A. Potemra, Chatanika/TRIAD observations of unstable ionization enhancements in the auroral *F* region, *Geophys. Res. Lett.*, **7**, 789, 1980.
- Whitaker, J. H., The transient response of the ionosphere to precipitation, *Planet. Space Sci.*, **25**, 773, 1977.

(Received March 5, 1982;

revised May 9, 1982;

accepted May 14, 1982.)

## Recent results in auroral-zone scintillation studies

C. L. RINO and J. F. VICKREY

Radio Physics Laboratory, SRI International, Menlo Park, CA 94025, U.S.A.

(Received in final form 17 May 1982)

**Abstract**—Nighttime data from the Defense Nuclear Agency's Wideband satellite have consistently shown a pronounced scintillation enhancement at the point where the propagation vector lies within the local  $L$ -shell. Simultaneous observations at two well-separated stations and spaced-receiver measurements have shown that this feature is caused by a latitudinally narrow, unstable  $F$ -region ionization enhancement that produces sheet-like intermediate-scale structures. A more detailed characterization of the source region has been derived from simultaneous measurements from the TRIAD satellite and the Chatanika radar.

The source region is typically convecting southward, whereby the poleward gradient at its southern boundary is stable to the gradient-drift instability. Thus, OSSAKOW and CHATURVEDI (1979) postulated the current-convective instability as a source mechanism. Birkeland currents, when sufficiently intense, can destabilize a region that is otherwise stable to the gradient-drift instability.

The sheet-like anisotropy of the irregularities is perhaps the most intriguing feature of the instability. Two mechanisms have been postulated to explain it. This paper reviews the development and current status of our understanding of this recently discovered high-latitude instability.

### 1. INTRODUCTION

Scintillation effects are commonly observed on auroral-zone transionospheric VHF and UHF satellite signals (AARONS *et al.*, 1969; AARONS and ALLEN, 1971; BASU and AARONS, 1980). Moreover, electron density irregularities of the type that cause such scintillation effects have been measured *in situ* (CLARK and RAITT, 1976; PHELPS and SAGALYN, 1976; KERSLEY *et al.*, 1980; KELLEY *et al.*, 1980). Detailed studies of the associations of high-latitude scintillation with energetic particle precipitation, substorms, and other phenomena have also been made (BASU, 1974; AARONS, 1976; MARTIN and AARONS, 1977; BUCHAU *et al.*, 1978; WEBER and BUCHAU, 1980).

Over the past few years, however, a prominent auroral-zone scintillation feature has attracted considerable interest in the ionospheric research community. In nighttime scintillation data from low-altitude, polar-orbiting satellites, a narrow burst of amplitude and phase scintillation is commonly observed at the point where the propagation vector lies within the plane of the local  $L$ -shell. Several examples are shown in Fig. 1, which is taken from FREMOUW *et al.* (1977). The plots are processed VHF amplitude and phase records from midnight-sector Wideband satellite passes recorded at Poker Flat, Alaska (65.6° invariant latitude, 140°3' west longitude).

To characterize quantitatively the scintillation pattern, the intensity and phase scintillation indices

$$S_4 = [\langle I^2 \rangle - \langle I \rangle^2]^{1/2} / \langle I \rangle, \quad (1)$$

and

$$\sigma_\phi = [\langle \delta\phi^2 \rangle - \langle \delta\phi \rangle^2]^{1/2}, \quad (2)$$

respectively, are used. Computations of  $S_4$  and  $\sigma_\phi$  over consecutive 20-s data intervals for a Wideband satellite pass containing a well-defined scintillation enhancement are shown in Fig. 2. The Briggs-Parkin (BP) angle is the angle between the propagation vector and the local magnetic field vector. The dip latitude,  $\psi_d$ , is computed from the magnetic dip angle,  $\psi$ , by using the formula

$$\psi_d = \tan^{-1} (0.5 \tan \psi). \quad (3)$$

For our purposes here, the small difference between dip and invariant latitudes is not important.

The nighttime Wideband satellite passes progress from north to south nearly parallel to the magnetic meridian. Thus, the minimum BP angle, where the main peak of the scintillation enhancement occurs, is close to the point where the propagation vector lies within an  $L$ -shell. Scintillation enhancements of this type were observed in nearly 40% of the nighttime Wideband passes recorded at Poker Flat while the satellite was operational between May 1976 and August 1979.

The propagation of radio waves through highly anisotropic irregularities is such that the scintillation is greatly enhanced whenever the propagation path coincides with an axis or plane of irregularity elongation (SINGLETON, 1973; RINO and FREMOUW, 1977). Thus, if the ionospheric irregularities in the auroral zone are elongated transverse to the magnetic

field along the direction of the local  $L$ -shell, scintillation enhancements such as those shown in Figs 1 and 2 can be explained, although it should be noted that a highly localized source region could produce a similar effect. The available evidence, however, firmly supports the geometric hypothesis. Moreover, through combined incoherent scatter radar and scintillation measurements, we have learned considerably more about the structure and dynamics of the source region.

Rapid progress is being made in understanding the physics of the convective instabilities that are believed to cause the electron density irregularities. Much of our current understanding is based on the striking parallels between equatorial spread- $F$  phenomena and the instability processes thought to produce scintillation at high latitudes. This paper reviews our present understanding of this high-latitude scintillation phenomenon. The experimental results that defined the source region are reviewed in Section 2. Section 3 reviews the theories that have been put forth to explain the occurrence and structure of the instability. The results are discussed in Section 4, together with recent hypotheses about the general features of high-latitude irregularities that have resulted from these studies.

Most of the material was presented in an invited review talk at the XXth URSI General Assembly held in Washington, D.C., 10–19 August 1981. We have taken this opportunity, however, to add some new material not published previously.

## 2. EXPERIMENTAL RESULTS

The regularity of the scintillation pattern associated with the Wideband high-latitude instability is its most striking feature. This is illustrated in Fig. 3, which is taken from RINO and MATTHEWS (1980). The amplitude and phase scintillation levels that exceeded 50% of the time in the nighttime Wideband satellite passes recorded at Poker Flat are shown for two consecutive one-year observation periods. The scintillation peak at 64° dip latitude is attributed to a geometrical enhancement, as discussed in Section 1.

MARTIN and AARONS (1977) evidently first postulated  $L$ -shell aligned, sheet-like irregularities to explain a systematic enhancement of ATS-3 VHF scintillation as observed from several auroral-zone stations. RINO *et al.* (1978) analyzed Wideband satellite spaced-receiver measurements and verified that the anisotropy of the diffraction pattern was in agreement with theoretical predictions that assume  $L$ -shell aligned sheets.

An example of such spaced-receiver data is illustrated in Fig. 4, which shows the predicted and measured axial ratio and orientation angle of the

spatial correlation ellipse that characterizes the anisotropy of the diffraction pattern. The anisotropy of the *in-situ* irregularities is characterized by two elongation factors (denoted  $a$  and  $b$ , respectively) that quantify the spatial coherence along and transverse to the magnetic field relative to the minimum cross-field value. The 10:10:1 anisotropy for this particular pass is extreme, however; 8:5:1 is more nearly typical. The orientation angle is measured from true north (RINO and LIVINGSTON, 1982). At the point where the scintillation enhancement peaks, the diffraction pattern has a high degree of coherence in the east–west direction.

Wideband satellite data recorded in other longitude sectors also show a prominent peak in the latitudinal pattern of nighttime scintillation activity (FREMOUW, 1981; BASU *et al.*, 1982). For the most part, daytime data show only an enhancement for propagation paths very near the magnetic zenith. Since the daytime auroral oval is generally north of the observing stations, however, the full latitudinal extent of the sheet-like irregularities may not be completely sampled. Indeed, more recent data analyzed by BASU *et al.* (private communication) have shown daytime enhancements that could be caused by sheet-like structures.

Figure 5 shows a breakdown by local magnetic activity of the data in Fig. 3. The geometrical enhancement disappears for the lowest activity levels ( $K \leq 1$ ) even though scintillation activity is present where the enhancement should occur. This suggests either that the source region of the sheet-like irregularities lies poleward of the Poker Flat station when magnetic activity is very low or that the degree of anisotropy is dependent on magnetic activity.

To confirm that the observed scintillation enhancements are caused mainly by a geometrical effect, simultaneous Wideband satellite scintillation measurements were made during November 1977 from Poker Flat and from Fort Yukon, Alaska, which is ~200 km north of Poker Flat. Displaced scintillation enhancements as predicted by the theoretical computations shown in Fig. 6 were expected. The observing period was magnetically quiet, however, and the pattern shown in Fig. 7 was more commonly observed. The expected enhancement was observed only at the Fort Yukon station. Thus, the sheet-like structures are not evenly distributed throughout the oval band of high-latitude irregularities (SAGALYN and SMIDDY, 1974).

Figure 8 shows the variation of total electron content (TEC) corresponding to the Fort Yukon data in Fig. 7. The TEC enhancement coincident with the main scintillation enhancement clearly suggests a latitudinally narrow source region. Indeed, through a painstaking modeling procedure, RINO and OWEN

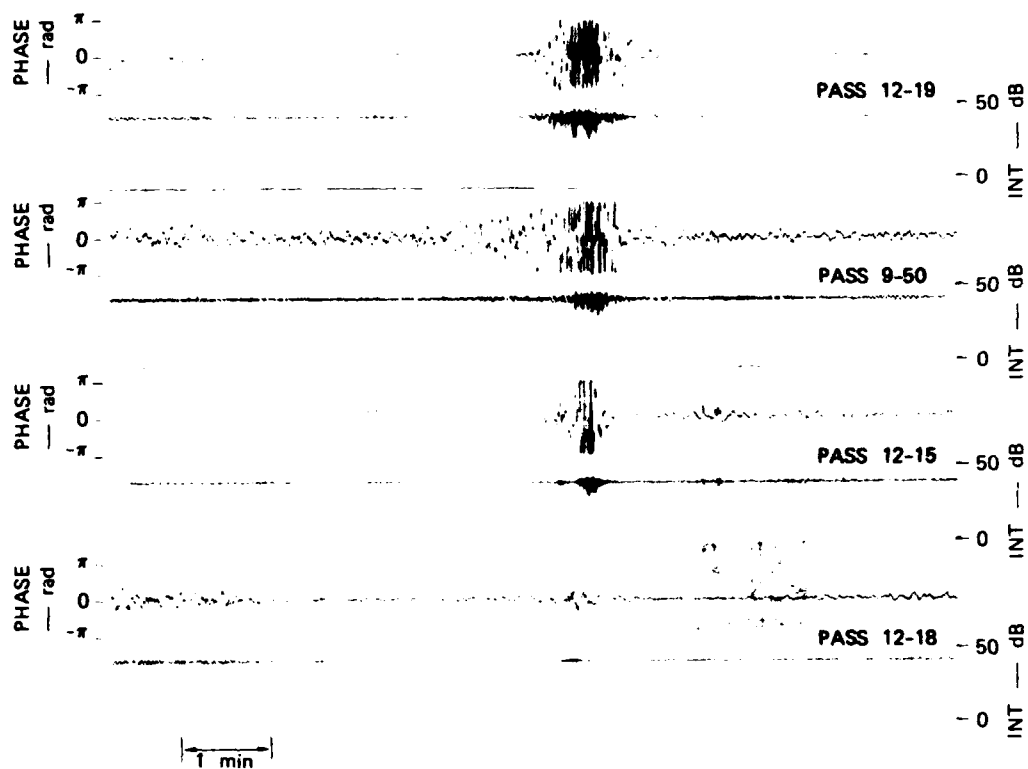


Fig. 1. Examples of localized scintillation enhancement in nighttime Wideband satellite passes (taken from FREMOUW *et al.*, 1977).

**BLANK PAGE**

AD-A128 612

LATITUDINAL VARIATIONS OF AURORAL-ZONE IONIZATION  
DISTRIBUTION(U) SRI INTERNATIONAL MENLO PARK CA  
J F VICKREY ET AL. FEB 83 AFOSR-TR-83-0389

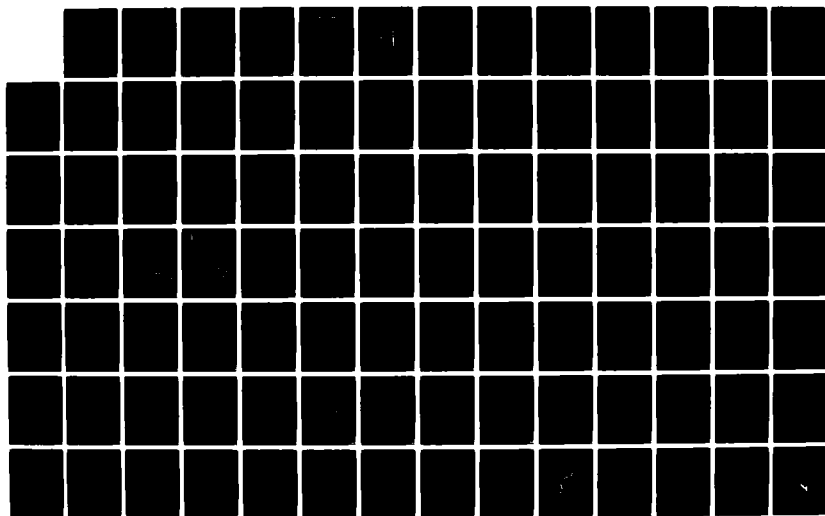
2/3

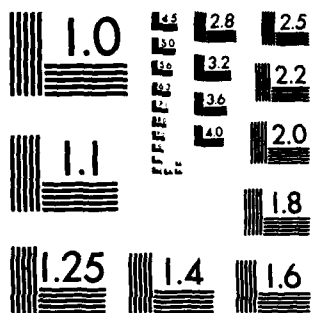
UNCLASSIFIED

F49620-80-C-0014

F/G 4/1

NL





MICROCOPY RESOLUTION TEST CHART  
NATIONAL BUREAU OF STANDARDS-1963-A



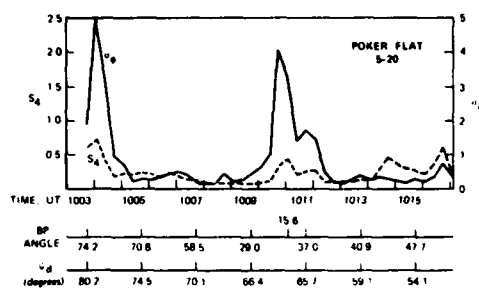


Fig. 2. Amplitude and phase scintillation summary parameters for a typical nighttime enhancement.

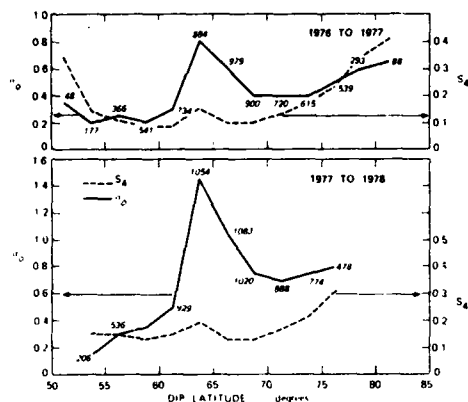


Fig. 3. Fifty-percent amplitude and phase exceedance level for two consecutive years of Poker Flat data (taken from RINO and MATTHEWS, 1980).

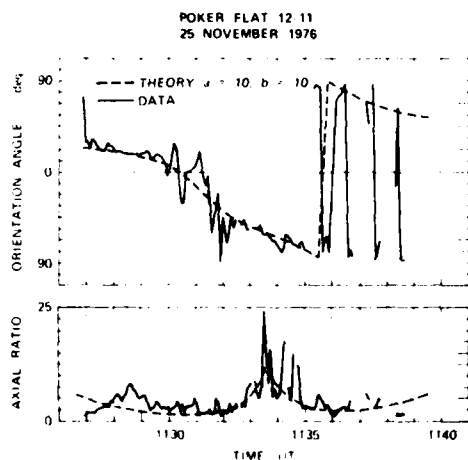


Fig. 4. Measured orientation angle and axial ratio for a wideband satellite pass showing pronounced enhancement together with theoretical prediction for 10:10:1 anisotropy (taken from RINO *et al.*, 1978).

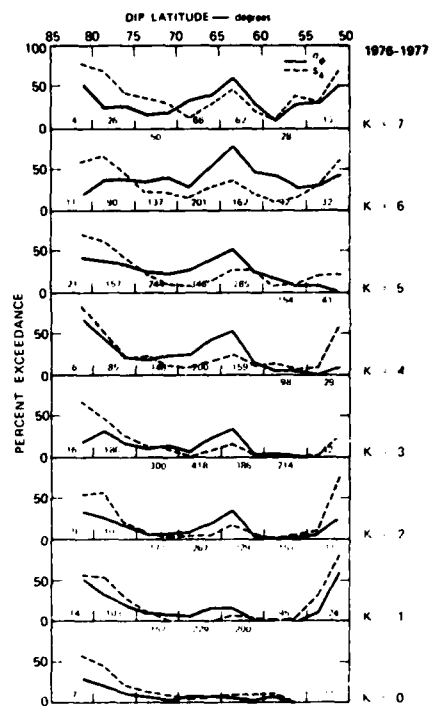


Fig. 5. Wideband satellite exceedance statistics for amplitude and phase scintillation sorted by local magnetic activity (taken from RINO and MATTHEWS, 1980).

(1980) were able to construct latitudinal ionization profiles, as shown in Fig. 9.

These results show that the source region is a latitudinally narrow enhanced *F*-layer with a steep poleward gradient on the equatorial edge. Analysis of Chatanika data indicated that there is no direct relationship between the location of the enhanced *F*-layer and the diffuse auroral *E*-layer (see VICKREY *et al.*, 1982). This is reasonable since the *F*-region features have long lifetimes and can convect independently of the *E*-region precipitation source. The middle frame in Fig. 9 shows that multiple source regions can occur as well.

FREMOUW *et al.* (1977) emphasized the close association of the local scintillation enhancements with steep TEC gradients. Model calculations demonstrate, moreover, that the TEC gradients themselves are most likely manifestations of an enhanced *F*-region. For example, an *E*-layer boundary, as shown in Fig. 9, produces a sharp TEC gradient only if it lies within  $\pm 0.5^\circ$  latitude of the observing station, whereas an enhanced *F*-region produces a sharp TEC gradient if it lies within  $\pm 2^\circ$  latitude.

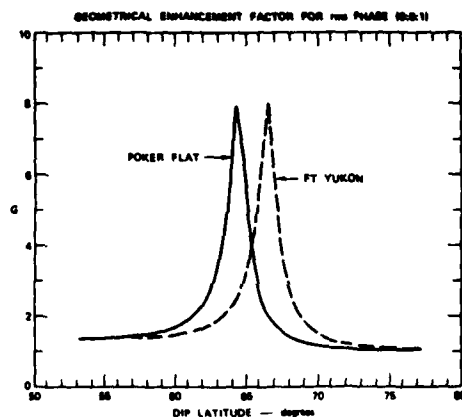


Fig. 6. Theoretical prediction of the displacement of the geometrical enhancement as observed at Poker Flat and Fort Yukon, Alaska (taken from RINO and OWEN, 1980).

Figure 10 shows the variation of the 3-month average TEC gradient (present in ~40% of the nighttime passes recorded at Poker Flat) with increasing solar-cycle activity. The average maximum nighttime *F*-region peak density as measured by the nearby Chatanika radar is also plotted to emphasize the control of the *F*-region density on this particular scintillation phenomenon. As shown in the figure, both the absolute electron density and the latitudinal density gradients increase with increasing solar activity. It is not surprising, then, that scintillation activity increases dramatically at polar latitudes during the peak of the solar cycle (AARONS *et al.*, 1981).

During February 1980, a series of combined scintillation and incoherent scatter radar observations were made using the TRIAD satellite as a signal source (VICKREY *et al.*, 1980). The TRIAD satellite is in a 90°

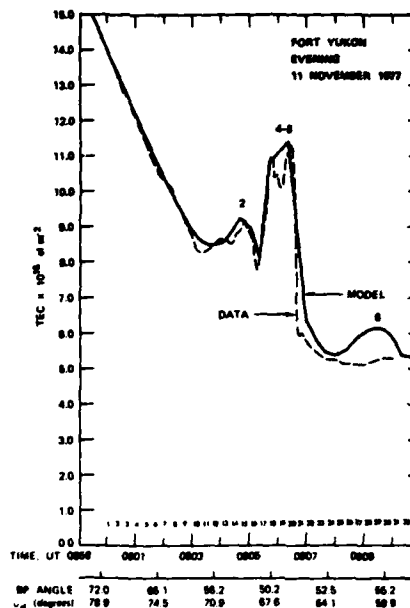


Fig. 8. Total electron content variation showing evidence of localized enhancement (taken from RINO and OWEN, 1980).

inclination circular orbit, so that the high-elevation passes at Poker Flat follow the geographic meridian. Thus, the geometric enhancement due to *L*-shell aligned sheets occurs at a different magnetic latitude from where it occurred in the Wideband satellite data.

Figure 11 shows a TRIAD satellite pass with three distinct scintillation enhancements labeled A, B, and C from north to south. The peak of the central enhancement corresponds to the point of coincidence of the line of sight with the plane of the local *L*-shell. By using the nearby Chatanika radar to measure electron

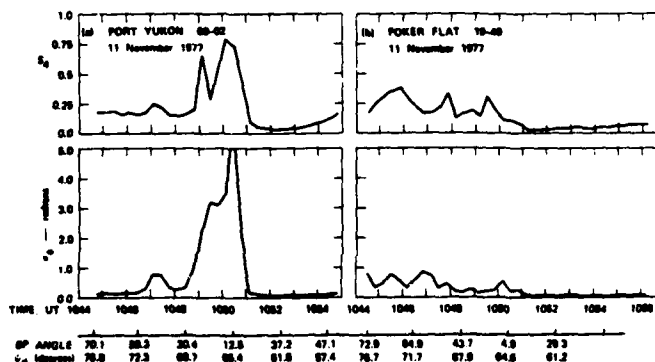


Fig. 7. Typical scintillation enhancement occurrence pattern during a magnetically quiet period (taken from RINO and OWEN, 1980).

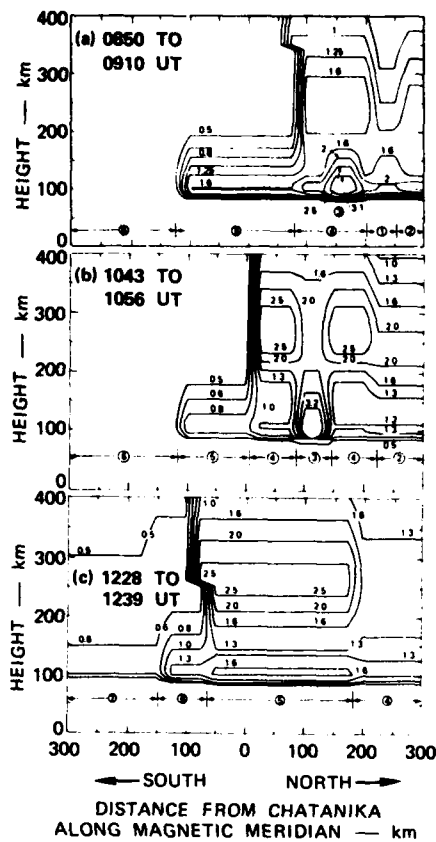


Fig. 9. Reconstructed meridional density profiles of  $F$ -region electron density. Model electron density profiles did not vary within the numbered regions.

density profiles in the magnetic meridian, VICKREY *et al.* (1980) were able to reconstruct electron density contours as shown in Fig. 12, which corresponds to the TRIAD pass summarized in Fig. 11. The vertical dimension is height in a coordinate system with vertical magnetic field lines.

By compensating for the measured southward plasma drift, VICKREY *et al.* (1980) were able to associate the enhanced  $F$ -region features marked (1) and (2) in Fig. 12 with the scintillation enhancements B and C in Fig. 11. The geometry of the experiment is shown in Fig. 13. The radar data clearly reveal the large-scale structure of the  $F$ -region enhancements, in particular, the alternating poleward and equatorward gradients that were not detected in TEC reconstructions.

The incoherent-scatter radar data can also be used to measure electron and ion temperatures. VICKREY (1981) noted that the ion temperature showed little change within and outside the  $F$ -region enhancement,

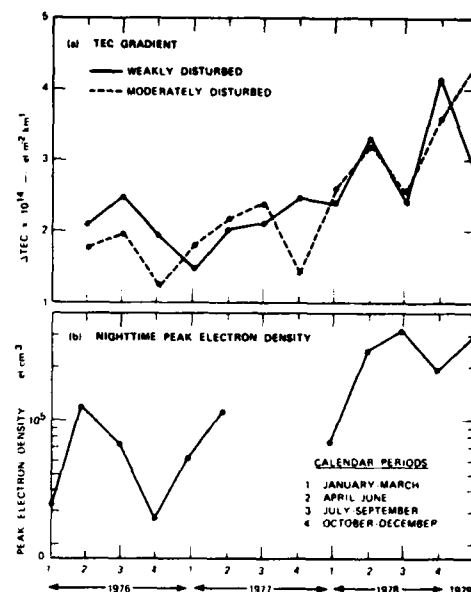


Fig. 10. Temporal variation of average TEC gradient measured in nighttime Poker Flat Wideband Satellite passes over three-year period, together with peak nighttime electron density averaged over all the Chatanika radar runs for the periods indicated.

whereas the electron temperature was typically reduced within the enhanced  $F$ -region. Since the electron cooling rate is density dependent, VICKREY *et al.* (1982) concluded that the enhancement was not locally produced and that convection is an important factor in the scintillation morphology. This is discussed in more detail in Section 4.

### 3. THEORY

A convecting plasma enhancement is a natural candidate for the  $E \times B$  gradient-drift instability, which is known to be the dominant mechanism for structuring ionospheric barium clouds. [The reader is referred to the review papers by OSSAKOW (1979) and FEJER and KELLEY (1980) for background material and references.] However, a poleward density gradient, as shown in Fig. 9, in the presence of a westward electric field (equatorward convection) is a stable configuration. These measurements led OSSAKOW and CHATURVEDI (1979) to consider the role of strong field-aligned currents that can destabilize an otherwise stable  $E \times B$  configuration, and they proposed the current convective instability to explain the presence of irregularities that can cause the observed scintillation enhancement.

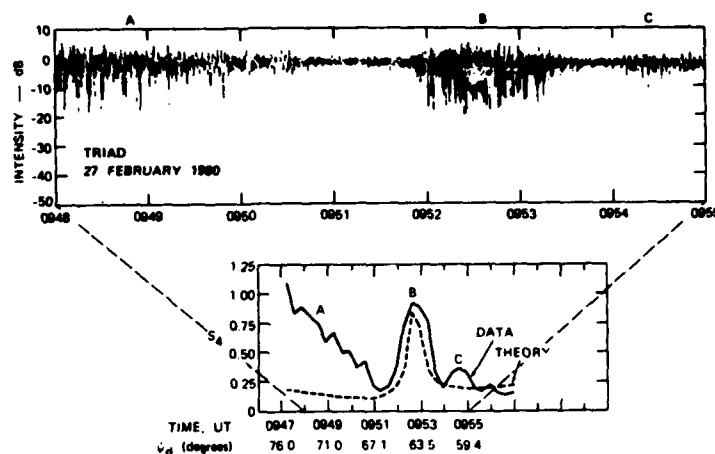


Fig. 11. Plot of TRIAD signal intensity measured at Poker Flat, Alaska, together with the  $S_4$  index and a prediction of the geometrical scintillation enhancement.

The current convective instability is an attractive mechanism for high latitude instabilities because intense field-aligned currents are known to occur throughout the auroral zone. Instability develops because of a parallel polarization field component sustained by the parallel current flow. The linear growth rate derived by OSSAKOW and CHATURVEDI (1979) is given as

$$\gamma = \frac{-\frac{1}{L} \left[ \frac{-E_x}{B} \left( \frac{v_{in}}{\Omega_i} \right) + V_d \left( \frac{k_{||}}{k_{\perp}} \right) \right]}{\left( \frac{\Omega_i}{v_{in}} + \frac{\Omega_e}{v_{ei}} \right) k_{\perp}^2 + \frac{v_{in}}{\Omega_i} - k_{\perp}^2 \left( \frac{v_{ei}}{\Omega_e \Omega_i} \right) C_s^2 - \frac{k_{||}^2 C_s^2}{v_{in}}} \times \left[ 1 + \frac{v_{in}^2 / \Omega_i^2}{\frac{v_{ei} v_{in}}{\Omega_e \Omega_i} + \left( \frac{k_{||}}{k_{\perp}} \right)^2} \right], \quad (4)$$

where

$$L^{-1} = \frac{1}{N_0} \left( \frac{\partial N_0}{\partial y} \right),$$

$$V_d = \frac{J_{||}}{N_0 q_e},$$

$C_s$  = ion acoustic speed,

$v_{in}$  = ion-neutral collision frequency,

$v_{ei}$  = electron-ion collision frequency,

$\Omega_{e,i}$  = electron, ion gyro frequency,

$B$  = magnetic field strength (T),

$E_x$  = eastward electric field.

The field-aligned currents cause a weak shear in the magnetic field that can act to damp the instability. HUBA and OSSAKOW (1980) have analyzed this effect and found that the reduction in growth rates is not significant, but the unstable modes are localized in the gradient direction. CHATURVEDI and OSSAKOW (1981) have also analyzed ion inertial and collisional effects, which become important at altitudes other than the  $F$ -layer peak. In all cases, the current convective instability is a viable high-latitude intermediate-scale structure-producing mechanism provided that the field-aligned currents are strong enough.

The sheet-like anisotropy, however, is the most distinctive feature of the irregularity structure. Thus, a viable theory of irregularity production must account for enhanced growth of spatial modes parallel to the initial gradient. The onset of  $E \times B$  instability invariably favors the modes orthogonal rather than parallel to the initial gradient. When viewed along the magnetic field, barium clouds, for example, develop orthogonal finger-like striations oriented parallel to the initial gradient.

CHATURVEDI and OSSAKOW (1979) proposed a mechanism whereby growth could favor the modes oriented parallel to  $\nabla N$ . The simplest forms of the equations that govern the nonlinear evolution of a convected plasma enhancement are

$$\frac{\partial N}{\partial t} + \frac{\delta}{B} \times \nabla_{\perp} \delta \phi \cdot \nabla_{\perp} N = D \nabla_{\perp}^2 N, \quad (5)$$

and

$$\nabla(N \nabla \delta \phi) = E_0 \cdot \nabla N, \quad (6)$$

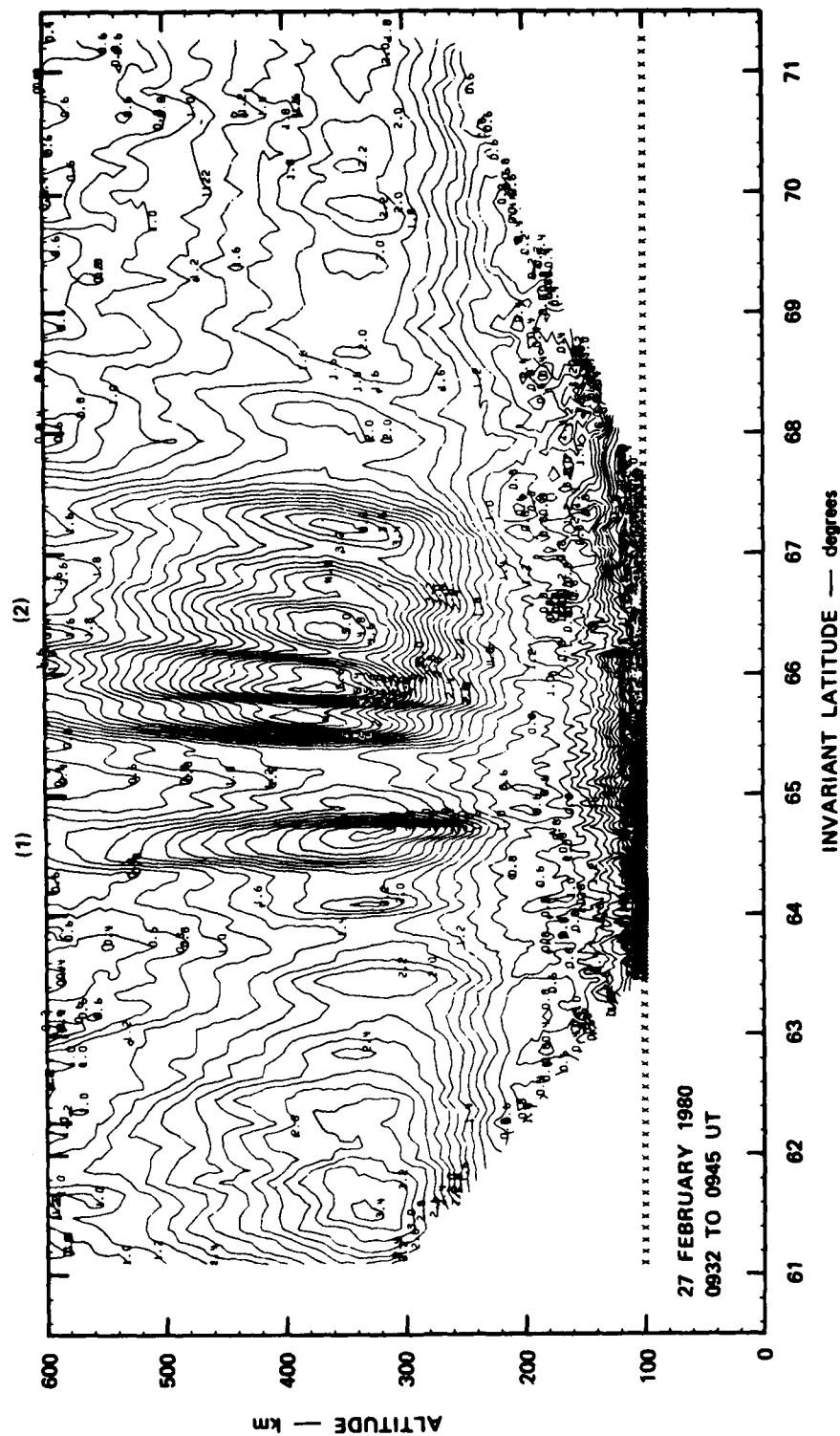


Fig. 12. Meridional electron density profile measured by the Chatanika radar prior to TRIAD pass shown in Fig. 11.

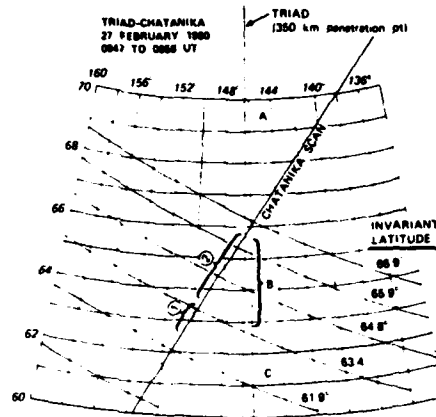


Fig. 13. Geometry of the TRIAD satellite pass and Chatanika radar scan showing the association of *F*-region features 1 and 2 from Fig. 12 and scintillation enhancements B and C from Fig. 11.

where the total electric field is

$$\mathbf{E} = \mathbf{E}_0 - \nabla \delta \phi, \quad (7)$$

and  $\hat{b}$  is a unit vector along the magnetic field. Equations (5) and (6) are written in a frame moving with the drift velocity  $\mathbf{v}_0 = \mathbf{E} \times \mathbf{B}/B^2$ . The term  $D$  is a diffusion coefficient, whose detailed form depends on the complexity of the model.

Following ROGNLIEN and WEINSTOCK (1974), CHATURVEDI and OSSAKOW (1979) linearized the potential equation (6) about a mean density configuration with gradient scale  $L$ , but retained the nonlinear term in equation (5), which dominates the neglected nonlinear term in equation (6). A coupled mode analysis was then performed on the resultant simplified equation. An initially unstable orthogonal mode couples to a parallel mode whose nonlinear growth, under appropriate conditions, can dominate the initially linear unstable mode. CHATURVEDI and OSSAKOW (1979) showed that typical auroral-zone parameters thus favor the parallel mode.

The ROGNLIEN and WEINSTOCK (1974) scheme, however, does not accommodate the dynamic evolution of the plasma configuration. Thus, although the analysis can be applied locally, it is not clear that the analysis correctly predicts the quasi-stationary saturated state of the instability. Numerical simulations are a powerful tool for resolving such questions. KESKINEN *et al.* (1980) performed a simulation of the current instability acting on an otherwise  $\mathbf{E} \times \mathbf{B}$  stable configuration. Although rather large field-aligned currents were assumed, their results verified the

destabilization of the poleward gradient. Moreover, the simulations showed local development of parallel modes as predicted by CHATURVEDI and OSSAKOW's (1979) analysis. The dominant structure variation, however, was east-west, and the simulation retained the main characteristics familiar in barium-cloud simulations.

In the Chatanika-TRIAD experiment discussed in Section 2, VICKREY *et al.* (1980) were able to estimate the field-aligned currents associated with the scintillation event shown in Fig. 11. They showed that the parallel currents ( $\sim 1 \mu\text{A m}^{-2}$ ) were not sufficient to destabilize the poleward gradient in the presence of the measured  $10 \text{ mV m}^{-1}$  westward electric field. The equatorward gradient, however, was highly unstable to the ordinary  $\mathbf{E} \times \mathbf{B}$  instability. Thus, in light of the increased complexity of the enhanced *F*-region structure, a purely current-driven convective instability is not necessary, at least at those latitudes.

This motivated KESKINEN and OSSAKOW (1982) to run a second simulation with a two-sided initial plasma configuration that more closely represented the meridional density profile measured by VICKREY *et al.* (1980). The most recent simulations also included a northward electric field component as well as the westward component. This is reasonable for the auroral zone because the northward (in the evening sector) or the southward (the morning sector) electric field component normally is larger than the east-west component. The effect of a nonorthogonal field on the  $\mathbf{E} \times \mathbf{B}$  instability had been analyzed earlier by PERKINS and DOLES (1975), who showed that the most unstable mode (linearly) lies orthogonal to the total field. Thus, the main effect is to tilt the finger-like striations that evolve in a barium cloud and reduce the growth rate somewhat.

KESKINEN and OSSAKOW's (1982) results show the expected rapid development of structure on the trailing edge of the two-sided plasma enhancement and the tilt of the dominant structure. Figure 14, which is taken from KESKINEN and OSSAKOW (1982), shows the structural development after 1600 s. There is also some evidence of 'secondary' structure developing on the eastern boundaries of the plasma enhancements, which are destabilized by the northward electric field component. Indeed, the secondary structure is another possible source of the sheet-like irregularities. If the mechanism is a viable one, however, the observed strict  $L$ -shell alignment must be verified and explained.

As mentioned in the Introduction, there are striking parallels between equatorial spread-*F* generated by the gravity-driven Rayleigh-Taylor instability and the  $\mathbf{E} \times \mathbf{B}$  gradient drift instability. OSSAKOW (1979) has shown that the phenomena are mathematically similar.

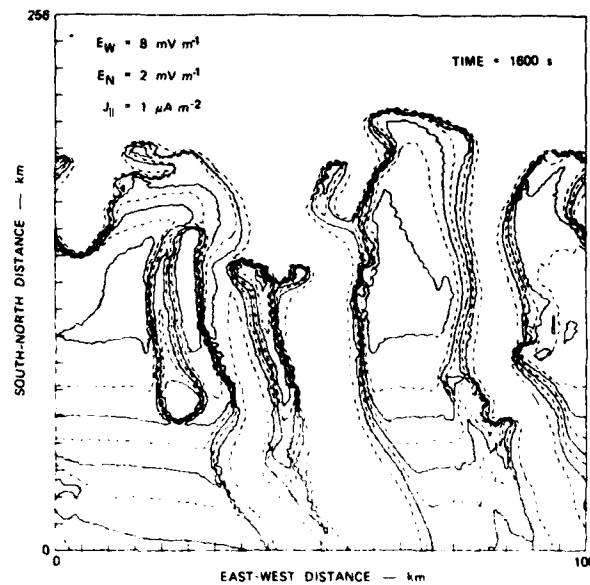


Fig. 14. Simulation of the nonlinear evolution of the Wideband high-latitude instability after 1600 s (from KESKINEN and OSSAKOW, 1982).

With regard to secondary structure, recent equatorial measurements (RINO *et al.*, 1981; SINGH *et al.*, 1981) have shown that the dominant intermediate-scale structure develops on the westward wall of the plasma depletions that are delineated by enhanced 1-m radar backscatter. TSUNODA (1981) has attributed this structure to a secondary gradient drift instability driven by an eastward neutral wind. This process is exactly analogous to the secondary structure in the auroral-zone configuration that is driven by a northward (or southward) electric field component.

Thus, although open questions remain, rapid progress is being made towards a detailed understanding of the role of convective instabilities in generating intermediate-scale structure (0.1–1 km) in general, and toward explaining the high-latitude irregularity geometry in particular.

#### 4. DISCUSSION

The experimental and theoretical results presented in this paper have mainly addressed the local characteristics of a prominent nighttime auroral-zone scintillation enhancement. KELLEY *et al.* (1982) and VICKREY and KELLEY (1982) have argued, however, that the zone of structured soft-particle precipitation at the poleward edge of the auroral oval is a likely source region for the enhanced *F*-layers that cause the scintillation features. They showed that the input (or

outer) scale associated with the main enhancement in Fig. 12 is nearly identical to the corresponding scale observed in the polar cusp by *in-situ* soft-particle detectors. They therefore postulated that the macro-scale structure is imparted by the precipitating electron flux.

VICKREY and KELLEY (1982) performed model computations to compute the lifetimes of kilometer-scale irregularities subject to classical diffusion in the presence of a conducting *E*-layer. KELLEY *et al.* (1982) applied that model to estimate the average high-latitude irregularity distribution, assuming constant generation of large-scale irregularities at the equatorward boundary of the polar cap and a realistic average convection pattern. Their model reproduced many of the known morphological features of high-latitude irregularities.

For example, the model showed a reduction of irregularity intensity in the central polar cap. The degree of reduction of irregularity intensity observed in the polar cap, however, is much less than that expected by classical diffusion. Therefore, intermediate-scale irregularities must be continuously generated by instabilities operating on the edges of the precipitation-produced large-scale features as they convect across the polar cap. The model further shows that it is the convection boundary that defines the equatorward extent of high-latitude irregularities, which explains why the scintillation boundary is not always collocated

with the more readily defined auroral boundaries, such as the diffuse auroral precipitation boundary or the plasmopause. Their model is only a first attempt, however, and certainly can be improved by: (1) more accurately specifying the source region of large-scale irregularities, including polar cap *F*-layer arcs; (2) accommodating varying convection patterns that are known to be dependent on parameters such as the interplanetary magnetic field; and (3) taking into account the effects of anomalous (turbulent) cross-field diffusion in the *F*-region.

Thus, although the detailed morphology of high-latitude irregularities cannot yet be predicted from first principles, it seems clear that soft- ( $< 1$  keV) particle precipitation, convective plasma instabilities, *E*-layer conductivity, and the high-latitude convection pattern must play important roles in controlling that morphology. The associated scintillation enhancements observed by the Wideband satellite have been prominent in nighttime auroral-zone scintillation data recorded throughout the current solar cycle. The

intensity of the scintillation has increased dramatically through the peak of the current solar cycle, however, the background electron density is also an important factor.

In summary, combined measurements of high-latitude radio wave scintillation and large-scale ionospheric structure using the Chatanika incoherent-scatter radar have provided a detailed characterization of an *F*-region irregularity source. These experimental results have stimulated theoretical activity to examine the role of field-aligned currents in convective instability processes and how these instabilities might ultimately result in plasma density irregularities which have sheet-like anisotropy. Finally, this experimental work has stimulated analysis of the roles of particle precipitation, convection, and the highly conducting auroral *E*-layer in determining the morphology of high-latitude scintillation.

*Acknowledgement*—The authors' work was supported by the Defense Nuclear Agency under Contract DNA-001-81-C-0076.

## REFERENCES

- |  |      |   |
|--|------|---|
| AARONS J.  | 1976 | <i>J. geophys. Res.</i> <b>81</b> , 661.  |
| AARONS J. and ALLEN R. S.  | 1971 | <i>J. geophys. Res.</i> <b>76</b> , 170.  |
| AARONS J., MULLEN J. P. and WHITNEY H. E.  | 1969 | <i>J. geophys. Res.</i> <b>74</b> , 884.  |
| AARONS J., WHITNEY H. E. and MACKENZIE E.  | 1981 | <i>Radio Sci.</i> <b>16</b> , 939.  |
| BASU S.  | 1974 | <i>J. geophys. Res.</i> <b>79</b> , 3155.   |
| BASU S. and AARONS J.  | 1980 | <i>Radio Sci.</i> <b>15</b> , 59.   |
| BUCHAU J., AARONS J., MULLEN J. P.,<br>WEBER E. J., WHALEN J. A., WHITNEY H. E.<br>and CRAMPTON E. E., JR. | 1978 | <i>Effect of the Ionosphere on Space and Terrestrial Systems</i><br>(Edited by J. M. GOODMAN). Ionosphere Effects<br>Symposium. |
| CHATURVEDI P. K. and OSSAKOW S. L.   | 1981 | <i>J. geophys. Res.</i> <b>86</b> , 4811.   |
| CLARK D. H. and RAITT W. J.  | 1976 | <i>J. atmos. terr. Phys.</i> <b>38</b> , 1245.  |
| FEJER B. G. and KELLEY M. C.   | 1980 | <i>Rev. Geophys.</i> <b>18</b> , 401.   |
| FREMOUW E. J.  | 1981 | <i>J. atmos. terr. Phys.</i> <b>42</b> , 775.   |
| FREMOUW E. J., RINO C. L., LIVINGSTON R. C.<br>and COUSINS M. C.   | 1977 | <i>Geophys. Res. Lett.</i> <b>4</b> , 539.  |
| HUBA J. D. and OSSAKOW S. L.   | 1980 | <i>J. geophys. Res.</i> <b>85</b> , 6874.   |
| KELLEY M. C., VICKREY J. F., CARLSON C. W.<br>and TORBERT R.   | 1982 | <i>J. geophys. Res.</i> <b>87</b> , 4469.   |
| KELLEY M. C., BAKER K. D., RINO C. L.,<br>ULWICK J. C. and BARON M. J.                                     | 1980 | <i>Radio Sci.</i> <b>15</b> , 491.  |
| KERSLEY L., AARONS J. and KLOBOUCHAR J. A.   | 1980 | <i>J. geophys. Res.</i> <b>85</b> , 4214.   |
| KESKINEN M. J. and OSSAKOW S. L.   | 1982 | <i>J. geophys. Res.</i> <b>87</b> , 144.  |
| KESKINEN M. J., OSSAKOW S. L. and<br>MCDONALD B. E.  | 1980 | <i>Geophys. Res. Lett.</i> <b>7</b> , 573.  |
| MARTIN E. and AARONS J.  | 1977 | <i>J. geophys. Res.</i> <b>82</b> , 2717.   |
| OSSAKOW S. L.  | 1979 | <i>Rev. Geophys. Space</i> <b>17</b> , 521.   |
| OSSAKOW S. L. and CHATURVEDI P. K.   | 1979 | <i>Geophys. Res. Lett.</i> <b>6</b> , 322.  |
| PERKINS F. W. and DOLES J. H., III   | 1975 | <i>J. geophys. Res.</i> <b>80</b> , 211.  |
| PHILIPS A. D. R. and SAGALYN R. C.   | 1976 | <i>J. geophys. Res.</i> <b>81</b> , 515.  |
| RINO C. L. and MATTHEWS S. J.  | 1980 | <i>J. geophys. Res.</i> <b>85</b> , 4139.   |
| RINO C. L. and OWEN J.   | 1980 | <i>J. geophys. Res.</i> <b>85</b> , 2941.   |
| RINO C. L., LIVINGSTON R. C. and MATTHEWS S. J.  | 1978 | <i>Geophys. Res. Lett.</i> <b>5</b> , 1039.   |
| RINO C. L. and FREMOUW E. J.   | 1977 | <i>J. atmos. terr. Phys.</i> <b>39</b> , 859.   |
| RINO C. L., TSUNODA R. T., PETRICEKS J.,<br>KELLEY M. C. and BAKER K. D.                                   | 1981 | <i>J. geophys. Res.</i> <b>86</b> , 2411.   |
| ROGNLIEN T. D. and WEINSTOCK J.  | 1974 | <i>J. geophys. Res.</i> <b>79</b> , 4733.   |



VARIABILITY OF THE HARANG DISCONTINUITY AS OBSERVED BY THE  
CHATANIKA RADAR AND THE IMS ALASKA MAGNETOMETER CHAIN

Y. Kamide

NOAA Space Environment Laboratory  
Boulder, Colorado 80303

J. F. Vickrey

Radio Physics Laboratory, SRI International  
Menlo Park, California 94025

ABSTRACT

The relative location of ionospheric parameters and ground magnetic perturbations in the vicinity of the Harang discontinuity is examined. For this purpose, we use combined observations of the Chatanika incoherent scatter radar and of the IMS Alaska meridian chain of magnetometers, which were continuously measuring the crucial ionospheric parameters near the Harang discontinuity when a sizeable substorm took place. The Harang discontinuity, as defined by the reversal of the north-south electric field, is found to be located at  $1-2^\circ$  poleward of the discontinuity identified by the conventional method of using ground magnetic perturbations. It is also found that the relative location of auroral conductivity enhancements is quite variable, depending perhaps upon substorm time. During relatively quiet times and the early stage of a substorm, a conductivity enhancement occurs only on the poleward side of the Harang discontinuity defined by the electric field reversal, whereas the enhancement surges equatorward extending beyond the discontinuity during the maximum to recovery phase of a substorm.

1. INTRODUCTION

One of the most prominent features seen in electric fields and currents in the high-latitude ionosphere is a reversal in the direction of these vectors at the Harang discontinuity region (Harang, 1946; Heppner, 1972; Kamide, 1978). The discontinuity line crosses different latitudes at different local times in the premidnight sector. Auroral optical displays also change their characteristics across the discontinuity. An understanding of the electrodynamics of the Harang discontinuity region is particularly important in that this region represents the key locus of magnetospheric convection and substorm injection (e.g., Lezniak and Winckler, 1970; Brekke, 1977) and furthermore, substorm onset appears to start near this discontinuity (e.g., Nielsen and Greenwald, 1979).

In spite of such importance, the Harang discontinuity is at present poorly understood. This is illustrated by the fact that there have been many statements in the literature concerning the Harang discontinuity which contradict each other. For example, an intense upward field-aligned current was reported to flow out of the Harang discontinuity by Rostoker et al. (1975), while other authors suggested that it is possible for the Harang discontinuity to form the boundary between upward and downward field-aligned currents, i.e., the region of null field-aligned current (e.g., Kamide and Akasofu, 1976). It has also been shown that either case can occur (Baumjohann et al., 1980). In terms of ionospheric conductance, Wedde et al. (1977) and Vickrey et al. (1981) reported respectively an increase and a decrease of the Hall to Pedersen conductivity ratio (or hardening and softening of precipitating particles) in the Harang discontinuity region.

The purpose of this paper is to shed some light on this complicated region by presenting fortuitous, combined observations in which the Chatanika incoherent scatter radar and the IMS Alaska magnetometer chain were continuously measuring ionospheric parameters along the

same meridian on July 7, 1978, when a sizeable substorm took place. It is thus possible to see both the spatial and temporal structure of the Harang discontinuity.

2. DATA

The operating mode of the Chatanika radar employed for the measurements used in this paper consists of elevation scans in the magnetic meridional plane. In this mode the radar beam is able to probe the altitude latitude distribution of electron density and line-of-sight plasma drift. See Vondrak and Baron (1976) for details of the experimental technique. The height-integrated Hall and Pedersen conductivities ( $\Sigma_H$  and  $\Sigma_P$ ) were deduced from the measured electron density and an atmospheric model (Vickrey et al., 1981). From the ion drift velocity data, the electric field  $E$  ( $E_x$ ,  $E_y$ ) was calculated in a coordinate system where  $X$  and  $Y$  are directed geomagnetic east and north, respectively.

Since the antenna line of sight was constrained to lie within the magnetic meridional plane, no direct measurement of the north-south electric field component (east-west ion drift in the  $F$  region) was made. This component can be inferred, however, by using the method described by Doupnik et al. (1977) and de la Beaujardiere et al. (1977, 1981). Briefly, if one assumes that the ion velocity component parallel to  $B$  can be ignored in comparison with the perpendicular component (which is usually a very good assumption in the auroral zone), then at  $F$  region heights the line of sight ion drift is a measure of the east-west electric field component, provided the angle between the radar beam and  $B$  is sufficiently large. The range gate centered in the  $E$  region, however, measures an ion velocity that is not caused solely by  $E \times B$  drift. Rather, at these low altitudes ion-neutral collisions rotate the ion velocity vector toward the direction of  $E$ . By using a model collision frequency profile, the degree of rotation can be assessed, and the ion equations of motion can be solved simultaneously at two heights (one where collisions are important and one where they are not) for the two components of  $E$ . A comparison of this technique with simultaneous barium cloud drifts has shown good agreement [see Mikkelsen et al., 1981]. For a discussion of the uncertainties in determining the two components of electric field using this technique, see de la Beaujardiere et al. (1981) and Mikkelsen et al. (1981). Note, however, that to avoid latitudinal smearing at low elevation angles we have converted the line of sight electron density and velocity data to magnetic coordinates. This technique eliminates that systematic error which was present in the papers referred to above.

Magnetometer data from the IMS Alaska meridian chain of stations were used to estimate the location of the auroral electrojets. Note that Harang (1946) originally defined the discontinuity, coined as the Harang discontinuity later by Heppner (1972), on the basis of ground magnetic data obtained from a chain of magnetometers located in Scandinavia. There are five stations altogether within and just outside of the radar's latitudinal field of view; note that data from Talkeetna ( $\lambda = 62.9^\circ$ ) are not shown in Figure 1 because of the poor quality of the analog recording device. The amplitudes of each of the  $H$ ,  $D$ , and  $Z$  component perturbations were plotted as a function of invariant latitude for the times of the radar operation. A standard technique (see Kisabeth and Rostoker, 1977) was employed to infer the latitudes of the auroral electrojets. We estimate that it is possible to locate the electrojet boundaries to an accuracy of  $0.5^\circ-1^\circ$  latitude, depending on the local density of the stations.

Copyright 1983 by the American Geophysical Union.

Paper number 3L0104.  
0094-8276/83/003L-0104\$3.00

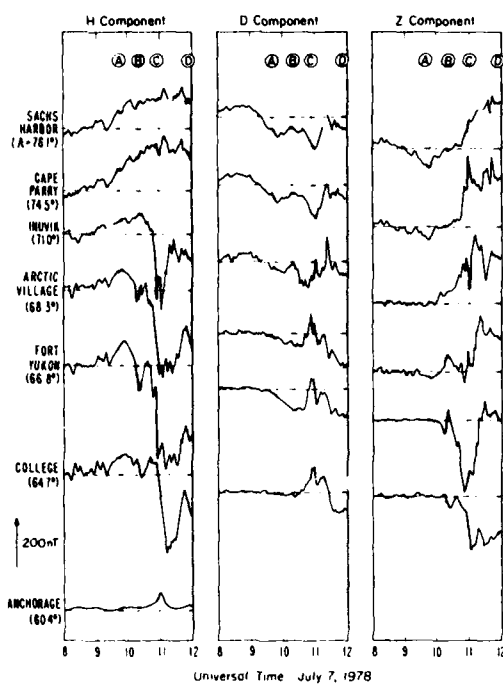


Figure 1 Three component magnetic records from the IMS Alaska meridian chain of magnetometers for July 7, 1978. Data from Anchorage were available for the H component only. Four vertical lines, A, B, C, and D, indicate four times of radar operation for which detailed latitudinal profiles of ionospheric parameters are compared in Figure 2a, 2b, 2c, and 2d respectively.

### 3. OBSERVATIONS

Figure 1 shows three component magnetograms from seven stations along the IMS Alaska meridian chain for four hours on July 7, 1978. During the four-hour interval, the Chatanika radar, located at A (invariant latitude) =  $64.8^\circ$ , surveyed first an eastward electrojet and then after 1055 UT, an intense westward electrojet associated with a substorm expansion. There was a brief intrusion of a weak westward electrojet at about 1020 UT. Thus, the radar, capable of probing  $\pm 3^\circ$  in latitude, scanned continuously the key region of the ionosphere near the Harang discontinuity. To demonstrate the latitudinal profiles of the electric fields and conductivities as well as the ionospheric currents, four epochs, A, B, C and D, have been chosen and are marked by vertical lines in Figure 1. The corresponding profiles of the ionospheric parameters deduced from the Chatanika radar are displayed in Figures 2a, b, c, and d, respectively. Note that it takes approximately 12 minutes for the radar to make a complete meridian scan, so that we neglect any rapid changes occurring within that time. The parameters shown in Figure 2 are calculated from 30 s averages of the radar data.

#### a. Quiet Times (Figure 2a)

An inspection of worldwide magnetograms during epoch A indicates that no substorm was in progress at this time and that a steady-state eastward electrojet prevailed in the region from Siberia to Alaska. This eastward electrojet is produced by a large 20–25 mV/m northward electric field which is accompanied by a weak enhancement in the conductivities. Since the Hall and Pedersen conductivities were nearly equal ( $\sim 5$  mhos), the ionospheric current was flowing in the northeastward direction across the Alaska meridian. If we assume that the ionospheric current is totally responsible for the ground magnetic perturbations, this northeastward current should have generated positive  $\Delta H$

and negative  $\Delta D$  perturbations of almost equal intensity. However,  $\Delta D \sim 0$  in the latitudinal range of the eastward electrojet, suggesting the importance of field-aligned currents. For example, an upward (or net) field-aligned current on the poleward side of the electrojet could have generated positive  $\Delta D$  which cancelled the effects of the northward ionospheric current. If this is the case, one can detect the existence of such an upward current through the divergence of the northward current deduced from the radar observations;  $J_z$  appears to decrease with increasing latitude, starting at  $68^\circ$ .

The Harang discontinuity defined by the north-to-south reversal of the electric field (cf. Maynard, 1974) is indicated in Figure 2a. It is seen that the westward component of the electric field dominates the meridional component in this region. This tendency is well documented (e.g., Banks et al., 1973; Horwitz et al., 1978). The sign change in the east-to-west ionospheric current occurs at a slightly lower latitude than the electric field reversal, indicating that the Pedersen as well as the Hall current is important in determining the electrojet intensity when the zonal electric field is significant, during quiet times. The most striking point is, however, that there is no conventional indication of the Harang discontinuity in the ground magnetic records at this epoch. The H component is positive throughout the Alaska chain, although the positive intensity at Inuvik ( $\sim 50$  nT), where a westward ionospheric current is expected to flow, appears to be a minimum. It is thus important to contend that the electric field should be used to best identify the Harang discontinuity especially during quiet periods. It should also be noted that earlier observations (e.g., Maynard, 1974; Nielsen and Greenwald, 1979) have shown that during low geomagnetic activity, the Harang discontinuity is roughly east-west oriented near or above  $70^\circ$  invariant latitude. In our case, however, the discontinuity was found to be located well below  $70^\circ$  and within the radar's line of sight.

#### b. Times Immediately Preceding Major Substorm Onset (Figure 2b)

The epoch B was chosen as representative of Harang discontinuity signatures just before the onset of a major substorm which, in this case, started at about 1035 UT. The development of a weak westward electrojet is seen as a negative  $\Delta H$  excursion at Arctic Village and Fort Yukon. This penetration of the westward electrojet is evidenced also by

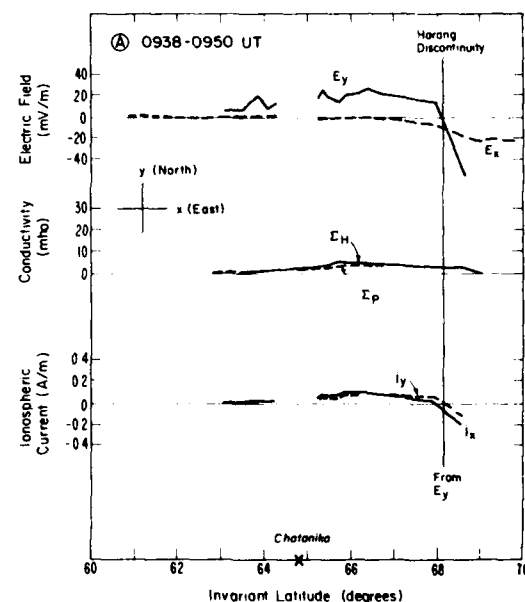


Figure 2a Latitudinal profiles of the electric field, conductivity, and ionospheric current for 0938–0950 UT on July 7, 1978. The Harang discontinuity identified by the reversal of the north-south electric field is shown by a vertical line.

a sharp positive  $Z$  excursion at these stations as well as a negative  $Z$  component at College. From this information we can estimate the location of the conventional Harang discontinuity from the traditional definition to be  $65.5^\circ$ .

As marked by a solid vertical line in Figure 2b, the north-to-south reversal of the electric field occurred at  $66.1^\circ$ . Again the westward field prevails at latitudes near the reversal. The conductivities are intensified as a whole by a factor of 2 to 3, compared with those at epoch A. The typical ratio between the Hall and Pedersen conductivities is 1.3 in this case; however, there is an indication of a decrease in this ratio at the Harang discontinuity itself, a feature that is consistent with the observations of Vickrey et al. (1981), but inconsistent with those of Wedde et al. (1977). The most interesting feature in this particular case is that an intense enhancement reaching more than 20 mhos in  $\Sigma_H$  occurs only on the poleward side of the Harang discontinuity, i.e., in the region of the southward field.

#### c. Expansion Phase of Substorm (Figure 2c)

The epoch C corresponds to the expansive phase of an intense substorm. At Alaska magnetometer stations higher than Chatanika in latitude, like Inuvik and Arctic Village, the negative  $H$  perturbations were about to reach their peak, whereas the College  $H$  record still showed positive excursion (see Figure 1). This indicates that the strong westward electrojet was penetrating into the evening sector along the poleward edge of the eastward electrojet.

The latitudinal profiles of the electric fields and conductivity components for this epoch are similar in a qualitative manner to those in Figure 2b, but significantly different quantitatively. The electric field profile is characterized by a relatively large northward field below  $65.4^\circ$ , which is the Harang discontinuity, and a very small southward field at higher latitudes. In other words, the electric field, especially its southward component, is very small in the region of the intense westward electrojet, which is produced mainly by high conductivities. The location of conductivity enhancements relative to the Harang discontinuity does not differ very much from that in epoch B; i.e., they peaked well north of the Harang discontinuity. However, the ratio  $\Sigma_H/\Sigma_P$  increased considerably in the westward electrojet region, reaching a maximum of

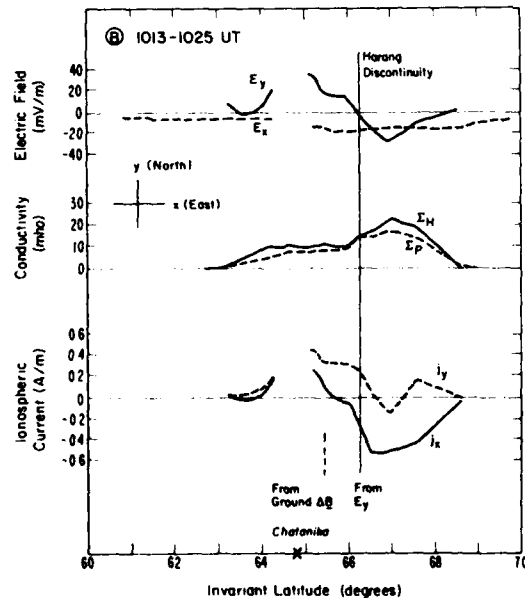


Figure 2b Same as Figure 2a, except for the radar operation time: 1013-1025 UT. The Harang discontinuity inferred from ground magnetic perturbations is indicated by a vertical dashed line.

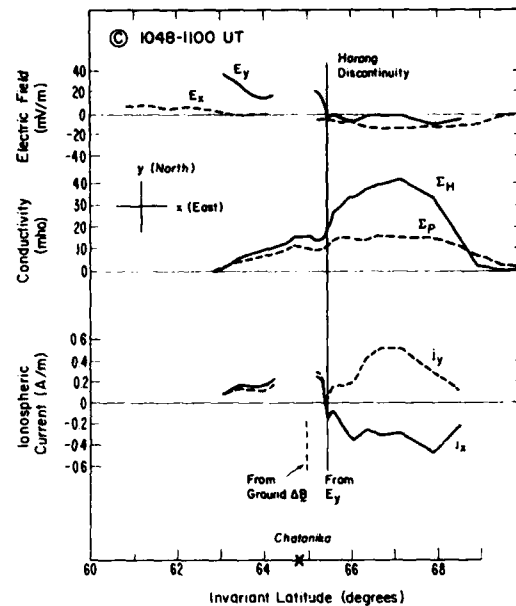


Figure 2c Same as Figure 2a, except for the radar operation time: 1048-1100 UT.

2.5. It is also important to point out that as a result of the large Hall conductivity and the westward electric field, the westward electrojet has a large northward component as well. Note in this connection that in spite of this northward current,  $\Delta D$  below  $69^\circ$  was positive (see Figure 1), probably indicating once again the existence of an upward field-aligned current.

#### d. Substorm Maximum and Recovery Phase (Figure 2d)

The epoch D occurred when the substorm was already in its recovery phase at the Alaska chain (see Figure 1), but, the electrojet activity on a global scale was still in its maximum epoch. In other words, by this time, the longitudinal center of the westward electrojet had moved into the morning sector.

The Harang discontinuity determined by the electric field reversal is located at  $66.1^\circ$ . In contrast to the earlier profiles, the area of Hall and Pedersen conductivity enhancement has a wide latitudinal breadth extending on both the north and south sides of the Harang discontinuity. The peak of total conductivity, however, was located a little northward of the discontinuity.

If one uses the latitudinal profile of the ground magnetic perturbations to infer the Harang discontinuity, the locus of the  $\Delta H$  reversal does not coincide with electric field reversal, but instead, is located about  $2^\circ$  south of the electric field reversal. This probably indicates that the total intensity of the westward electrojet is greater than that of the eastward electrojet. This is verified by radar measurements which show the maximum current density of the westward electrojet to be  $0.4 \text{ A/m}$  which is more than a factor of 3 larger than that of the eastward electrojet. Other circumstances leading to the equatorward shift of the  $\Delta H$  reversal are that the westward electric field, which we showed earlier to prevail in the Harang discontinuity region, and the enhanced Pedersen conductivity region, have both moved equatorward.

#### 4. DISCUSSION

Although the Harang discontinuity has been identified in terms of various phenomena in the literature, the loci defined by those different signatures do not always coincide with each other. In the present paper, it has been shown that the difference between the electric field reversal and the Harang discontinuity traditionally defined by ground magnetic field perturbations can amount to a few degrees.

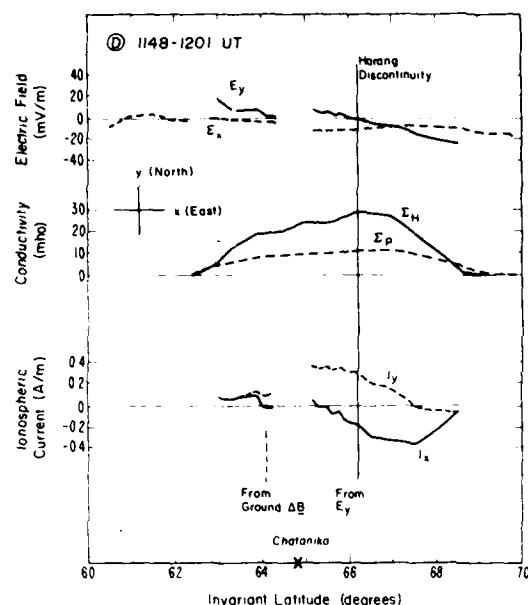


Figure 2d Same as Figure 2a, except for the radar operation time 1148-1201 UT

Implicit in the interpretation of the results presented above, however, is that the Harang discontinuity can be best defined in terms of the reversal of the north-south electric field. By "best" we mean that the physical processes occurring in the Harang discontinuity can most effectively be understood by using the electric field signatures. The original definition of the discontinuity in terms of  $\Delta H$  demarcation, while convenient, offers only an indirect means of sensing what is happening in the magnetosphere-ionosphere system. As we have shown, the magnetic signature of the Harang discontinuity is affected by both the conductivity and electric field, as well as the relative widths and intensities of the overlapping electrojets.

In this report, the variability of conductivity enhancements with respect to the electric field has been illustrated. We should point out, however, that the Chatanika radar operated in a mode that can provide information only about latitudinal "slices" of the ionosphere. This leaves an ambiguity to a certain extent between spatial and temporal changes in the data. Measurements from the STARE radar (Greenwald et al., 1978) do not suffer this limitation and, hence, two-dimensional maps of the electric field covering invariant latitudes from 68° to 72° can be produced. However, STARE cannot measure the conductivity distribution. We would like to note that it is probably inappropriate to address the question of signatures of ionospheric conductivities and field-aligned currents at the Harang discontinuity without taking into account their variability with respect to substorm dynamics. Along these same lines, Baumjohann et al. (1980) cautioned that the relative configuration of these parameters depends upon local time.

During relatively quiet periods and the early epoch of substorms, the conductivity is enhanced only on the poleward side of the electric field reversal, i.e., in the westward electrojet region. As the substorms progress, the region of conductivity enhancement appears to expand equatorward, penetrating the eastward electrojet region. The conductivity enhancement generally indicates that there is intense auroral electron precipitation in that region, which in turn carries upward field-aligned currents and provides bright auroral optical displays. The field-aligned current density has been estimated from the divergence of the height-integrated north-south ionospheric current by assuming variations in the east-west direction are negligible (e.g., de la Beaujardiere et al., 1981). However, such a simple scheme cannot be applied to the Harang discontinuity region because east-west variations cannot be ignored.

**Acknowledgments** The authors are grateful to S.-I. Akasofu and A. D. Richmond for their illuminating discussions, and to B.-H. Ahn for his assistance in preparing magnetometer data used in the present paper. Support for Y. Kamide has come from an NRC Resident Research Associateship. The work at SRI International was supported by the Air Force Office of Scientific Research under contract F49620-80-C-0014. Radar operations were supported by the Defense Nuclear Agency under contract DNA001-77-C-0042.

## REFERENCES

- Banks, P. M., J. R. Doupnik and S.-I. Akasofu, Electric field observations by incoherent scatter radar in the auroral zone, *J. Geophys. Res.*, **78**, 6607, 1973.
- Baumjohann, W., J. Untiedt, and R. A. Greenwald, Joint two-dimensional observations of ground magnetic and ionospheric electric fields associated with auroral zone currents. 1. Three-dimensional current flows associated with a substorm-intensified eastward electrojet, *J. Geophys. Res.*, **85**, 1963, 1980.
- Brekke, A., The relationship between the Harang discontinuity and the substorm injection boundary, *Planet. Space Sci.*, **25**, 2019, 1977.
- de la Beaujardiere, O., R. Vondrak, and M. Baron, Radar observations of electric fields and currents associated with auroral arcs, *J. Geophys. Res.*, **82**, 5051-5062, 1977.
- de la Beaujardiere, O., R. Vondrak, R. Heelis, W. Hanson, and R. Hoffman, Auroral arc electrodynamic parameters measured by AE-C and the Chatanika radar, *J. Geophys. Res.*, **86**, 4671, 1981.
- Doupnik, J. R., A. Brekke, and P. M. Banks, Incoherent scatter radar observations during three sudden commencements and a Pc 5 event on August 4, 1972, *J. Geophys. Res.*, **82**, 499-514, 1977.
- Greenwald, R. A., W. Weiss, E. Nielsen, and N. R. Thomson, STARE: A new radar auroral backscatter experiment in northern Scandinavia, *Radio Sci.*, **13**, 1021, 1978.
- Harang, L., The mean field of disturbance of the polar earth-magnetic storm, *Geophys. Publ.*, **16**, 12, 1946.
- Heppner, J. P., The Harang discontinuity in auroral belt ionospheric currents, *Geophys. Publ.*, **29**, 105, 1972.
- Horwitz, J. L., J. R. Doupnik, and P. M. Banks, Chatanika radar observations of the latitudinal distributions of auroral zone electric fields, conductivities, and currents, *J. Geophys. Res.*, **83**, 1463, 1978.
- Kamide, Y., On current continuity at the Harang discontinuity, *Planet. Space Sci.*, **26**, 237, 1978.
- Kamide, Y., and S.-I. Akasofu, The auroral electrojet and field-aligned current, *Planet. Space Sci.*, **24**, 203, 1976.
- Kisabeth, J. L., and G. Rostoker, Modelling of three-dimensional current systems associated with magnetospheric substorms, *Geophys. J. R. Astr. Soc.*, **49**, 655, 1977.
- Lezniak, E. W., and J. R. Winckler, Experimental study of magnetospheric motions and the acceleration of energetic electrons during substorms, *J. Geophys. Res.*, **75**, 7075, 1970.
- Maynard, N. C., Electric field measurements across the Harang discontinuity, *J. Geophys. Res.*, **79**, 4620, 1974.
- Mikkelsen, I. S., I. S. Jørgensen, M. C. Kelley, M. F. Larsen, I. Pereira, and J. F. Vickrey, Neutral winds and electric fields in the dusk auroral oval. 1. measurements, *J. Geophys. Res.*, **86**, 1513-1524, 1981.
- Nielsen, E., and R. A. Greenwald, Electron flow and visual aurora at the Harang discontinuity, *J. Geophys. Res.*, **84**, 4189, 1979.
- Rostoker, G., J. C. Armstrong, and A. J. Zmuda, Field-aligned current flow associated with intrusion of the substorm-intensified westward electrojet into the evening sector, *J. Geophys. Res.*, **80**, 357, 1975.
- Wedde, J., J. R. Doupnik, and P. M. Banks, Chatanika observations of the latitudinal structure of electric fields and particle precipitation on November 21, 1975, *J. Geophys. Res.*, **82**, 2743, 1977.
- Vickrey, J. F., R. R. Vondrak, and S. J. Matthews, The diurnal and latitudinal variation of auroral zone ionospheric conductivity, *J. Geophys. Res.*, **86**, 65, 1981.
- Vondrak, R. R., and M. J. Baron, Radar measurements of the latitudinal variation of auroral ionization, *Radio Sci.*, **11**, 939, 1976.

(Received October 4, 1982;  
accepted January 11, 1983.)

- SAGALYN R. C. and SMIDDY M. 1974 *J. geophys. Res.* **79**, 4252.
- SINGH M., SZUSZCZEWICZ E. P. and HOLMES J. C. 1981 IES Proc., 14-16 April 1981, NRL, Office of Naval Research, Air Force Geophysics Laboratory.
- SINGLETON D. G. 1973 *J. atmos. terr. Phys.* **35**, 2253.
- TSUNODA R. T. 1981 *J. geophys. Res.* **86**, 139.
- VICKREY J. F. and KELLEY M. C. 1982 *J. geophys. Res.* **87**, 4461.
- VICKREY J. F., RINO C. L. and PTEMRA T. A. 1980 *Geophys. Res. Lett.* **7**, 789.
- Reference is also made to the following unpublished material:*
- BASU S., BASU S., LIVINGSTON R. C. and WHITNEY H. E. 1982 Comparison of ionospheric scintillation statistics from the North Atlantic Sectors of the auroral oval using the Wideband Satellite, unpublished manuscript.
- RINO C. L. and LIVINGSTON R. C. 1982 On the analysis and interpretation of spaced-receiver measurements of transionospheric radio waves, *Radio Sci.*, accepted for publication.
- VICKREY J. F. 1981 Radar observations of structural plasma in the high latitude *F*-region, DNA report 5645F, SRI International.
- WEBER E. J. and BUCHAU J. 1980 Polar cap *F*-layer auroras, *Geophys. Res. Lett.*, submitted for publication.

EVIDENCE OF EAST-WEST STRUCTURE IN LARGE-SCALE  
F-REGION PLASMA ENHANCEMENTS IN THE AURORAL ZONE

By

R. T. Tsunoda and J. F. Vickrey

SRI International

Menlo Park, California 94025

## ABSTRACT

Large-scale (10- to 100-km) plasma-density enhancements appear to be an integral feature of the auroral F-layer ionosphere. These enhancements, called F-region "blobs," have been detected with the Chatanika incoherent-scatter radar, and are particularly noticeable during recent years of high solar activity. Blobs have attracted considerable interest because of their propensity for structuring, apparently via the gradient-drift and current-convective instabilities. Although both mechanisms predict the generation of longitudinal structure, no measurements have been made to verify this hypothesis. In this paper, we present the first direct evidence that blobs have east-west structure. The observed longitudinal structure is shown to be consistent with the production of a blob by locally intense particle precipitation at the largest scales ( $\geq 500$  km) and the structuring of the blob by the gradient-drift instability at intermediate scales ( $\sim 150$  km).

## I INTRODUCTION

The presence of large-scale, plasma-density enhancements in the auroral F layer has become increasingly evident in recent years, their existence has been detected with the Chatanika incoherent-scatter radar (Vickrey et al., 1980, Robinson et al., 1982). Because of the appearance of these plasma-density enhancements in isodensity-contour maps, constructed from elevation-scan data obtained in the magnetic meridian, these features have become known as F-region "blobs." These blobs, which were not very noticeable in Chatanika radar measurements during periods of low solar activity (e.g., Robinson et al., 1982), have become a dominant feature in the auroral ionosphere during recent years of high solar activity. Peak plasma densities in these enhancements range from about  $10^5$  el/cm<sup>3</sup> during solar minimum, to  $10^6$  el/cm<sup>3</sup> or more during solar maximum. Blobs have spatial dimensions of about a few hundred kilometers in altitude, and from several tens of kilometers to a few hundred kilometers in latitude. They have been observed as single, isolated features or as multiple structures in the auroral zone.

Initial interpretation of radar data regarding the three-dimensional shape of blobs has been in terms of a magnetic-field-aligned slab of enhanced plasma density that extends over many degrees of longitude along an L shell, much akin to visual auroral arcs. This interpretation is natural if blobs and visual aurora are thought of as structures produced by particle precipitation.



The existence of east-west (or longitudinal) variations in blob plasma density was not given serious consideration until the discovery that latitudinally confined regions of scintillation-producing irregularities (Fremouw et al., 1977, Rino et al., 1978, Rino and Owen, 1980) were spatially collocated with F-region blobs (Vickrey et al., 1980). The occurrence of smaller-scale ( $\leq 1$ -km) irregularities in the vicinity of horizontal gradients in plasma density associated with the walls of blobs, and the presence of an auroral electric field suggested that gradient-drift instability was probably operative as a structuring mechanism (Simon, 1963, Linson and Workman, 1970). The occasional occurrence of small-scale irregularities on a blob wall that apparently should be stable to the gradient-drift instability has led researchers to propose current-convective instability as an alternate structuring mechanism (Ossakow and Chaturvedi, 1979, Keskinen et al., 1980).

Both the gradient-drift and current-convective instabilities predict the development of east-west structure along the walls of blobs that are characterized by latitudinally directed gradients in plasma density. Locally intense particle precipitation and sources of irregular electric fields other than the above-mentioned plasma instabilities can also produce east-west plasma-density structure. Whether one or several of these mechanisms are operative, there is good reason to expect east-west structure in F-region blobs.

In this paper, we present the first direct evidence that F-region blobs do indeed have east-west plasma-density structure. A two-week experiment was conducted with the Chatanika radar in November 1981

using antenna scan modes designed so that the radar measurements would characterize the blobs in three dimensions. In addition, the electric field and meridional neutral wind were measured to determine the expected structuring configuration that would be produced by the gradient-drift instability. We selected an exceptional data set for the initial analysis and preliminary results presented here. We show that the observed structure in the blob is consistent with the gradient-drift instability driven by a southward neutral wind blowing through the equatorward wall of the blob and by a southward electric field acting on the western wall of the blob. The blob region, interpreted as being produced by soft-particle precipitation, is, therefore, envisioned as having a large quasi-elliptical cross-section in the latitude-longitude plane before being distorted by the instability.

## II EXPERIMENT

The Chatanika incoherent-scatter radar was operated periodically from 5 to 16 November 1981 specifically to determine the presence (or absence) of east-west horizontal structure in the auroral F layer. If discovered, we hoped to characterize the blob structure in three dimensions. Because three-dimensional spatial mapping of plasma structure in a dynamic environment is extremely difficult to do with an incoherent-scatter radar, we sought to minimize space-time ambiguities by compromising on the spatial coverage sampled by the radar. Advantage was taken of the interactive capability and real-time graphic information available at the Chatanika radar facility. Various radar scan modes were designed, each intended for spatial characterization of east-west plasma structure under different electrodynamic conditions. The data set analyzed in this paper was obtained using what we call the "zipzap" mode.

The zipzap mode consists of a sequence of five elevation scans in the magnetic meridian, followed by two fixed-position measurements to determine the electric-field vector and the meridional neutral wind. This mode is most suited for mapping east-west blob structure in the presence of a large zonal plasma flow. The basic approach is to scan in the meridional plane as rapidly as possible while the blob drifts eastward (or westward) through the scan plane at a measured rate. The sector scanned was restricted in latitudinal extent to minimize the time between scans. Each scan was made in 100 s and a complete zipzap cycle was completed in 13 min.

The interactive capability of the radar was used extensively during the experiment. Elevation scans covering approximately  $10^\circ$  of latitude at F-region altitudes were used on a patrol basis to search for blobs. Range-time-intensity (RTI) maps of the elevation scans were made in real time and used to determine blob location. The zipzap mode was then initiated with the limited-scan sector centered on the latitude of the blob(s). With this approach, we were able to track the latitudinal movement of blobs while collecting scan sequences of the blob cross-section in latitude versus altitude.

The radar was operated using two pulse widths, 60 and 320  $\mu\text{s}$ , which were transmitted alternately with a pulse repetition frequency of  $36\text{ s}^{-1}$  for each pulse width. The elevation scans were continuous and covered a spatial sector corresponding to 300-km horizontal distance at an altitude of 350 km. The data were recorded on magnetic tape after a 5-s, on-line integration period. The fixed-position measurements were made for 60 s each, one with the radar beam directed to the east of the magnetic meridian for the meridional electric-field component and the other looking along the geomagnetic field line,  $\vec{B}$ . The second measurement gives the plasma velocity along  $\vec{B}$  from which the meridional component of neutral wind can be deduced.

The plasma densities presented in this paper were computed using the 320- $\mu\text{s}$  pulse width and a 10-s integration period. The 10-s integration results in a 30-km horizontal distance resolution at the 350-km altitude in the meridional plane. The plasma densities were sorted into a matrix with the data columns aligned along the

geomagnetic field, and then smoothed along  $\vec{B}$ . These smoothed data were then used to construct the isodensity contour maps presented in the following section.

### III RESULTS

The data set presented in this section was obtained on 10 November 1981 between 1104 and 1117 Universal Time (UT). Alaskan Standard time (AST) lags UT by 10 hours. The results, therefore, pertain to a period shortly after local midnight. The data set consists of six limited-sector meridian scans and corresponding electric-field and neutral-wind measurements. We present the electric-field and neutral-wind results first to establish the dynamic conditions that prevailed when the plasma-density structure was observed. We then proceed to describe the meridian-scan data and present isodensity contour maps that reveal the east-west plasma-density structure associated with F-region blobs.

The electric-field ( $\vec{E}$ ) results are presented in Figure 1. The figure shows the (geomagnetic) southward and eastward components of the electric-field vector, plotted as a function of time. The electric-field vector was computed by combining the radial Doppler velocity measured during the elevation scans with the fixed-position measurements. Two estimates of the radial Doppler velocity out of the magnetic meridian plane were available, one obtained before the limited-sector elevation scans and the other during the period between the fifth and sixth elevation scans. The first measurement was made around 1103 UT with the antenna pointed towards geomagnetic east. The second was made around 1116 UT with the antenna pointed  $15^\circ$  east of magnetic north and at  $66^\circ$  elevation. Thus, in addition to the temporal

difference between the two estimates of  $\vec{E}$ , they are latitudinally separated. The first is more representative of the zonal drift overhead, while the second estimate of zonal drift was centered on the latitude of the blob. The results of both computations are presented in Figure 1.

The electric-field vector is important in determining the spatial location of F-region blobs as a function of time. From Figure 1, we see that the eastward electric field was small, typically  $\pm 2$  mV/m and reached a maximum of  $-7$  mV/m around 1110 UT. A 2-mV/m eastward (or westward) electric field only displaces the blob 4-km latitudinally in 100 s (the scan time), the maximum value of 7 mV/m would displace the blob 14 km in 100 s. Thus, we conclude that a blob centered in the scanned sector could not have been convected latitudinally out of that sector ( $\pm 150$  km) by the time of the following scan.

The southward electric field was nominally 22 mV/m, although somewhat variable with time. The zonal plasma drift during this period was, therefore, eastward at a speed of  $\sim 440$  m/s (26.4 km/min). During the 100 s it took to complete an elevation scan, a blob could have moved 44 km in longitude. With this sampling rate, therefore, we cannot resolve east-west structure with scale sizes less than 88 km.

Knowledge of the electric field is also important (together with the neutral wind) for estimating the growth rate of the gradient-drift instability. East-west structure can be produced by that instability when a north-south component of the difference (or "slip") velocity between the F-region plasma and the neutral gas exists. The meridional

component of the neutral wind was  $\sim 380$  m/s at 1103 UT and  $\sim 370$  m/s at 1117 UT, both directed southward. The slip velocity, therefore, must have been in the range from 230 m/s to 420 m/s, and directed poleward. With this slip-velocity direction, the equatorward wall of a blob should have been unstable and thus, subject to east-west plasma structuring.

We now describe the meridian-scan data set, presented in Figure 2. The first five panels (Figures 2(a) to 2(e)) contain isodensity contour maps of the auroral ionosphere above the 200-km altitude, obtained between the times of the neutral-wind measurements. The fifth scan (Figure 2(e)) was followed by electric-field and neutral-wind measurements, and then the sixth scan shown in Figure 2(f). The isodensity contours are plotted in a format such that the geomagnetic field is vertical in the altitude versus invariant-latitude coordinates. The magnetic dip angle at Chatanika is  $76.9^\circ$  at the 300-km altitude. Heavy lines have been used for contours with values of 4, 6, 8, and  $10 \times 10^5$  el/cm<sup>3</sup>. The first five scans were made at approximately 2-min intervals, and the sixth scan was completed about 5 min after the fifth scan.

The blobs can be characterized by their peak plasma density, altitude of peak plasma density, and their latitudinal gradient. The peak plasma density is seen to vary from  $4 \times 10^5$  el/cm<sup>3</sup> to  $1.1 \times 10^6$  el/cm<sup>3</sup>. The largest of these values is about two times greater than that reported by Vickrey et al. (1980). The altitude of maximum plasma density is somewhat variable, ranging from 380 to 420



km. These plasma densities and F-layer peak altitudes are in reasonable agreement with the computational results of Watkins and Richards (1979). Using a soft-particle precipitation model, they found that an equatorward-directed neutral wind increases both the altitude of the F layer peak and the peak plasma density. Finally, we note that the latitudinal plasma-density gradient is steeper on the equatorward side of the blob. A steeper equatorward wall is consistent with our prediction of gradient-drift structuring based on the electrodynamic conditions described above.

Beside the physical characteristics of blobs seen in a given contour map, important evidence for east-west structure is contained in the variability of blob characteristics from map to map. From Figure 2, we see that blobs found in successive maps do not correlate well. A blob found in one map cannot be easily identified with a blob in the next map without invoking an anomalously large (1) production by particle precipitation, (2) latitudinal transport by east-west electric fields, or (3) loss rate. The only reasonable interpretation appears to be in terms of east-west structure.

For example, the blob in Figure 2(a) at the 380-km altitude might be associated with the intense blob in Figure 2(b) if both anomalously large production and equatorward transport occurred between scans. Watkins and Richards (1979) showed, however, that the e-folding time for F-region plasma density production by particle precipitation is about one hour. Even if anomalously large production rates were not needed, we find that the observed latitudinal displacement requires a

westward electric field of about 30 mV/m. The westward electric field was not larger than 3 mV/m.

Other examples can be found in Figure 2. The intense blob in Figure 2(b) could have decayed or moved latitudinally out of the scanned sector by the time of the scan corresponding to Figure 2(c). At a nominal altitude of 400 km, the e-folding decay time is about 16 hours. With this extremely slow decay rate, the peak plasma density of  $8 \times 10^5$  el/cm<sup>3</sup> (Figure 2(b)) should not have decayed by more than 0.25 percent in the time between scans. We see from Figure 2(c), however, that the peak plasma density was  $\sim 6.5 \times 10^5$  el/cm<sup>3</sup>, which corresponds to a 20 percent decrease. Moreover, we note that the poleward displacement would require an eastward electric field of 50 mV/m. The measured eastward electric field was smaller by more than an order of magnitude.

As a final example, the changes in the blob seen in each of the maps in the bottom row of Figure 2 could reasonably be interpreted in terms of latitudinal transport. The decay rate, however, is unreasonable. The peak plasma density of the blob in Figure 2(f) should not have decayed to less than  $9 \times 10^5$  el/cm<sup>3</sup>. Instead, we find that the peak plasma density has decreased to about  $4 \times 10^5$  el/cm<sup>3</sup>. This apparent rapid decay, however, could have easily been produced by an east-west gradient scale length of 120 km moving zonally at 440 m/s.

Interpretation of the data in Figure 2 in terms of east-west structure is best illustrated by plan views of the isodensity contours

at selected altitudes. To do this, we have taken the plasma-density variations as a function of invariant latitude, at selected altitudes (horizontal lines in the maps in Figure 2), and fitted isodensity contours to the values obtained from the six scans. The zonal displacements between scans were computed by using the measured southward electric field of 22 mV/m. No attempt was made to compensate for any latitudinal displacement because the east-west electric field was small. The resulting isodensity contour maps for altitudes of 360, 400, and 440 km are presented in Figure 3.

Analysis of the contour maps in Figure 3 reveals three important features. First, the lower-valued isodensity contours (e.g.,  $5 \times 10^5$  el/cm<sup>3</sup>) are aligned northwest-southeast, instead of along a contour of constant invariant latitude. Such a tilt could have been produced by a 6 mV/m eastward electric field. However, the fact that the zonal electric-field component was westward on average suggests that the tilted contours simply outline a large region of enhanced plasma density produced by localized particle precipitation. The abrupt termination of the blob at the west end of the maps provides more conclusive evidence that the tilt is actual spatial structure.

To determine the total east-west extent of the enhanced plasma-density region produced (presumably) by locally intense particle precipitation, we examined elevation-scan data taken before to the first scan in Figure 2. In a full-elevation scan made from 1052:44 to 1101:00 UT, a blob was detected at  $67.6^\circ$  invariant latitude and at 350-km altitude. The peak plasma density of the blob was  $1.3 \times 10^6$

$\text{el/cm}^3$ . In an even earlier scan, made from 1040:32 to 1048:48 UT, a blob was not seen near this latitude. Using an average southward electric field of 15 mV/m (the southward electric field was 10 mV/m at 1041 UT), we estimate that the eastern boundary of the blob must have extended about 400 km to the right of the contour maps in Figure 3. The full east-west extent of the blob, therefore, must have been close to 600 km.

From the above analysis, we envision all of the F-region blobs in Figure 2 as parts of a single, large-scale region of enhanced plasma density, perhaps similar in cross-section to an ellipse with the major axis oriented in the geomagnetic east-west direction and having a 600-km extent. The portion of the ellipse seen in Figure 3 would be the southwest quadrant of the elliptically shaped blob. In this interpretation, the tilted, lower-isodensity contours in Figure 3 can be thought of as describing the ellipse. The north-south extent is not completely sampled, but is at least 300 km. This large region of enhanced plasma density, presumably produced by locally intense particle precipitation, is imbedded in a background F-layer plasma density of perhaps  $2 \times 10^5 \text{ el/cm}^3$ .

The second feature of interest in the contour maps of Figure 3 is the pattern created by the higher-valued isodensity contours. Two regions of enhanced plasma density are seen to have a form like "fingers" extending southward and to be separated in east-west direction by regions of depleted plasma density. Similar patterns of east-west structure are seen in the three contour maps taken at

different altitudes. The east-west separation of the fingers is about 150 km. The enhanced (and depleted) plasma density regions are also characterized by a tilt away from Magnetic North (vertical direction in Figure 3) i.e., the major axis of the enhancements are aligned northeast-southwest. The alignment of the enhancements (and depletions) are nearly orthogonal to the lower-valued isodensity contours (first feature).

The plasma density in the center finger (at the 400- and 440-km altitudes) exceeds  $10^6$  el/cm<sup>3</sup> by about a factor of two greater than that in the depleted region along its east side. The peak plasma density in the east finger, however, is smaller than that in the center finger. This difference cannot be explained by flux-tube interchange processes such as those associated with the gradient-drift instability without assuming some initial structure produced by locally intense particle precipitation.

Finally, the third feature of interest is an apparent structuring of the west wall of the center finger in Figure 3. The structure is in the form of an eastward penetration of a low plasma-density contour between two regions of higher plasma density. This structure is most evident at the 400-km altitude, although there is also some evidence of the eastward penetration (of a lower-valued contour) at the 360 km altitude. West-wall structuring is consistent with the gradient-drift instability driven by a southward electric field.

To summarize, the blobs observed during the six scans in Figure 2 are clearly not latitudinal cross-sections of independent plasma-

density structures that are uniformly extended in longitude. The variations of the blobs in latitudinal location and peak plasma density cannot be explained in terms of latitudinal transport by the measured electric fields nor by reasonable production or decay rates of plasma density. The simplest and most consistent interpretation of the data in Figures 2 and 3 is that a single large-scale blob was originally produced with a quasi-elliptical cross-section (600 km in longitude,  $\geq 300$  km in latitude), by locally intense particle precipitation. That initial configuration was then structured zonally along its equatorward wall by the gradient-drift instability on an intermediate scale ( $\sim 150$  km). The observed north-south structure is also consistent with that produced by the same instability.

Of course, the F-region plasma configuration does not have to be locally unstable to produce the structure we have observed. Indeed, the original precipitation structure itself may be quite complicated. Moreover, the long lifetime of F-region ionization and relatively slow cross-field diffusive decay rates lead to the situation where structural evolution is cumulative. In other words, the amount of structure observed on a given set of flux tubes depends in a complicated way on the structuring influences encountered by those flux tubes during their past history (e.g. Vickrey and Kelley, 1982a). Nevertheless, the fact that the structure observed consistently agrees with that expected from the local dynamics is highly suggestive that local instabilities are indeed operating.

#### IV DISCUSSION AND CONCLUSIONS

We have presented a data set in which the spatial distribution of the observed F-region plasma density can most easily be explained in terms of a single, large-scale plasma blob having significant east-west structure. The blob itself was interpreted as being initially produced by locally intense particle precipitation at the largest horizontal scales ( $\sim 300$  by  $600$  km), and being structured by the gradient-drift instability at smaller scales ( $\sim 150$  km). Although the smaller-scale structure could, in principle, also be interpreted as being produced by locally intense particle precipitation, the characteristics of this structure are consistent with that of structure produced by the gradient-drift instability. That is, in the presence of a poleward-directed slip velocity between F-region ions and neutrals, (1) steeper latitudinal gradients in plasma density were found along the equatorward side of blobs, and (2) the intermediate-scale structure appeared to be associated with the equatorward side of the enhanced plasma-density region. We note that the current-convective instability (Ossakow and Chaturvedi, 1979) does not have to be invoked to explain these observations because the slip velocity, controlled by a southward-directed neutral wind, was directed poleward. The current-convective instability contributes a destabilizing factor to the irregularity growth rate; however, that factor acts on both the poleward and equatorward gradients and, hence, does not alter the basic conclusions.

In the case of an isolated F-region blob, whose density dominates the height-integrated Pedersen conductivity of the flux tube, the linear growth rate of the gradient-drift instability can be estimated for simple slab geometry from the results of Linson and Workman (1970). (This conventional formula, applied originally to barium ion-cloud structuring at lower altitudes, has been shown by Ossakow et al. (1977) to be valid at the altitudes and conditions of this data set.) In our case, for a southward neutral wind of 370 m/s acting on a mean plasma-density gradient with scale length of  $\sim 50$  km, the irregularity e-folding growth time is 2.3 min. This growth rate would appear large enough to have produced the pattern of east-west structure presented in Figure 3. For example, if the initial perturbation amplitude was 1 km, the observed wave amplitude of about 150 km would have occurred in a period of seven e-folding times, or about 15 min.

While the southward neutral wind acted on the northward-directed gradient to produce the east-west structure, the southward electric field should have acted on the eastward-directed gradient to produce north-south structure. A 22-mV/m electric field acting on a 120-km gradient scale length gives an e-folding time of 4.5 min. However, the zonal neutral wind is not known. Its contribution to the slip velocity will determine the actual e-folding time. The observed eastward penetration of lower-valued isodensity contours into the center enhancement in Figure 3 is consistent with our expectation that the zonal neutral wind was less eastward than the bulk plasma motion. The neutral wind, determined primarily by ion drag, would have been



directed westward in the premidnight sector until the reversal in plasma flow (in the Harang discontinuity region). Its subsequent eastward velocity would be expected to lag that of the plasma. The relative lack of structure along the west wall of the east finger (right side of Figure 3) as compared to the center finger, also supports the concept that north-south structuring of the center finger occurred simultaneously with east-west structuring, i.e., no secondary process is required.

The above discussion of gradient-drift structuring in the two orthogonal directions as independent processes may not be realistic. Perkins and Doles (1975) and Keskinen and Ossakow (1982) showed that for a slab geometry, the electric-field component parallel to the gradient can act to dampen the irregularity growth rate of the gradient-drift instability. The stabilization results from a shear in the  $E \times B$  velocity, because the electric field along the plasma-density (conductivity) gradient must necessarily be locally intense to maintain a horizontally divergence-free current. The velocity shear produced in their treatment also acts to tilt the structures with a sense dictated by slower velocities in higher plasma-density regions. For our data set where the southward electric field is antiparallel to the plasma-density gradient, the east-west structures would be expected to be rotated counter-clockwise in Figure 3 from the direction perpendicular to the initial gradient if the velocity-shear mechanism is valid.

The alignment of the east-west structure in Figure 3 is seen to be roughly orthogonal to the direction of the plasma-density gradient. The absence of a tilt in the fingers suggests that the velocity-shear mechanism is not operative. Its absence in the auroral ionosphere, however, is expected. The requirement for a divergence-free current in the F layer can be satisfied by field-aligned currents that close in a highly-conducting auroral E layer. Further discussion of the effects of conducting background on the gradient-drift instability is given in later paragraphs.

The observed spatial wavelength of 150 km in east-west structure also deserves some discussion. Keskinen et al. (1980) suggested that the outer scale of gradient-drift-produced structure is always comparable to the initial gradient scale length. This prediction, made on the basis of numerical simulations of an isolated (i.e., no E region) plasma cloud model, would appear to be borne out by our observations. The spatial wavelength of 150 km is only three times the estimated gradient scale length.

All of the theoretical work mentioned above is strictly valid only for an F-region blob that is insulated from a conducting E layer or background ionosphere. More precisely, it is assumed that the integrated Pedersen conductivity along magnetic flux tubes through the F-region blob is much greater than the flux-tube-integrated Pedersen conductivity of the background ionosphere. Although the E-region measurements corresponding to this data set were not available, this assumption is not usually valid in the auroral zone. For example, Vickrey et al. (1980) showed that the ratio of integrated Pedersen

conductivity between the E and F layers can be as large as a factor of 100. Moreover, we have seen from Figure 3 that the background F-layer plasma density is only two to three times smaller than the peak plasma density within the blob. The presence of a conducting background, particularly that of an auroral E layer, leads to several complications.

Perhaps the most obvious effect of a conducting E layer is that of polarization charge neutralization by field-aligned currents that close in the E layer. Because polarization electric fields are responsible for driving the gradient-drift instability as well as the velocity shear mechanism (Perkins and Doles, 1975), we expect a strong reduction of the gradient-drift growth rate and suppression of the velocity shear in the presence of an auroral E layer. As a first guess, we would expect the growth rate to be proportional to  $(1 + \lambda)$  where  $\lambda$  = ratio of the integrated Pedersen conductivity of the blob to that of the background ionosphere (primarily the E layer). Shiau and Simon (1974) analyzed shorting effects of a conducting background and found that all modes for the barium ion cloud case are stable for  $\lambda$  slightly less than 0.5. The critical value of  $\lambda$  for the auroral F-region blob case should be lower because blobs occur at higher altitudes and because larger electric fields and neutral winds are found in the auroral zone, compared to values used by Shiau and Simon (1974). The growth time required to produce the observed east-west structure therefore, is likely to have been much longer than a few tens of minutes. The virtual absence of tilts in the east-west structure also is consistent

with the expected effects of a conducting E layer mentioned above.

Many other complications of auroral F layer instabilities remain to be sorted out. A highly conducting E layer can lead to cross-field diffusion of the F-region at the ion rate rather than at the electron (or ambipolar-diffusion) rate because electrons can move freely up and down field lines to and from the E layer where the ion gas is compressible (Simon, 1955, Vickrey and Kelley, 1982b). On the other hand, the compressibility of the E-region plasma allows images of F-region structure to form in the E layer (at least at small scales), which retards diffusion at those scales in the F layer. Image effects have been considered by Volk and Haerendel (1971), Goldman et al. (1974), Scannapieco et al. (1974), Francis and Perkins (1975), Doles et al. (1976), and Vickrey and Kelley (1982b). Assessment of the ultimate impact of E-region images on F-layer instabilities will require further theoretical work. For example, the fact that E-region images must grow by compressing the ion gas faster than it is recombined by chemistry, means that the formation of images depends on scale size (see, for example, the discussion by Vickrey and Kelley (1982b)). Smaller-scale images grow faster than large scale images. However, the efficiency with which the image "source" electric-field maps from the F layer to the E region decreases rapidly at small scale sizes. These competing effects may lead to a preferred scale size of irregularities in both the E and F layers. Moreover, important effects are associated, with the fact that for a given driving electric field, F-layer irregularities drift rapidly in the Hall direction, whereas the E-

region ion gas that is compressed to form images, drifts substantially in the Pedersen direction. Another complicating effect for E-region images is that the auroral E-region density may be already structured on scale sizes comparable to the image size because of structured particle precipitation. To date, no theoretical investigation has treated all of these mechanisms together.

In summary, direct evidence has been presented for the presence of east-west structure in F-region plasma-density enhancements, or blobs. The spatial dimensions of the blob analyzed in this data set however, should not necessarily be considered typical. Other observations have shown that blobs can extend in longitude over many hundreds of kilometers. Moreover, we do not know whether structuring always occurs with a preferred wavelength of 150 km. A more complete investigation of blob characterization is underway and will be the topic of future papers.

The interpretation of the data set presented as being consistent with ongoing structuring via the gradient-drift process must also be viewed with caution. Although the interpretation is qualitatively consistent with theory, we must recognize the possibility of complicating contributions. For example, it is conceivable that significant structuring via the gradient-drift instability is not possible in the auroral zone (because of the conducting E layer) and that the observed structure is produced by other means or elsewhere (e.g., nighttime polar cap) where E region conductivity effects are less significant.

#### ACKNOWLEDGEMENTS

This work was supported by the Defense Nuclear Agency under contract DNA001-82-C-0021, and by the Air Force Office of Scientific Research under contract F49620-80-C-0014. Radar operations were supported by the National Science Foundation under grant ATM7823658.

# REFERENCES

- Doles, J. H., N. J. Zabusky, and F. W. Perkins, Deformation and striation of plasma clouds in the ionosphere, 3. Numerical simulations of a multilevel model with recombination chemistry, J. Geophys. Res., 81, 5987, 1976.
- Fremouw, E. J., C. L. Rino, R. C. Livingston, and M. C. Cousins, A persistent subauroral scintillation enhancement observed in Alaska, Geophys. Res. Letters, 4, 539, 1977.
- Francis, S. H., and F. W. Perkins, Determination of striation scale sizes for plasma clouds in the ionosphere, J. Geophys. Res., 80, 3111, 1975.
- Goldman, S. R., S. L. Ossakow, and D. L. Book, On the nonlinear motion of a small barium cloud in the ionosphere, J. Geophys. Res., 79, 1471, 1974.
- Keskinen, M. J., and S. L. Ossakow, Nonlinear evolution of plasma enhancements in the auroral ionosphere, 1: Long wavelength irregularities, J. Geophys. Res., 87, 144, 1982.
- Keskinen, M. J., S. L. Ossakow, and B. E. McDonald, Nonlinear evolution of diffuse auroral F region ionospheric irregularities, Geophys. Res. Letters, 7, 573, 1980.
- Keskinen, M. J., B. E. McDonald, and S. L. Ossakow, Preliminary numerical study of the outer scale size of ionospheric plasma cloud striations, J. Geophys. Res., 85, 2349, 1980.
- Linson, M., and J. B. Workman, Formation of striations in ionospheric plasma clouds, J. Geophys. Res., 75, 3211, 1970.
- Ossakow, S. L., and P. K. Chaturvedi, Current convective instability in the diffuse aurora, Geophys. Res. Letters, 6, 332, 1979.
- Ossakow, S. L., P. K. Chaturvedi, and J. B. Workman, High altitude limit of the gradient drift instability, NRL Memorandum Report 3639, Naval Research Laboratory, Washington D.C. (November 1977).
- Perkins, F. W., and J. H. Doles III, Velocity shear and the  $E \times B$  instability, J. Geophys. Res., 80, 211, 1975.
- Rino, C. L., and J. Owen, The structure of localized nighttime auroral-zone scintillation enhancements, J. Geophys. Res., 85, 2941, 1980.

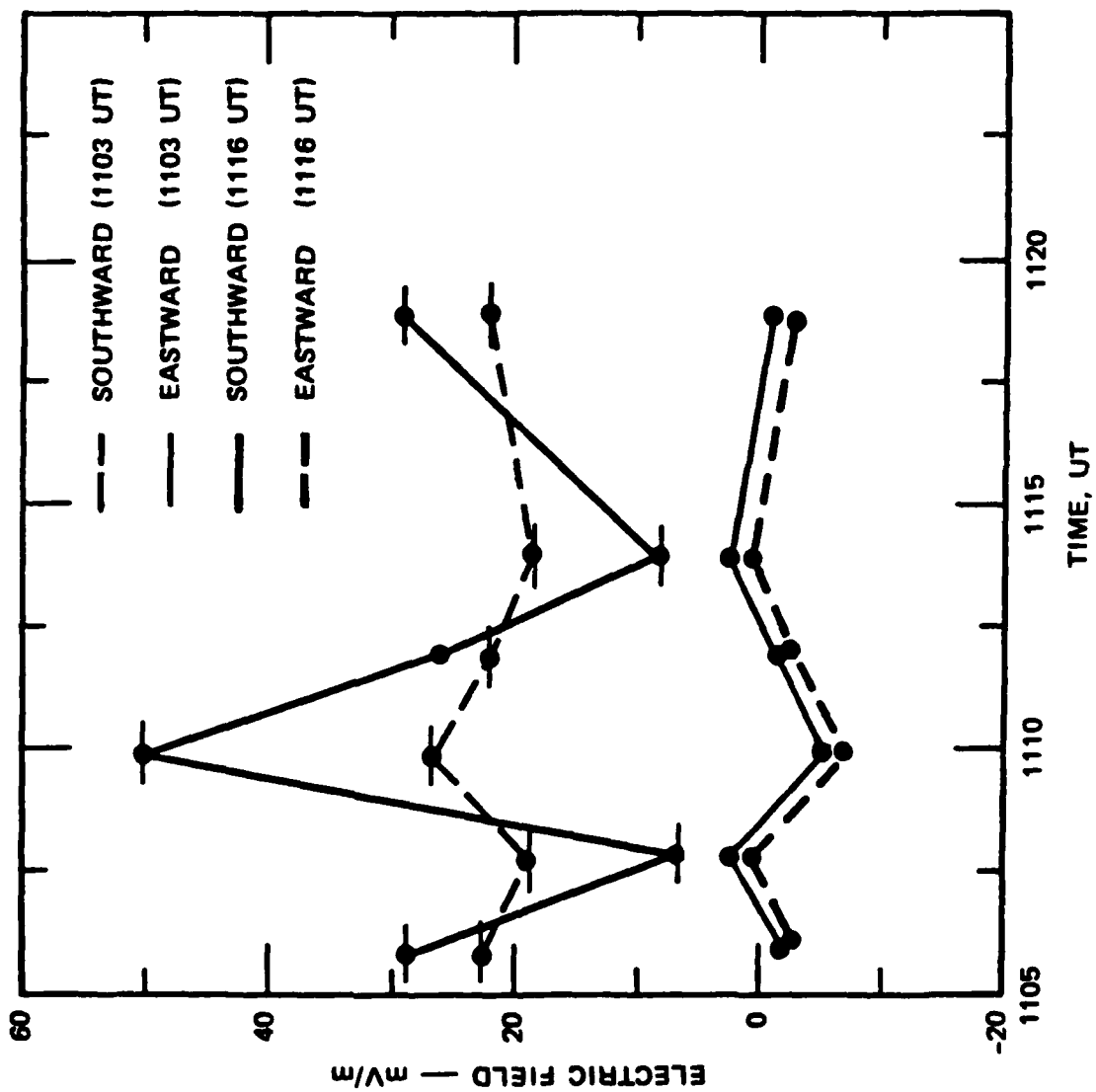
# REFERENCES concluded

- Rino, C. L., R. C. Livingston, and S. J. Matthews, Evidence for sheet-like auroral ionospheric irregularities, Geophys. Res. Letters, 5, 1039, 1978.
- Robinson, R. M., R. R. Vondrak, and T. A. Potemra, Electrodynamic properties of the evening-sector ionosphere within the region 2 field-aligned current sheet, J. Geophys. Res., 87, 731, 1982.
- Scannapieco, A. J., S. L. Ossakow, D. L. Book, B. E. McDonald, and S. R. Goldman, Conductivity ratio effects on the drift and deformation of F region barium clouds coupled to the E region ionosphere, J. Geophys. Res., 79, 2913, 1974.
- Shiau, J., and A. Simon, Barium cloud growth and striation in a conducting background, J. Geophys. Res., 79, 1895, 1974.
- Simon, A., Instability of a partially ionized plasma in crossed electric and magnetic fields, Phys. Fluids, 6, 382, 1963.
- Simon, A., Ambipolar diffusion in a magnetic field, Phys. Rev., 98, 317, 1955.
- Vickrey, J. F., and M. C. Kelly, Irregularities and instabilities in the auroral F region, in High-Altitude Space Plasma Physics (Plenum Publishing Corp., New York, NY, in press, 1982a).
- Vickrey, J. F., and M. C. Kelley, The effects of a conducting E-layer on classical F-region cross-field plasma diffusion, J. Geophys. Res., accepted for publication, 1982b.
- Vickrey, J. F., C. L. Rino, and T. A. Potemra, Chatanika/TRIAD observations of unstable ionization enhancements in the auroral F region, Geophys. Res. Letters, 7, 789, 1980.
- Volk, H. F., and G. Haerendel, Striations in ionospheric ion clouds, 1, J. Geophys. Res., 76, 4541, 1971.
- Watkins, B. J., and P. G. Richards, A theoretical investigation of the role of neutral winds and particle participation in the formation of the auroral F-region ionosphere, J. Atmos. Terr. Phys., 41, 179, 1979.

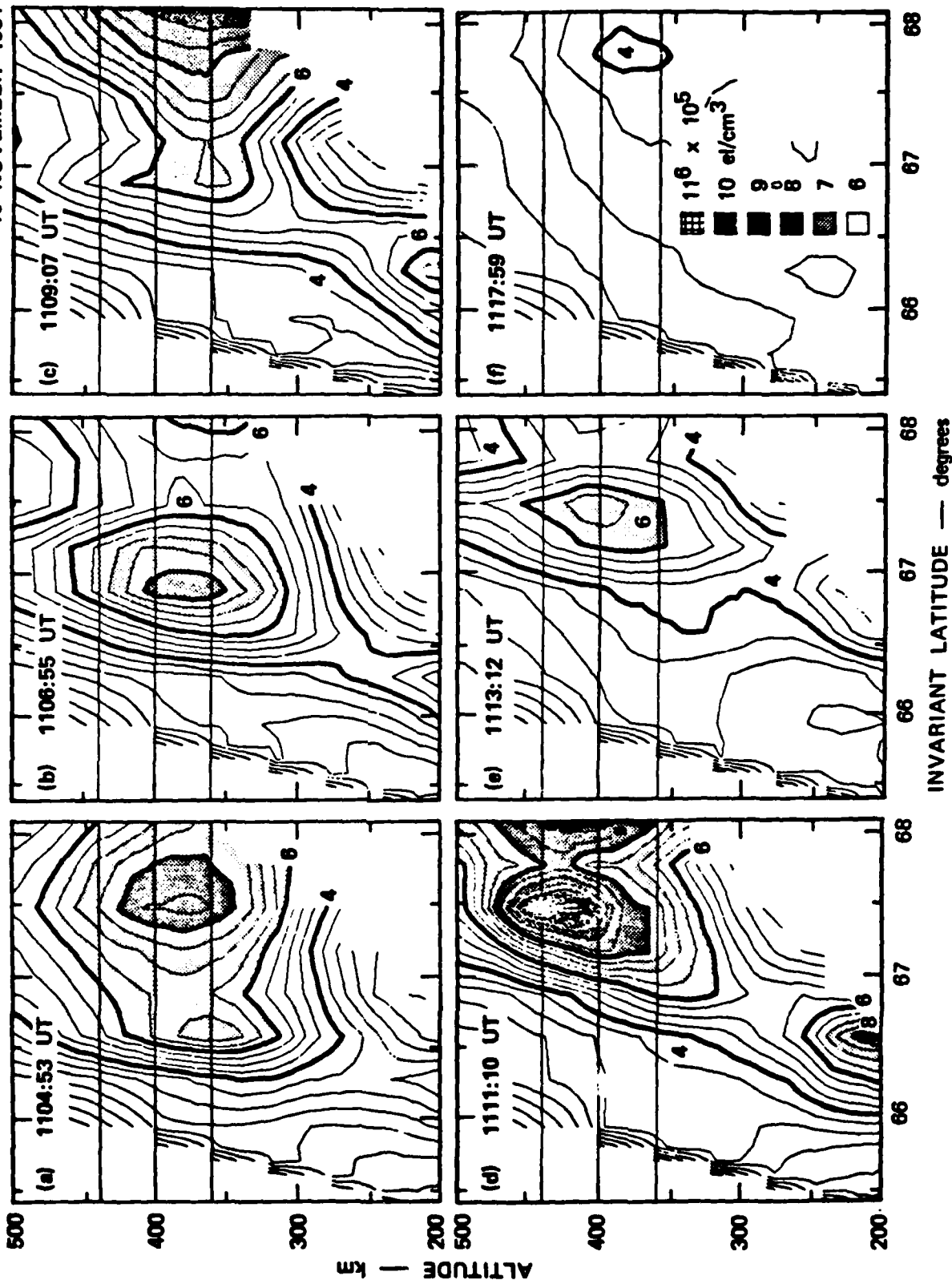


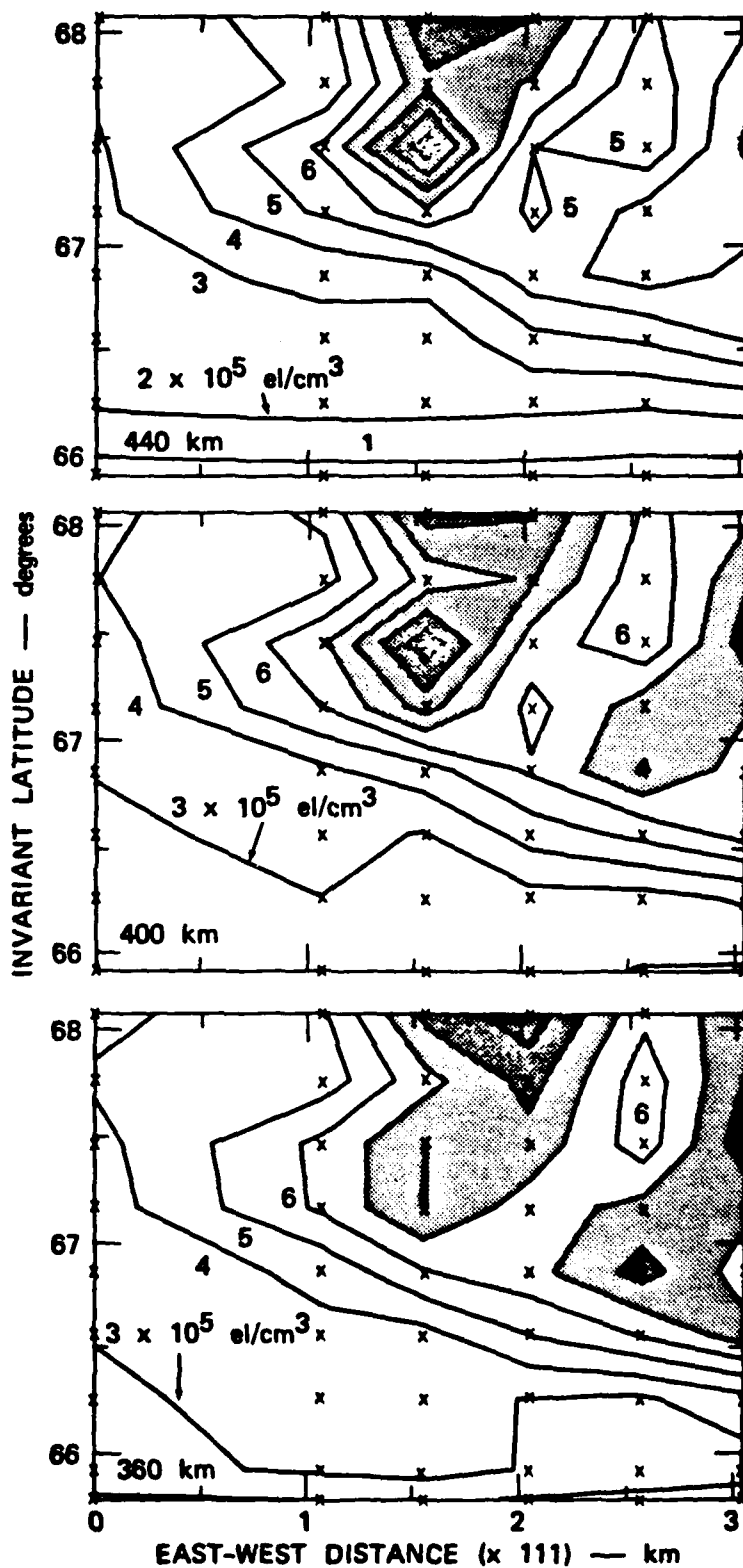
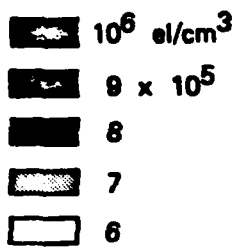
#### LIST OF ILLUSTRATIONS

- 1 The Ionospheric Electric-Field Variations as a Function of time
- 2 Six Meridian-Scan Maps of Isodensity Contours Showing the Variability in Blob Plasma-Density Structure
- 3 Plan Views of Blob East-West Structure, at three Different Altitudes



10 NOVEMBER 1981





RELATIVE CONTRIBUTION OF IONOSPHERIC CONDUCTIVITY AND ELECTRIC FIELD  
TO THE AURORAL ELECTROJETS

By

Y. Kamide

NOAA Space Environment Laboratory

Boulder, Colorado 80303

J. F. Vickrey

Radio Physics Laboratory, SRI International

Menlo Park, California 94025

RELATIVE CONTRIBUTION OF IONOSPHERIC CONDUCTIVITY AND ELECTRIC FIELD  
TO THE AURORAL ELECTROJETS

Y. Kamide

NOAA Space Environment Laboratory

Boulder, Colorado 80303

J. F. Vickrey

Radio Physics Laboratory, SRI International

Menlo Park, California 94025

ABSTRACT

Data from continuous scans of the Chatanika radar beam along the magnetic meridian plane are utilized to determine the latitudinal profile of height-integrated ionospheric conductivities and horizontal electric fields, from which the latitudinal distribution of ionospheric currents is deduced. The observations cover invariant latitudes between  $62^\circ$  and  $68^\circ$ , where the IMS Alaska meridian chain of magnetometers was also in operation. Although the conductivities and the electric fields are interrelated, the relative importance of the two in driving the eastward and westward auroral electrojet currents can be assessed. It is found that for moderate and large current densities (i.e.,  $\gtrsim 0.2$  A/m), the northward electric field strength increases as the magnitude of the eastward electrojet in the evening sector increases. The height-integrated Hall conductivity stays generally at the level of 10 mhos even when the current density becomes as large as 1 A/m. However, when the eastward electrojet is small, substantial electric fields of 10-20 mV/m may still exist as if the magnetosphere has a persistent voltage source. There appear to be two distinct components to the westward electrojet. In the midnight and early morning sectors (<0300 MLT) intensity is characterized by a weak southward electric field and a high Hall conductivity, whereas its late morning portion (>0300 MLT) is dominated by a strong southward electric field.

## 1. INTRODUCTION

In a long history of studies of polar magnetic disturbances, magnetic field vectors observed on the "two-dimensional" earth's surface have been the only tool with which the responsible "three-dimensional" current system was inferred. It is only during the last decade that several new powerful techniques have become available for studying the three-dimensional current system and, as a result, our knowledge of the large-scale current distribution in the ionosphere and magnetosphere as well as the driving electric field has evolved greatly; see Kamide (1982) and Troshichev (1982) for recent reviews on this topic. Polar orbiting satellites established that field-aligned currents (e.g., Zmuda and Armstrong, 1974; Burrows et al., 1976) which supply the major portions of the auroral electrojets are a permanent feature of the magnetosphere. Measurements of the ionospheric electric field from satellites, rockets, balloons, and radars have revealed that, on the average, a two-celled electric potential pattern reflecting magnetospheric convection exists at high latitudes (e.g., Mozer and Lucht, 1974; Heppner, 1977; Greenwald, 1977; Evans et al., 1980). By combining these new observations with improved meridian chain magnetometer observations, it is now possible to discuss the extent to which the ionosphere and magnetosphere are electrically coupled (Kamide et al., 1976; Maurer and Thiele, 1978; Hughes and Rostoker, 1979; Baumjohann et al., 1978, 1980). The first-approximation model of the three-dimensional current system appears to be consistent with computer simulations and theoretical calculations (e.g., Boström, 1964; Swift, 1971; Fukushima, 1971; Wolf, 1974; Kamide and Matsushita, 1979; Harel et al., 1981).

This first-approximation model of the substorm current system is characterized by the eastward and westward electrojets in the regions of the northward and southward electric field, respectively, with a considerable deformation in between at the Harang discontinuity in the premidnight sector. Crucial questions remain, however, regarding the dominant physical processes responsible for the

generation of the auroral electrojets. For example, is it changes in the conductivity ( $\sigma$ ) or electric field  $E$  that is most important in producing enhanced current  $j$  in different regions of the ionosphere? Of course, the conductivity and electric field are not totally independent in the ionosphere, in the sense that the spatial nonuniformity of ( $\sigma$ ) results in changes in  $E$ . However, our interest here is to learn the relative role of the electric field and the conductivity in intensifying the auroral electrojets. For this purpose, it is desirable to measure more than one ionospheric parameter simultaneously at more than one site (see de la Beaujardiere et al., 1977). One of the merits of the Chatanika incoherent scatter radar is that in certain modes of operation, the radar beam is able to probe the altitude/latitude distribution of electron density and line-of-sight plasma drifts from which the electric fields, conductivities, and currents in the ionosphere can be determined (see Banks and Doupnik, 1975; Vondrak, 1982). Using this advantage, the latitudinal structure of the electric fields and conductivities have been examined by Wedde et al. (1977), Horwitz et al. (1978a, b), and Vickrey et al. (1981). However, those studies put their main emphasis on the latitudinal distribution on an event-by-event basis.

In this paper, we present synoptic Chatanika radar observations of the latitudinal structure of the auroral electrojets in a wide local time range. In this way we can assess the relative importance of the electric fields and conductances at different auroral latitude locations. We have selected eight sets of data from continuous observations of more than 12-hrs. duration, which are November 13, December 17, 1976; April 6, December 20, 1977; July 7, July 28, August 10 and August 24, 1978. These same data have been utilized to examine the latitude and local time variations of auroral energy deposition by precipitating particles and Joule heating (see Vickrey et al., 1982). For most of the eight days, data from the IMS Alaska meridian chain of magnetometers were also available.



## 2. EXPERIMENTAL TECHNIQUE AND DATA

The operating mode of the Chatanika radar employed for the measurements discussed in this paper consists of elevation scans in the magnetic meridian. Details on the experimental technique were described in Vondrak and Baron (1976), Vickrey et al. (1981), de la Beaujardiere and Vondrak (1982), Robinson et al. (1982), and Senior et al. (1982). It takes 10 to 12 min. for each complete scan to cover, in the E region, invariant latitudes from  $62^\circ$  to  $68^\circ$ . Electron density samples were obtained at intervals of 4.5 km from 70 km to 700 km altitude. The height-integrated Pedersen and Hall conductivities ( $\Sigma_p$  and  $\Sigma_H$ , respectively) were then calculated from the measured electron density profile and a neutral atmosphere model. As discussed by Vickrey et al. (1981), a suitable reduction factor for the collision frequency coefficient has been taken, resulting in a (5% to 30%) reduction of the height-integrated conductivity values over those calculated in previous studies (e.g., Brekke et al., 1974; Horwitz et al., 1978a). This point is important, however, only for direct comparisons, because the absolute collision frequency profile, as well as the neutral density, are poorly known and produce uncertainties in  $\Sigma$  that are larger than this difference.

Another important difference between the technique used in the present study and those of, for example, Horwitz et al. (1978a, b) and Foster et al. (1981a, b) is the inference of two component electric field vectors from the measured line-of-sight ion velocities. In those studies, velocities were combined from off-meridian points (at slightly different local time) to determine the east-west ion drift. Since, for the present data set, the antenna line-of-sight was constrained to lie within the magnetic meridional plane, no direct measurement of the north-south electric field component (east-west ion drift in the F region) was made. This component can be inferred, however, by using the method described by Doupnik et al. (1977) and de la Beaujardiere et al. (1977, 1981). Briefly, if one assumes that the ion velocity component parallel to  $\mathbf{B}$

Table 1. Location of the IMS Alaska Chain of Magnetometer Stations Whose Data Are Used in the Present Study

<u>Station (Code)</u>		<u>Geographic</u>		<u>Invariant Latitude</u>
		<u>Latitude</u>	<u>Longitude</u>	
Sachs Harbor	(SAH)	72.0°	235.9°	76.1°
Cape Parry	(CPY)	70.2°	235.3°	74.5°
Inuvik	(INK)	68.3°	226.7°	71.0°
Arctic Village	(AVI)	68.1°	214.4°	68.3°
Fort Yukon	(FYU)	66.6°	214.7°	66.8°
College	(COL)	64.9°	212.0°	64.7°
Talkeetna	(TLK)	62.3°	209.9°	62.7°
Anchorage	(ANC)	61.2°	210.2°	60.6°
Chatanika	(CHA)	65.1°	212.4°	64.8°

To compare properly the meridian chain magnetometer records with the ionospheric information derived from the radar measurements, the amplitudes of each of the H and Z component perturbations were plotted as a function of invariant latitude for the time of the radar operation. Such latitudinal profiles were then interpreted by using a standard technique to infer the latitudes of the auroral electrojets in terms of key parameters such as the center and the breadth of the electrojets. See Kisabeth (1972) and Rostoker (1972) for a detailed description of the technique, and Kamide and Rostoker (1977) for its application. We estimate that it is possible to locate the auroral electrojets to accuracy  $<1^\circ$  invariant latitude.

### 3. OBSERVATIONS

Figure 1 shows, as an example, H component magnetograms for the Alaska meridian chain of magnetic observatories along with the AU and AL indices for July 7, 1978.

During the interval of the Chatanika radar operation (0400-1600 UT), continuous substorm activity of considerable magnitude occurred. Thus, this data set is ideal for examining the relationship between the auroral electrojets and the electric field and conductivity as a function of local time under substorm conditions. To represent the radar and ground magnetic observations along the Alaska meridian, three epochs, A, B and C, have been chosen and marked by vertical lines in Figure 1. The latitudinal profiles of electric field, height-integrated conductivity, ionospheric current density, and ground magnetic H and Z perturbations corresponding to these three epochs are displayed in Figures 2a, b, and c, respectively. The coordinate system used in the diagram is such that X and Y are directed geomagnetic east and north, respectively.

The epoch A was chosen because the positive H perturbations, an indication of the eastward electrojet, at AVI, FYU and COL were about to reach their maximum and because the Chatanika radar data were of very high quality. As seen from Figure 1, the AU index was reaching about 200 nT (at Cape Chelyuskin), 150° west of Alaska. This indicates that the Alaska chain was located at nearly the eastern end of the eastward electrojet. Since it takes 12 minutes for the radar to make a complete scan along the meridian, the plotted ground magnetic perturbations represent average values for the 0938-0950 interval. The scatter in the H and Z amplitudes over this time period was only ~10%. It is further noted that there is a gap in the electric field measurement in the vicinity of the Chatanika radar site. This is caused by unacceptably large errors in the derived ion drift velocity when the radar is looking nearly antiparallel to the direction of the local magnetic field line.

With these provisions in mind, several points of interest are evident from Figure 2a. First, the electric field features a relatively large northward component. This northward field strength tends to increase monotonically with increasing latitude up to 67.5°, in agreement with Horwitz et al. (1978a), and

then decreases rather sharply with latitude (20 mV/m per  $0.5^\circ$ ). Although the east-west component of the electric field is generally small ( $<5$  mV/m), there is an indication of an increasing westward field near the poleward edge of the region containing a northward field, perhaps signifying the Harang discontinuity (Maynard, 1974). Second, the maximum height-integrated Hall and Pedersen conductivities,  $\Sigma_H$  and  $\Sigma_P$ , are 6 mhos and 5 mhos, respectively. These are in reasonable agreement with earlier observations by Vickrey et al. (1981) who have shown that the Hall and Pedersen conductivities within the diffuse aurora are generally 4-12 mhos and 2-6 mhos, respectively. Although no optical auroral data were available for this date because of the northern summer sunlit conditions, it can be inferred on the basis of past experience (e.g., Kamide and Rostoker, 1977) that the northward field is embedded in the diffuse aurora in the premidnight sector. The ratio  $\Sigma_H/\Sigma_P$ , a measure of the hardness of auroral particle precipitation, is not high (between 1 and 1.3), indicating also that less bright, structureless aurora and a sunlit E layer probably dominate the conductivity pattern at this time. A third point of interest is that the ionospheric current has a northward component throughout the latitude region surveyed. This region is within the so-called eastward electrojet. Finally, we note that the center of the eastward electrojet deduced from the radar measurements agrees with that estimated from the crossover point of the latitudinal Z component profile, both giving  $66.0$ - $66.5^\circ$  invariant latitude for the electrojet center. It is of interest to see that this location coincides with the point where the Hall conductivity, not the northward electric field, is maximum. Note, however, that an additional current peak exists at  $67.5^\circ$ , reflecting the maximum of the electric field as well as of  $\Sigma_H$ .

In Figure 2b, we show a similar comparison for the westward electrojet in the midnight sector. The epoch B corresponds to the maximum phase of an intense substorm which happened to take place with the electrojet center (in longitude) fortunately located at the Alaska chain. Comparing this profile with that in Figure 2a, one can notice significant changes which occur between the evening eastward electrojet and midnight sector westward electrojet. One striking feature

is that the relative contribution of the electric field and the conductivity to the auroral electrojet is reversed: In Figure 2b the southward electric field is less intense than the northward field in Figure 2a, whereas both the Hall and Pedersen conductivities are much larger than those in the eastward electrojet. The net result is a larger current density in the westward electrojet.

From a more detailed spatial comparison of the latitudinal profiles of these parameters, the following points are noticed: (1) In the main body of the westward electrojet, the electric field is directed southward as well as westward. This corresponds to the region just eastward of the Harang discontinuity in the large-scale electric field pattern (see Heppner, 1977). The magnitude of the electric field is generally less than  $\sim 10$  mV/m. Equatorward of  $63^\circ$ , the electric field has a large northward component. The apparent discontinuity in the westward field near the radar site is a result of the radar pointing as was already discussed. (2) With the southward turning of the electric field, the Hall conductivity is enhanced significantly (maximum  $\Sigma_H = 40$  mhos at  $66.7^\circ$ ), with small-scale latitudinal variations. On the other hand, the Pedersen conductivity does not change very much along the meridian, making the  $\Sigma_H/\Sigma_P$  ratio variable as a function of latitude. (3) The westward electrojet has a northward component as well. The center of the electrojet ( $66.5^\circ$ - $67.0^\circ$ ) appears to be determined by the maximum in the Hall conductivity. This center is in agreement with that inferred from the latitudinal profile of the ground magnetic perturbations, i.e.,  $\Delta Z = 0$  and  $\Delta H = \text{minimum}$ . (4) Although it is not possible to determine accurately the equatorward boundary of the electrojet because of the lack of Z perturbation records south of COL, there is an indication that  $\Delta H$  is negative even in the region of eastward current. Thus, this indicates that the common practice of using the magnetic H component records to infer the east-west ionospheric current direction can at times be in error.

The epoch C (Figure 2c) occurred when the Chatanika radar and the Alaska magnetometer chain were observing signatures of the morning sector westward electrojet. At the epoch C, the westward electrojet at COL, the nearest station to the Chatanika radar, reached its maximum stage, although the maximum phase of the entire substorm was attained at a later time (see Figure 1).

The latitudinal profile of the ionospheric current indicates that the westward electrojet was flowing in the region between  $63^{\circ}$  and  $68^{\circ}$ , having a northward (southward) component in the equatorward (poleward) half of the electrojet. The fact that the center of the westward electrojet is located in the vicinity of Chatanika makes it difficult to assign a single value for the center, but from the cross-over point of the  $\Delta Z$  profile by a simple linear interpolation of the COL and FYU values, it is inferred that the latitude of the electrojet center is a little north of COL, most probably at  $65.2^{\circ}$ .

An interesting feature of the latitudinal profiles of the electric field and the conductivities is that in the equatorward half of the westward electrojet in this local time sector, the conductivity was high while the electric field was small. The situation is reversed in the poleward half, where the southward electric field was very intense (note the scale change between Figure 2c and Figures 2a and 2b) but the conductivities dropped drastically. This implies that bright auroras and the corresponding energetic electron precipitation were present only in the equatorward half of the morning westward electrojet. The center of the electrojet (defined by the  $\Delta Z$  cross-over) seems to be located in the region sandwiched by two peaks in the southward electric field and the conductivity in this particular case.

#### 4. STATISTICAL RESULTS

The observations displayed in the previous section indicate that the magnitude of the auroral electrojets are dominated by different ionospheric parameters in different regions. In this section, we examine the local time dependence of these

parameters using a bulk data set. From the eight days of Chatanika operations listed in the Introduction, a total of 160 12-min. intervals have been selected. Noisy data were excluded along with any complicated latitudinal profiles in which multiple peaks in the east-west current density were present. These 160 cases span a variety of substorm activity and local time sectors. For each of the cases, the location of the electrojet center (eastward or westward) was first identified on the basis of either the radar-measured  $j_x$  or the ground magnetic perturbations, or both. Then, the Hall conductivity and the north-south electric field were determined along with the geomagnetic local time (MLT) at the electrojet center. Figures 3 and 4 show the statistical results of this study.

Figure 3a is a scatter plot of the Hall conductivity and the east-west ionospheric current density at the center latitude of the auroral electrojets. From this relationship, one may be able to gain some insight into the degree of the conductivity contribution to the auroral electrojet. Different symbols are used to distinguish the eastward electrojet and westward electrojet. The points for the westward electrojet are grouped into two categories corresponding to times before and after 0300 MLT. The choice of 0300 MLT as a dividing time is somewhat arbitrary but turned out to best order the points as a whole.

In Figure 3b the north-south electric field is plotted against the east-west ionospheric current in a format similar to Figure 3a. From this we can discern the different behavior of the electric field in the different temporal regimes of the auroral electrojets.

In spite of the considerable scatter in Figures 3a and 3b, it is apparent that the eastward electrojet in the evening sector and the westward electrojet during local times after 0300 MLT have statistically a common character. Namely, when the current intensity is relatively small, say  $|j_x| < 0.2$  A/m, the increase in the current density appears to be caused by an increase in both the conductivity and the electric field. A least-squares fit to both the eastward electrojet and the

late morning westward electrojet within  $|j_x| < 0.2$  gives that  $\Sigma_H = 50 |j_x|$  and  $|E_y| = 15 + 80 \cdot |j_x|$ . These relations are, at first, puzzling because we normally consider the electrojets to be purely Hall currents; i.e.,  $j_x = \Sigma_H E_y$ . If this were true then the first relation would imply that the electric field were constant at 20 mV/m and independent of  $j_x$ , whereas the second implies a linear relationship between the two. The problem arises partially because of the assumption of a pure Hall current. We see, for example, in Figures 2a and 2c that  $\Sigma_H > \Sigma_P$  but  $\Sigma_P$  is certainly not negligible. It is also important to note that  $E_y$  remains at the level of 10-30 mV/m, even when  $j_x$  approaches zero. Between the eastward electrojet and the late morning westward electrojet, there are some differences as well which should also be pointed out. First, in Figure 3a the strength of the eastward electrojet does not become very large, whereas the westward electrojet can become large, say more than 1 A/m. In our data set, all the points for the eastward electrojet are less than 0.9 A/m. Second, the conductivity in regions where the eastward electrojet exceeds 0.2 A/m does not increase very much with increasing current strength. This means that the increase in the current density is accomplished mainly by the increase in the northward electric field, a tendency clearly seen in Figure 3b. On the other hand, in the region of the westward electrojet in the late morning sector, the conductivity as well as the southward electric field still continues to increase substantially with increasing current strength.

However, such differences are relatively minor, when contrasted with differences between the eastward electrojet and the westward electrojet in the midnight sector earlier than 0300 MLT. It is a striking feature in Figures 3a and 3b that the points corresponding to the westward electrojet in the premidnight and early morning sectors are well separated from those for the eastward electrojet. Conductivity values for the midnight sector westward electrojet are significantly higher, on the average, than those for the same intensity of the eastward



electrojet and of the westward electrojet in the late morning sector. This feature has been pointed out by Brekke et al. (1974), Horwitz et al. (1978a), and Vickrey et al. (1981). For example, in an evening eastward or late morning westward current of 0.5 A/m, a Hall conductivity of 10-20 mhos is typical, while the Hall conductivity ranges from 20 to 50 mhos for the same magnitude of the midnight sector westward electrojet. In contrast, the intensity of the southward field in the midnight sector westward electrojet is relatively small ( $\sim 10$  mV/m).

In order to further clarify the different roles and the relative importance of the conductivity and electric field in the different electrojet regions we plot in Figure 4 the ratio  $\Sigma_H/|E_y|$  as a function of magnetic local time. If we use commonly adopted units, mho and mV/m, the average ratio for the eastward electrojet is found to be 0.40, whereas that for the midnight sector westward electrojet before 0300 MLT is 3.71. The Hall conductivity to the midnight sector westward electrojet is sometimes 15 times larger than that in the eastward electrojet. The average ratio of  $\Sigma_H$  and  $E_y$  for the westward electrojet in the late morning sector (1.39) is smaller than the midnight electrojet, but somewhat larger than that in the eastward electrojet.

## 5. DISCUSSION

In this paper observations of the auroral electrojets by the Chatanika radar and the IMS Alaska meridian magnetometer chain have been combined to examine the different roles of ionospheric conductivities and electric fields in controlling the strength of the auroral electrojets in different local time sectors. Until the last decade, studies of the auroral electrojet current had relied primarily upon magnetic records obtained on the earth's surface. From the distribution of the ground magnetic perturbations, however, it was possible to infer only the equivalent current vectors. The availability of electron density and ion drift data from the Chatanika incoherent scatter radar has opened a new era of unveiling the cause of the large-scale ionospheric currents flowing in the auroral oval

(Brekke et al., 1974), since the radar observations make it possible to deduce the ionospheric conductivities and electric fields simultaneously. Of course, sounding rockets are also able to sense simultaneously variations in several parameters of the ionosphere (e.g., Maynard et al., 1977; Evans et al., 1977; Theile and Wilhelm, 1980, Marklund et al., 1982; Ziesolleck et al., 1982), but those rocket measurements are able to survey only a relatively small-scale portion of the auroral current system and for only a brief time.

It has been shown in the previous sections that in the region of the eastward electrojet in the evening sector, the northward electric field is the main contributor to the magnitude of electrojet current, in the sense that the field magnitude is larger, compared to the southward field magnitude in the westward electrojet. However, when the eastward electrojet is very weak, say  $j_x < 0.2$  A/m, the electric field can maintain a reasonably large value of 10-20 mV/m. It is thus possible that the intensification of an already moderate eastward electrojet is mainly caused by an enhancement of the northward electric field. If the eastward electrojet current density is very small, however, any increase or decrease may depend on small changes (maximum 10 mhos) in the Hall conductivity. The eastward electrojet is known to develop in the diffuse aurora (Tsunoda et al., 1976) that is probably caused by relatively low-energy precipitating particles. It is important to note that in the region of the eastward electrojet, the Hall and Pedersen conductivities seem to change in unison (Vickrey et al., 1981), but the Pedersen currents are associated with the northward electric field connected to field-aligned currents in this region (Baumjohann et al., 1980).

Another point of interest found in the present study is that there may be essentially two modes of the westward electrojet; one in which the contributions to the electrojet magnitude are "conductivity dominant" (see discussion below) and the other "electric field dominant," (as was discussed above for the eastward electrojet. The exact classification into these two modes of the westward electrojet using observed data is difficult, however, because the corresponding currents are

contiguous everywhere. In this paper, by paying attention only to the latitudinal center of the westward electrojet, it has been shown statistically that the westward electrojet near midnight and in early morning hours is characterized mainly by the relatively high Hall conductivity, whereas the westward electrojet in the late morning sector is dominated by the large southward electric field. The latter behavior is similar to that of the eastward electrojet in the evening sector, although the sense of the electric field is reversed. However, an important difference is that the Hall conductivity can become high in the late morning westward electrojet (as high as 50 mhos) while the maximum conductivity for the evening eastward electrojet was less than 20 mhos in our data set. The high conductivity values in the morning electrojet are probably generated by keV electron precipitation in patchy auroras, moving eastward from the midnight sector with the development of substorms. In other words, both the southward field and the Hall conductivity appear to be important contributors to the intense westward electrojet in the late morning sector.

It is important to illustrate that the behavior we have described is not restricted to the center of the electrojets. In Figure 5, we show data from a Chatanika radar experiment during a moderate magnetic storm on April 16, 1973. This time interval was characterized by the frequent occurrence of substorms, giving us an opportunity to examine the local time dependence of ionospheric parameters under continuously disturbed conditions. We emphasize, however, that those parameters do not necessarily represent the center of the auroral electrojets. The electric field was large and northward in the evening sector and the conductivity was from the beginning of the radar experiment to approximately 0830 UT.

The north-to-south turning of the electric field between 0830 and 1000 UT was characterized by complicated fluctuations in the field direction. This transition corresponds to the Harang discontinuity. Between 1000 and 1300 UT, the southward electric field was relatively small ( $<30$  mV/m), but there were large

changes in the Hall conductivity and only small changes in the Pedersen conductivity. This conductivity behavior suggests the sporadic precipitation of electrons with energies of several keV and more. This region near midnight is where the substorm westward electrojet is most intense. It should be noted that the region of the high conductivity westward electrojet tends to penetrate into the evening sector along the poleward boundary of the eastward electrojet. This penetration is presumably associated with a westward traveling surge, although such a feature cannot be seen in Figure 5, since the radar was not operated in a meridian-scan mode.

Later in the morning sector (until about 1900 UT), the westward electrojet was driven by a comparatively large southward electric field (maximum 60 mV/m). The Hall conductivity in this local time sector was lower than that in the midnight sector, although much higher than in the evening sector. Note that the peak intensity of the morning westward electrojet was of the same order as the peak of the midnight electrojet (i.e., 1.5-2.0 A/m) generating  $\sim 800$  nT negative H excursions at College (see Kamide and Brekke, 1977).

In summary, a schematic diagram is presented in Figure 6. The Harang discontinuity is clearly manifested as a switch from the eastward electrojet to the westward electrojet, and in more detail as a switch from the "electric field-dominant" electrojet to the "conductivity-dominant" electrojet. The relative location of the conductivity switch with respect to the Harang discontinuity is still uncertain, partly because the Harang discontinuity has a finite thickness within which the electrodynamic nature of the ionospheric quantities changes in a complicated fashion (Kamide, 1978). The boundary between the conductivity dominant and the electric field dominant westward electrojet is not as clear as is indicated in Figure 6. However, an important point is that, although it has been a common practice to assume that the westward electrojet is associated during substorms with a conductivity enhancement, a part of the westward electrojet in

the later morning sector can be intensified without having high conductivity values. In particular, the latitudinal profile of the westward electrojet in the early morning sector (0100-0300 MLT) would indicate that its poleward portion has a relatively strong southward electric field while its equatorward portion has a relatively high Hall conductivity, as reported recently by Ziesolleck et al. (1982). Using simultaneous measurements of horizontal ionospheric and field-aligned currents by the Chatanika radar and Triad, respectively, Senior et al. (1982) have found that downward field-aligned currents are the dominant feature of the poleward half of the morning westward electrojet where the southward electric field is relatively large. It is interesting in this connection to ask whether or not the auroral oval includes this poleward half of the westward electrojet, where we do not necessarily expect intense auroral forms. It is also interesting to speculate whether the eastward electrojet in the evening sector and the westward electrojet in the late morning sector may be driven by a voltage source in the magnetosphere, while the substorm westward electrojet in the midnight sector is supplied from a current source by, for example, the disruption of the magnetotail current.

#### ACKNOWLEDGMENTS

We would like to acknowledge helpful discussions with S.-I. Akasofu, B.-H. Ahn, and A. D. Richmond during the preparation of this paper. The work at NOAA Space Environment Laboratory was sponsored by the National Research Council under a Resident Research Associateship granted to Y. Kamide. The work at SRI International was supported by the Air Force Office of Scientific Research under Contract F49620-80-C-0014. Radar operations were supported by the Defense Nuclear Agency under Contract DNA001-77-C-0042.

#### REFERENCES

- Banks, P. M., and J. R. Doupnik, "A review of auroral zone electrodynamics deduced from incoherent scatter radar observations," J. Atmos. Terr. Phys., 37, 951, 1975.
- Baumjohann, W., R. A. Greenwald, and F. Küppers, "Joint magnetometer array and radar backscatter observations of auroral currents in Northern Scandinavia," J. Geophys. Res., 44, 373, 1978.
- Baumjohann, W., J. Untiedt, and R. A. Greenwald, "Joint two-dimensional observations of ground magnetic and ionospheric electric fields associated with auroral zone currents, 1. Three-dimensional current flows associated with a substorm-intensified eastward electrojet," J. Geophys. Res., 85, 1963, 1980.
- Boström, R., "A model of the auroral electrojets," J. Geophys. Res., 69, 4983, 1964.
- Brekke, A., J. R. Doupnik, and P. M. Banks, "Incoherent scatter measurements of E region conductivities and currents in the auroral zone," J. Geophys. Res., 79, 3773, 1974.
- Burrows, J. R., M. D. Wilson, and I. B. McDiarmid, "Simultaneous field-aligned current and charged particle measurements in the cleft," in Magnetospheric Particles and Fields, edited by B. M. McCormac, pp. 111, D. Reidel, Hingham, Mass., 1976.
- de la Beaujardiere, O., R. Vondrak, and M. Baron, "Radar observations of electric fields and currents associated with auroral arcs," J. Geophys. Res., 82, 5051, 1977.
- de la Beaujardiere, O., and R. Vondrak, "Chatanika radar observations of the electrostatic potential distribution of an auroral arc," J. Geophys. Res., 87, 797, 1982.
- Doupnik, J. R., A. Brekke, and P. M. Banks, "Incoherent scatter radar observations during three sudden commencements and a Pc 5 event on August 4, 1972," J. Geophys. Res., 82, 499-514, 1977.

- Evans, D. S., N. C. Maynard, J. Trøim, T. Jacobsen, and A. Egeland, "Auroral vector electric field, and particle comparisons, 2. Electrodynamics of an arc," J. Geophys. Res., 82, 2235, 1977.
- Evans, J. V., J. M. Holt, W. L. Oliver, and R. H. Wand, "Millstone Hill incoherent scatter observations of auroral convection over  $60^\circ \leq \Lambda \leq 75^\circ$ , 2, Initial results," J. Geophys. Res., 85, 41, 1980.
- Foster, J. C., J. R. Doupnik, and G. S. Stiles, "Ionospheric convection and currents in the midnight sector on November 8, 1979," J. Geophys. Res., 86, 2143-2148, 1981a.
- Foster, J. C. J. R. Doupnik and G. S. Stiles, "Large-scale patterns of auroral ionospheric convection observed with the Chatanika radar," J. Geophys. Res., 86, 11357-11,371, 1981b.
- Foster, J. C., P. M. Banks, and J. R. Doupnik, "Electrostatic potential in the auroral ionosphere derived from Chatanika radar observations, J. Geophys. Res., 87, 7513-7524, 1982.
- Fukushima, N., "Electric current systems for polar substorms and their magnetic effect below and above the ionosphere," Radio Sci., 6, 269, 1971.
- Greenwald, R. A., "Recent advances in the use of radar auroral backscatter to measure ionospheric electric fields," in Dynamical and Chemical Coupling Between the Neutral and Ionized Atmosphere, edited by B. Grandal and J. A. Holtet, pp. 291, D. Reidel, Hingham, Mass., 1977.
- Harel, M., R. A. Wolf, P. H. Reiff, R. W. Spiro, W. J. Burke, F. J. Rich, and M. Smiddy, "Quantitative simulation of a magnetospheric substorm, 1. Model logic and overview," J. Geophys. Res., 86, 2216, 1981.
- Heppner, J. P., "Empirical models of high-latitude electric field," J. Geophys. Res., 82, 1115, 1977.

- Horwitz, J. L., J. R. Doupnik, and P. M. Banks, "Chatanika radar observations of the latitudinal distributions of auroral zone electric fields, conductivities, and currents," J. Geophys. Res., **83**, 1463, 1978a.
- Horwitz, J. L., J. R. Doupnik, P. M. Banks, Y. Kamide, and S.-I. Akasofu, "The latitudinal distributions of auroral zone electric fields and ground magnetic perturbations and their response to variations in the interplanetary magnetic field," J. Geophys. Res., **83**, 2071, 1978b.
- Hughes, T. J., and G. Rostoker, "A comprehensive model current system for high latitude magnetic activity - I. The steady state system," J. R. Astr. Soc., **58**, 525, 1979.
- Kamide, Y., "On current continuity at the Harang discontinuity," Planet Space Sci., **26**, 237, 1978.
- Kamide, Y., "The relationship between field-aligned currents and the auroral electrojets: A review," Space Sci. Rev., **31**, 127, 1982.
- Kamide, Y. R., and A. Brekke, "Altitude of the eastward and westward auroral electrojets," J. Geophys. Res., **82**, 2851, 1977.
- Kamide, Y., and S. Matsushita, "Simulation studies of ionospheric electric fields and currents in relation to field-aligned currents, 1. Quiet periods," J. Geophys. Res., **84**, 4083, 1979a.
- Kamide, Y., and G. Rostoker, "The spatial relationship of field-aligned currents and auroral electrojets to the distribution of nightside auroras," J. Geophys. Res., **82**, 5589, 1977.
- Kamide, Y., F. Yasuhara, and S.-I. Akasofu, "A model current system for the magnetospheric substorm," Planet. Space Sci., **24**, 215, 1976b.
- Kisabeth, J. L., "The dynamical development of the polar electrojets," Ph.D. thesis, Univ. of Alberta, Edmonton, 1972.

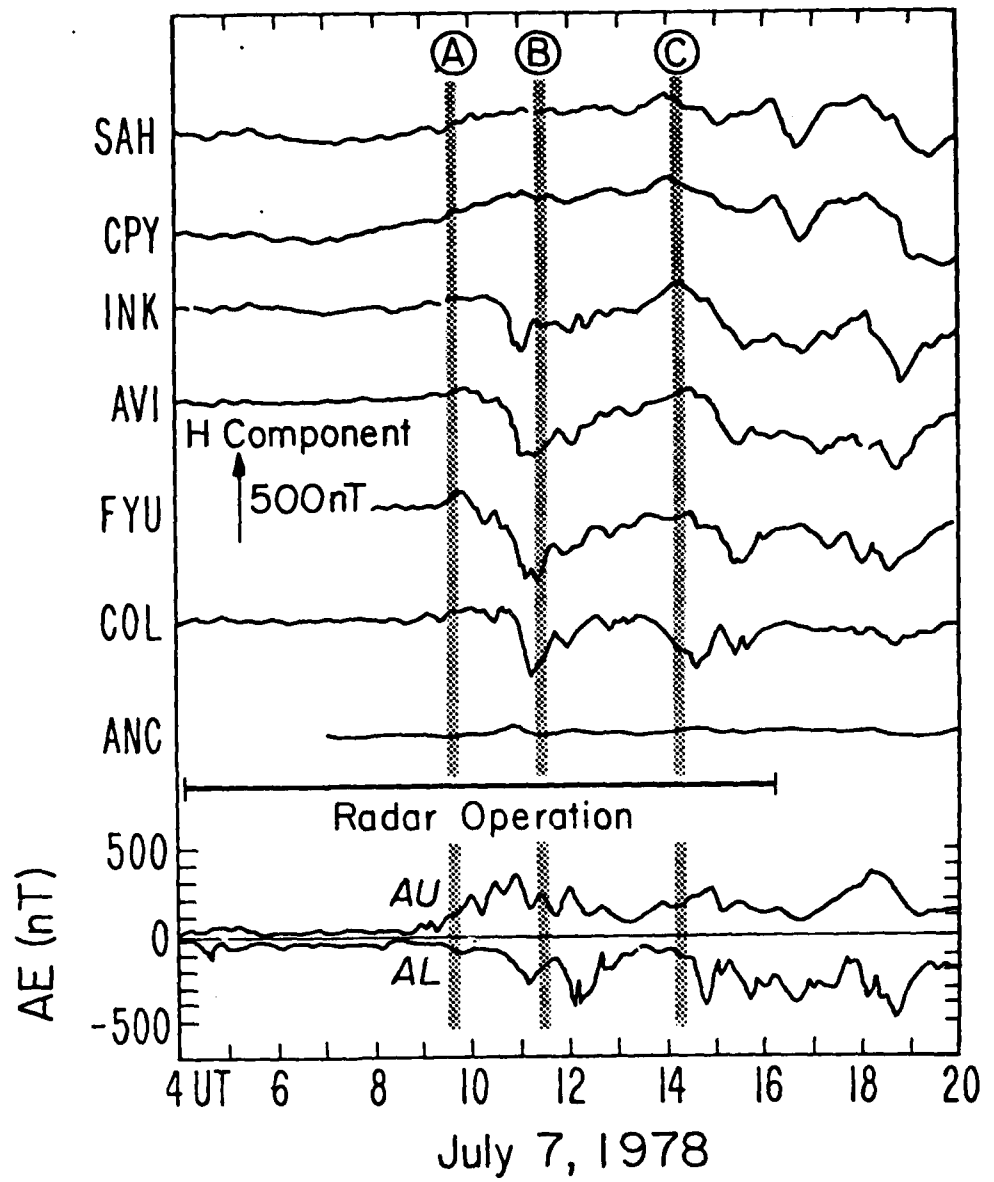


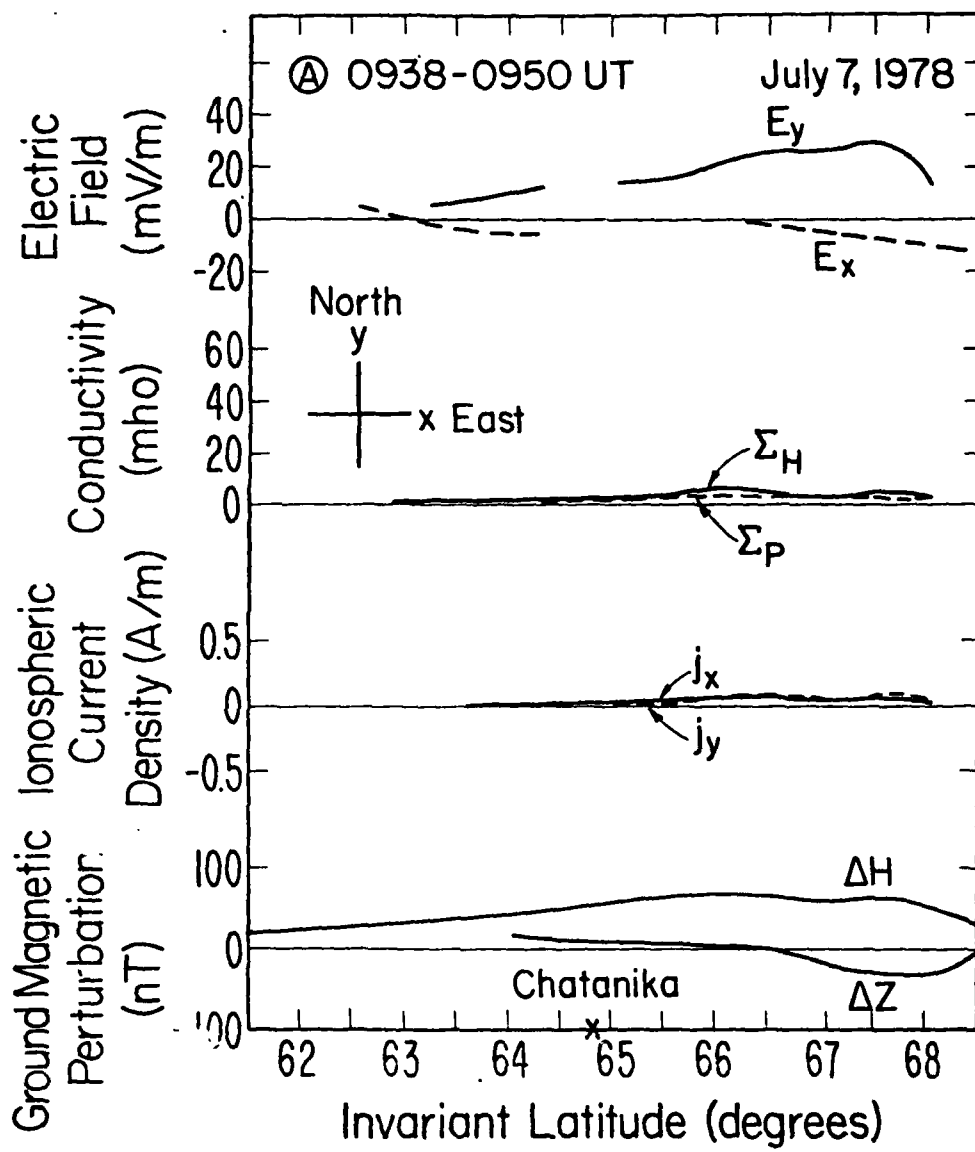
- Marklund, G., W. Baumjohann,, and I. Sandahl, "Rocket and ground-based study of an auroral breakup event," Planet. Space Sci., 30, in press, 1982.
- Maurer, H., and B. Theile, "Parameters of the auroral electrojet from magnetic variations along a meridian," J. Geophys. Res., 44, 415, 1978.
- Maynard, N. C., "Electric field measurements across the Harang discontinuity," J. Geophys. Res., 29, 4620, 1974.
- Maynard, N. C., D. S. Evans, B. Maehlum, and A. Egeland, "Auroral vector electric field and particle comparisons, 1. Premidnight convection topology," J. Geophys. Res., 82, 2227, 1977.
- Mikkelsen, I. S., T. S. Jorgensen, M. C. Kelley, M. F. Larsen, E. Pereira, and J. F. Vickrey, "Neutral winds and electric fields in the dusk auroral oval, 1, measurements," J. Geophys. Res., 86 1513-1524, 1981.
- Mozer, F. S., and P. Lucht, "The average auroral zone electric field," J. Geophys. Res., 79, 1001, 1974.
- Robinson, R. M., R. R. Vondrak, and T. A. Potemra, "Electrodynamic properties of the evening sector ionosphere within the region 2 field-aligned current sheet," J. Geophys. Res., 87, 731, 1982.
- Rostoker, G., "Interpretation of magnetic field variations during substorms," in Earth's Magnetospheric Processes, edited by B. M. McCormac, p. 379, D. Reidel, Hingham, Mass., 1972.
- Senior, C., R. M. Robinson, and T. A. Potemra, "Relationship between field-aligned currents, diffuse auroral precipitation, and the westward electrojet in the early morning sector," J. Geophys. Res., 87, 10469, 1982.
- Swift, D. W., "Possible mechanisms for formation of the ring current belt," J. Geophys. Res., 76, 2276, 1971.
- Thiele, B., and K. Wilhelm, "Field-aligned currents above an auroral arc," Planet. Space Sci., 28, 351, 1980.

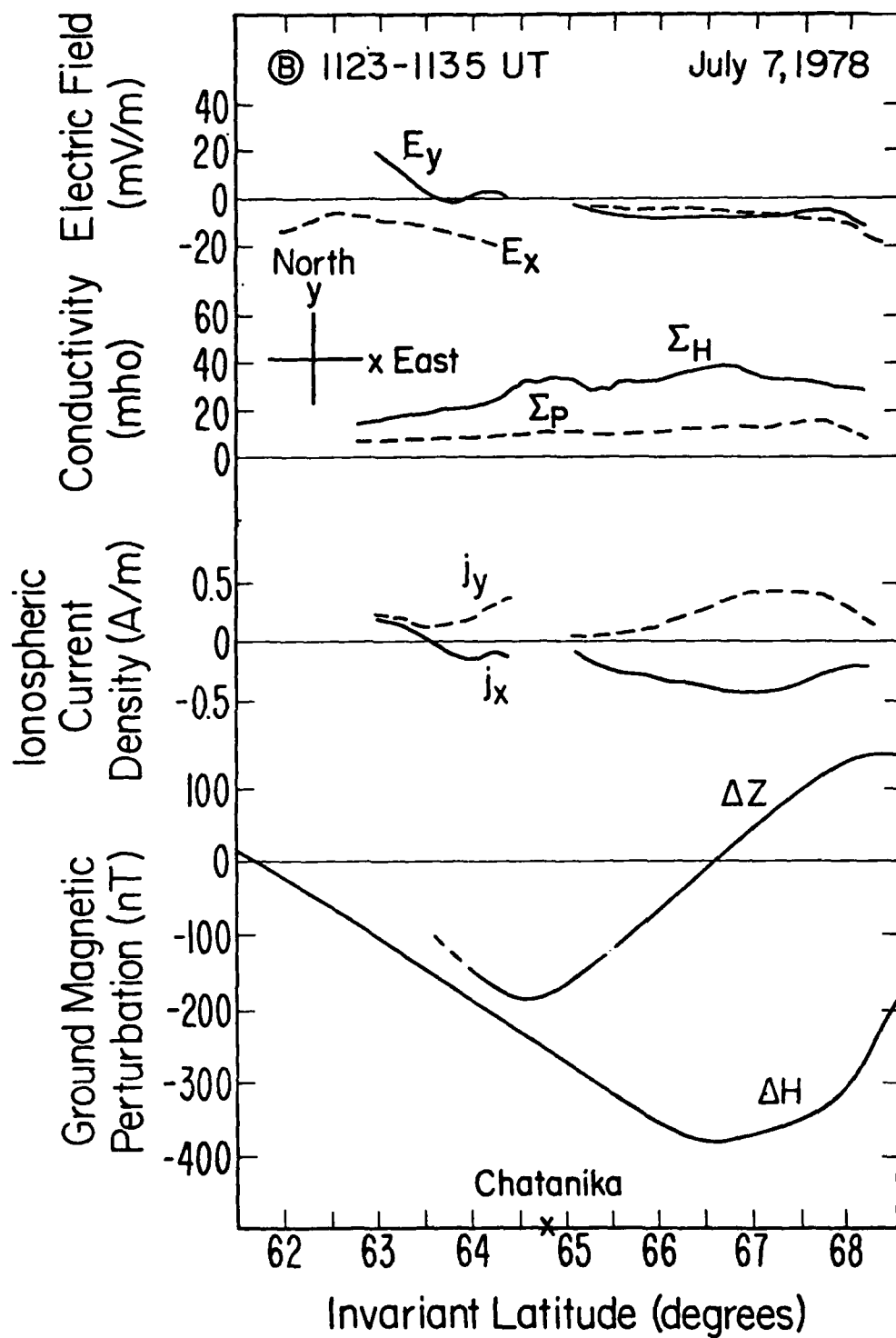
- Troschichev, O. A., "Polar magnetic disturbances and field-aligned currents," Space Sci. Rev., 31, in press, 1982.
- Tsunoda, R. T., R. I. Presnell, Y. Kamide, and S.-I. Akasofu, "Relationship of radar aurora, visual aurora, and auroral electrojets in the evening sector," J. Geophys. Res., 81, 6005, 1976b.
- Vickrey, J. F., R. R. Vondrak, and S. J. Matthews, "The diurnal and latitudinal variation of auroral zone ionospheric conductivity," J. Geophys. Res., 86, 65, 1981.
- Vickrey, J. F., R. R. Vondrak, and S. J. Matthews, "Energy deposition by precipitating particles and Joule dissipation in the auroral ionosphere," J. Geophys. Res., 87, 5184, 1982.
- Vondrak, R. R., "Incoherent-scatter radar measurements of electric field and plasma in the auroral ionosphere," in High Latitude Space Plasma Physics, co-edited by B. Hultqvist and T. Hagfors, in press, Plenum Press, New York, 1982.
- Vondrak, R. R., and M. J. Baron, "Radar measurements of the latitudinal variation of auroral ionization," Radio Sci., 11, 939, 1976.
- Wedde, T., J. R. Doupnik, and P. M. Banks, "Chatanika observations of the latitudinal structure of electric fields and particle precipitation on November 21, 1975," J. Geophys. Res., 82, 2743, 1977.
- Wolf, R. A., "Calculations of magnetospheric electric fields," in Magnetospheric Physics, edited by B. M. McCormac, pp. 167, D. Reidel, Hingham, Mass., 1974.
- Ziesolleck, C., W. Baumjohann, K. Brüning, C. W. Carlson, and R. I. Bush., "Comparison of height-integrated current densities derived from ground-based magnetometer and rocket-borne observations during the porcupine F3 and F4 flights," J. Geophys. Res., 87, in press, 1982.
- Zmuda, A. J., and J. C. Armstrong, "The diurnal flow of field-aligned currents," J. Geophys. Res., 79, 4611, 1974b.

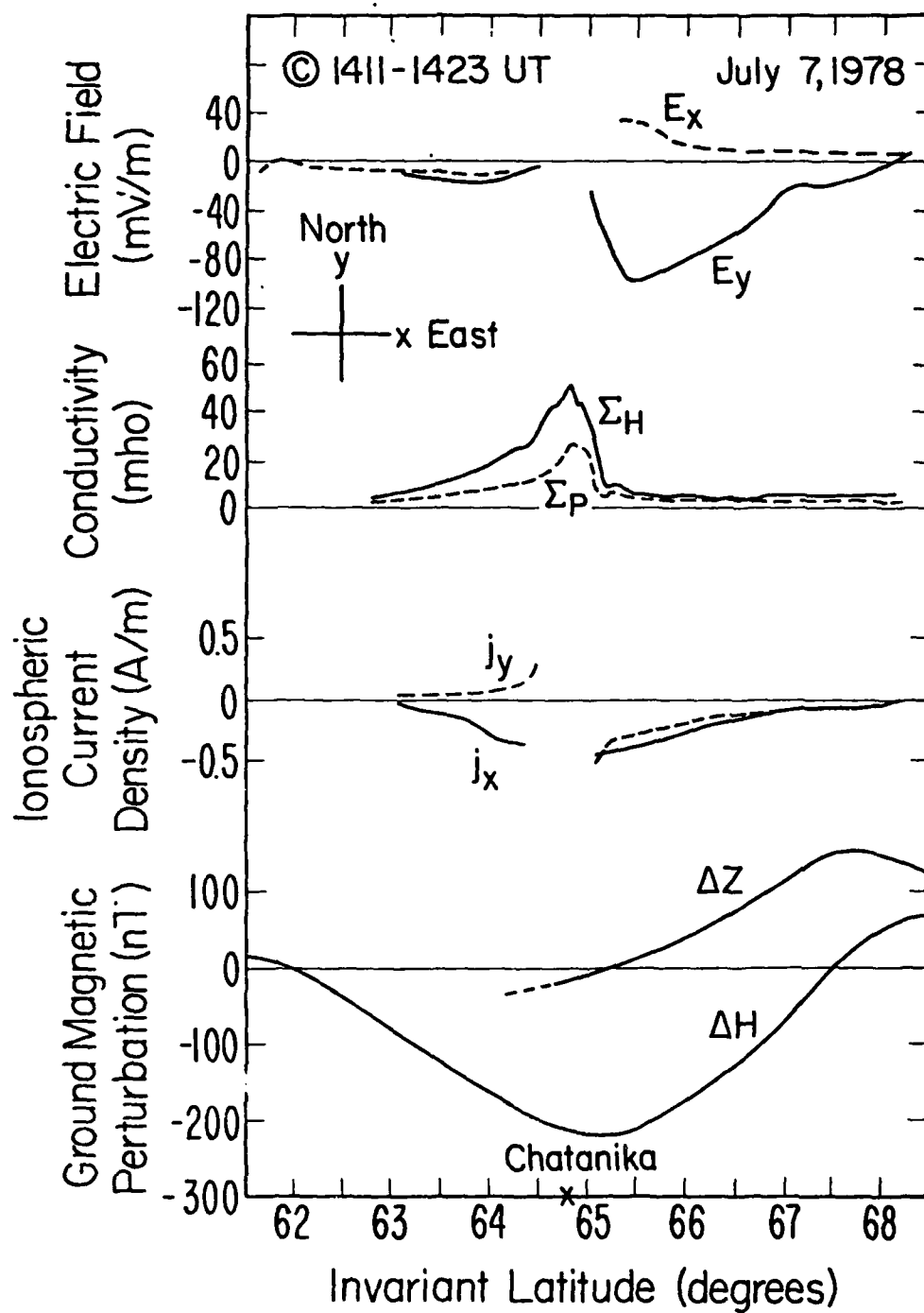
### FIGURE CAPTIONS

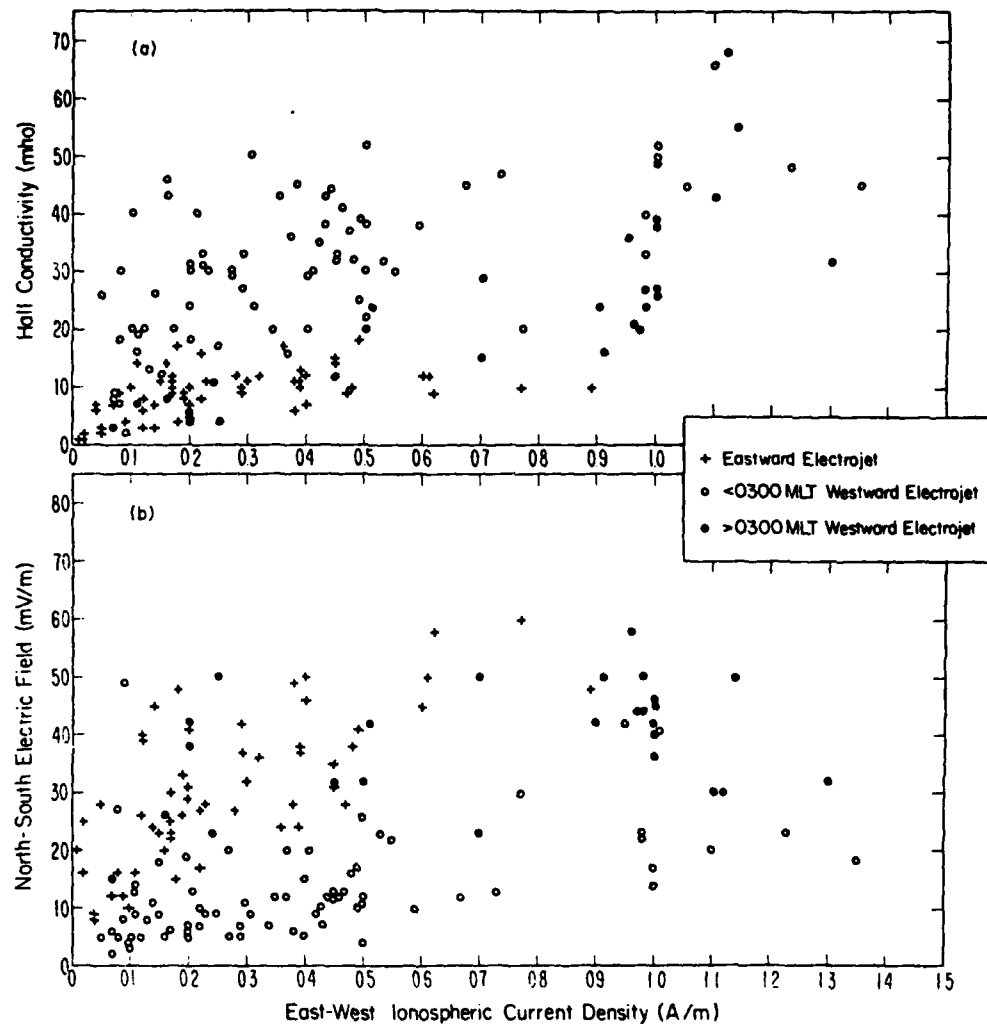
- Fig. 1 H component records from the IMS Alaska meridian chain of magnetometers for July 7, 1978. For code names of stations, see Table 1. AE (12) from Kamei and Maeda (1981) is also shown. Three vertical lines A, B and C indicate three times for which detailed latitudinal profiles of the auroral electrojet parameters are given in Figures 2a, b and c, respectively.
- Fig. 2a Latitudinal profiles of the electric field, conductivity, ionospheric current, and ground magnetic perturbations for 0938-0950 UT on July 7, 1978.
- Fig. 2b Same as Figure 2a, except for time: 1123-1135 UT.
- Fig. 2c Same as Figure 2a except for time: 1411-1423 UT.
- Fig. 3 (a) Dependence of the east-west ionospheric current on the Hall conductivity. (b) Dependence of the east-west ionospheric current on the north-south electric field. Different symbols are used to differentiate the eastward and westward electrojets. Furthermore, the westward electrojet is grouped into two depending on whether it occurred before or after 0300 MLT. All points represent quantities at the latitudinal center of the auroral electrojets.
- Fig. 4 Ratio of the Hall conductivity to the strength of the north-south electric field in the eastward and westward electrojets plotted as functions of magnetic local time.
- Fig. 5 Variations of the electric field and height-integrated conductivities for April 16, 1973, in which intense substorms occurred successively. (After Kamide and Brekke, 1977.)
- Fig. 6 Schematic diagram showing the relative importance of the ionospheric conductivities and the electric fields in the eastward and westward electrojets.



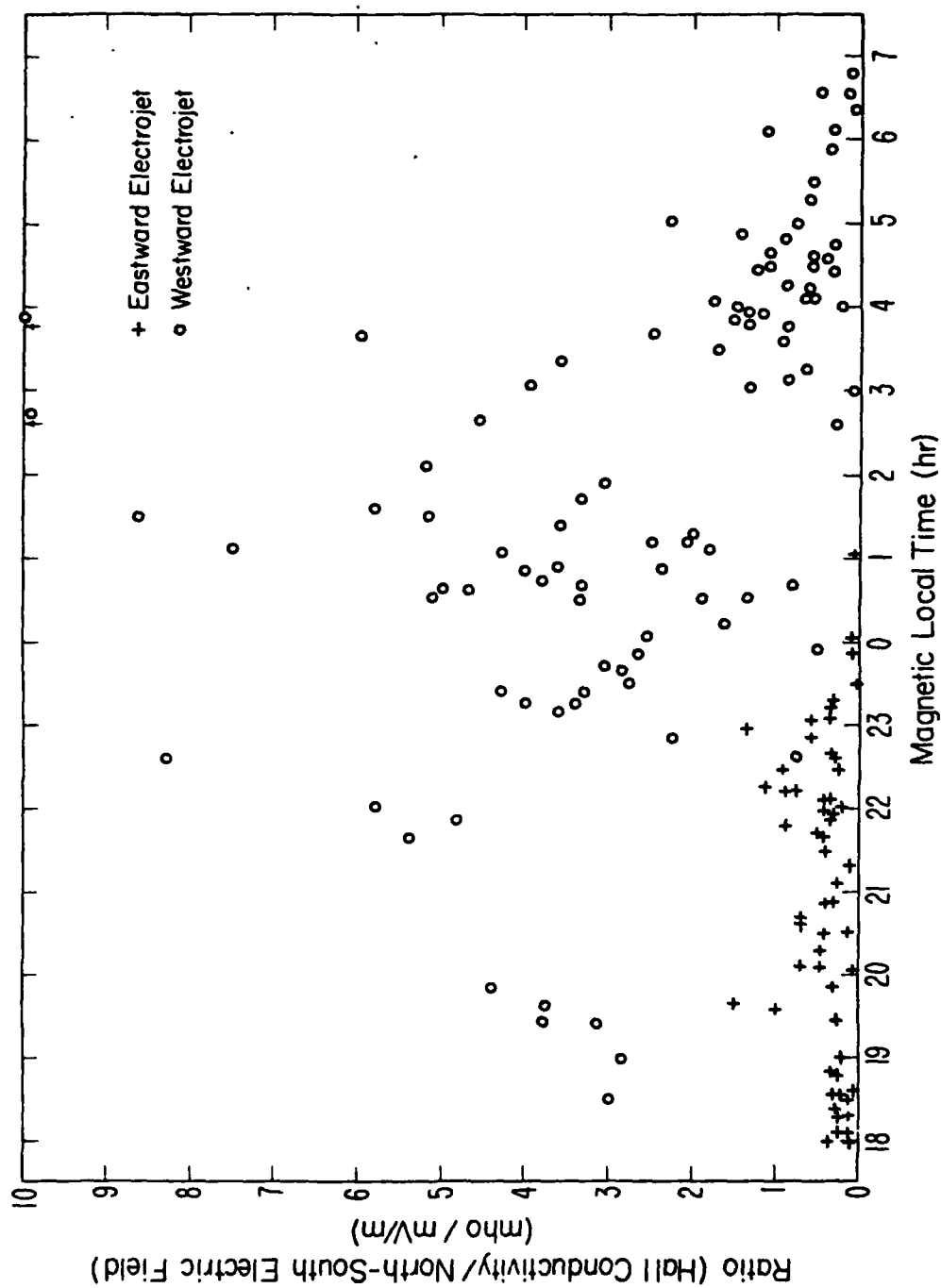


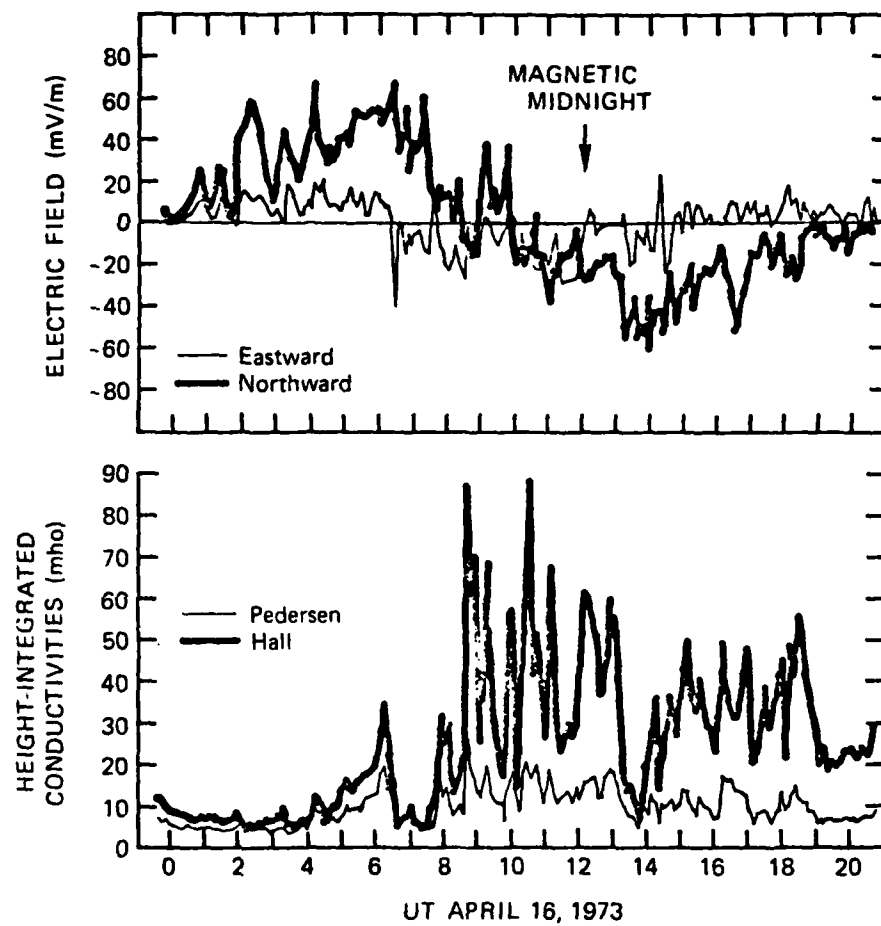


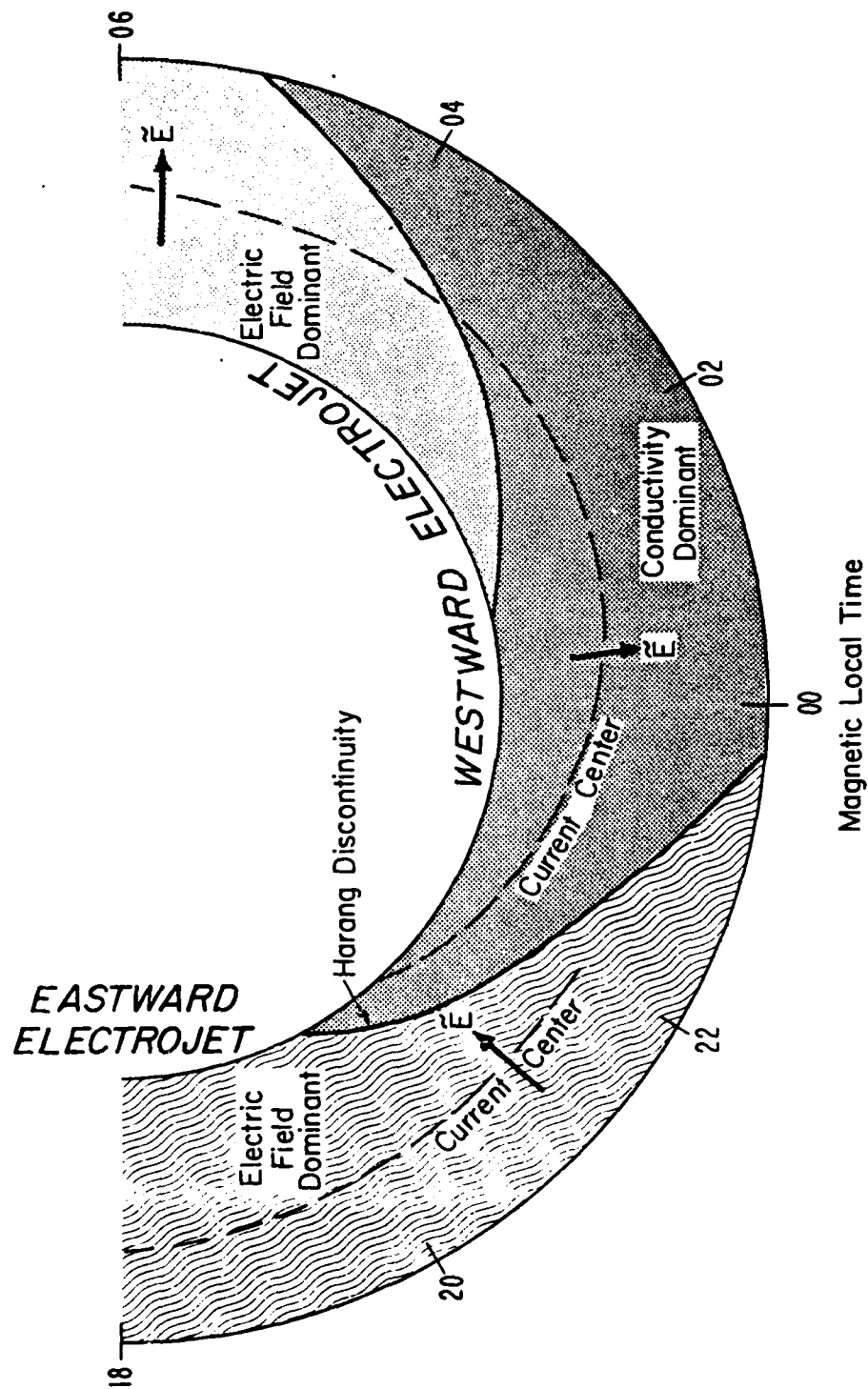












LOW-ALTITUDE IMAGE STRIATIONS ASSOCIATED WITH  
BOTTOMSIDE EQUATORIAL SPREAD F -- OBSERVATIONS AND THEORY

by

James F. Vickrey  
SRI International  
Radio Physics Laboratory  
Menlo Park, CA 94025

Michael C. Kelley and Robert Pfaff  
Cornell University  
School of Electrical Engineering  
Ithaca, New York 14853

ABSTRACT

Ionospheric plasma instabilities are usually discussed in terms of local parameters. However, because electric fields of scale size  $\lambda \gg 1$  km map along magnetic field lines, plasma populations far away from a locally unstable region may be affected by the instability process. An example is the formation of "image" striations in the E and  $F_1$  regions in response to the electric field produced in the unstable F layer above. The image results principally from a converging velocity field operating on a compressible ion gas. The theory of image formation, including its dependence on scale size, is discussed in detail. Rocket measurements of electron density irregularities are also presented. The spectrum of density structure observed off the magnetic equator is consistent with that expected from the image formation process (which is scale size and density dependent) driven by the gravitational Rayleigh-Taylor instability operating on the bottomside F layer at the equator itself.

## I INTRODUCTION

Ionospheric plasma instabilities are often discussed in terms of local parameters. However, magnetic field lines can link unstable regions to other plasma populations that may affect the evolution of the instability process. An example is the role of a conducting E region in diffusive damping of F-region structures and in the suppression of electrostatic instabilities [Volk and Haerendel, 1971; Goldman et al., 1976; Vickrey and Kelley, 1982].

Another effect most often studied in conjunction with F-region barium-cloud striations is the generation of image striations in the background medium. As discussed in more detail below, an image forms at altitudes where the ion gas is compressible, namely, the E and lower  $F_1$  regions. To date the existence of images has not been experimentally verified although computer simulations have predicted their generation [Goldman et al., 1976; Lloyd and Haerendel, 1973].

The data discussed here come from fixed bias Langmuir probes flown on two rockets launched just off the magnetic equator during equatorial spread F conditions. One, a Javalin sounding rocket, was launched by NASA from Natal, Brazil, on 18 November 1973 at 2122 UT [Kelley et al., 1976, 1979; Costa and Kelley, 1978]. The second, a Terrier-Malemute, was launched by the Defense Nuclear Agency from Kwajalein Atoll on 17 July 1979 at 1233 UT [Szuszcwicz et al., 1980; Rino et al., 1981; Kelley et al., 1982]. We will show that the spectrum of density structure observed in the  $F_1$ -layer valley (160 to 200 km altitude) off the magnetic equator is consistent with that expected from the image formation process (which depends on scale length and density) driven by the

gravitational Rayleigh-Taylor instability operating on the bottomside F layer at the equator itself.

## II DATA PRESENTATION

A plasma density profile from the downleg of the Natal rocket flight is reproduced in Figure 1(a) with an expanded plot of the F-layer valley and E-region density profiles in Figure 1(b). The plasma density profile was extremely structured throughout the flight. Near and just below the F-region peak, the turbulence has been interpreted in terms of the non-linear gravitational Rayleigh-Taylor instability [see earlier references]. The low-altitude (90 to 130 km) structure is the result of classic sporadic E layers and is not produced by the "image" process. Of interest to the present study are the quasi-sinusoidal fluctuations in the  $F_1$ -layer valley (170 to 200 km) where the zero-order vertical plasma density gradient nearly vanishes. Because of the finite dip angle at Natal, these fluctuations project along magnetic field lines to the magnetic equator at heights ranging from 280 km to 315 km. Note that this altitude range corresponds to heights where the local equatorial F region was unstable to the gravitational Rayleigh-Taylor process. The geometry is illustrated schematically in Figure 2.

Another example from the Plumex rocket downleg is presented in Figure 3. Again, quasi-sinusoidal oscillations were observed in the  $F_1$ -layer valley region at heights that map to the magnetic equator in the region at which local equatorial spread F was detected. Conversely, the electron density profiles reported by Morse et al., [1977] and Prakash [private communication, 1982], which were obtained very near the dip

equator in Peru and India respectively, showed no such structure in the  $F_1$ - layer valley. Thus, in all, five equatorial rocket flights have shown E-region structure or the lack thereof in a manner consistent with low altitude structure being formed by the image process.

A series of spectra corresponding to different altitude ranges from Figure 1 are presented in Figures 4 and 5. The Figure 4 spectra all correspond to bottomside equatorial spread F. The spectrum from the lowest altitude displays a form that varies as  $k^{-2}$  over the regime from  $\lambda = 5000$  m to  $\lambda = 50$  m, where the instrument noise level was reached. The highest altitude spectrum seems to have a somewhat shallower spectral form at the long wavelengths (500-5000 m). These results are in good agreement with the Plumex I results reported by Rino et al., [1981], and Kelley et al. [1982].

The  $F_1$  layer valley spectra in Figure 5 are quite different from those in Figure 4, as are the waveforms. The spectra peak between 2 and 3 Hz which corresponds to wavelengths of 700 to 1400 m. The peak in the spectra is consistent with the quasi-sinusoidal nature of the waveforms. We show in the next section that such a peak in the spectra should be expected on the basis of the image formation process.

### III ANALYSIS

#### A. The F-Layer Gravitational Rayleigh-Taylor Instability

The mechanisms whereby plasma irregularities are formed in the F-layer ionosphere can be studied by considering the continuity equation:

$$\frac{\partial n^F}{\partial t} + \nabla \cdot (n^F \mathbf{v}) = P - L \quad (1)$$

where  $n$  is the electron density,  $\underline{v}$  is the flow velocity,  $P$  the production rate and  $L$  the loss rate. In the nighttime F layer, the latter two terms can be ignored yielding

$$\frac{\partial n^F}{\partial t} + \underline{v} \cdot \underline{\nabla} n^F + n^F (\underline{\nabla} \cdot \underline{v}) = 0 \quad (2)$$

Ignoring variations along the direction of the magnetic field, the primary velocity is given by  $\underline{E} \times \underline{B}/B^2$ , which is divergence free, and thus

$$\frac{\partial n^F}{\partial t} = - \underline{v} \cdot \underline{\nabla} n \quad (3)$$

In effect, the irregularities are formed by incompressibly mixing an existing background density gradient by means of the perturbation electric fields generated in the instability process. These processes are reasonably well understood and well documented [see recent reviews by Fejer and Kelley (1980) and Ossakow (1981)]. For our purposes here, we need only describe the perturbation electric field (or equivalent velocity) structure in the unstable F layer because it is this structure that maps to lower altitudes and drives the image process.

It can be shown from nonlinear Rayleigh-Taylor instability theory with no zero order zonal electric field [Keskinen and Ossakow, 1981], that the electric-field and density fluctuations are related by

$$\delta E = \frac{gB}{v_{in}^F} \left[ \frac{\delta n}{n} \right]^F \quad (4)$$

where  $g$  is gravitational acceleration,  $B$  is the magnetic-field strength,  $v_{in}^F$  is the ion-neutral collision frequency, and  $\left[ \frac{\delta n}{n} \right]^F$  are density fluctuations such as those whose spectra are shown in Figure 3. Thus, the velocity



turbulence that drives image formation can be specified in terms of our measurements of the density fluctuations. Our goal then is to show that the spectrum of image irregularities observed is the result of a balance between this driver, which depends on scale size, and the image formation and diffusive damping processes, which are also scale size dependent. Equation (4) also applies to mid-latitude barium clouds if  $(g/v_{in}^F)$  is replaced by  $(E'/B)$ , where  $E'$  is the electric field measured in the neutral frame of reference.

The Rayleigh-Taylor process will not create structure in the F-layer valley if the zero-order density gradient vanishes. The electric field will still map to the region where density structure is observed, but with no density gradient the stirring will not produce structured density.

#### B. The Image Formation Process

To understand the formation of images, we must examine a more complicated version of the continuity equation. As will be discussed in more detail below, images form at altitudes where the incompressibility assumption utilized in Section III.A breaks down. Compressibility arises from non-negligible Pedersen drifts  $(v_P = \frac{\sigma_P}{nq} E)$ , which must be added to the  $\bar{E} \times \bar{B}$  flow considered above. Here  $\sigma_P$  is the Pedersen conductivity, which for E and F<sub>1</sub> layer heights, is given by

$$\sigma_P = \frac{nq^2 v_{in}^E}{m_i \Omega_i^2} \quad (5)$$

where  $q$  is the electron charge;  $m_i$  and  $\Omega_i$  are the ion mass and gyrofrequency, respectively; and  $v_{in}^E$  is the ion neutral collision frequency at

the image altitude. Throughout the following, the superscript E denotes quantities at the image altitude even though we are concentrating principally on the  $F_1$ -layer valley region. Additional complications to the continuity equation include the effects of relatively rapid cross-field plasma diffusion and chemical recombination. If we include these effects, Eq. (2) becomes

$$\frac{\partial n^E}{\partial t} + \left( \frac{\bar{g}}{v_{in}^E} + \frac{\bar{E} \times \bar{B}}{B^2} \right) \cdot \nabla_Z n^E - n_o^E \frac{q v_{in}^E}{m_i \Omega_i^E} \nabla \cdot \bar{E} - D_{\perp} \nabla_{\perp}^2 n^E - \alpha n_o^{E^2} = 0 \quad (6)$$

where we have ignored any horizontal variation in electron density but have, for completeness, included a vertical gradient term, which is weak in the valley region.  $D_{\perp}$  is the cross-field plasma diffusion rate and  $\alpha$  is the effective recombination coefficient. Dividing through by  $n_o^E$ , we obtain an expression for the linear growth rate of the image striation,  $\gamma_{image} = \frac{1}{n_o^E} \frac{\partial n^E}{\partial t}$ .

$$\gamma_{image} = \left( \frac{\bar{g}}{v_{in}^E} + \frac{\bar{E} \times \bar{B}}{B^2} \right) \cdot \frac{\nabla_Z n^E}{n_o^E} - \frac{q v_{in}^E}{m_i \Omega_i^E} \nabla_{\perp} \cdot \bar{E} - D_{\perp} \nabla_{\perp} \cdot \left( \frac{\nabla_{\perp} n^E}{n_o^E} \right) - \alpha n_o^E \quad (7a)$$

Thus, growth of images will occur if

$$\gamma_{image} = \gamma_{stir} + \gamma_{conv} - \gamma_{diff} - \gamma_{chem} > 0 \quad (7b)$$

Before discussing the physical significance of each of the terms we should recall that the electric field,  $\underline{E}$ , is the perturbation electric field associated with the driving instability operating on the bottom-

side F layer and mapped to the lower altitude image region. For the electric field fluctuations to map, they must be of scale sizes larger than several hundred meters [Farley, 1959]. Also, for the steady state conditions considered here, images must form at the same scale size as the driving F layer instability striations [see Vickrey and Kelley, 1982]. An additional subtlety of Eqs. (6) and (7a) is that we have assumed that  $D_{\perp}$  is independent of density so that we could bring it outside the divergence operator. In reality,  $D_{\perp}$  depends on electron density through electron-ion collisions, but at the altitudes of present interest this dependence is negligible when compared to the dependence on ion-neutral collisions.

The physical processes that compete to determine whether or not an image forms at a given scale size and background density may be described as follows: the stirring term  $v_{\text{stir}}$  in Eq. (7) can produce an image if plasma of different densities (from different heights in the equatorial situation) is mixed on a time scale that is short compared to the time it takes for the plasma to recombine. This time scale is determined by the magnitude of the mixing velocity and the steepness of the density gradient. In the present situation the density gradient of interest is the vertical scale height at the image altitude. However, because this scale height  $L_v$  was so large in the present case [ $L_v \sim 60$  km in Figure 1(a)], this term is important only at very large scales. It may be noteworthy for other situations, however, that the scale size dependence of  $v_{\text{stir}}$  is the same as that of the driving velocity fluctuations in the unstable F layer.

The second term in Eq. (7),  $\gamma_{\text{conv}}$ , represents the formation of an image due to a converging velocity field operating on the compressible ion gas. The electron gas is still incompressible at image altitudes and so electrons must flow up and down along magnetic field lines to maintain charge balance [Vickrey and Kelley, 1982]. The divergence operator introduces an additional scale-size dependence to the  $\gamma_{\text{conv}}$  term. Small-scale fluctuations in the velocity field form images more readily than do large-scale fluctuations of the same magnitude [Vickrey and Kelley, 1982]. As was the case with the stirring term, however, the convergence of plasma must proceed at a rate faster than the recombination rate in order for an image to form. Thus, as the background density is increased, smaller-scale image growth will be favored.

The term  $\gamma_{\text{chem}}$  in Eq. (7) represents chemical recombination of the image region plasma. At altitudes where the ion gas is compressible, the ionospheric ion composition tends to be dominated by molecular ions (i.e.,  $\text{NO}^+$  and  $\text{O}_2^+$ ). The recombination rate for these species varies as  $\alpha n^E$ , which produces a strong dependence on density in contrast to the F layer plasma where the driving instability operates. At F-layer heights the recombination rate of  $\text{O}^+$  is proportional to  $n^F$  instead of  $n^{F^2}$ . Hence, the time constant for recombination,  $\frac{1}{n_o} \frac{\partial n^F}{\partial t}$  is independent of electron density.

Now let us examine the scale-length dependence of the image growth rate expression. Making use of Eq. (4) we can Fourier Transform Eq. (7) to obtain

$$\gamma_{\text{image}}(k_o) = \left[ \frac{1}{L_v} \left( \frac{g}{v_{in}^F} + \frac{g}{v_{in}^E} \right) + \frac{v_{in}^E}{\Omega_i} \left( \frac{g}{v_{in}^F} \right) k_o \right] \left[ \int_{k_o - \Delta k/2}^{k_o + \Delta k/2} P^2(k) dk \right]^{\frac{1}{2}} - k_o^2 D_{\perp} - 2\alpha n_o \quad (8)$$

where  $P(k) = \frac{\delta n_F}{n_0}(k)$ . The spectra in Figure 3 are well represented by

$$P^2(k) = \frac{1}{1 + \left(\frac{k}{k_c}\right)^2} = \frac{1}{1 + 2.6 \times 10^4 k^2} \quad (m) \quad (9)$$

corresponding to  $k_c = 6.2 \times 10^{-3} \text{ m}^{-1}$ .

Figure 6 shows plots of  $\gamma_{\text{image}}(k)$  versus  $k$  for typical F-layer valley conditions corresponding to the observations discussed above, i.e.,  $v_{\text{in}}^E / \Omega_i = 0.1$ ,  $g/v_{\text{in}}^F = 100 \text{ ms}^{-1}$ ,  $D_{\perp} = 10 \text{ m}^2 \text{ s}^{-1}$ , and  $\alpha = 5 \times 10^{-8} \text{ cm}^3 \text{ s}^{-1}$  [Vickrey et al., 1982]. It is important to point out that the detailed shape of the curve as well as the magnitude of  $\gamma(k)$  depends on the choice of the integration interval  $\Delta k$  in Eq. (8). To produce the figures we have chosen values of  $\Delta k$  that are roughly equal to the bandwidth of the observed irregularity spectrum. This interval represents a "band-pass" of driving fluctuation wavenumbers about the image scale size of interest. Because the choice of integration interval is arbitrary, one should not attach too much significance to the magnitude of the growth rates in Figure 6. Nonetheless, the theoretical prediction of a narrow band of preferred image scale size is very significant. A comparison of the curves labeled (a) and (b) in Figure 6 illustrates the effect of doubling the integration interval  $\Delta k$ . As one would expect, the growth rate increases for all scales with the integration interval. Also, the most preferred value of  $k$  increases, but only by about twenty percent. Thus, the prediction of a preferred scale is not highly sensitive to the integration interval chosen.

The scale size dependence of the image growth rate also depends, of course, on the irregularity spectrum of bottomside spread F,  $P^2(k)$ , which

is assumed to drive the image process. To examine the sensitivity of  $\gamma_{\text{image}}(k)$  to the assumed spectral shape, we have halved and doubled the value of  $k_c$  in Eq. (9) to construct curves (c) and (d) in Figure 6. The integration interval was the same as for curve (a). As can be seen in the figure, even these rather dramatic changes in the driving spectral characteristics do not drastically change the preferred scale size produced. Our best estimate of the conditions appropriate to the observations presented above corresponds to curve (a) which predicts a preferred image scale of  $\sim 750$  m. This prediction is in good agreement with the preferred irregularity scale sizes shown in Figure 5. One must keep in mind, however, that while a peaked growth rate is conceptually pleasing in a process that ultimately results in a narrow spectrum of density irregularities, there is no fundamental reason why the fully developed (nonlinear) density spectrum should necessarily match the linear growth rate exactly.

In order to determine whether the magnitude of the predicted image growth rates is significant, we can compare it to the linear growth rate of the driving process,  $\gamma_{\text{RT}}$ . Thus,

$$R = \frac{\gamma_{\text{conv}}}{\gamma_{\text{RT}}} = \frac{k_o \left( \frac{v_{in}^E}{\Omega_i} \right) \left( \frac{g}{v_F} \right) \left( \frac{\delta n}{n} \right) \Delta k}{\left( \frac{g}{v_{in}^F} \right) \left( \frac{1}{L_F} \right)} \quad (10)$$

where  $L_F$  is the zero-order vertical gradient on the bottomside of the F layer, and

$$\left(\frac{\delta n}{n}\right)\Delta k = \left[ \int_{k_o - \Delta k/2}^{k_o + \Delta k/2} P^2(k) dk \right]^{\frac{1}{2}} \quad (11)$$

Because  $\left(\frac{\delta n}{n}\right)\Delta k$  is about 5 percent in the bandpass interval of the observed images,  $(v_{in}^E/\Omega_i) \sim 0.1$ ,  $L_F \sim 20$  km, and the value of  $k_o$  at the peak of the image growth rate is  $\sim 10^{-2} \text{ m}^{-1}$ ,  $R \approx 1$ . Thus, the growth of images should occur on a similar time scale to that of the "parent" striations. We show below that  $\gamma_{\text{image}}$  is even faster at lower altitudes for comparable electron densities. Thus, because the occurrence of bottomside spread F is well known and documented, the formation of image striations should not be too surprising.

Although we have no direct observations of image formation in the E region, the process should proceed more rapidly there [provided the density is low enough, e.g., Vickrey and Kelley, (1982)] because the ion gas is more compressible at E-region heights. In Figure 7 we have calculated the image growth rate  $\gamma_{\text{image}}(k)$  for E-region conditions; i.e.,  $v_{in}/\Omega_i = 1$ ,  $D_{\perp} = 100 \text{ m}^2 \text{ s}^{-1}$ , and  $\alpha = 2 \times 10^{-7} \text{ cm}^{-3} \text{ s}^{-1}$  [Vickrey et al., 1982]. The integration interval and  $k_c$  are the same as curve (a) on Figure 6. We find, as at higher altitudes, a preferred image scale size of  $\sim 700$  m is produced. In this case, however, the image growth rate is approximately two orders of magnitude faster than at  $F_1$  layer altitudes provided the electron density is comparable.

#### IV DISCUSSION AND APPLICATION

In this paper we have presented what we believe is the first direct evidence for the formation of image irregularities in the ionospheric

medium. We have also computed a linear growth rate for the structures and find that the  $k$  dependence matches the observed spectrum quite well.

The case we have studied involves images of F-region irregularities created by the Rayleigh-Taylor process in equatorial spread F. A similar analysis should apply however, to mid-latitude barium-cloud striations, which should also create E-region images in the same scale-size regime as presented here. For example, Kelley et al. [1979] showed that power spectral measurements in a striated barium cloud matched quite closely the bottomside spread F spectrum measured in the Natal flight discussed here both in absolute magnitude and scale size. Thus, E-region structures should have formed with comparable scales to those reported here and with growth rates on the order of seconds.

At auroral latitudes the application is not so clear because the chemical damping term,  $\alpha n_0$ , is larger than at mid-latitudes owing to particle precipitation. Exceptions might be in the winter polar cap or in the region just equatorward of the diffuse auroral zone where the E-region density should be comparable to mid-latitude values.

ACKNOWLEDGEMENT: This work was supported by the Defense Nuclear Agency and the Air Force Office of Scientific Research.



# REFERENCES

- Costa, E., and M. C. Kelley, "On the Role of Steepened Structures and Drift Waves in Equatorial Spread F," J. Geophys. Res., 83, 4359, 1978.
- Farley, D. T., Jr., "A Theory of Electrostatic Fields in a Horizontally Stratified Ionosphere Subject to a Vertical Magnetic Field," J. Geophys. Res., 64, 1225, 1959.
- Fejer, B. G., and M. C. Kelley, "Ionospheric Irregularities," Rev. Geophys. & Space Phys., 18, 401, 1980.
- Goldman, S. R., L. Baker, S. L. Ossakow, and A. J. Scannapieco, "Striation Formation Associated with Barium Clouds in an Inhomogeneous Ionosphere," J. Geophys. Res., 81, 5097, 1976.
- Kelley, M. C., G. Haerendel, H. Kappler, A. Valenzuela, B. B. Balsley, D. A. Carter, W. L. Ecklund, C. W. Carlson, B. Hausler, and R. Torbert, "Evidence for a Rayleigh-Taylor Type Instability and Upwelling of Depleted Density Regions During Equatorial Spread F," Geophys. Res., Lett., 3, 48, 1976.
- Kelley, M. C., K. D. Baker, and J. C. Ulwick, "Late Time Barium Cloud Striations and their Relationships to Equatorial Spread F," J. Geophys. Res., 84, 1898, 1979.
- Kelley, M. C., R. Pfaff, K. D. Baker, J. C. Ulwick, R. Livingston, C. Rino and R. Tsunoda, "Simultaneous Rocket Probe and Radar Measurements of Equatorial Spread F--Transitional and Short Wavelength Results," J. Geophys. Res., 87, 1575, 1982.
- Keskinen, M. J., and S. L. Ossakow, "On the Spatial Power Spectrum of the E X B Gradient Drift Instability in Ionospheric Plasma Clouds," J. Geophys. Res., 86, 6947, 1981.
- Lloyd, J. H., and G. Haerendel, "Numerical Modeling of the Drift and Deformation of Ionospheric Plasma Clouds and of their Interaction with Other Layers of the Ionosphere," J. Geophys. Res., 78, 7389, 1973.

#### REFERENCES concluded

- Morse, F. A., B. C. Edgar, H. C. Koons, C. J. Rice, W. J. Heikkila, J. H. Hoffman, B. A. Tinsley, J. D. Winningham, A. B. Christensen, R. F. Woodman, J. Pomalaza, and R. N. Teixeira, "Equion, An Equatorial Ionospheric Irregularity Experiment," J. Geophys. Res., **72**, 578, 1977.
- Ossakow, S. L., "Spread-F Theories--A Review," J. Atmos. Terr. Phys., **43**, 437, 1981.
- Rino, C. L., and J. Owen, "The Structure of Localized Nighttime Auroral-Zone Scintillation Enhancements," J. Geophys. Res., **85**, 2941, 1980.
- Rino, C. L., R. T. Tsunoda, J. Petriceks, R. C. Livingston, M. C. Kelley and K. D. Baker, "Simultaneous Rocketborne Beacon and in situ Measurements of Equatorial Spread F--Intermediate Wavelength Results," J. Geophys. Res., **86**, 2411, 1981.
- Szuszcwicz, E. P., R. T. Tsunoda, R. Narcisi, and J. C. Holmes, "Coincident Radar and Rocket Observations of Equatorial Spread F," Geophys. Res. Lett., **7**, 537, 1980.
- Vickrey, J. F., and M. C. Kelley, "The Effects of a Conducting E Layer on Classical F Region Cross-Field Plasma Diffusion," J. Geophys. Res., **87**, 4461, 1982.
- Vickrey, J. F., R. R. Vondrak, and S. J. Matthews, "Energy Deposition by Precipitating Particles and Joule Dissipation in the Auroral Ionosphere," J. Geophys. Res., **87**, 5184, 1982.
- Volk, H. J., and G. Haerendel, "Striations in Ionospheric Ion Clouds, 1," J. Geophys. Res., **76**, 4541, 1971.

## FIGURE CAPTIONS

- Figure 1 (a) Downleg of the Natal Rocket Flight  
(b) Expanded Plot of F-Layer Valley and E-Region Density Profiles
- Figure 2 Schematic Diagram of the Magnetic Field Geometry
- Figure 3 Plumex Rocket Downleg
- Figure 4 (a) Spectrum of Irregularities between 303 and 322 km altitude  
(b) Spectrum of Irregularities between 294 and 312 km altitude  
(c) Spectrum of Irregularities between 267 and 287 km altitude
- Figure 5 (a) Spectrum of Irregularities Observed Between 194 and 204 km Altitude  
(b) Spectrum of Irregularities Observed Between 173 and 184 km Altitude
- Figure 6 Wavelength Dependence of the Image Growth Rate for  $F_1$  Region Valley Altitudes. The various curves illustrate the sensitivity of the results to changes in the integration interval  $\Delta/k$  and driving spectrum  $P(k)$ . (see text)
- Figure 7 Wavelength Dependence of the Image Growth Rate for E-Region Altitudes

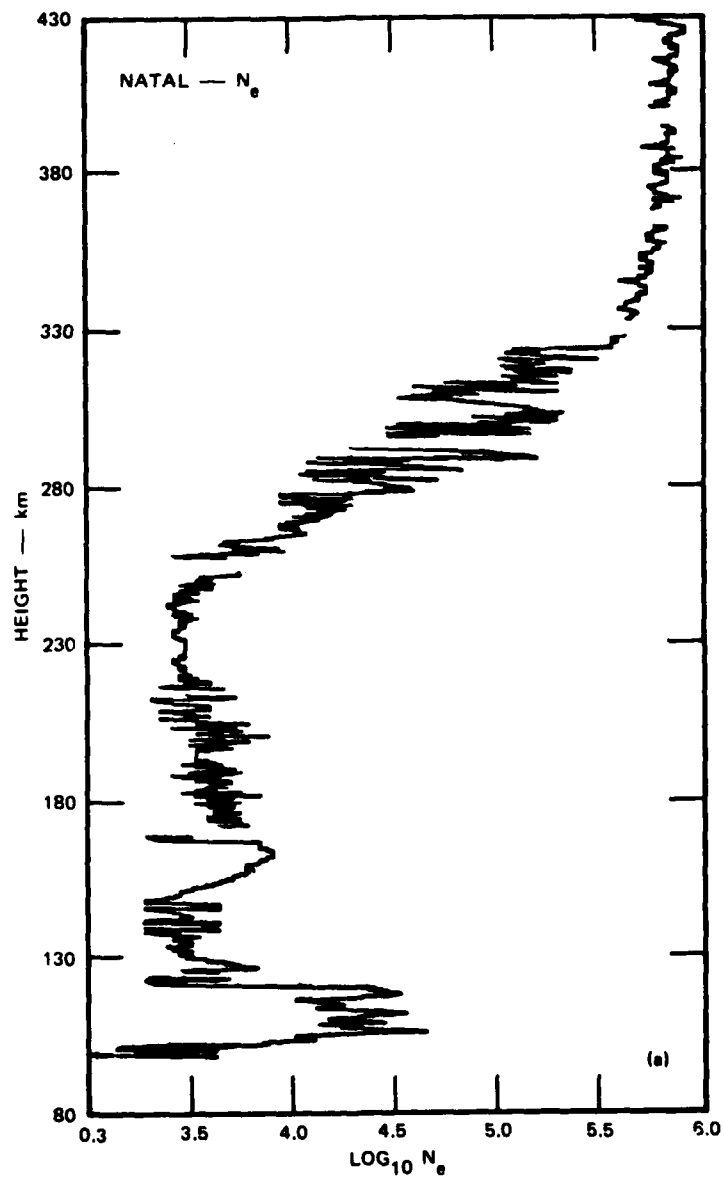


Figure 1(a) Downleg of the Natal Rocket Flight

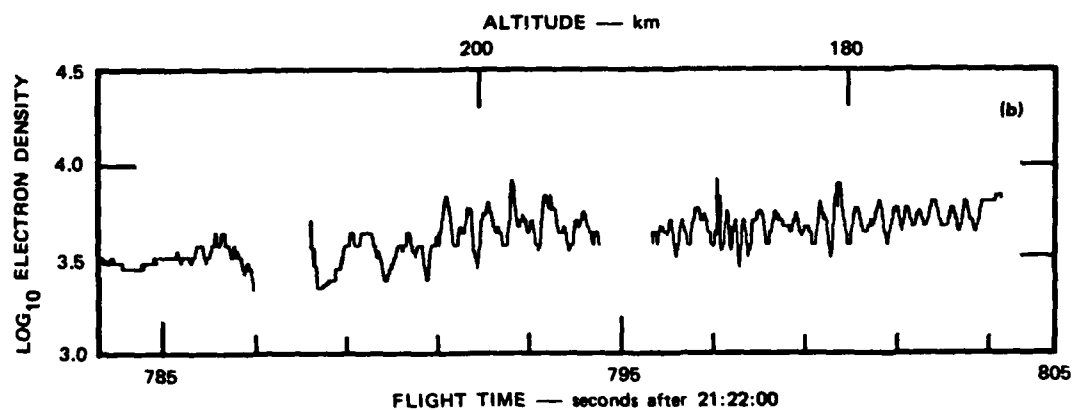


Figure 1(b) Expanded Plot of F-Layer Valley and E-Region Density Profiles

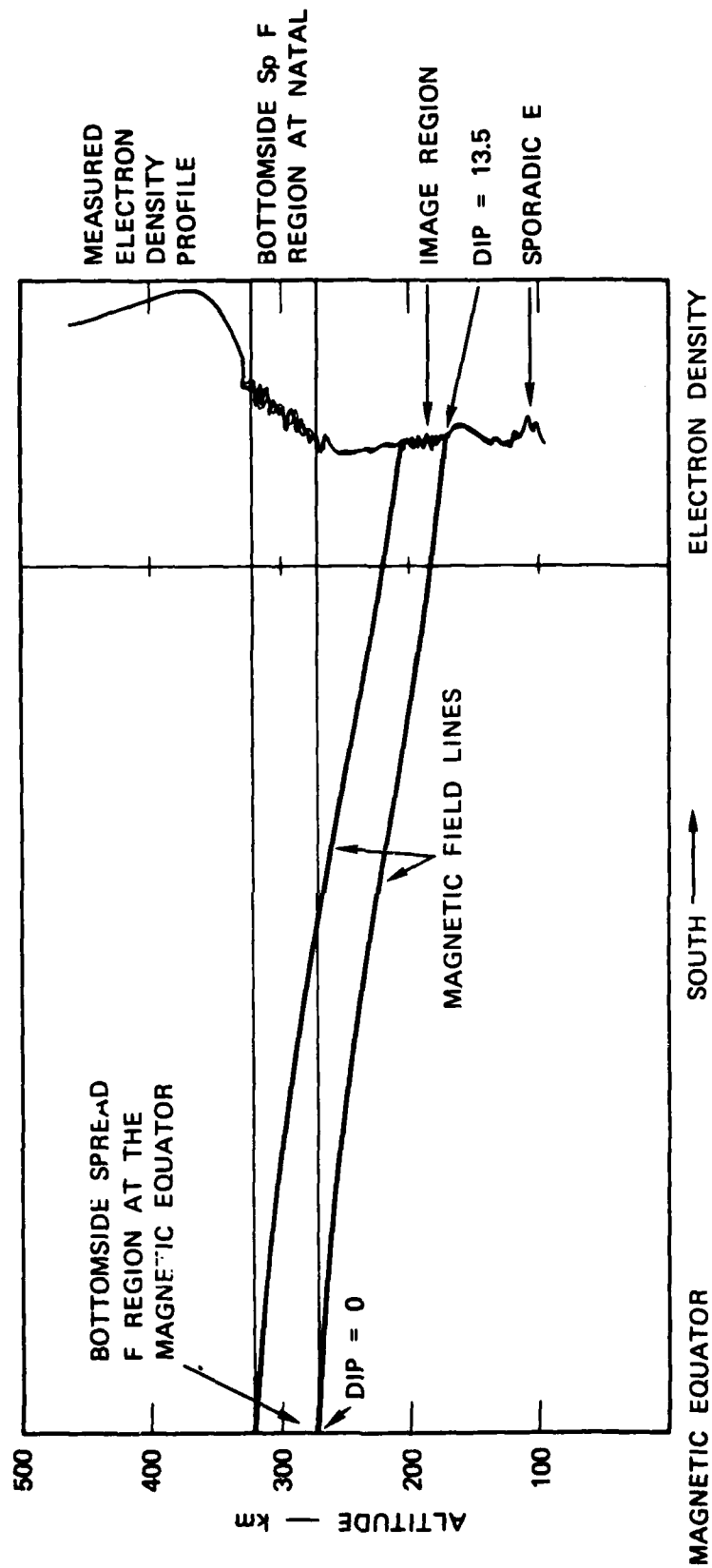


Figure 2 Schematic Diagram of the Magnetic Field Geometry

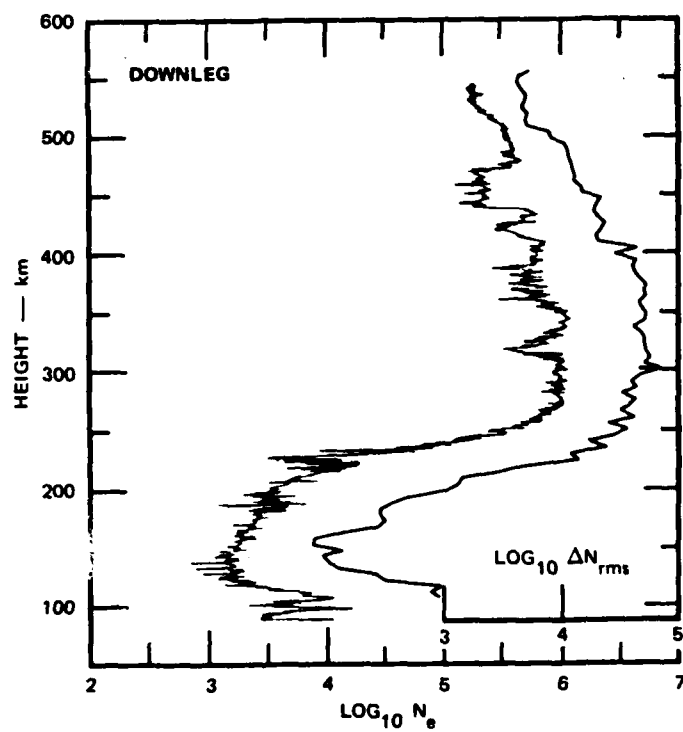


Figure 3 Plumex Rocket Downleg

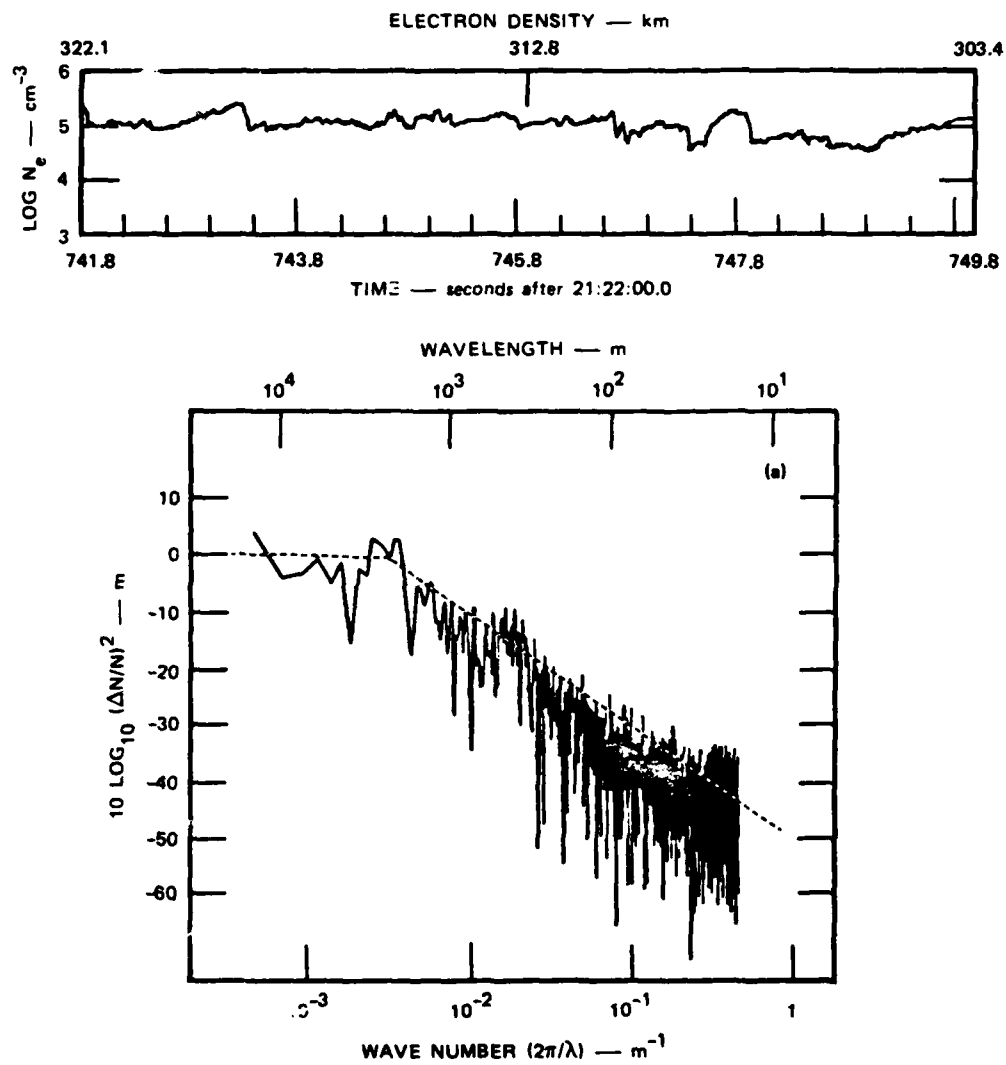


Figure 4(a) Spectrum of Irregularities Between 303 and 322 km Altitude



AD-A128-612

LATITUDINAL VARIATIONS OF AURORAL-ZONE IONIZATION  
DISTRIBUTION(U) SRI INTERNATIONAL MENLO PARK CA

3/3

J F VICKREY ET AL. FEB 83 AFOSR-TR-83-0389

UNCLASSIFIED

F49620-80-C-0014

F/G 4/1

NL

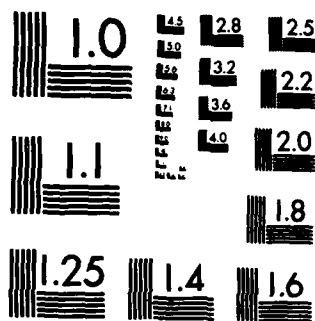


END

DATE

FILED

DTIC



MICROCOPY RESOLUTION TEST CHART  
NATIONAL BUREAU OF STANDARDS-1963-A

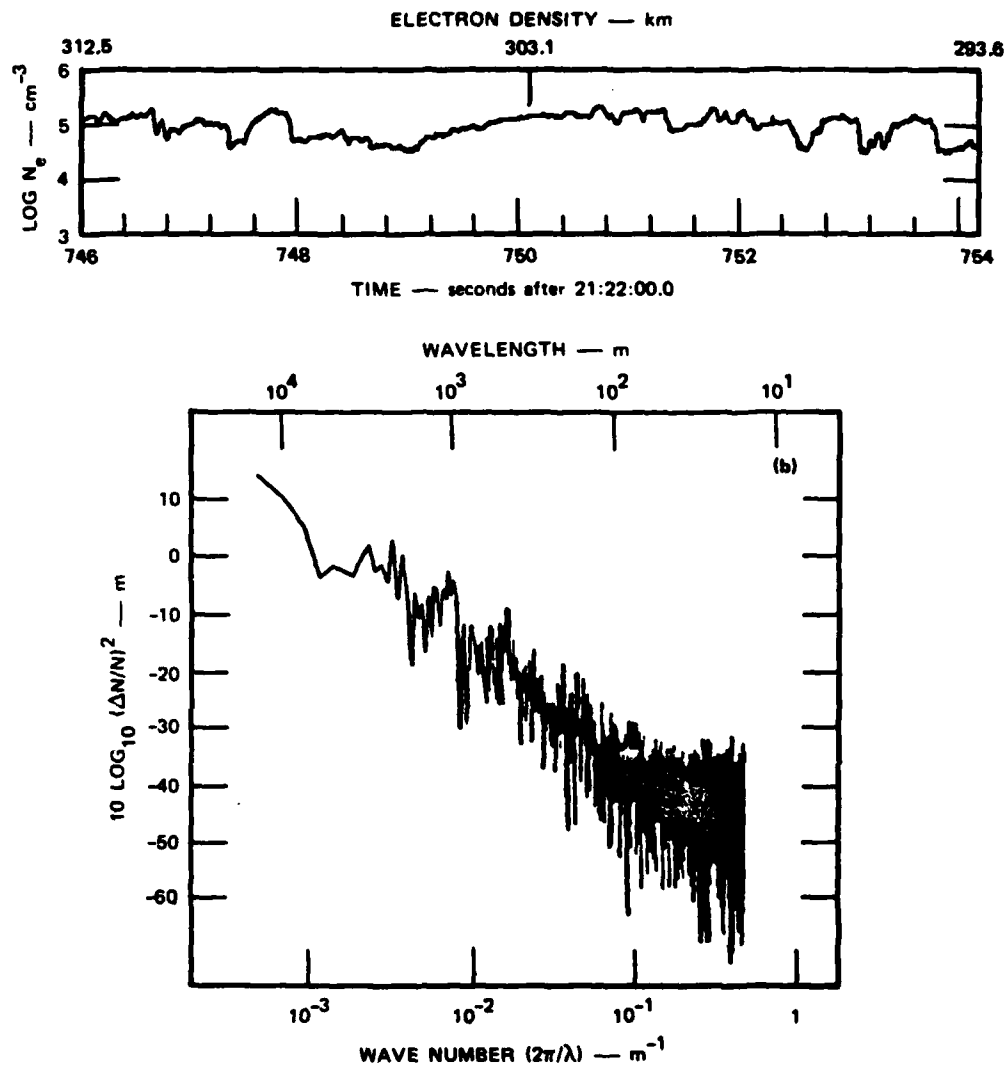


Figure 4(b) Spectrum of Irregularities Between  
294 and 312 km Altitude

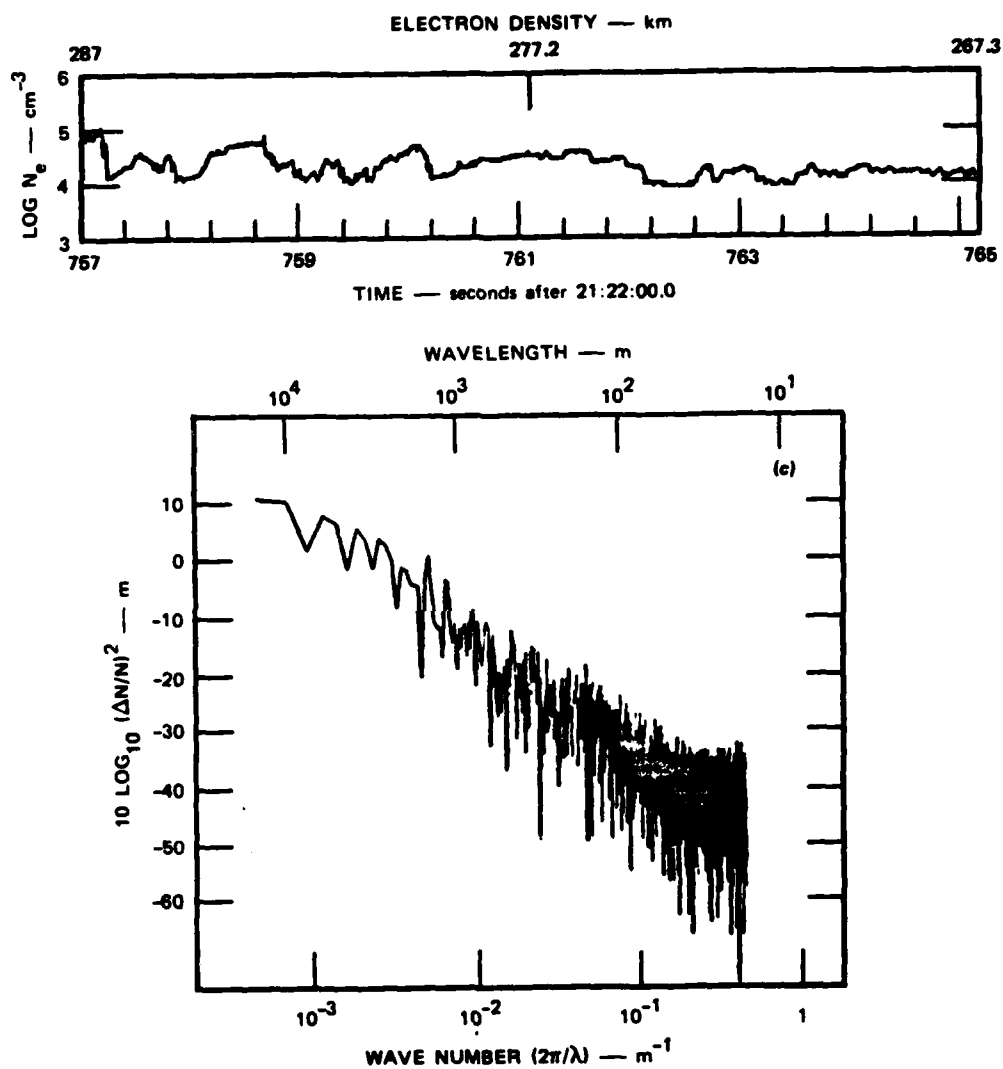


Figure 4(c) Spectrum of Irregularities Between 267 and 287 km Altitude

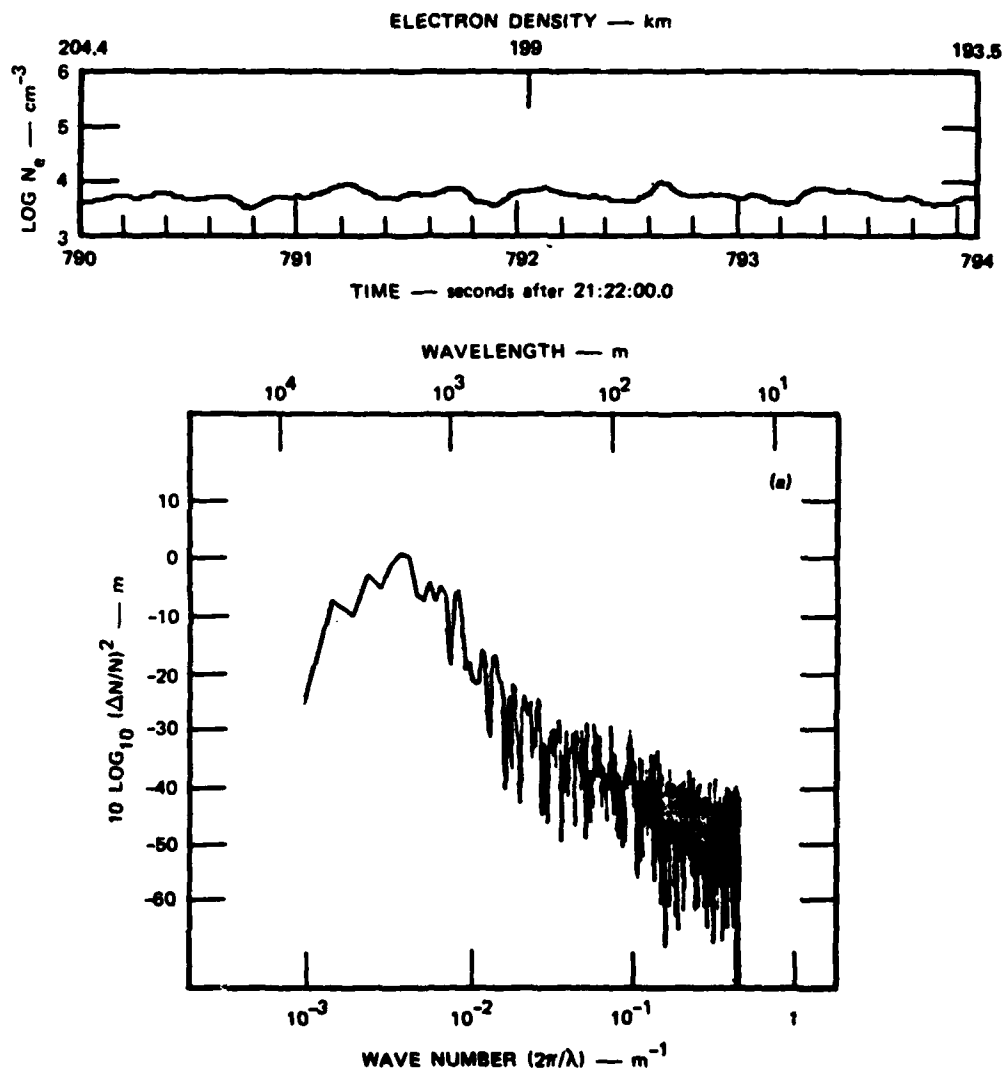


Figure 5(a) Spectrum of Irregularities Observed  
Between 194 and 184 km Altitude

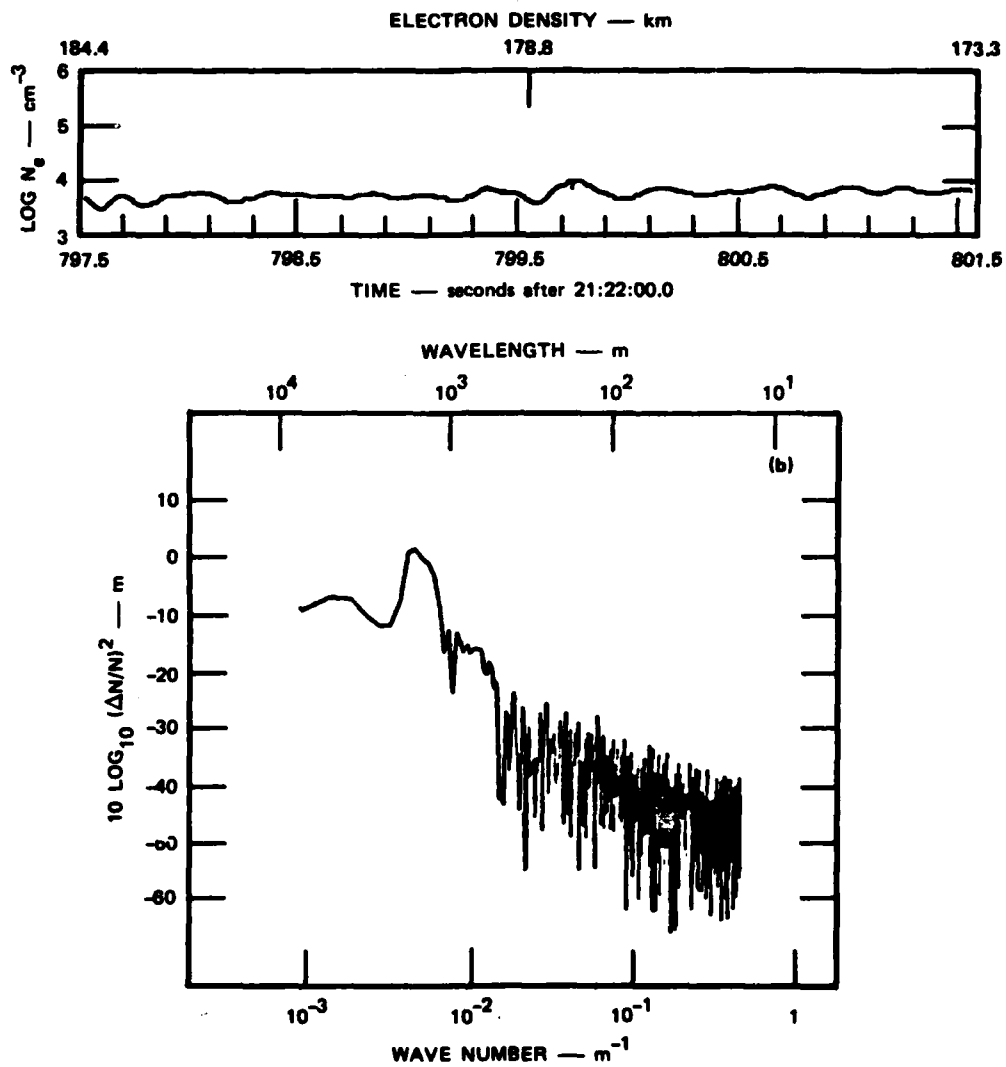


Figure 5(b) Spectrum of Irregularities Observed Between 173 and 184 km Altitude

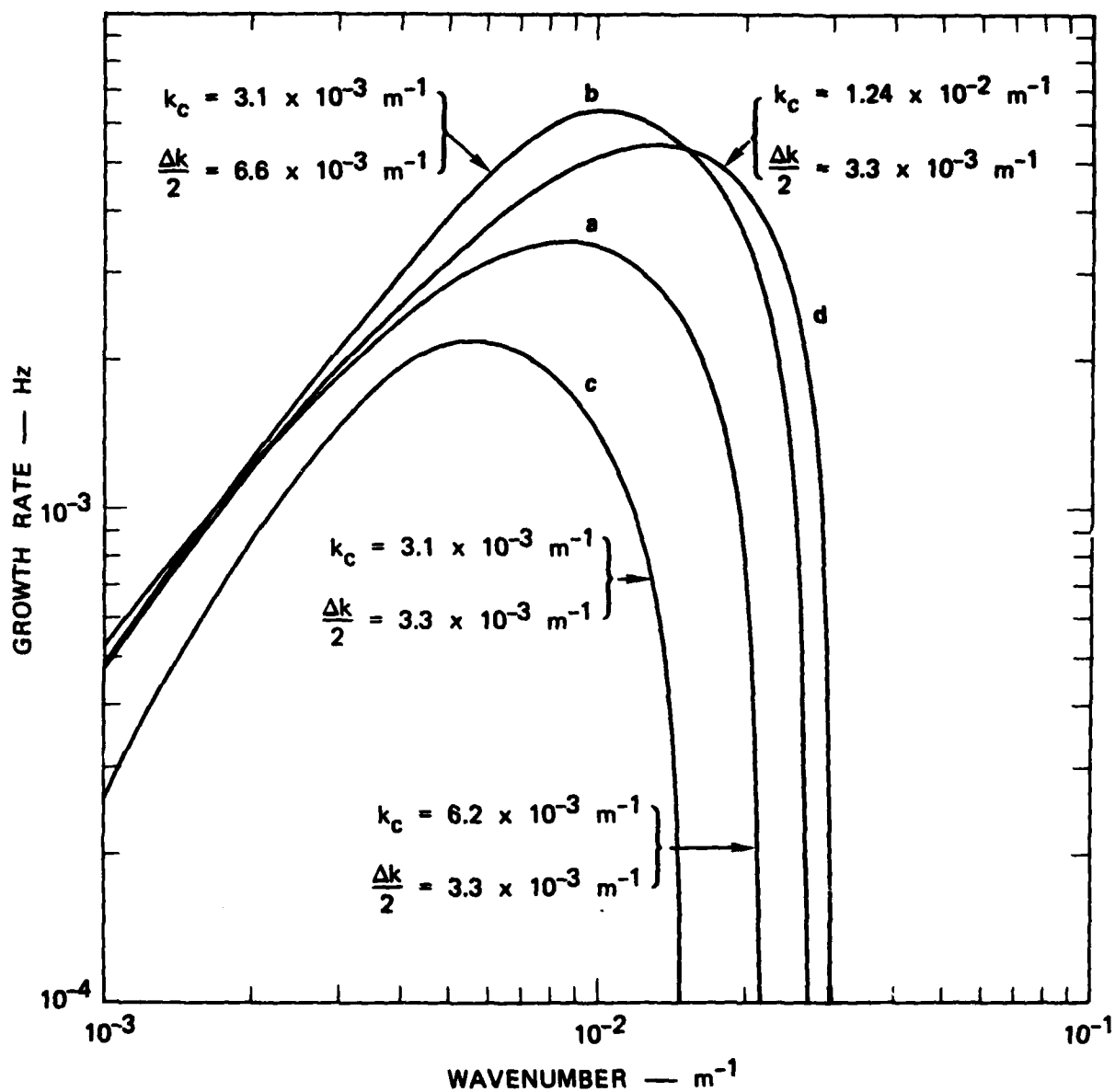


Figure 6 Wavelength Dependence of the Image Growth rate for F<sub>1</sub> Region Valley Altitudes. The various curves illustrate the sensitivity of the results to changes in the integration interval  $\Delta/k$  and driving spectrum  $P(k)$ .

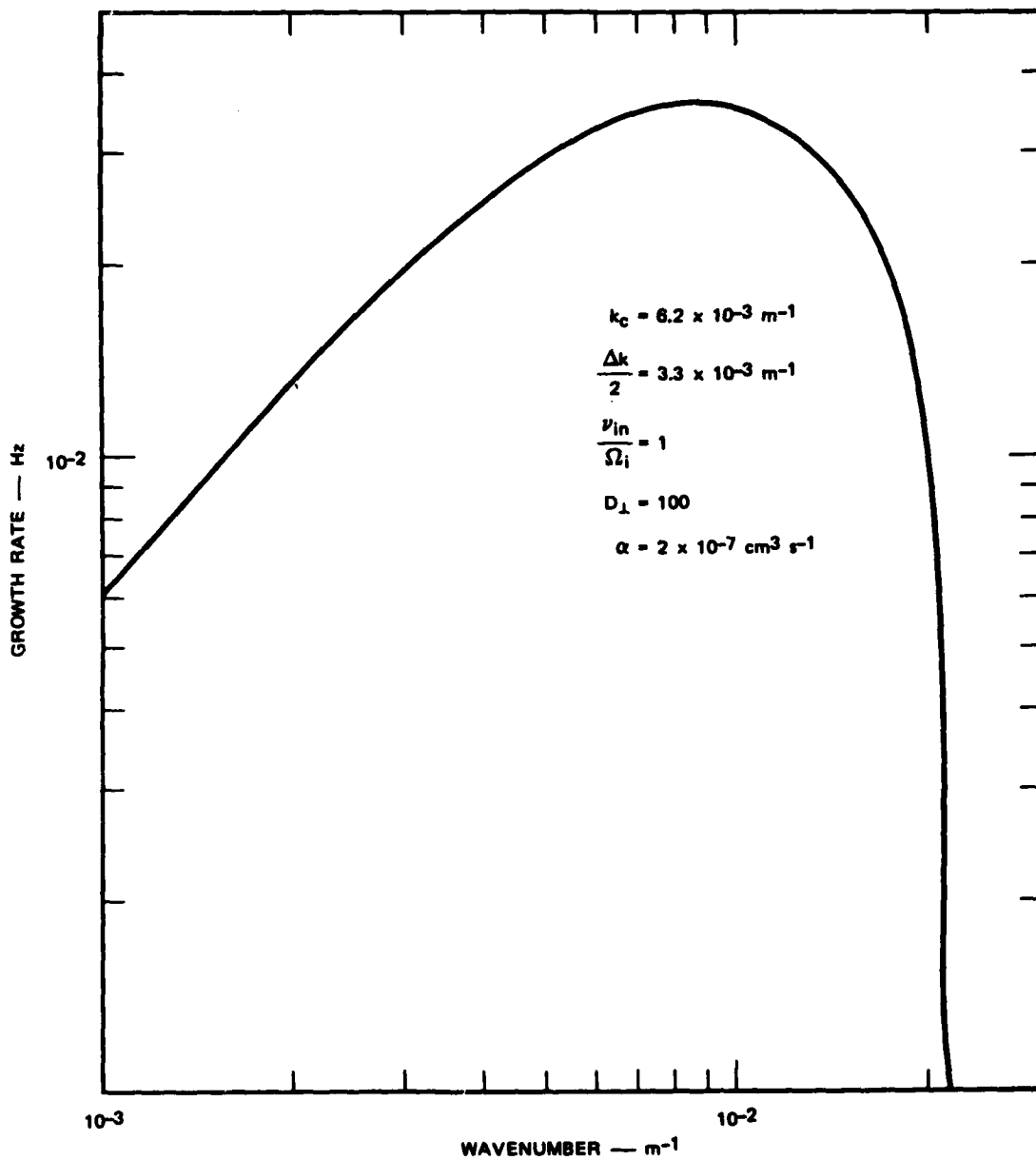


Figure 7 Wavelength Dependence of the Image Growth Rate for E-Region Altitude